Measurement of same-sign W boson pair production and a study of polarization fractions in $W^{\pm}W^{\pm}$ final states with the ATLAS experiment at $\sqrt{s} = 13$ TeV

a Dissertation

submitted to
University of Freiburg
in partial fulfillment of the requirements for the degree of
Doctor rerum naturalium

by

Prasham Jain

universität freiburg

University of Freiburg
Physikalisches Institut
Hermann-Herder-Str. 3
79104 Freiburg, GERMANY.

13 February, 2026

Supervisor: Prof. Dr. Beate Heinemann

© Prasham Jain 2026

All rights reserved

Dean
Prof. Dr. Annette Huber-Klawitter

Supervisor
Prof. Dr. Beate Heinemann

Date of defense: 13 February, 2026

Defense examiners
Prof. Dr. Beate Heinemann
Prof. Dr. Karl Jacobs
Prof. Dr. Heidi Rzehak

Dissertation examiners
Prof. Dr. Beate Heinemann
Prof. Dr. Marc Shumann

Dekanin
Prof. Dr. Annette Huber-Klawitter

Betreuer der Arbeit
Prof. Dr. Beate Heinemann

Datum der mündlichen Prüfung: 13 February, 2026

Prüfer
Prof. Dr. Beate Heinemann
Prof. Dr. Karl Jacobs
Prof. Dr. Heidi Rzehak

Gutachter
Prof. Dr. Beate Heinemann
Prof. Dr. Marc Shumann

In loving memory, I dedicate this dissertation to my late grandfather Dr. Vimal Chand Jain, whose memory continues to inspire me to work hard, stay kind & humble.

Acknowledgments

Writing this doctoral dissertation has been a childhood dream and an incredibly challenging yet immensely rewarding journey. I owe my deepest gratitude to all those who have been a part of this significant chapter of my life.

To my supervisors, Prof. Dr. Beate Heinemann and Dr. Oleg Kuprash, your guidance and unwavering support have been the compass that steered me through the complexities of academic research. Your expertise, patience, and mentorship have not only shaped this dissertation but have also contributed significantly to my personal and professional growth. Your backing and patience have been crucial to my mental well-being, helping me stay balanced and focused.

The unexpected move towards the end of my PhD was certainly a challenge, but I am deeply grateful to Prof. Ingrid Maria-Gregor for ensuring such a smooth transition. I had the great fortune of working with Dr. Ludovica Aperio Bella, whose energy and passion for the field are palpable and infectious. I am also sincerely thankful to Dr. Chilufya Mwewa for her crucial support in achieving my final results.

A huge thank you to my friends and colleagues Prasanna, Saumil, Avani, José, Vlad, Daniel, Shalu, Ksenia, Jessica, Kim and Constantin. This dissertation is not just a product of my own effort but also a testament to the friendships that have sustained me, providing the encouragement and support necessary to reach this milestone. I am profoundly grateful for each of you and the roles you've played in shaping this accomplishment.

A special thanks to Mrs. Skorek for making my life in Germany possible. I am also grateful to Prof. Herten, Prof. Jakobs, and their groups for warmly welcoming me, for the fun lunches and BBQs.

To my family, your endless love and support have been my bedrock. I am profoundly grateful for your sacrifices and belief in my dreams. You all made *my* dream into *our* collective dream and

showered me with immense affection and care to actualize it. I hope I am able to return this love all throughout my lifetime.

To my life partner Shreya, your boundless patience, encouragement, and understanding have been my anchor. You've stood by me through the difficult times, the moments of frustration, and the celebrations of small victories. Your unwavering belief in me and our shared dreams have been the driving force behind my perseverance. I am eagerly waiting for our future together.

I also wish to extend my gratitude to all my teachers, colleagues, and everyone who played a part, no matter how small, in this academic endeavor. Throughout my doctoral journey, I had the incredible opportunity to work with and learn from amazing women, strengthening my belief that science needs more women.

This Ph.D. journey has been a collective effort, and this dissertation is a testament to the incredible support and love that have surrounded me. I am truly blessed to have such an amazing network of people in my life.

Abstract

Vector boson scattering offers a sensitive test of electroweak symmetry breaking, particularly through the scattering of longitudinally polarized W bosons whose amplitudes are regulated by the Higgs mechanism. Same-sign $W^{\pm}W^{\pm}jj$ production provides a clean environment for studying this process due to its distinctive topology and large quark-induced contribution.

This dissertation presents a measurement of the longitudinal-longitudinal (LL) contribution to $W^{\pm}W^{\pm}jj$ scattering using the full Run 2 ATLAS proton–proton dataset at $\sqrt{s} = 13$ TeV, corresponding to 139 fb^{-1}. Events are selected in the fully leptonic final state and analyzed using a profile likelihood fit with independent LL and transverse signal-strength parameters.

The expected sensitivity corresponds to a one-standard-deviation probe of the Standard Model LL contribution. In data, no significant LL excess is observed. The fitted LL signal strength yields an observed longitudinal fraction of $f_{LL}^{\text{obs}} = 0.02^{+0.06}_{-0.05}$, consistent with both zero and the Standard Model expectation of $f_{LL}^{\text{SM}} = 0.096$. The corresponding fiducial cross section is $\sigma_{LL}^{\text{fid, obs}} = 0.05^{+0.19}_{-0.17}$ fb, and a one-sided 95% confidence-level upper limit of $f_{LL} < 0.15$ is set. The measurement is dominated by statistical uncertainties, with systematic effects found to be subdominant.

These results represent an important step toward isolating the LL scattering amplitude. With the increased luminosity of Run 3 and the High-Luminosity LHC, significantly improved precision—and potentially the first observation of the LL component—is expected.

Zusammenfassung

Die Streuung von Vektorbosonen bietet einen empfindlichen Test des elektroschwachen Symmetriebruchs, insbesondere durch die Streuung longitudinal polarisierter W-Bosonen, deren Amplituden durch den Higgs-Mechanismus reguliert werden. Die Produktion von gleichnamigen $W^{\pm}W^{\pm}jj$-Ereignissen stellt aufgrund ihrer charakteristischen Topologie und des großen quarkinduzierten Beitrags ein sauberes Umfeld zur Untersuchung dieses Prozesses dar.

Diese Dissertation präsentiert eine Messung des longitudinal–longitudinalen (*LL*) Beitrags zur $W^{\pm}W^{\pm}jj$-Streuung unter Verwendung des vollständigen ATLAS Run 2 Datensatzes von Proton–Proton-Kollisionen bei $\sqrt{s} = 13$ TeV, entsprechend 139 fb^{-1}. Ereignisse im vollleptonischen Endzustand werden selektiert und mit einem Profil-Likelihood-Fit analysiert, der unabhängige Signalstärkenparameter für *LL* und transversale Beiträge verwendet.

Die erwartete Sensitivität entspricht einem Ein-Standardabweichungs-Test des Standardmodell-*LL*-Beitrags. In den Daten wird kein signifikanter *LL*-Überschuss beobachtet. Die gefittete *LL*-Signalstärke führt zu einem beobachteten longitudinalen Anteil von $f_{LL}^{\text{obs}} = 0.02^{+0.06}_{-0.05}$, konsistent sowohl mit Null als auch mit der Standardmodellvorhersage von $f_{LL}^{\text{SM}} = 0.096$. Der entsprechende fiduzielle Wirkungsquerschnitt beträgt $\sigma_{LL}^{\text{fid, obs}} = 0.05^{+0.19}_{-0.17}$ fb, und es wird ein einseitiges 95%-Konfidenzniveau-Oberlimit von $f_{LL} < 0.15$ gesetzt. Die Messung wird von statistischen Unsicherheiten dominiert, während systematische Effekte untergeordnet sind.

Diese Ergebnisse stellen einen wichtigen Schritt zur Isolierung der *LL*-Streuamplitude dar. Mit der erhöhten Luminosität von Run 3 und des High-Luminosity LHC wird eine deutlich verbesserte Präzision — und möglicherweise die erste Beobachtung der *LL*-Komponente — erwartet.

List of Tables

2.1 Gauge quantum numbers of the Standard Model fields. 8

3.1 Comparison of predicted cross sections for fully leptonic final states in EW and QCD processes. Table also presents the EW-to-QCD cross-section ratio. 27

5.1 Configuration parameters for the modules relevant to trim settings, detailing both chip-level and channel-level settings. 51

7.1 Summary of single-lepton triggers used in the analysis. 70
7.2 Baseline (or preselected) and signal lepton selections. IP denotes Impact Parameter. 72
7.3 Event selection criteria for the Signal Region. Note that $\ell = e/\mu$. 75
7.4 Event selection criteria for the $W^{\pm}Z$ control region. Note that $\ell = e/\mu$. The characteristic selections of the region are given in blue color. 76
7.5 Event selection criteria for the fiducial signal region. Note that $\ell = e/\mu$. The characteristic selections of the region are given in blue color. 77

10.1 Summary of the LHC Run 2 ATLAS data-taking periods, including average pile-up and integrated luminosities. "Delivered" refers to the luminosity provided by the LHC, "Recorded" to luminosity successfully recorded by ATLAS, and "Good for Physics" to data passing ATLAS data quality requirements. 97
10.2 A summary of the Standard Model Monte Carlo samples used as signal in the analysis. 98
10.3 Comparison of cross sections, polarization fractions, and generated MC events for MadGraph and Sherpa samples. Event counts correspond to selections in the particle-level phase space. The numbers for Sherpa are from Ref. [1]. 98
10.4 A summary of the Standard Model Monte Carlo samples used as background in the analysis. 99
10.5 A summary of the Standard Model Monte Carlo samples used as prompt lepton sources in the data-driven estimation of the non-prompt and fake background. . . 99

11.1 Complete list of variables considered in this study. Definitions given for one instance apply analogously to all similar variables. 103
11.2 DNN hyperparameters optimized using `Optuna`. 109
11.3 Best hyperparameter configurations for each DNN architecture, obtained from 1000 `Optuna` trials per model, selected to maximize the significance Z as defined in Eq. 11.4. 111

12.1 Comparison of statistical-only and statistical plus flat systematic (10%) uncertainties for the expected and observed fiducial cross sections. 128
12.2 Summary of the expected and observed fit results for the longitudinal (LL) and transverse (TX=TL+TT) polarization components in the $W^{\pm}W^{\pm}jj$ electroweak process. All uncertainties are statistical only. The 95% CL upper limits (UL) are derived assuming a one-sided Gaussian approximation. 129

F.1 Yields of the analysis (Asimov pre-fit). 160

List of Figures

2.1 Overview of the prarticle content of the Standard Model of Particle Physics. . . . 4
2.2 Visual representation of Higgs mexican hat potential $V(H)$ of the complex scalar field. . . . 9
2.3 NNPDF3.1 parton distribution functions of a proton evaluated at two different energy scales. . . . 14
2.4 Illustration of a hadron-hadron collision event simulated with a MC event generator. 16

3.1 A typical illustration of vector boson scattering process at leading order 20
3.2 Role of Higgs boson in preserving unitarity 21
3.3 Cross section as a function of center of mass energy in $V_LV_L \to V_LV_L$ scattering with and without Higgs contribution 22
3.4 Overview of multiple Standard Model total and fiducial production cross-section measurements conducted with the ATLAS experiment 23
3.5 Schematic Feynman diagram illustrating VBS EW $VVjj$ processes at the LHC. . 24
3.6 Representative Feynman diagrams: VBS EW $VVjj$ production. 24
3.7 Representative Feynman diagrams: non-VBS EW $VVjj$ production 25
3.8 Representative Feynman diagrams: QCD $VVjj$ production 26
3.9 Branching ratios (in %) for some of the common W,Z boson decay modes 27
3.10 A simplistic picturisation of VBS $W^{\pm}W^{\pm}jj$ event topology 28
3.11 Contributing perturbative orders of the $VVjj$ process at LO and NLO at the LHC 29
3.12 Visual depiction of leptonic W^+ boson decay ($W^+ \to \ell^+\nu$) 31
3.13 For $W^+ \to \ell^+\nu$, differential cross section in $\cos\theta$ is shown for all W polarizations according to theory predictions 31
3.14 Visual depiction of the $W^{\pm}W^{\pm}jj$ process in partonic and diboson center-of-mass frames of references. 32

4.1 Existing CERN accelerator complex. 36
4.2 Luminosity summary results for 2011-2025. 38
4.3 Schedule of the LHC and HL-LHC operation. 39
4.4 Schematic view of the ATLAS detector at the LHC. 40
4.5 The ATLAS coordinate system. 41
4.6 The ATLAS Inner Detector. 42
4.7 A schematic of the ATLAS calorimeter. 44
4.8 The ATLAS Muon Spectrometer. 45
4.9 The ATLAS magnet system. 46
4.10 Schematic of the ATLAS trigger and data acquisition system in Run 2. 48

5.1 ASIC response schematic. . . . 50
5.2 The effect of application of trim settings. . . . 52
5.3 Graphs of trim against *vt50* for each chip, each channel and best range. . . . 52
5.4 Trim vs. channel and trim step histograms for each chip. . . . 53
5.5 Fit defects: channels representing Dead and Under defect. . . . 55
5.6 Pre-fit scan of the problematic channel showing the occupancy *S*-curve. . . . 56
5.7 One of the threshold scans shows an irregular non-linear curve. Implementation of a *vt50* value check for all channels at the fit-level. . . . 56
5.8 Trim–channel plots with a channel with problematic *vt50* value in a chip is shown before and after applying the mask. . . . 57

6.1 Visualization of a track. . . . 60
6.2 Illustration of particle detection in ATLAS. . . . 61
6.3 A schematic view of the passage of an electron through the various detector layers depicting the technique of electron reconstruction [2]. . . . 62
6.4 Different kinds of muons reconstructed in the ATLAS detector [3]. . . . 64
6.5 Illustration of the anti-k_t clustering algorithm forming a conical structure around the highest-momentum track. . . . 65
6.6 Distributions of the outputs of the DL1r *b*-tagging algorithm for *b*-jets, *c*-jets and light-flavour jets in $t\bar{t}$ simulated events. . . . 66

8.1 Expected yields in the Signal Region according to Ref. [4] . . . 79
8.2 A schematic illustrating the two main sources of electron charge misidentification: Fig. 8.2(a) illustrates incorrect track-to-electron association, and Fig. 8.2(b) shows mismeasurement of track curvature. Figs. taken from [5]. . . . 83
8.3 Schematic illustration of (a) muon and (b) electron fake leptons. In Fig. 8.3(a), a partial ATLAS cross section shows fake and non-prompt muons leaving signals comparable to real muons. In Fig. 8.3(b), the detector cross section excluding the MS shows fake and non-prompt electrons producing lepton-like calorimeter deposits in the ECal and HCal, leading to misidentification. Figs. taken from [6]. 86

9.1 Observed $\cos\theta$ distributions for mixed polarization modes (LT and TL) showing incorrect polarization assignment for final states with τ leptons. Note that 0 denotes L in plot legend. . . . 92
9.2 $\cos\theta$ distributions for mixed polarization modes (LT and TL) after applying the fix. Clear agreement can be seen between the syntaxes. Note that 0 denotes L in the plot legend. . . . 94

10.1 A schematic overview of the ATLAS data and Monte Carlo processing chains. The data path is shown on the left and the MC production path on the right. The final PAOD samples from both data and simulation are used as inputs to the analysis. Fig. taken from [6]. . . . 96

11.1 Distributions of variables m_{jj} and Δy_{jj} in the Signal Region. . . . 102
11.2 Correlation matrix displaying the correlation coefficients (in %) between the variables. . . . 105
11.3 Pictorial representation of a DNN for classification . . . 105
11.4 Illustration of commonly used activation functions that introduce non-linearity into neural networks, enabling them to model complex patterns. . . . 106

11.5 The effect of dropout regularization technique. . . . 107
11.6 Permutation feature importance algorithm showing ranks of input features after the first round of hyperparameter optimization . . . 110
11.7 ROC curve (left) and DNN output distribution (right) for signal and background, highlighting the 49-variable model's classification performance and discriminative power. . . . 111
11.8 Comparison of DNN classifier outputs after second round of hyperparameter optimization. . . . 112
11.9 DNN classifier output in the signal region for the 20-variable model. The signal is additionally shown as a red dashed line scaled by a factor 50 to enhance visibility relative to the background. . . . 113

12.1 A summary of the pre-fit yields in the signal and control regions under the partially blinded fit strategy. . . . 121
12.2 Signal strengths and the normalization factor of $W^{\pm}Z$-QCD obtained from the maximized likelihood fit on partially unblinded data. . . . 122
12.3 Asimov fit: Signal Region stat-only. . . . 122
12.4 A summary of the post-fit yields in the signal and control regions after unblinding. The total expectations agree with the observed data in the three regions. . . . 124
12.5 Signal strengths and the normalization factor of $W^{\pm}Z$-QCD obtained from the maximized likelihood fit on measured data. . . . 125
12.6 Unblinded fit: Signal Region stat-only. . . . 126

A.1 VBS diboson scattering involving W bosons. . . . 134
A.2 Scattering angle θ_1 between quarks q_1 and q_3. . . . 134

C.1 49-variable DNN performance plots. $Z = 2.2407$. . . . 144
C.2 5-variable DNN performance plots. $Z = 1.2513$. . . . 144
C.3 10-variable DNN performance plots. $Z = 1.6922$. . . . 145
C.4 20-variable DNN performance plots. $Z = 2.1249$. . . . 145
C.5 Validation loss (FI) ratio distributions are shown for all 49 variables after 500 permutations. They are all roughly Guassians and indicate sufficient statistics being used. . . . 146
C.6 Variables distributions of all 49 variables for signal (top) and backrounds (bottom). 147
C.7 Comparison of overlaid distributions for all 49 variables: raw distributions (top) and normalized distributions (bottom). . . . 148

D.1 Variable plots in Signal Region: Part 1. . . . 149
D.2 Variable plots in Signal Region: Part 2. . . . 150
D.3 Variable plots in Signal Region: Part 3. . . . 151
D.4 Variable plots in Signal Region: Part 4. . . . 152

F.1 Asimov fit: CRs (stat-only). . . . 158
F.2 Unblinded fit: CRs (stat-only). . . . 159
F.3 Asimov and Unblinded fit: Yields (stat-only). . . . 160
F.4 Asimov and Unblinded fit: Signal Contribution (stat-only). . . . 161
F.5 Asimov and Unblinded fit: Correlation Matrix. . . . 161

Contents

Abstract ix

Zusammenfassung xi

1 Introduction 1

2 Theoretical Overview 3
2.1 The Standard Model of Particle Physics . . . 3
2.2 Phenomenology of Proton–Proton Collisions . . . 13

3 Vector Boson Scattering 19
3.1 Electroweak Vector Boson Scattering in the Standard Model . . . 19
3.2 Electroweak Vector Boson Scattering at the LHC . . . 21
3.3 Polarization in Vector Boson Scattering . . . 30

4 The ATLAS Experiment at the Large Hadron Collider 35
4.1 The Large Hadron Collider . . . 35
4.2 The ATLAS Experiment . . . 39

5 Semiconductor Tracker: Calibration and Trim Settings 49
5.1 Trimming and Calibration tests . . . 49
5.2 Defects and Masking . . . 54
5.3 High Masking Rates and Troubleshooting . . . 55

6 Reconstruction and Particle Identification in ATLAS 59
6.1 Reconstruction Techniques . . . 59
6.2 Tracking and Vertex Reconstruction . . . 60
6.3 Physics Objects . . . 61

7 Object and Event Selection 69
7.1 Object Selection . . . 69
7.2 Event Selections . . . 74

8 Background Processes **79**
8.1 Prompt Lepton Backgrounds . . . 80
8.2 e/γ Conversion Backgrounds . . . 82
8.3 Non-Prompt and Fake Lepton Backgrounds . . . 85

9 Polarized Signal Sample Generation **89**
9.1 Sample Generation Configuration . . . 89
9.2 Observed Behaviour and Validation Strategy . . . 90
9.3 Diagnosis of the Issue . . . 91
9.4 Resolution and Generator Fix . . . 93
9.5 Outcome . . . 93

10 Data and Simulated Samples **95**
10.1 From Detector Signals to Analysis Samples . . . 95
10.2 Datasets . . . 96
10.3 Monte Carlo Samples . . . 97

11 Machine Learning for Classification **101**
11.1 Variables separating longitudinal modes . . . 101
11.2 Classification using Deep Neural Networks . . . 104
11.3 DNN Optimization Results . . . 111

12 Extraction of $W_L^\pm W_L^\pm$ polarization fraction **115**
12.1 Statistical Analysis . . . 115
12.2 Expected Sensitivity . . . 121
12.3 Observed Sensitivity . . . 124
12.4 Impact of a Flat Systematic Uncertainty . . . 127
12.5 Summary of the Longitudinal Polarization Results . . . 128

13 Conclusion and Outlook **131**

Appendix **133**

A Theory and VBS **133**
A.1 Mandelstam Variables . . . 133
A.2 VBS Event Signature Theoretical Justification . . . 133

B Standard Model Lagrangian **137**

C Neural Network Details **143**
C.1 DNN Training Details . . . 143

D Signal Region Variable Distributions **149**

E Mathematical Formalism for Polarization Results **153**

E.1 Profile-Likelihood Fit and Signal Strength Parameters 153
E.2 Fiducial Cross Section Determination 154
E.3 Polarization Fraction and Upper Limit 154

F Fit Results **157**
F.1 Limits and Significances 157
F.2 Fit Plots and Tables 158

Bibliography **158**

Declaration **177**

Chapter 1

Introduction

Many curious minds have wondered over generations about the fundamental building blocks of our universe and how they interact with each other. One of the most successful answers is described by the Standard Model (SM) of Particle Physics. Within the SM, the basic building blocks are considered to be the matter particles called fermions which are held together with interactions mediated by force-carriers called bosons. The forces between these particles are carried by special mediator particles: the photon for electromagnetism, gluons for the strong force, and the W and Z bosons for the weak force. Unlike the massless photon and gluons, the weak bosons are heavy, a fact that hints at something deeper in the structure of the SM.

In the early universe, electromagnetic and weak interactions were unified into electroweak interactions as postulated by the electroweak theory. The discovery of the W and Z bosons confirmed this unification within the framework of the SM. These massive gauge bosons, which carry the weak force, possess an intriguing property absent in massless force-carriers like the photon — they can exist in a *longitudinally polarized state*, where the orientation of their spin aligns with their direction of motion. This feature arises as a direct consequence of the *Higgs mechanism*, the process that breaks electroweak symmetry and gives mass to the weak bosons. Studying the behaviour of longitudinally polarized W and Z bosons therefore provides a direct probe of the very mechanism responsible for mass generation in the Standard Model.

One of the most powerful ways to access this phenomenon experimentally is through *vector boson scattering (VBS)* — a rare process in which two vector bosons are radiated from quarks (a type of fermion) and subsequently scatter off one another. Within this class of interactions, the longitudinally polarized modes play a special role, as they are intimately linked to the dynamics of electroweak symmetry breaking and are sensitive to possible deviations from SM predictions. If the Higgs mechanism functions precisely as described, the scattering amplitude for longitudinally

polarized bosons remains well-behaved at high energies. Any deviation from this behaviour could signal new physics, such as anomalous gauge couplings or the presence of additional scalar states.

Recent measurements by the ATLAS Collaboration, using the full 2015-2018 dataset of proton–proton collisions at the Large Hadron Collider (LHC), have provided the first evidence (3.3σ significance) for the presence of longitudinally polarized W bosons in same-sign WW scattering events. This represents a crucial step forward in isolating the individual polarisation components of VBS and in validating the Higgs mechanism through direct experimental observation. However, an even more elusive target remains: the doubly longitudinally polarized (LL) VBS component, where *both* W bosons are longitudinally polarized. This configuration is expected to contribute only a small fraction of the total VBS cross section, yet it carries the clearest imprint of electroweak symmetry breaking and is the most sensitive channel to potential new physics effects.

The work presented in this thesis is motivated by this challenge. It aims to deepen the understanding of vector boson scattering as a probe of the electroweak sector, with a particular focus on strategies to enhance sensitivity to the LL component. By exploring theoretical predictions, simulation techniques, and data-driven analysis methods, this dissertation makes an effort to isolate and measure doubly longitudinally polarized VBS — a milestone that will provide one of the most direct tests yet of the Standard Model's mechanism for mass generation.

In this dissertation, Natural Units are used, where Planck's constant and speed of light are taken to be unity. This simplifies the dimensions of relevant physical quantities in terms of mass or energy dimensions.

This dissertation begins by establishing the theoretical foundations necessary to understand the physics of electroweak vector boson scattering. Chapter 2 introduces the Standard Model and explains how the Higgs mechanism gives mass to the weak bosons, setting the stage for the presented studies. To place the experimental context, the chapter also reviews the dynamics of proton–proton collisions at the LHC. Chapter 3 then examines vector boson scattering and highlights the importance of probing polarization as a window into electroweak symmetry breaking. The following chapters describe the experimental tools and methods: Chapter 4 presents the LHC and the ATLAS detector and Chapter 5 focuses on the Semiconductor Tracker. Chapters 6 and 7 develop the event reconstruction and selection strategy, followed by background modelling in Chapter 8 and the generation of polarized signal samples in Chapter 9. The use of data, simulation, and machine-learning techniques is discussed in Chapters 10 and 11. Finally, Chapter 12 details the extraction of the longitudinal polarization fraction using a profile-likelihood approach, and Chapter 13 concludes with results and their implications for future measurements.

Chapter 2

Theoretical Overview

This chapter gives a brief overview of the theoretical foundation underlying the study presented in this dissertation. Section 2.1 introduces the Standard Model of particle physics, outlining its particle content (Sec. 2.1.1), mathematical formalism (Sec. 2.1.2), an overview of Higgs mechanism and Electroweak Symmetry Breaking (Sec. 2.1.3), and inherent limitations of SM (Sec. 2.1.4). The content of this section is mainly inspired by Ref. [7–10]. Section 2.2 presents the phenomenology of proton–proton collisions relevant to LHC physics, covering the internal structure of the proton at high energies (Sec. 2.2.1), the theoretical framework for cross-section calculations (Sec. 2.2.2), the dynamics of a typical proton–proton collision (Sec. 2.2.3), and the role of Monte Carlo event generators in simulating these processes (Sec. 2.2.4).

2.1 The Standard Model of Particle Physics

The Standard Model (SM) of particle physics is a theory of fundamental interactions in nature. It is a remarkably successful model explaining a plethora of natural phenomena ranging from atomic miscroscopy to high-energy particle collisions. Ordinary matter in the universe is composed of a small set of fundamental particles, whose behavior is governed by the four fundamental forces of nature: gravitational, electromagnetic, weak, and strong. SM provides the theoretical framework that describes the known elementary particles and their interactions, incorporating all fundamental forces except gravity[1]. Over the past decades, this theory has been tested with remarkable precision, yet there remain indications of physics beyond its scope.

In the SM, matter particles are *fermions*, characterized by ½-integer spins ($\frac{1}{2}, \frac{3}{2}, \ldots$). Their

[1] Gravity is about 10^{37} times weaker than the other forces and negligible at the particle scale.

interactions are mediated by force carriers, known as *bosons*, which possess integer spins $(0, 1, \ldots)$. Fermions carry different charge quantum numbers — such as color charge, hypercharge, and weak isospin — that determine the nature of their interactions. A summary of the constituents of the SM is presented in Figure 2.1.

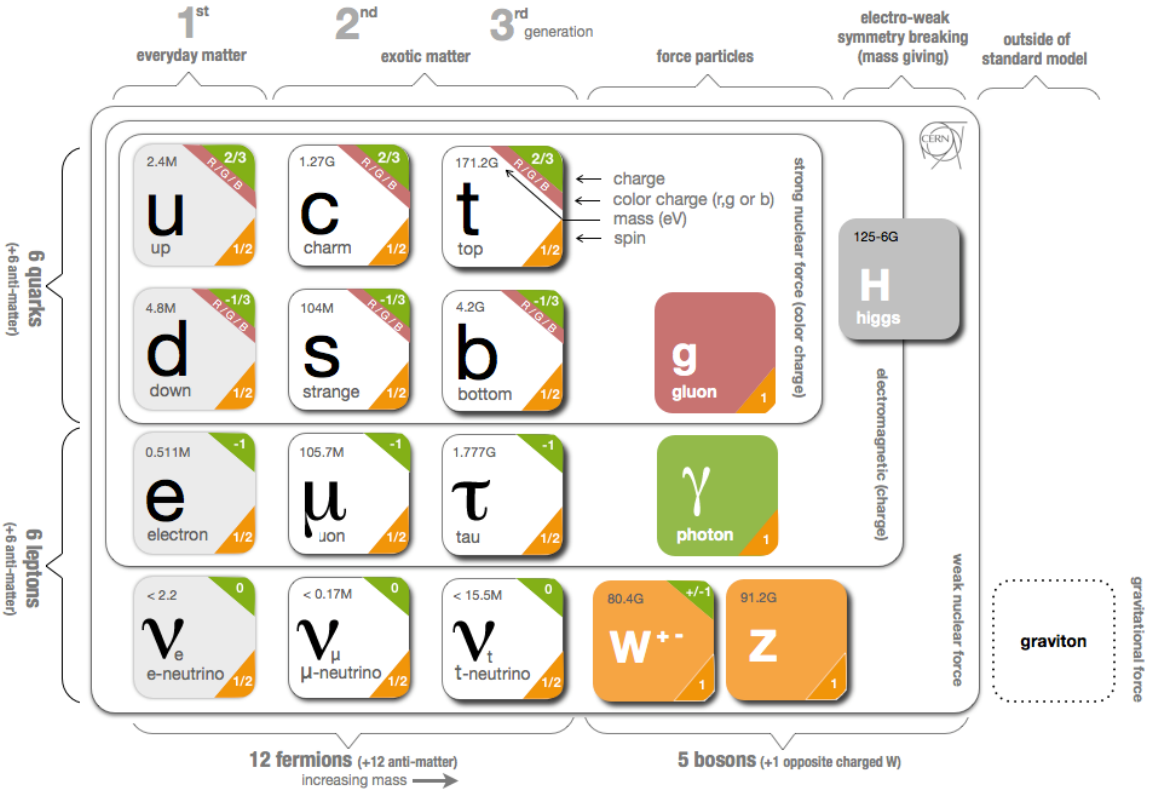


Figure 2.1: Overview of the prarticle content of the Standard Model of Particle Physics [11].

The SM is based on simple physical assumptions including Lorentz invariance, locality, and gauge symmetries. The SM Lagrangian ($\mathscr{L}_{\text{SM}}$) obeys $\text{SU}(3)_C \otimes \text{SU}(2)_L \otimes \text{U}(1)_Y$ gauge symmetries [12–14], where the three groups gauge the quantum numbers of color charge (C), weak isospin (I_3), and hypercharge (Y), respectively. The three constituent Lie groups describe the strong force ($\text{SU}(3)_C$), and the unified electromagnetic and weak forces ($\text{SU}(2)_L \otimes \text{U}(1)_Y$). $\text{SU}(3)_C$ acts on all particles carrying a color charge, $\text{SU}(2)_L$ acts only on left-handed particles with a weak isospin, while $\text{U}(1)_Y$ acts on particles carrying a weak hypercharge. The invariance of $\mathscr{L}_{\text{SM}}$ under local gauge transformations necessitates the introduction of gauge fields, whose quanta — *vector bosons* — mediate interactions among fermions. Mass generation arises via spontaneous electroweak symmetry breaking through the Higgs mechanism, which also predicted the spin-0 Higgs boson, discovered at the LHC in 2012 [15, 16].

2.1.1 Particle Content of the Standard Model

The particle spectrum of the SM is organized according to the quantum numbers associated with its gauge structure. Before electroweak symmetry breaking (EWSB), the relevant internal quantum numbers are color, weak isospin, and hypercharge. After the breaking of $\mathrm{SU}(2)_L \otimes \mathrm{U}(1)_Y$ to the electromagnetic subgroup $\mathrm{U}(1)_{\mathrm{EM}}$, the appropriate physical quantum numbers reduce to color and electric charge. The connection between the pre- and post-EWSB assignments is given by the Gell-Mann–Nishijima relation,

$$Q = T_3 + \frac{Y}{2}, \tag{2.1}$$

where T_3 denotes the third component of weak isospin (the generator of $\mathrm{SU}(2)_L$ acting on left-handed fermion doublets), and Y is the weak hypercharge (the generator of $\mathrm{U}(1)_Y$).

The resulting mass eigenstates consist of three generations of quarks and leptons (½-integer spin), four vector bosons (spin 1), and the scalar Higgs boson (spin 0). This spectrum represents the observable particle content encoded in the SM, as summarized in Figure 2.1.

Fermions are organized into three generations, each containing one charged lepton, one neutrino, and two quarks. Generations differ only in mass, with ordinary matter composed solely of first-generation fermions. Each fermion has a corresponding antiparticle with opposite charge. *Quarks* carry both electric and color charge, interacting via the strong, electromagnetic, and weak forces. Each generation contains one up-type quark (up, charm, top; $Q = +\frac{2}{3}$) and one down-type quark (down, strange, bottom; $Q = -\frac{1}{3}$). Due to color confinement [17], quarks exist only in bound states called hadrons: baryons (three quarks) and mesons (quark-antiquark pairs). More exotic states of quarks, such as the pentaquark and the tetraquark exist additionally [18]. *Leptons* consist of the electron, muon, and tau, together with their neutrinos. Charged leptons ($Q = -1$) interact electromagnetically, while neutrinos, massless in the SM, carry no electric or color charge and interact only via the weak force.

The *gauge* or *vector bosons* mediate interactions: the photon γ for electromagnetism, the massive $W^{\pm}$ and Z bosons for the weak force, and eight[2] gluons (g) for the strong force. The vector bosons γ, $W^{\pm}$, and Z arise from the unified electroweak theory. Finally, the *Higgs boson*, the sole scalar particle, gives mass to SM particles through electroweak symmetry breaking.

Throughout this work, references to electrons, muons, taus, and quarks are understood to include both particles and antiparticles unless otherwise specified.

[2]The number 8 comes directly from the fact that SU(3) has 8 independent generators.

2.1.2 Mathematical Formalism

The SM of particle physics is the culmination of decades of progress in quantum field theory. Its structure combines three key developments: *Quantum Electrodynamics (QED)*, describing electromagnetic interactions through an Abelian $\mathrm{U}(1)$ gauge theory; *Quantum Chromodynamics (QCD)* [19, 20], a non-Abelian $\mathrm{SU}(3)_C$ theory describing the strong interaction; and the *Glashow-Weinberg-Salam electroweak theory* [12–14], unifying weak and electromagnetic interactions under the group $\mathrm{SU}(2)_L \otimes \mathrm{U}(1)_Y$. These pieces fit together into the gauge group

$$\mathscr{G}_{\mathrm{SM}} = \mathrm{SU}(3)_C \otimes \mathrm{SU}(2)_L \otimes \mathrm{U}(1)_Y \,, \tag{2.2}$$

which dictates the interactions, and symmetries of the theory.

Gauge symmetry and Matter fields

The chiral nature of the electroweak interaction determines how fermions transform under $\mathrm{SU}(2)_L$, grouping only their left-handed components into weak doublets,

$$Q = \begin{pmatrix} u_L \\ d_L \end{pmatrix}, \qquad L = \begin{pmatrix} \nu_L \\ e_L \end{pmatrix}, \tag{2.3}$$

accompanied by right-handed singlets u_R, d_R, and e_R. Hence, only the left-handed fermions participate in the weak interaction, while the right-handed states remain singlets under $\mathrm{SU}(2)_L$. Since a right-handed neutrino would be an $\mathrm{SU}(2)_L$ singlet with no gauge interactions, it is not included in the SM.

The gauge fields associated with each factor of the symmetry group are: eight gluons ($G^A_{\mu\nu}$), three weak bosons ($W^I_{\mu\nu}$), and one hypercharge boson ($B_{\mu\nu}$). These vector fields mediate the interactions between the matter fields.

Structure of the Lagrangian

The complete SM Lagrangian can be written schematically as

$$\mathscr{L}_{\mathrm{SM}} = \mathscr{L}_{gauge} + \mathscr{L}_{fermion} + \mathscr{L}_{Higgs} + \mathscr{L}_{\mathrm{Yukawa}} \,. \tag{2.4}$$

Each of these terms is invariant under the gauge group $\mathscr{G}_{\mathrm{SM}}$. The derivation of various terms in $\mathscr{L}_{\mathrm{SM}}$ is detailed in Appendix B.

Gauge sector. The gauge part of the Lagrangian describes the dynamics of the force carriers and is given by

$$\mathscr{L}_{gauge} = -\frac{1}{4}G^A_{\mu\nu}G^{A\mu\nu} - \frac{1}{4}W^I_{\mu\nu}W^{I\mu\nu} - \frac{1}{4}B_{\mu\nu}B^{\mu\nu}\,, \tag{2.5}$$

where the gauge-field strengths are defined as

$$G^A_{\mu\nu} = \partial_\mu G^A_\nu - \partial_\nu G^A_\mu + g_s f^{ABC} G^B_\mu G^C_\nu\,, \tag{2.6}$$
$$W^I_{\mu\nu} = \partial_\mu W^I_\nu - \partial_\nu W^I_\mu + g\varepsilon^{IJK} W^J_\mu W^K_\nu\,, \tag{2.7}$$
$$B_{\mu\nu} = \partial_\mu B_\nu - \partial_\nu B_\mu\,. \tag{2.8}$$

Here, f^{ABC} and ε^{IJK} are the structure constants of the unitary Lie groups SU(3) and SU(2), respectively, defined through the commutation relations $[T^A, T^B] = if^{ABC}T^C$ for $SU(3)$ and $[\sigma^I/2, \sigma^J/2] = i\varepsilon^{IJK}\sigma^K/2$ for SU(2), where T^A and $\sigma^I/2$ are the group generators. The coupling strengths of gluon fields and weak fields are denoted by g_s and g respectively.

Fermion sector. The fermionic part of SM Lagrangian encodes the kinetic terms for the matter fields and their interactions with the gauge bosons. For a generic left-handed fermion doublet ψ_L and right-handed fermion singlet ψ_R, it takes the form

$$\mathscr{L}_{fermion} = \bar{\psi}_L i\gamma^\mu D_\mu \psi_L + \bar{\psi}_R i\gamma^\mu D_\mu \psi_R\,, \tag{2.9}$$
$$= i\big(\overline{L}D_\mu\gamma^\mu L + \overline{e}_R D_\mu\gamma^\mu e_R + \overline{Q}D_\mu\gamma^\mu Q + \overline{u}_R D_\mu\gamma^\mu u_R + \overline{d}_R D_\mu\gamma^\mu d_R\big)\,, \tag{2.10}$$

The covariant derivative is defined as

$$D_\mu q_L = (\partial_\mu - ig_s T^A G^A_\mu - igS^I W^I_\mu - ig' Y_q B_\mu) q_L \tag{2.11}$$

for the left-handed quark q_L, for instance. Here, $T^A = \frac{\lambda^A}{2}, S^I = \frac{\sigma^I}{2}$, and g' is the coupling constant for the hypercharge gauge field B_μ.

Higgs sector. The SM incorporates a complex scalar doublet, the Higgs field $H = \binom{\phi^+}{\phi^0}$, with Lagrangian

$$\mathscr{L}_{Higgs} = (D_\mu H)^\dagger (D^\mu H) + \mu^2 H^\dagger H - \lambda (H^\dagger H)^2\,, \tag{2.12}$$

which introduces EWSB. When the potential develops a nonzero vacuum expectation value, the symmetry

$$\mathrm{SU}(2)_L \otimes \mathrm{U}(1)_Y \to \mathrm{U}(1)_{EM} \tag{2.13}$$

is spontaneously broken, giving mass to the weak bosons and leaving the photon massless. The physical excitation of the field corresponds to the Higgs boson, discovered at the LHC in 2012 [15, 16]. A more detailed discussion of the Higgs mechanism and EWSB follows in Sec. 2.1.3.

Yukawa sector. Fermion masses arise through Yukawa interactions between the fermion fields with the Higgs doublet:

$$\mathscr{L}_{Yukawa} = -\left(\overline{L} Y_e \, e_R H + \overline{Q} Y_u \, u_R \widetilde{H} + \overline{Q} Y_d \, d_R H + \text{h.c.}\right), \tag{2.14}$$

where $\widetilde{H} = i\sigma_2 H^*$, $Y_{e,u,d}$ are the Yukawa coupling matrices in flavor space, and the hypercharge is normalized such that $Y_Q = 1/6$. The field $\widetilde{H}$ transforms in the same way as H under the SU(2) symmetry group, but carries opposite hypercharge. Its introduction is therefore required to construct gauge-invariant Yukawa couplings, not because of the SU(2) structure itself. After EWSB, these terms generate fermion masses proportional to their respective Yukawa couplings [13].

The gauge quantum numbers of each field are summarized in Table 2.1. The schematic SM Lagrangian density (Eq. 2.4) finally transforms into its full expression as

$$\begin{aligned}
\mathscr{L}_{\text{SM}} = & -\frac{1}{4} G^A_{\mu\nu} G^{A\mu\nu} - \frac{1}{4} W^I_{\mu\nu} W^{I\mu\nu} - \frac{1}{4} B_{\mu\nu} B^{\mu\nu} && \to \mathscr{L}_{gauge} \\
& + (D_\mu H)^\dagger (D^\mu H) + \mu^2 H^\dagger H - \lambda (H^\dagger H)^2 && \to \mathscr{L}_{Higgs} \\
& + i\left(\overline{L} D_\mu \gamma^\mu L + \overline{e}_R D_\mu \gamma^\mu e_R + \overline{Q} D_\mu \gamma^\mu Q + \overline{u}_R D_\mu \gamma^\mu u_R + \overline{d}_R D_\mu \gamma^\mu d_R\right) && \to \mathscr{L}_{fermion} \\
& - \left(\overline{L} Y_e \, e_R H + \overline{Q} Y_u \, u_R \widetilde{H} + \overline{Q} Y_d \, d_R H + \text{h.c.}\right) && \to \mathscr{L}_{Yukawa} \,.
\end{aligned} \tag{2.15}$$

Symmetry \ *Field*	G^A_μ	W^I_μ	B_μ	$L = \begin{pmatrix} \nu_L \\ e_L \end{pmatrix}$	e_R	$Q = \begin{pmatrix} u_L \\ d_L \end{pmatrix}$	u_R	d_R	$H = \begin{pmatrix} \phi^+ \\ \phi^0 \end{pmatrix}$
$SU(3)_C$	8	1	1	1	1	3	3	3	1
$SU(2)_L$	1	3	1	2	1	2	1	1	2
$U(1)_Y$	0	0	0	$-1/2$	-1	$1/6$	$2/3$	$-1/3$	$1/2$

Table 2.1: Gauge quantum numbers of the Standard Model fields.

2.1.3 Higgs mechanism

The SM beautifully describes the interactions of fundamental particles through gauge symmetries. However, this elegant structure by itself cannot explain why many of the observed particles have mass. Simply adding mass terms to the Lagrangian would break gauge invariance and spoil the consistency of the theory. In the 1960s, Higgs, Brout, Englert, Guralnik, Hagen, and Kib-

ble showed that this apparent contradiction could be resolved through the idea of spontaneous symmetry breaking (SSB) [21–26].

By introducing a new scalar field, known as the Higgs field, the SM is able to endow gauge bosons and fermions with mass while keeping the gauge symmetries intact at the fundamental level. The Higgs mechanism works by exploiting the fact that the vacuum of the theory is not symmetric, even though the equations themselves are. This allows particles to interact with the Higgs field in such a way that they effectively acquire mass, without explicitly violating gauge symmetry.

The Higgs field is introduced as a complex scalar doublet:

$$H = \begin{pmatrix} \phi^+ \\ \phi^0 \end{pmatrix}, \tag{2.16}$$

with a potential of the form

$$V(H) = -\mu^2 H^\dagger H + \lambda (H^\dagger H)^2 . \tag{2.17}$$

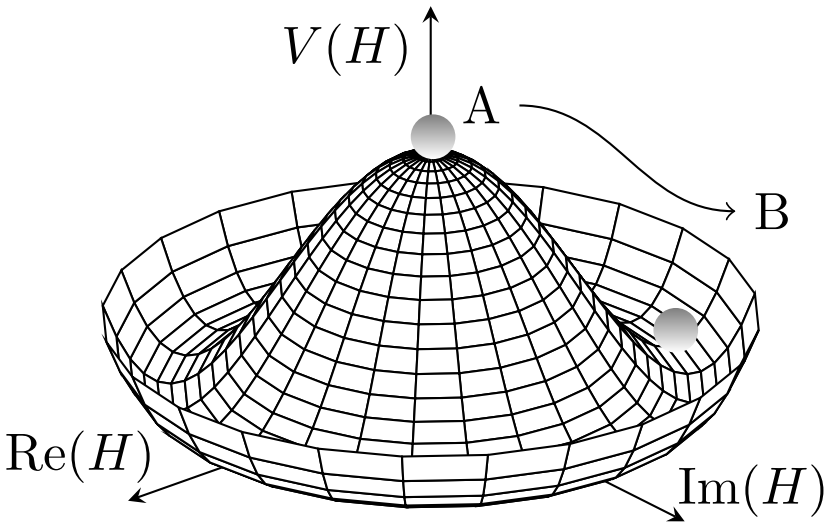


Figure 2.2: Visual representation of Higgs mexican hat potential $V(H)$ of the complex scalar field. Figure modified from Ref. [27].

When $\lambda > 0$ and $\mu^2 > 0$, the potential takes the shape of a "Mexican hat", with infinitely many degenerate minima as illustrated in Fig. 2.2. The system spontaneously chooses one of these minima, leading to a non-zero VEV:

$$\langle H \rangle = \frac{1}{\sqrt{2}} \begin{pmatrix} 0 \\ v \end{pmatrix}, \qquad v = \frac{\mu}{\sqrt{\lambda}} . \tag{2.18}$$

This choice of vacuum breaks the electroweak symmetry group

$$\mathrm{SU}(2)_L \otimes \mathrm{U}(1)_Y \to \mathrm{U}(1)_{EM}\,, \tag{2.19}$$

leaving electromagnetism as the only unbroken symmetry, which is the reason photons are still massless after SSB. In unitary gauge, the Higgs field H is written in terms of the vacuum expectation value v (VEV), and the physical Higgs field h:

$$H = \frac{v}{\sqrt{2}} \begin{pmatrix} 0 \\ 1 + \dfrac{h}{v} \end{pmatrix}. \tag{2.20}$$

Gauge Boson Masses

The Higgs kinetic term then yields the mass terms of the gauge bosons (as well as hVV and $hhVV$ interactions, where V refers to vector bosons):

$$\begin{aligned}(D_\mu H)^\dagger (D^\mu H) = {} & \frac{1}{2}(\partial_\mu h)^\dagger (\partial^\mu h) + M_W^2 W_\mu^- W^{+\mu} + \frac{1}{2} M_Z^2 Z_\mu Z^\mu \\ & + \frac{g^2 v^2}{4}\left(\frac{2h}{v} + \frac{h^2}{v^2}\right) W_\mu^- W^{+\mu} + \frac{1}{2}\frac{(g^2 + g'^2)v^2}{4}\left(\frac{2h}{v} + \frac{h^2}{v^2}\right) Z_\mu Z^\mu\,,\end{aligned} \tag{2.21}$$

where g and g' are the $\mathrm{SU}(2)_L$ and $\mathrm{U}(1)_Y$ gauge couplings. The physical gauge-boson fields are defined as

$$W_\mu^\pm = \frac{1}{\sqrt{2}}(W_\mu^1 \mp i W_\mu^2)\,, \tag{2.22}$$

depicting the massive charged gauge bosons $W^\pm$, while the neutral gauge bosons are given as

$$\begin{pmatrix} Z_\mu \\ A_\mu \end{pmatrix} = \begin{pmatrix} \cos\theta_W & -\sin\theta_W \\ \sin\theta_W & \cos\theta_W \end{pmatrix} \begin{pmatrix} W_\mu^3 \\ B_\mu \end{pmatrix}, \tag{2.23}$$

where the Z_μ field describes the massive Z boson and the A_μ field the massless photon. The weak mixing angle θ_W is defined by the relations:

$$\begin{aligned} \cos\theta_W &= \frac{g}{\sqrt{g^2 + g'^2}}\,, \\ \sin\theta_W &= \frac{g'}{\sqrt{g^2 + g'^2}}\,, \\ e^2 &= g^2 \sin^2\theta_W\,. \end{aligned} \tag{2.24}$$

For the electric charge, we adopt the sign convention $e = g \sin\theta_W$. In the Higgs kinetic term (Eq. 2.21), mass term for real vector field Z is $\frac{1}{2}m^2 Z_\mu Z^\mu$ and that for complex vector field W is $m^2 W^*_\mu W^\mu$. The masses of the W and Z bosons are, therefore, given by

$$m_W^2 = \frac{g^2 v^2}{4}, \qquad m_Z^2 = \frac{(g^2 + g'^2)v^2}{4}, \tag{2.25}$$

which imply $\cos^2\theta_W = M_W^2/M_Z^2$. The Higgs VEV ($v$) can be estimated as

$$v = \frac{1}{(\sqrt{2}\,G_F)^{1/2}} \approx 246\ \text{GeV}, \tag{2.26}$$

where $G_F = \frac{\sqrt{2}g^2}{8M_W^2}$.

Fermion Masses

Gauge-invariant mass terms for fermions are introduced via Yukawa couplings to the Higgs doublet modifying Eq. 2.14:

$$\begin{aligned} \mathscr{L}_{\text{Yukawa}} &= -\left(\overline{L} Y_e\, e_R H + \overline{Q} Y_u\, u_R \widetilde{H} + \overline{Q} Y_d\, d_R H\right) + \text{h.c.}, \\ &= -\frac{v+h}{\sqrt{2}}\left(\bar{e}_L Y_e\, e_R + \bar{u}_L Y_u\, u_R + \bar{d}_L Y_d\, d_R\right) + \text{h.c.} \end{aligned} \tag{2.27}$$

After EWSB, these terms reduce to effective fermion masses, with

$$m_f = \frac{Y_f v}{2}, \tag{2.28}$$

demonstrating that the Yukawa couplings determine the mass hierarchy of fermions.

The Higgs boson

Three of the four degrees of freedom of the scalar field are "eaten" by the gauge bosons W^+, W^-, Z, becoming their longitudinal polarizations. Hence, SSB is crucial as it provides an explanation for the observed longitudinally polarized states within the SM motivating the primary focus of this dissertation. The remaining physical degree of freedom manifests as a scalar particle, the Higgs boson, with mass

$$m_h = \sqrt{2\lambda}\, v. \tag{2.29}$$

The Higgs boson is a central prediction of the SM, providing direct evidence for the mechanism of EWSB. Its discovery, announced in 2012 by the ATLAS and CMS experiments at CERN [15, 16],

confirmed this long-standing theoretical idea nearly fifty years after its proposal.

2.1.4 Limitations of the Standard Model

The SM has proven remarkably effective (see Chapter 3) in describing the known elementary particles and three of the four fundamental forces of nature. Figure 3.4 shows a comparison of various SM cross-section measurements with their theoretical predictions. The results demonstrate excellent consistency between experimental data and theoretical expectations. Yet its very success has highlighted its limitations, motivating the search for a more complete theory. These shortcomings arise both from internal theoretical tensions and from experimental evidence that the SM cannot accommodate.

From a theoretical point of view, the SM does not provide a full unification of the forces. The electromagnetic and weak forces are combined into the electroweak theory, but the strong force remains separate, and gravity lies far beyond reach, becoming important only at the Planck scale ($\mathcal{O}(10^{19}$ GeV)). This gap in energy scales leads to the *hierarchy problem* [28], made sharper by the discovery of the Higgs boson. The Higgs mass can only be explained if large quantum corrections are almost perfectly canceled by the bare Higgs mass, a process known as fine-tuning. While mathematically possible, such extreme cancellations are considered unsatisfactory. Several ideas have been proposed to solve this issue: supersymmetry introduces new partner particles that stabilize the Higgs mass, extra dimensions (inspired by string theory) modify gravity at very small scales, and other models suggest the Higgs is not fundamental but instead a composite particle.

Experimentally, many observations point beyond the SM. *Dark matter* [29], which makes up about a quarter of the universe, has only been detected through its gravitational effects, and its particle nature remains unknown. *Dark energy* [30], driving the accelerated expansion of the universe, is even more mysterious. The observed imbalance between matter and antimatter or *matter-antimatter asymmetry* [31] in the universe is also far greater than the SM can explain with its small amount of CP violation. CP refers to the combined symmetry of charge conjugation (C), which transforms particles into antiparticles, and parity (P), which inverts spatial coordinates. *Neutrino oscillations* [32, 33], which show that neutrinos have mass, are another clear sign of physics beyond the SM. In addition, various experimental anomalies continue to hint at new phenomena.

These open questions provide strong motivation to search for physics beyond the Standard Model (BSM). Many proposed BSM theories predict the existence of new particles that could be discovered in high-energy collider experiments. So far, no such particles have been observed, but their discovery remains one of the central goals of the LHC program.

2.2 Phenomenology of Proton–Proton Collisions

The Large Hadron Collider (LHC) operates by accelerating and colliding two counter-circulating beams of protons at extremely high energies, reaching up to several tera-electron volts (TeV) in the center-of-mass frame. To properly interpret the outcomes of these collisions, it is essential to first understand the internal structure of the proton and how it governs the dynamics of high-energy interactions.

2.2.1 The Proton Structure at High Energies

Although protons appear as point-like particles at low energies, they are in fact composite systems made up of more fundamental constituents — quarks and gluons — collectively referred to as *partons* [34]. QCD predicts that the proton's structure depends on the energy scale (or equivalently, the momentum transfer Q^2) at which it is probed.

The proton can be approximated as a bound state of three valence quarks (two up and one down). However, as the energy scale increases, gluon radiation and quark–antiquark pair production lead to a dense sea of partons within the proton. This scale dependence of the parton content is quantitatively described by the *parton distribution functions* (PDFs), $f_i(x, Q^2)$, which represent the probability of finding a parton of type i (quark, antiquark, or gluon) inside the proton. Here, x is the Bjorken scaling variable representing the fraction of the proton's longitudinal momentum carried by the parton, and Q^2 is the momentum-transfer scale of the hard interaction, which determines the resolution at which the proton is probed. The evolution of these PDFs with Q^2 is governed by the DGLAP (Dokshitzer-Gribov-Lipatov-Altarelli-Parisi) [35–37] equations.

Figure 2.3 shows the proton PDFs for two different factorisation scales (denoted by μ^2 in the figures). At lower scales the valence quark distributions dominate at large x, while sea quarks and gluons are relatively suppressed. At higher scales, gluons and sea quarks are strongly enhanced due to QCD evolution, demonstrating how increasing the probing scale reveals a richer internal structure of the proton.

2.2.2 Cross-Section Calculations

The probability for a specific scattering process to occur is characterized by the *cross section*, a fundamental physical quantity with the dimensions of area, conventionally expressed in *barns* (b), where $1\ \text{b} = 10^{-28}\ \text{m}^2$. It quantifies the likelihood of an interaction between incident particles and

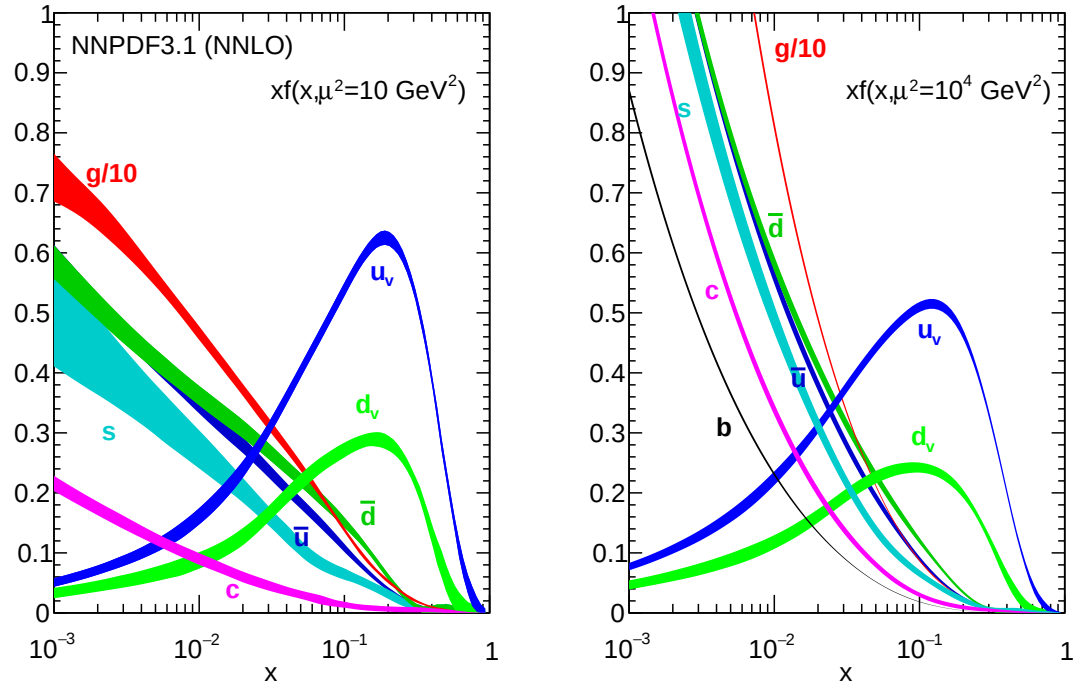


Figure 2.3: NNPDF3.1 NLO parton distribution functions of a proton evaluated at energy scales, μ^2, of 10 GeV^2 (left) and 10^4 GeV^2 (right) [38]. The width quantifies the uncertainty on the PDFs.

serves as the principal observable linking theory with experiment.

In high-energy proton–proton collisions, it is not the protons themselves that interact directly, but rather their constituent partons. At the microscopic level, the dynamics of a partonic subprocess $ij \to X$ are governed by the quantum mechanical transition amplitude, or matrix element (ME), $\mathscr{M}_{ij\to X}$. The corresponding partonic differential cross section is given by

$$d\hat{\sigma}_{ij\to X} = \frac{1}{2\hat{s}} \overline{\left|\mathscr{M}_{ij\to X}\right|^2} d\Phi_n(p_1+p_2;\{k_\ell\}), \tag{2.30}$$

where $\hat{s} = (p_1+p_2)^2$ is the partonic centre-of-mass energy squared, the bar denotes averaging over initial spin and colour states, $d\Phi_n$ represents the Lorentz-invariant phase space for an n-body final state, and $\{k_\ell\}$ represents the momenta of the final-state particles.

The *factorization theorem* [39] of perturbative QCD allows for the separation of the calculable short-distance partonic interaction from the long-distance non-perturbative structure of the proton. For hadronic collisions the observable cross section is obtained by convolution of the partonic cross section with the PDFs according to the factorization theorem:

$$\sigma_{pp\to X}(s) = \sum_{i,j} \int_0^1 dx_1 \int_0^1 dx_2\, f_i(x_1,\mu_F^2)\, f_j(x_2,\mu_F^2)\, \hat{\sigma}_{ij\to X}\left(\hat{s} = x_1x_2s;\mu_R^2,\mu_F^2\right), \tag{2.31}$$

where s is the hadronic centre-of-mass energy, $x_{1,2}$ are the parton momentum fractions, and μ_R and μ_F are the renormalization and factorization scales respectively. In practice $\hat{\sigma}_{ij\to X}$ is computed perturbatively as a power series in the strong coupling $\alpha_s(\mu_R)$:

$$\hat{\sigma} = \hat{\sigma}^{(0)} + \alpha_s(\mu_R)\,\hat{\sigma}^{(1)} + \alpha_s^2(\mu_R)\,\hat{\sigma}^{(2)} + \cdots, \tag{2.32}$$

with $\hat{\sigma}^{(0)}$ the tree-level or leading-order (LO) result, $\hat{\sigma}^{(1)}$ the next-to-leading order (NLO) correction, $\hat{\sigma}^{(2)}$ the NNLO term, and so on.

Perturbative and Non-Perturbative Regimes

The computation of cross sections in QCD depends on the energy scale of the process. At high momentum transfers ($Q^2 \gg \Lambda^2_{\text{QCD}}$), the strong coupling α_s becomes small, allowing reliable perturbative calculations. In this *perturbative regime*, higher-order corrections are systematically included, with divergences managed through renormalization and factorization. Parton showers (PS) extend these calculations by resumming leading logarithms to approximate multiple soft and collinear emissions.

At lower energy scales ($Q^2 \sim \Lambda^2_{\text{QCD}}$), the coupling grows large and perturbation theory breaks down. In this *non-perturbative regime*, phenomenological models describe processes such as the extraction of PDFs, hadronization of colored partons into hadrons, and multiple parton interactions that form the underlying event.

2.2.3 Structure of a Proton–Proton Collision

A typical proton–proton collision at the LHC involves multiple components. The *hard scatter* corresponds to the primary parton–parton interaction, which produces high-momentum final states such as jets, leptons, or bosons. Surrounding this is the *underlying event*, which includes softer QCD interactions, multiple parton interactions (MPI), and remnants of the incoming protons that did not participate in the hard scatter. Together, these components determine the observable characteristics of the event recorded by the detector.

The incoming and outgoing partons involved in the hard scatter may emit additional low-energy radiation, referred to as *Initial State Radiation* (ISR) and *Final State Radiation* (FSR), respectively. These emissions are considered "soft" because the energies of the radiated photons or gluons are small compared to those characterizing the primary hard interaction. Following the hard scattering, the remaining colored partons undergo a non-perturbative process known as

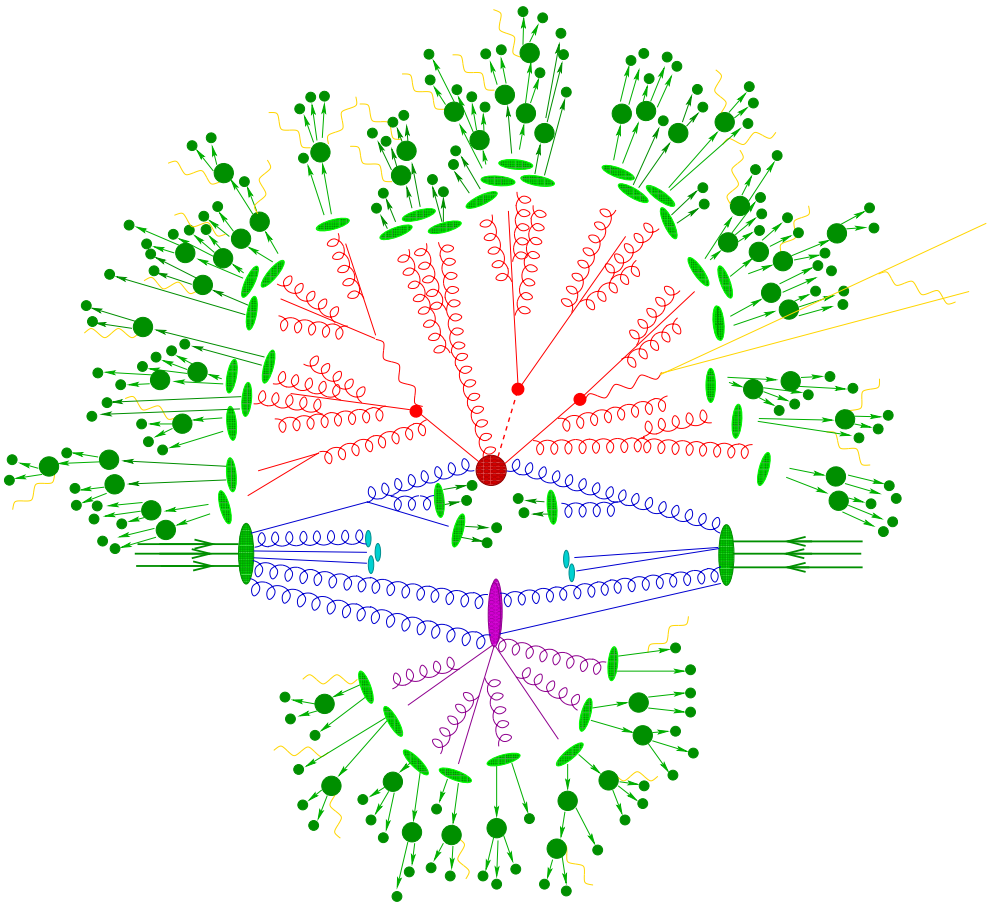


Figure 2.4: Illustration of a hadron-hadron collision event simulated with a MC event generator. The central red region represents the primary hard scattering, surrounded by tree-like structures illustrating QCD bremsstrahlung modelled by parton showers. The purple region denotes a secondary hard interaction. Transitions from partons to hadrons are shown in light green, hadron decays in dark green, and soft photon radiation is indicated by yellow lines [40].

hadronization, during which they recombine to form stable, color-neutral hadrons. A schematic representation of a typical proton–proton collision at the LHC, illustrating these components, is shown in Figure 2.4.

Due to the composite nature of protons and the variety of processes occurring in each collision, precise theoretical modeling is required for both signal and background predictions. The interplay of perturbative and non-perturbative QCD effects makes analytic treatment highly complex, motivating the use of computational tools known as *Monte Carlo (MC) event generators*.

2.2.4 Monte Carlo Event Generators

MC event generators for high-energy proton–proton collisions are generally classified as general-purpose or ME generators. General-purpose generators simulate the full event chain – from ME

calculation to PS, hadronization, and underlying event (UE) – though only a few include MEs beyond leading order. ME generators provide higher-order MEs for specific processes but require PS programs to produce complete events. To prevent double-counting in overlapping kinematic regions, matching schemes are employed.

MC generators simulate the full structure of proton–proton collisions by combining theoretical calculations with stochastic modeling of QCD effects. The event generation typically proceeds in several stages:

1. *Hard process generation:* The short-distance partonic interaction $ij \to X$ is calculated using perturbative QCD, often at NLO or NNLO accuracy.
2. *Parton showering (PS):* The outgoing partons undergo a sequence of emissions, modeled as a probabilistic cascade that approximates higher-order QCD radiation in the soft and collinear limits.
3. *Hadronization:* As partons lose energy, they combine to form color-neutral hadrons. This non-perturbative process is modeled phenomenologically using schemes such as the Lund string model [41], where the color field between a quark–antiquark pair is treated as a string that fragments into hadrons as it stretches, or cluster model [42], based on QCD pre-confinement, in which nearby partons form color-singlet clusters that decay into hadrons.
4. *UE & pile-up:* Additional soft interactions between proton remnants and simultaneous collisions in the same bunch crossing are included to reproduce realistic collider conditions.

In this analysis, several MC event generators are employed to model different aspects of the proton–proton collision process. MADGRAPH5_AMC@NLO [43] is used to generate parton-level hard-scattering events at LO and NLO accuracy using the aMC@NLO matching scheme [44]. PYTHIA 8 [45] performs PS, hadronization, and simulates the underlying event using the Lund string model. SHERPA [46] provides an alternative all-in-one framework with ME and PS merging, while HERWIG 7 [47] offers a complementary description based on angular-ordered showers and the cluster hadronization model. Together, these generators allow for detailed modeling of theoretical uncertainties and ensure a comprehensive description of the final-state observables. They are extensively used in both theoretical and experimental analyses to model SM processes and potential new physics signatures.

Chapter 3

Vector Boson Scattering

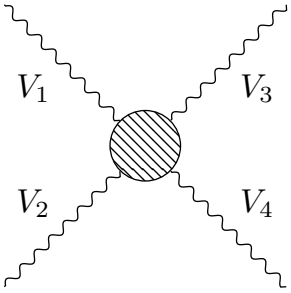
This chapter sheds light on vector boson scattering processes, which are one of the essential tests of the Standard Model as well as physics beyond the SM (BSM). Structured into three segments, this chapter initially explores the theoretical and experimental dimensions of the process of interest, transitioning into an exploration of its polarization properties.

The chapter begins with the description of electroweak vector boson scattering (VBS) in the Standard Model in Section 3.1. It further explores the theoretical definition of the process, relevant contributing classes of Feynaman diagrams, importance of studying VBS, and finally, the role played by the Higgs boson (Sec. 3.1.1). Section 3.2 delves into explanation of the VBS signature in hadron collision experiments (Sec. 3.2.1), followed by an examination of various final states (Sec. 3.2.2), and concludes with a discussion on the final state of interest for this dissertation, *i.e.*, the $W^{\pm}W^{\pm}jj$ production (Sec. 3.2.3). The final Section 3.3 further explores the significance of polarization in VBS.

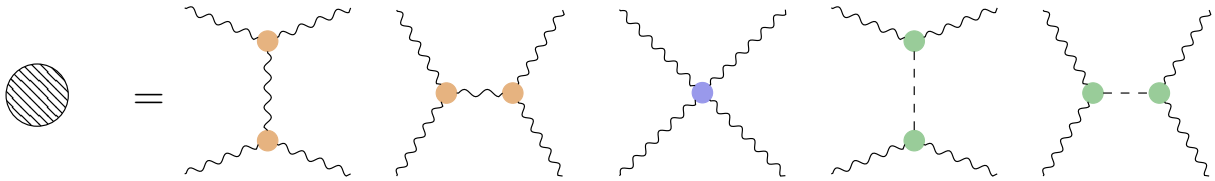
3.1 Electroweak Vector Boson Scattering in the Standard Model

Electroweak vector boson scattering or EW VBS refers to scattering processes, $V_1V_2 \rightarrow V_3V_4 (V_i = W, Z, \gamma)$, involving EW gauge boson self-interactions. The three relevant contributing classes of Feynman diagrams are: (a) diagrams involving only three-gauge-boson couplings, (b) diagrams involving only four-gauge-boson couplings, and (c) diagrams involving the Higgs boson (shown in Fig. 3.1). The existence of triple and quartic gauge boson couplings follows from the non-abelian structure of the EW gauge group in $\mathscr{L}_{SM}$, as described in Section 2.1. The interaction of the Higgs boson with EW gauge fields is encapsulated in the kinetic term of the Higgs sector of

$\mathscr{L}_{SM}$ (refer to Section 2.1.3).



(a) VBS process



(b) Blob represents triple, quartic gauge and Higgs couplings

Figure 3.1: A typical vector boson scattering process is shown in Fig. 3.1(a). Depending on the vector bosons V_1, V_2, V_3, V_4 of the scattering process, it can involve all or some of the leading order diagrams shown in Fig. 3.1(b).

VBS probes two key aspects of the SM. Firstly, the gauge boson self-interaction vertices have tree-level sensitivity to quartic or quadrilinear gauge couplings. It can also probe the non-abelian gauge structure of the SM since the SM EW bosons arise by virtue of the embedded SU(2) gauge symmetry group. Secondly, processes involving a Higgs exchange test couplings between the Higgs and gauge bosons at energy scales significantly different from the Higgs mass. VBS investigations test the Higgs mechanism of the spontaneously broken electroweak symmetry in the SM (discussed in Section 2.1.3). The Higgs mechanism is also sensitive to possible new physics effects leading to anomalous quartic gauge couplings, and to BSM physics which would manifest itself as an increase in differential cross sections [48].

3.1.1 Role of the Higgs boson

The presence of the Higgs boson is crucial in VBS. It preserves the basic principle of probability conservation called unitarity[1]. The scattering amplitude of longitudinally polarized vector bosons, $V_L V_L \to V_L V_L$, violates unitarity while considering only triple gauge or quartic gauge couplings. The production rate of the process grows faster with energy than the pp interaction rate, which is unphysical. The amplitude is regularized by including the interactions between the Higgs and EW gauge bosons. Graphical representation of this phenomenon for $W_L^+ W_L^- \to W_L^+ W_L^-$ scattering is

[1]Sum of probabilities of all the final states emerging from given initial states must equal to one.

shown in Fig. 3.2, while Fig. 3.3 shows the plots for $V_LV_L \to V_LV_L$ considering all gauge boson combinations.

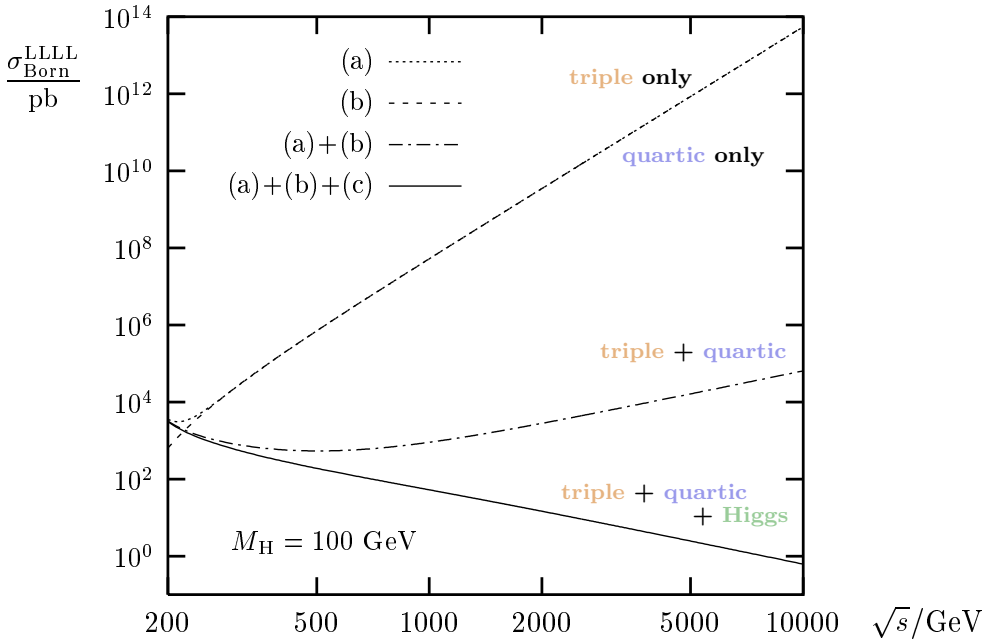


Figure 3.2: Cross sections as a function of center-of-mass energy ($\sqrt{s}$) in $W_L^+W_L^- \to W_L^+W_L^-$ resulting from subsets of the tree-level diagrams: (a) triple gauge couplings, (b) quartic gauge couplings, and (c) Higgs boson couplings. The combination of all three classes restores unitarity. Figure modified from Ref. [49].

The phenomena discussed above are exclusive to the case of longitudinal polarization. They can be better understood by looking at the general expressions of polarization vectors, ε^μ, of the gauge bosons:

$$\underbrace{\varepsilon^\mu_{T,R} = \frac{1}{\sqrt{2}}(0,1,i,0)}_{\textit{Transverse, right-handed}}, \qquad \underbrace{\varepsilon^\mu_{T,L} = \frac{1}{\sqrt{2}}(0,1,-i,0)}_{\textit{Transverse, left-handed}}, \qquad \underbrace{\varepsilon^\mu_{L} = \frac{1}{m}(p_z,0,0,E)}_{\textit{Longitudinal}}, \tag{3.1}$$

where m, E, and p_z are the mass, energy, and longitudinal momentum of the particle, respectively. Longitudinal polarization is exclusive to massive vector bosons, and uniquely, this mode exhibits energy dependence. Thus, measurement of the longitudinal polarization holds paramount significance and is the central focus of this dissertation.

3.2 Electroweak Vector Boson Scattering at the LHC

LHC experiments pioneer the search for electroweak vector boson scattering processes $V_1V_2 \to V_3V_4$. These processes have a low production cross section ($\sim \mathcal{O}$(fb)) even at the energy scales

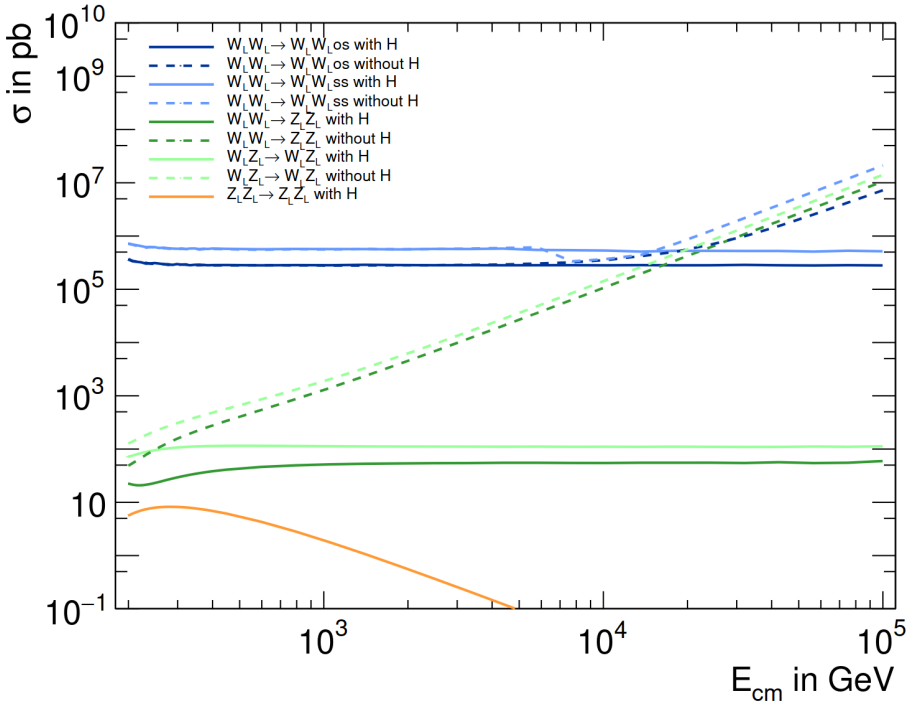


Figure 3.3: Cross section as a function of center-of-mass energy in $V_LV_L \to V_LV_L$ for $V = W,Z$. Solid and dashed lines represent the cross sections with and without the SM-like Higgs boson contribution, respectively. Figure taken from Ref. [50].

achieved by the LHC (refer to Fig. 3.4) [51]. In simpler words, the VBS process rate is so low that it accounts for only one in hundreds of trillions of proton-proton interactions. Yet, the LHC is the best place to look for this rare process as it collides protons with the highest energy and rate ever reached. The exploration of this phenomenon is discussed with the intention of motivating the study of the $W^{\pm}W^{\pm}jj$ production. Note that the term vector boson scattering is used here to refer to the scattering of massive gauge bosons ($V = W,Z$ – all except γ) unless specified otherwise[2].

3.2.1 Event signature of VBS at the LHC

A typical picture of EW VBS at the LHC involves two colliding quarks[3] emitting two electroweak gauge bosons. The vector bosons undergo interactions as illustrated in Fig. 3.1 and subsequently decay. The outgoing quarks hadronize due to colour confinement and manifest as collimated sprays of particles called jets. Hence, the process of interest is denoted as $VVjj$ and is illustrated via schematic and representative Feynman diagrams in Fig. 3.5 and Fig. 3.6 respectively.

The associated jets, termed as *tagging jets*, stand out as notable features in the VBS topology.

[2]Final state $\gamma\gamma$ processes have a different experimental signature. They also exclude the Higgs exchange diagrams since photons are massless.

[3]Strongly interacting gluons cannot emit EW vector bosons.

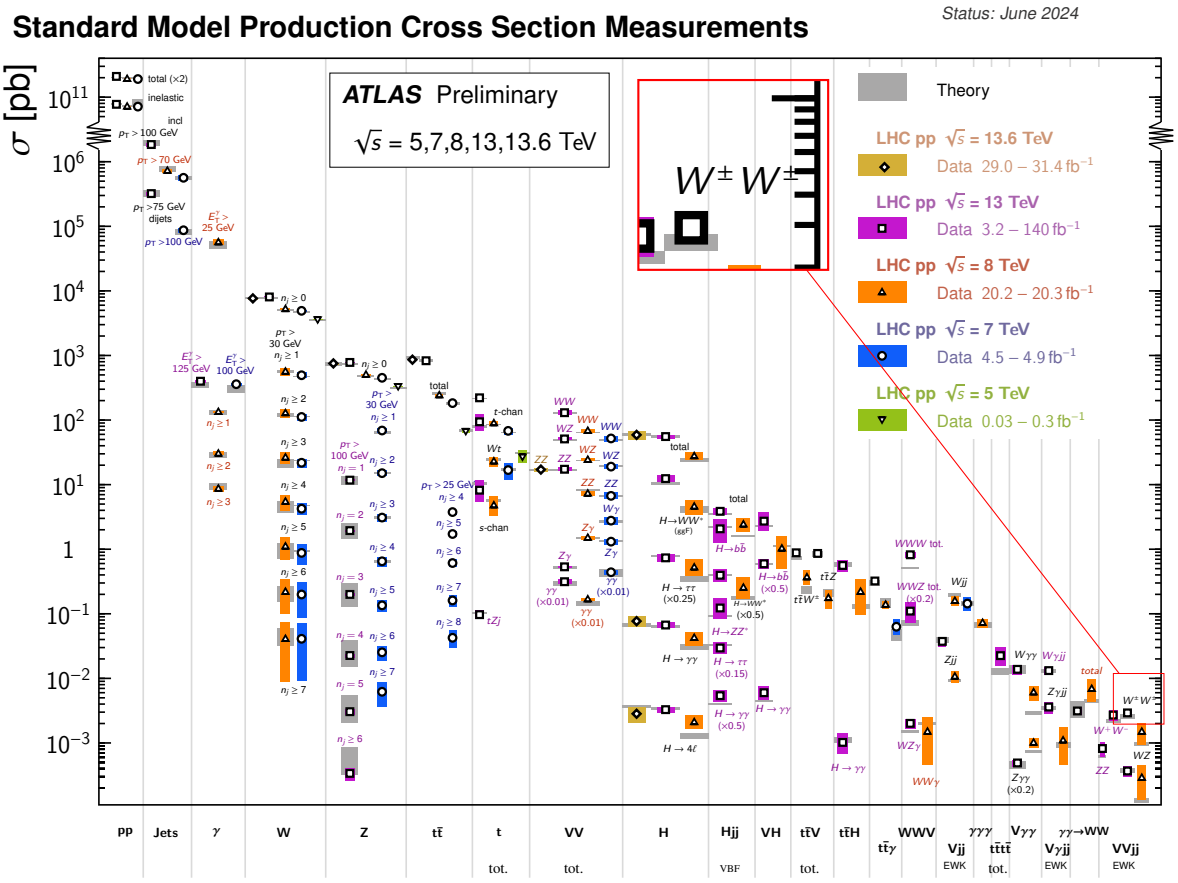


Figure 3.4: Overview of multiple Standard Model total and fiducial production cross-section measurements conducted with the ATLAS experiment, accounting for branching fractions, and compared with corresponding theoretical predictions at the precision level relevant to the processes. Figure modified from Ref. [52].

They are typically observed in the forward region of the detector since the incoming quarks are minimally deflected after V emission. These jets lie in the opposite hemispheres, make small scattering angles relative to the beam axis and have relatively high energies. The features of small scattering angles and large di-jet invariant mass can be mathematically derived using the squared matrix element [53] (refer to Appendix A.2). Thus, the experimental signature of EW VBS constitutes the observance of large di-jet rapidity separation (Δy_{jj}) and large di-jet invariant mass (m_{jj}).

Feynman diagrams at Leading Order

All the interactions in the VBS process at leading order are electroweak in nature, therefore it is defined at Born level as $\mathcal{O}(\alpha^6)$. However, experimental measurement of this signature necessarily implies the inclusion of other non-VBS contributiuons. Only the total amplitude is accessible for

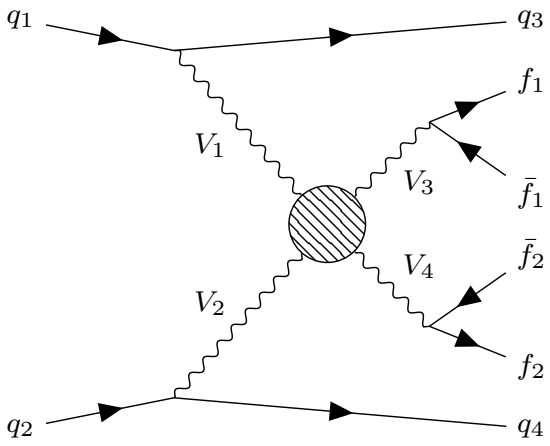


Figure 3.5: Schematic Feynman diagram illustrating electroweak vector boson scattering $VVjj$ processes at the Large Hadron Collider.

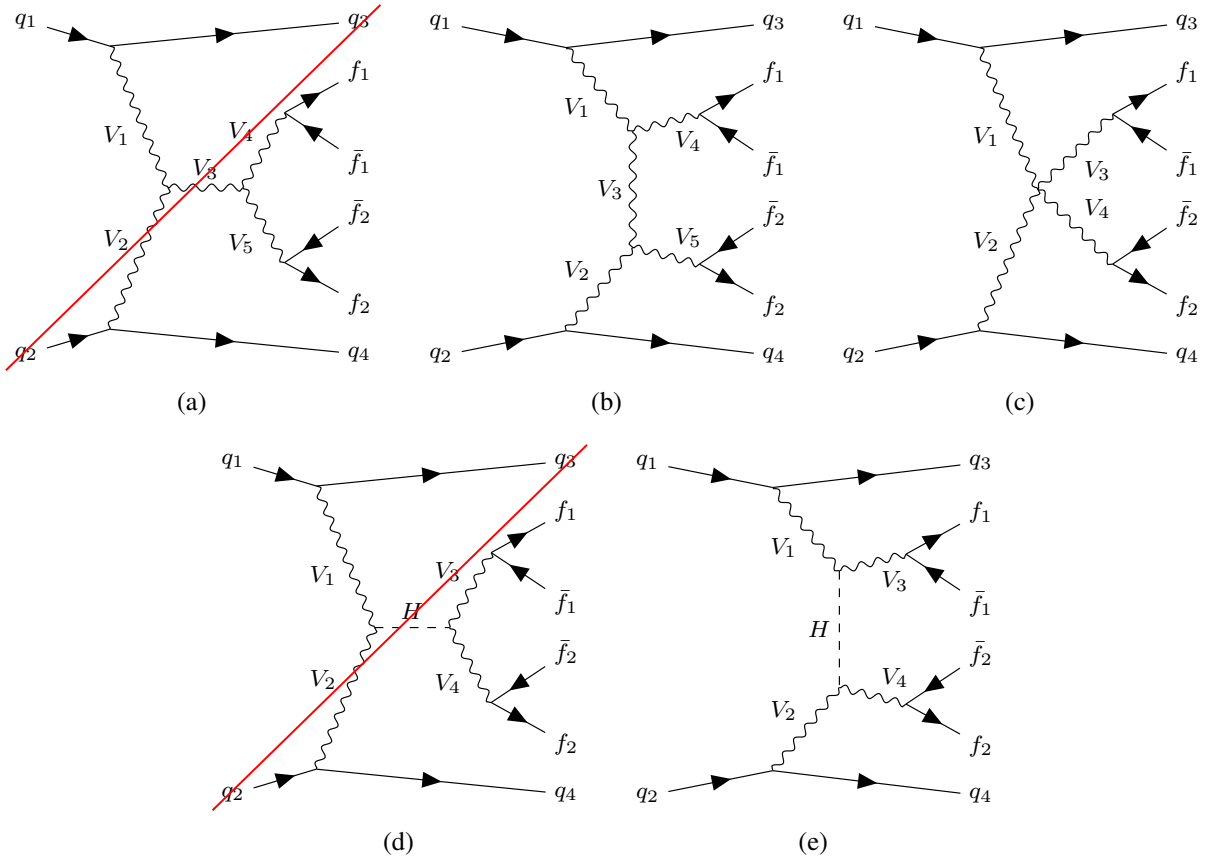


Figure 3.6: Representative Feynman diagrams: VBS EW $VVjj$ production. The diagram labels correspond to quarks (q), vector bosons ($V = W, Z, \gamma$), and fermions (f). The s-channel diagrams shown in Fig. 3.6(a) and 3.6(d) do not exist in $W^{\pm}W^{\pm}jj$ final states.

measurement giving the total cross section inclusive of other contributions: (i) EW at order $\mathcal{O}(\alpha^6)$, (ii) QCD at order $\mathcal{O}(\alpha_s^2\alpha^4)$ and (iii) interference at order $\mathcal{O}(\alpha_s\alpha^5)$,

$$\begin{aligned}\sigma &\propto |\mathscr{M}_{\mathrm{EW}} + \mathscr{M}_{\mathrm{QCD}}|^2 , \\ &\propto \underbrace{|\mathscr{M}_{\mathrm{EW}}|^2}_{\mathcal{O}(\alpha^6)} + \underbrace{|\mathscr{M}_{\mathrm{QCD}}|^2}_{\mathcal{O}(\alpha_s^2\alpha^4)} + \underbrace{2\cdot Re(\mathscr{M}_{\mathrm{EW}}\overline{\mathscr{M}}_{\mathrm{QCD}})}_{\mathcal{O}(\alpha_s\alpha^5)} , \\ &\equiv \underbrace{\sigma_{\mathrm{EW}}}_{+ve} + \underbrace{\sigma_{\mathrm{QCD}}}_{+ve} + \underbrace{\sigma_{\mathrm{INT}}}_{+ve/-ve} .\end{aligned} \tag{3.2}$$

The EW non-VBS diagrams, as shown in Fig. 3.7, are indistinguishable from VBS and constitute an irreducible background. Some undesirable components, however, can be suppressed using specific cuts. Triboson events with at least one boson decaying hadronically constitute one such example. They are suppressed by an invariant mass cut on the two jets well above the W/Z boson mass.

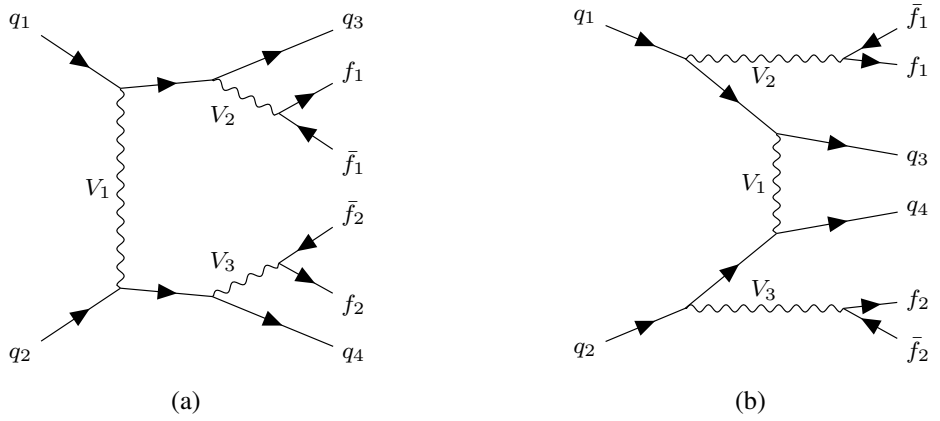


Figure 3.7: Representative Feynman diagrams: non-VBS EW $VVjj$ production. The diagram labels correspond to quarks (q), vector bosons ($V = W, Z, \gamma$), and fermions (f).

The QCD diagrams are shown in Fig. 3.8. The gluon-induced strong production typically has a much larger cross section owing to the abundance of gluons in a proton-proton collision (refer to Chapter 2). But the kinematic properties of QCD processes relative to EW processes are quite different and are primarily present in different phase-space regions. Colour interactions draw the gluons together, leading to the majority of hadronic activity taking place in the central region of the detector. Consequently, the rapidity separation between the two tagging jets is most pronounced at zero, showcasing a clear deviation from EW production.

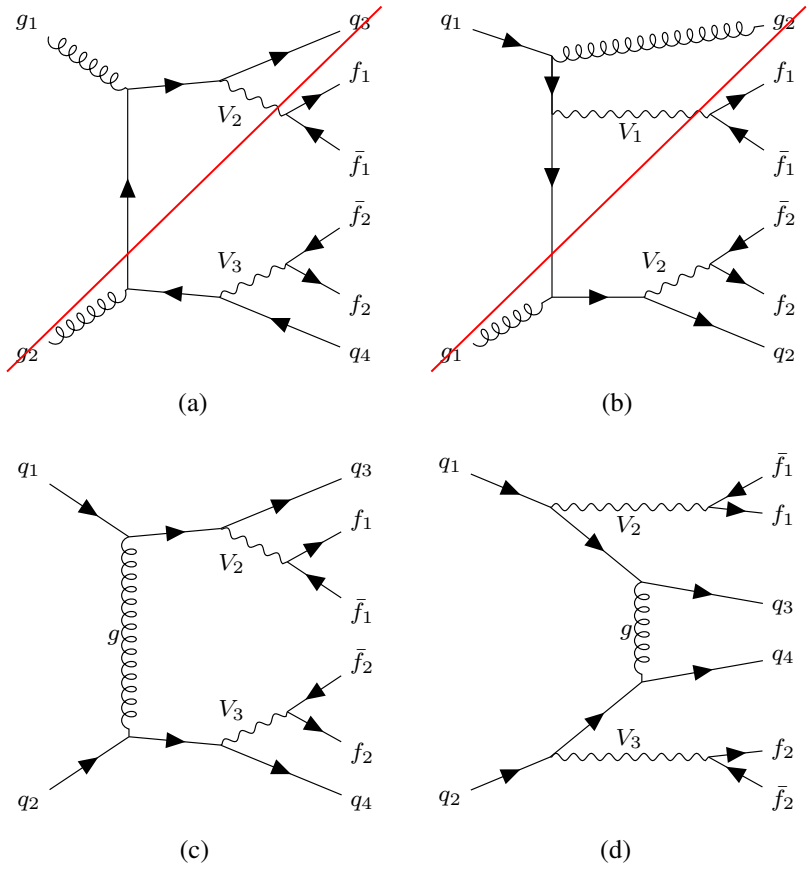


Figure 3.8: Representative Feynman diagrams: QCD $VVjj$ production. The diagram labels correspond to quarks (q), vector bosons ($V = W, Z$), gluons (g), and fermions (f). The gluon initial state diagrams shown in Fig. 3.8(a) and 3.8(b) do not exist in $W^{\pm}W^{\pm}jj$ final states.

3.2.2 Final states in experimental VBS signature

V decay dictates the final state particles. The probability of the vector boson's various decay modes is given by their branching ratios. Fig. 3.9 presents branching ratios of some common SM processes involving W, Z decays. Although the highest branching ratio is exhibited by the hadronic modes, measurement in these channels is challenging due to a large QCD jet background. Neutrinos in the final state are undetectable/invisible. τ leptons are heavy, unstable particles that decay further into hadrons or leptons. Therefore, lighter leptonic ($\ell = e, \mu$) final states appear to be the ideal choice owing to a clean signature of ℓ in the detector.

The VBS initial state consists of two quarks, while the final state includes at least two jets and up to four leptons. Consequently, three VBS signatures are possible at the LHC: (i) *fully leptonic* with 2 jets and 4 leptons, (ii) *semi-leptonic/semi-hadronic* with 4 jets and 2 leptons, and (iii) *fully hadronic* with 6 jets. The sensitivity in the fully hadronic channel is compromised due to overwhelming background contributions from multi-jet production. For leptonic channels, the major background is gluon-initiated processes, typically of order $\mathcal{O}(\alpha_s^2\alpha^4)$. VBS channels are

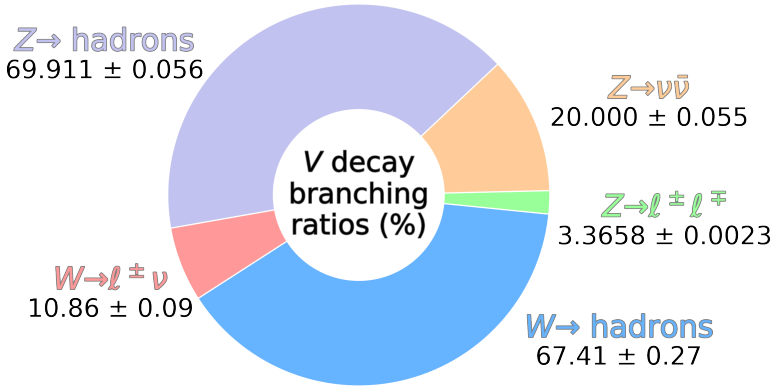


Figure 3.9: Branching ratios (in %) for some of the common W, Z boson decay modes [54]. In $W \to \ell^{\pm}\nu$ and $Z \to \ell^{\pm}\ell^{\mp}$, ℓ indicates each lepton flavor (e, μ and τ), not sum over them.

commonly categorized according to EW-to-QCD production ratio. This ratio and the fiducial cross sections of fully leptonic final states are shown in Table 3.1. All channels have this ratio $\lesssim$1 with the sole exception of $W^{\pm}W^{\pm}jj$ channel. It is clearly extraordinary and serves as one of the most preferred channels to probe EW VBS at the LHC with its enhanced background suppression.

Final State	**Diboson channel**	σ_{EW} (fb)	σ_{QCD} (fb)	$\frac{\sigma_{\text{EW}}}{\sigma_{\text{QCD}}}$
$\ell^+\ell^-\ell^+\ell^- jj$	ZZ	0.098	0.100	0.98
$\ell^{\pm}\nu\ell^+\ell^- jj$	$W^{\pm}Z$	2.34	4.38	0.53
$\ell^{\pm}\nu\ell^{\mp}\nu jj$	$W^{\pm}W^{\mp}, ZZ$	12.3	21.8	0.56
$\ell^{\pm}\nu\ell^{\pm}\nu jj$	$W^{\pm}W^{\pm}$	3.97	0.346	11.5
$\ell^{\pm}\nu\nu\nu jj$	$W^{\pm}Z$	7.64	15.5	0.49
$\nu\nu\nu\nu jj$	ZZ	1.68	1.38	1.22

Table 3.1: Comparison of predicted cross sections for fully leptonic final states in EW and QCD processes, calculated with Sherpa at LO in a typical phase space [55]. The labels $\ell = e, \mu$ and $\nu = \nu, \bar{\nu}$. Statistical uncertainties on the cross section from phase-space integration are below 2%. The final column presents the EW-to-QCD cross-section ratio.

3.2.3 The $W^{\pm}W^{\pm}jj \to \ell^{\pm}\nu\ell^{\pm}\nu jj$ final state

The $W^{\pm}W^{\pm}jj$ production is widely regarded as the *golden* channel in VBS studies and is unique in many ways. Despite its notably small cross section in the Standard Model, as depicted in Fig. 3.4, it remains a favourite. It has the largest EW-to-QCD production cross-section ratio (see Table 3.1). This is due to electric charge conservation prohibiting gluon-initiated QCD diagrams (refer to

Fig. 3.8). This significantly suppresses the QCD background as opposed to $W^{\pm}Z, ZZ$, or $W^{\pm}W^{\mp}$ mediated processes. The EW s-channel Higgs and V exchange diagrams are also forbidden by the same principle (refer to Fig. 3.6) but the overall EW contribution is enhanced through implementing event selections (refer to Sec. 3.2.1). The leptonic final states ensure cleaner detector signature and help in clear identification of the W boson electric charge. The same charge requirement further reduces several backgrounds. Hence, the $W^{\pm}W^{\pm}jj$ channel emerges as highly sensitive to potential new-physics phenomena, encompassing the effects of polarization and anomalous quartic gauge couplings.

Characteristic Signature at the LHC

The characteristic event signature at the LHC for the $W^{\pm}W^{\pm}jj$ process is illustrated in Fig. 3.10. It consists of the following: two *tagging* jets, two same-charge light leptons and two neutrinos manifested as missing transverse energy. The two tagging jets are typically initiated by u, d, c, s quarks, while b-initiated jets are exceedingly rare[4]. Positioned at opposite ends of the detector, these jets exhibit a large rapidity gap between them (Δy_{jj}) and a significant di-jet invariant mass (m_{jj}). No additional jet resides in the gap region. However, the W bosons and leptons lie in between these jets.

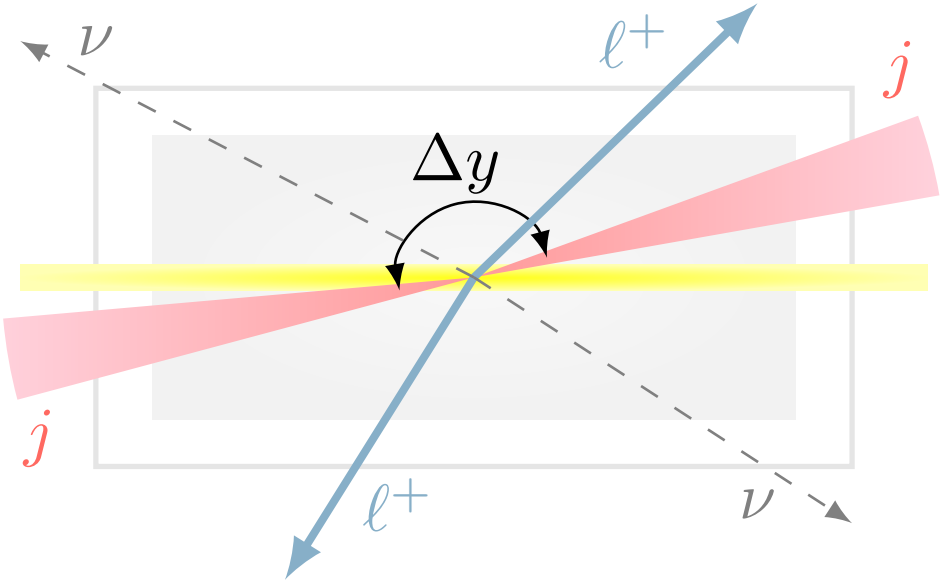


Figure 3.10: A simplistic picturisation of VBS $W^{\pm}W^{\pm}jj$ event topology. The final state includes two jets (j) in the forward regions with large rapidity gap (Δy), two outgoing leptons (ℓ) and neutrinos (ν) which come from W boson decays. Vector bosons lie in the central region. There is no additional jet in the gap region.

[4]Theoretically, b-jets are absent due to the same charge in $W^{\pm}W^{\pm}$ final states and t quark being a different signature up to NLO QCD.

Next-to-Leading Order (NLO) Corrections

The complete NLO corrections involve four orders: $\mathcal{O}(\alpha^7), \mathcal{O}(\alpha_s\alpha^6), \mathcal{O}(\alpha_s^2\alpha^5), \mathcal{O}(\alpha_s^3\alpha^4)$, as depicted in Fig. 3.11. Purely EW corrections to the LO EW $W^\pm W^\pm jj$ production result in an order $\mathcal{O}(\alpha^7)$ correction. Similarly, QCD corrections to the QCD LO $W^\pm W^\pm jj$ production yield an order $\mathcal{O}(\alpha_s^3\alpha^4)$ correction [56]. The orders $\mathcal{O}(\alpha_s\alpha^6)$ and $\mathcal{O}(\alpha_s^2\alpha^5)$ entail both EW and QCD corrections to at least two LO contributions, making it challenging to distinguish between EW-induced and QCD-induced modes. This distinction is impossible to make without relying on the VBS approximation in the theoretical framework [57, 58]. It is worth noting that the EW corrections are quite substantial, up to ~16%, which is one of the remarkable features of VBS.

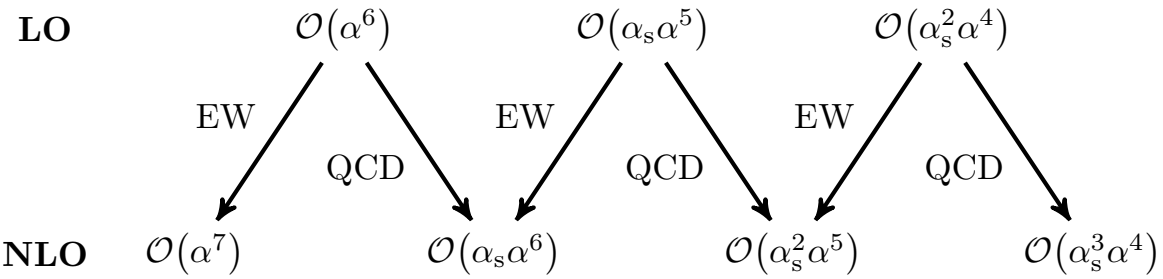


Figure 3.11: Contributing perturbative orders of the $VVjj$ process at LO and NLO at the LHC. Figure taken from Ref. [59].

Measurements at the LHC

The ATLAS Collaboration reported the first evidence for same-sign $W^\pm W^\pm jj$ electroweak production using 20.3 fb^{-1} of proton–proton collision data at $\sqrt{s} = 8$ TeV [60], observing a 3.6 σ excess above the background-only expectation. A complementary analysis by the CMS Collaboration found a 2.0 σ excess [61]. Subsequent measurements with partial Run 2 data from 2015–2016 at $\sqrt{s} = 13$ TeV led to the observation of the process, with observed (expected) significances of 5.5 (5.7) σ and 6.5 (6.5) σ reported by CMS [62] and ATLAS [63][5], respectively. These results were later followed by differential cross-section measurements of $W^\pm W^\pm jj$ production by both ATLAS [64] and CMS [65], employing the full Run 2 dataset from 2015–2018. More recently, using the complete Run 2 dataset, ATLAS presented the first evidence (3.3 σ) for VBS involving at least one longitudinally polarized same-sign W boson; in addition, the analysis set stringent upper limits on the doubly longitudinal (LL) component, where both W bosons are longitudinally polarized [1]. In this dissertation, upper limits are set on VBS involving same-sign W bosons — both longitudinally polarized ($W_L^\pm W_L^\pm$).

[5]The quoted expected significance corresponds to POWHEG; for SHERPA v2.2.2, the expected significance was 4.4 σ.

3.3 Polarization in Vector Boson Scattering

The Standard Model EW bosons acquire their masses and longitudinal polarizations via the Higgs mechanism of the spontaneously broken EW symmetry (details in Section 2.1.3). Measurements of polarization observables in multiboson interactions are direct probes of this mechanism. The inclusion of Feynman diagrams with Higgs boson exchange is crucial to prevent unitarity violation due to the rising scattering cross section of longitudinally polarized vector bosons, *i.e.* $V_LV_L \to V_LV_L$ scattering (as discussed in Section 3.1.1). Therefore, investigating polarization in VBS processes holds significant interest.

3.3.1 Polarization and its effects on Kinematics

Helicity (h) is the projection of the spin ($\vec{S}$) of a particle onto its direction of momentum ($\vec{p}$),

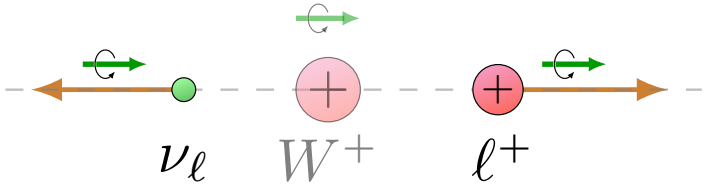
$$h = \vec{S} \cdot \hat{p}\,. \tag{3.3}$$

It is *not* Lorentz invariant for massive particles. The W boson is a spin-1 particle and therefore, its helicity can be $0, \pm 1$, meaning that the spin can be perpendicular, parallel or anti-parallel to the momentum of the parent W boson. Note that chirality refers to the intrinsic property of a particle's wavefunction, defining left-handed and right-handed components. In the ultra-relativistic limit ($E \gg m$), the chirality and helicity eigenstates are equivalent.

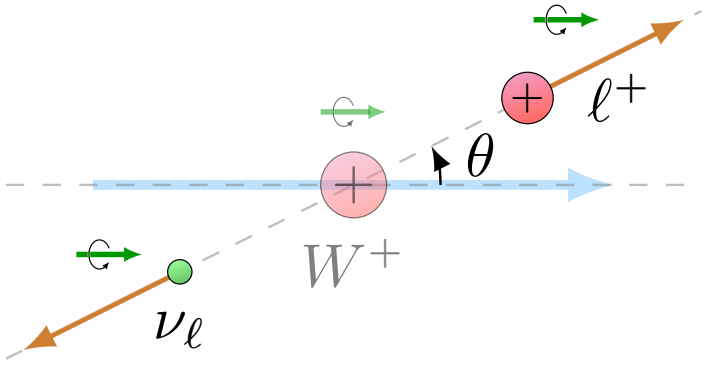
Weak interactions inherently violate parity. The W boson exclusively interacts with left-handed particles and right-handed anti-particles. For instance, in the leptonic decay of a positively charged W boson ($W^+ \to \ell^+\nu$), the W^+ boson can only decay into left-handed neutrino (ν) and right-handed anti-lepton (ℓ^+). Consequently, when the W boson is longitudinally polarized ($W_L, h = 0$), the resulting anti-lepton escapes perpendicular to the original W boson direction of flight. For transverse polarization, the anti-lepton decays in the same direction as the right-handed W^+ boson ($W_{T,R}, h = +1$), while it escapes in the opposite direction of the left-handed W^+ boson ($W_{T,L}, h = -1$). This concept is visually illustrated in Fig. 3.12 and Fig. 3.13.

The phenomena described above can be quantified using the observable θ, referred to as the polar angle. Considering the leptonic decay of the $W^\pm$ boson ($W^\pm \to \ell^\pm\nu$) in the W rest frame (and the azimuthal angle ϕ is integrated over), the differential cross section can be factorized as [66]

$$\frac{1}{\sigma}\frac{d\sigma}{d\cos\theta} = \underbrace{\frac{3}{8}(1 \mp \cos\theta)^2 f_{T,L} + \frac{3}{8}(1 \pm \cos\theta)^2 f_{T,R}}_{\textit{Transverse}} + \underbrace{\frac{3}{4}\sin^2\theta f_L}_{\textit{Longitudinal}}, \qquad \text{for } W^\pm, \tag{3.4}$$



(a) Helicity in $W^+ \to \ell^+ \nu_\ell$ decay in boson rest frame



(b) Polar angle θ

Figure 3.12: Visual depiction of leptonic W^+ boson decay. Momenta and spins directions are shown with brown and green arrows respectively. Polar angle θ is the angle between the charged lepton in the boson rest frame and direction of motion of the parent W boson in laboratory frame (shown with blue arrow). Figure modified from Ref. [27].

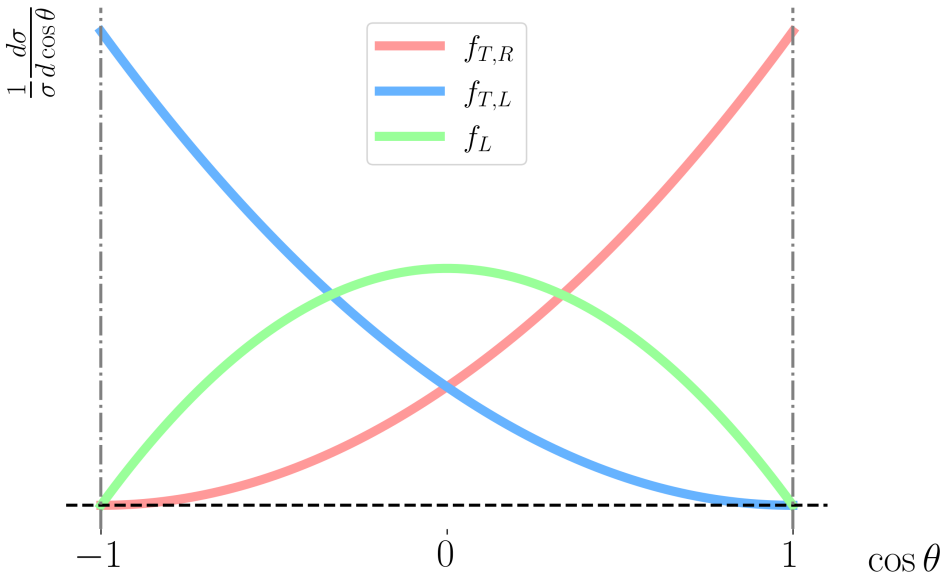
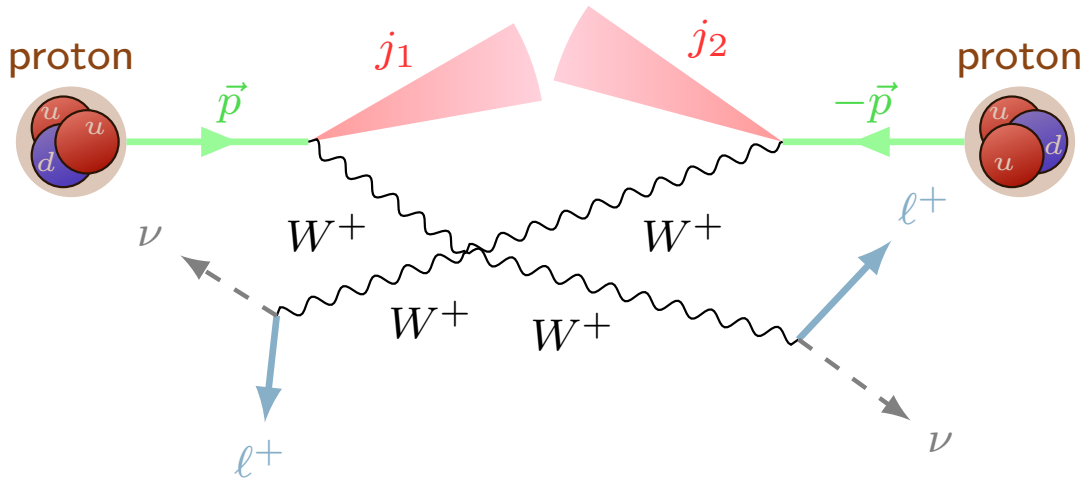
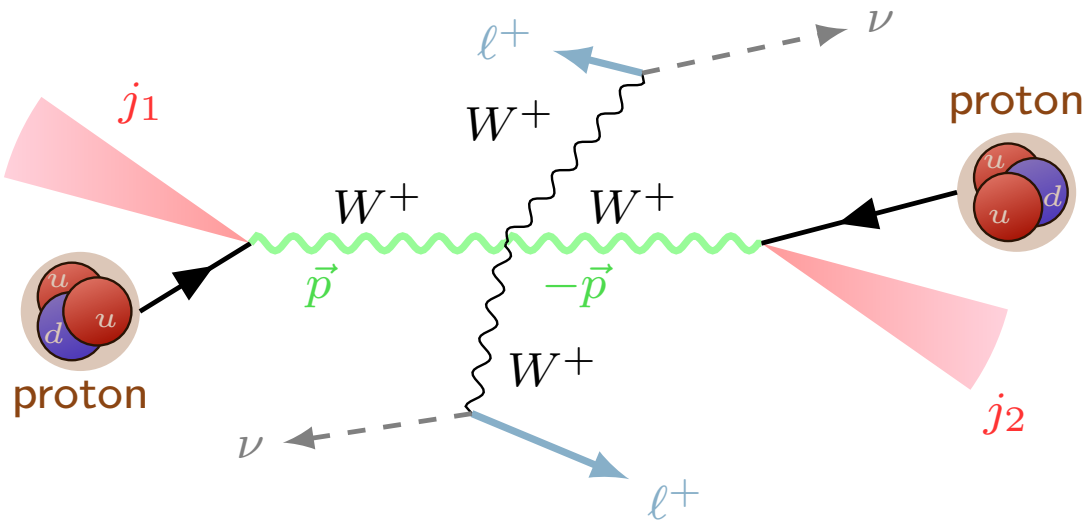


Figure 3.13: For $W^+ \to \ell^+ \nu$, differential cross section in $\cos\theta$ is shown for all W polarizations according to theory predictions (Eq. 3.4). The polarization fractions are denoted as follows: f_L for longitudinal, $f_{T,R}$ for transverse right-handed, and $f_{T,L}$ for transverse left-handed polarizations.



(a) Parton-parton center-of-mass frame or *ppcmf*



(b) *WW* center-of-mass frame or *WWcmf*

Figure 3.14: Visual depiction of the $W^{\pm}W^{\pm}jj$ process in partonic and diboson center-of-mass frames of references. The W boson polarization is defined in the chosen frame. Equal and opposite 3-momenta $\vec{p}$ (shown in green) cancel out in the figures. The arrows indicate incoming and outgoing particles. Proton figures modified from Ref. [27].

where polar angle θ is the angle between the charged daughter lepton $\ell^{\pm}$ in the boson rest frame and the parent $W^{\pm}$ boson's direction of motion in the laboratory frame. The three possible polarization fractions, denoted by $f_{T,L}$, $f_{T,R}$, and f_L for transverse left-handed, right-handed, and longitudinal polarizations, respectively, quantify the individual contributions of these polarizations to the cross section. Whenever the left-handed and right-handed polarizations are studied inclusively, it is denoted as the transverse polarization or W_T in this dissertation. The sum of the three contributions should equal unity, imposing the following constraint:

$$f_{T,L} + f_{T,R} + f_L = 1\,. \tag{3.5}$$

Validating the Monte Carlo signal samples of polarized $W^{\pm}W^{\pm}jj$ production requires fitting the angular distributions to Eq. 3.4 with the constraint in Eq. 3.5, as detailed in Chapter 9. This step is crucial to ensure the accuracy and reliability of the simulated data.

It is imperative to address that polarization vectors (refer to Eq. 3.1) are not Lorentz covariant, necessitating the selection of a reference frame. Typical choices include the laboratory frame, partonic center-of-mass frame, and diboson center-of-mass frame. This dissertation specifically examines the partonic center-of-mass frame (*ppcmf*) and diboson center-of-mass frame (*WWcmf*), as illustrated in Fig. 3.14.

Chapter 4

The ATLAS Experiment at the Large Hadron Collider

This chapter provides an overview of the experimental setup used to collect data relevant to this study. It begins with a concise introduction to the Large Hadron Collider (LHC) at the European Organisation for Nuclear Research (CERN[1]) in Section 4.1, followed by a closer look at the ATLAS detector in Section 4.2. Given the complexity of these systems, the chapter offers a general overview, with more detailed information available in Ref. [67–70].

4.1 The Large Hadron Collider

The LHC is presently the world's largest, most complex, and highest energy particle accelerator and collider experiment. Situated beneath the Franco-Swiss border at CERN, it is a circular tunnel 100 m underground, and 26.7 km in circumference. The LHC is part of a complex chain of accelerators that sequentially increase proton energy and intensity before injection into the collider ring. The LHC began operations in 2008 with phases of data-taking periods, termed as *Runs*, alternating with shutdowns for detector upgrade and maintenence. The LHC's principal data-taking periods to date comprise Run 1 (2010–2012), Run 2 (2015–2018), and the currently ongoing Run 3 (since 2022), as shown in Fig. 4.3.

Various particle accelerators have been built at CERN facilitating several notable discoveries, for example, the discovery of weak interaction neutral currents (1973) [71], W [72, 73] and Z [74, 75] bosons (1983), and more recently the Higgs boson (2012) [15, 16]. These accelerators include

[1] Conseil Européen pour la Recherche Nucléaire

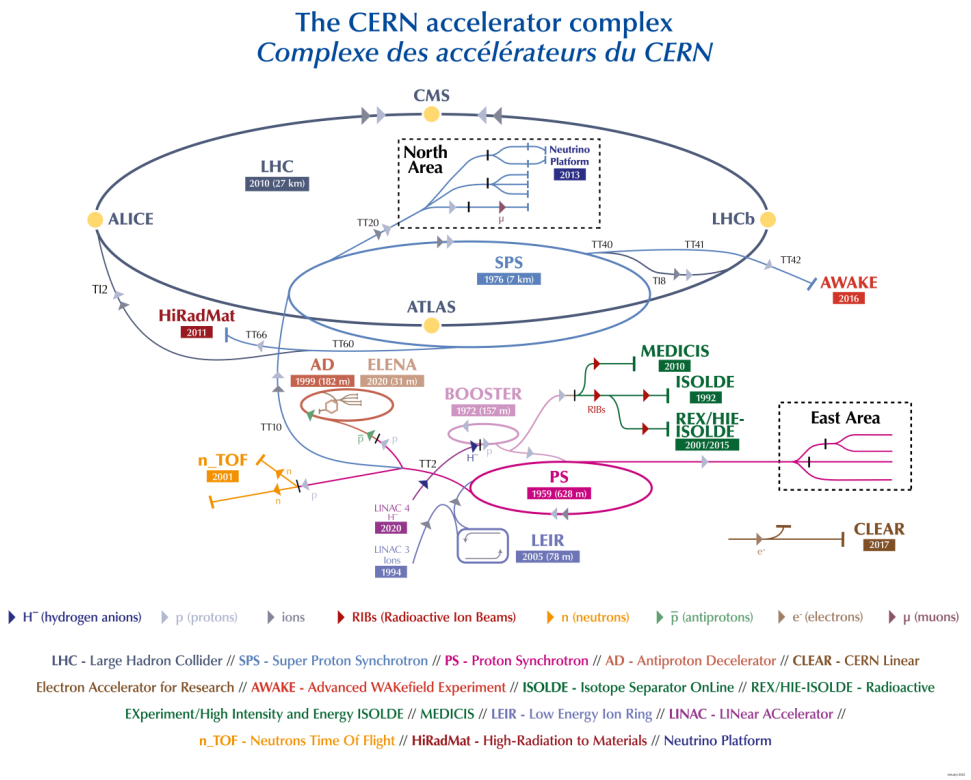


Figure 4.1: Existing CERN accelerator complex [77].

LINear ACcelerator (LINAC) built in 1959, the Proton Synchrotron (PS) in 1960, the Super Proton Synchrotron (SPS) in 1971, and the Large Electron Positron (LEP) collider [76] in 1989. Many of them are still used as parts of LHC's injector chain. The tunnel of the LEP collider, operational between 1989-2000, is currently used by the LHC.

4.1.1 Accelerator complex

The LHC serves as the final and most powerful stage in CERN's extensive accelerator complex, as shown in Fig. 4.1. Protons in the LHC originate from ionizing H_2 gas and stripping off electrons using electric fields. Pre-acceleration occurs in multiple stages, beginning with the linear accelerator LINAC 2 (used during Run 2), which accelerates protons up to 50 MeV. These protons are injected into the Proton Synchrotron Booster (PSB) and subsequently the PS, which raise the beam energies further up to 1.4 GeV and 26 GeV respectively. The final stage of pre-acceleration occurs in the SPS, which boosts the protons up to 450 GeV before injecting them into the LHC. The beam is bifurcated within the LHC, resulting in two different rings with proton beams circulting in opposite directions with peak energy of 6.5 TeV per beam. In the long shutdown during 2019–20, LINAC 4 [78] replaced LINAC 2 which accelerates beams to 160 MeV. Ultimately, in Run 3, the LHC achieves a peak energy of 6.8 TeV per beam.

4.1.2 Collider Systems and Parameters

After injection from the pre-accelerator chain, protons circulate within the 27 km LHC ring, which consists of eight arcs and eight straight sections. The beam is guided by nearly 1,232 superconducting dipole magnets producing fields of up to 8.33 T within ultra-high vacuum beam pipes. Quadrupole magnets focus the beams at the interaction points (IPs) to achieve small transverse beam sizes characterized by the β^* parameter. The entire magnet system is maintained at 1.9 K by the LHC's cryogenic infrastructure, while radio-frequency (RF) cavities operating at 400 MHz ensure longitudinal stability of the proton bunches, providing both acceleration and bunching.

The LHC beams are composed of discrete proton bunches, typically containing $\mathcal{O}(10^{11})$ protons each, with a nominal spacing of 25 ns corresponding to a 40 MHz bunch crossing frequency. Collisions take place when two bunches from the opposite beams inter-penetrate, which is termed as a *bunch crossing*. The collisions that occur in addition to an interesting collision in every bunch crossing are termed as *pile-up*. The bunches are organized into trains separated by abort gaps to allow for safe beam extraction and synchronization with the injection and dump systems. Transversely, the beams are focused to a few tens of micrometers at the IPs, while longitudinally, the bunch profiles are maintained by the RF system to preserve collision quality and timing.

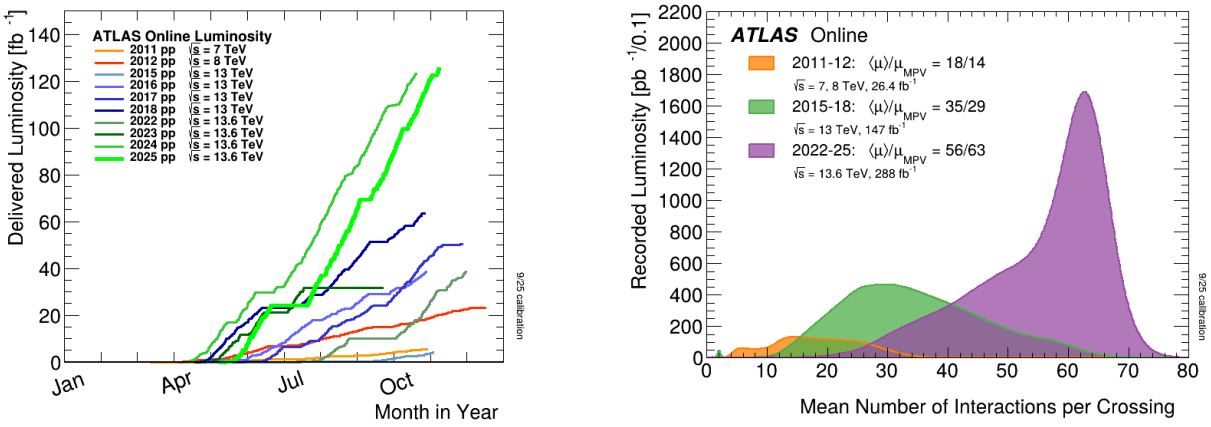
The performance of a particle collider is quantified by two important parameters *viz.* its center-of-mass energy and luminosity. The *centre-of-mass energy*, $\sqrt{s}$, defines the total energy available for particle production in collisions and sets the threshold for creating massive states. A higher $\sqrt{s}$ increases the likelihood of producing heavy or rare particles, following the principle of energy-mass equivalence. The LHC currently holds the world record with proton–proton collisions at 13 TeV, far exceeding the 2 TeV achieved by the Tevatron at Fermilab [79]. Secondly, the collider's ability to generate interactions is quantified by its *luminosity*. *Instantaneous luminosity*, L, representing the number of collisions produced per unit area per second, can be expressed as

$$L = \frac{f N_1 N_2}{4\pi \sigma_x \sigma_y}, \tag{4.1}$$

where f is the bunch crossing frequency, $N_{1,2}$ are the numbers of protons per bunch, and σ_x, σ_y are the transverse beam sizes at the IP assuming Gaussian beam profiles. At collider experiments, the rate (R) of a given physics process with a cross section σ depends on $\sqrt{s}$ and L as $R(t) = L(t) \cdot \sigma(\sqrt{s})$. Since running conditions vary with time, the *integrated luminosity*,

$$\mathscr{L} = \int_0^t L dt, \tag{4.2}$$

is a more relevant quantity for physics analyses, representing the total data collected over time. For a process with cross section σ, the total number of events produced is $N_{\text{events}} = \mathscr{L}\sigma$. While



(a) Delivered Luminosity vs time for *p*-*p* collisions

(b) Average interactions per bunch crossing $\langle\mu\rangle$

Figure 4.2: Luminosity summary results for the 2011-2025 data recorded by the ATLAS detector during stable beams and for high energy *p*-*p* collisions [80].

σ characterizes the physics process, luminosity reflects the collider's performance. A summary of the luminosity delivered and recorded by ATLAS over the years is shown in Figure 4.2. For this work, data from Run 2 (2015-2018) are used.

4.1.3 Experiments at the LHC

The LHC hosts a suite of experiments designed to explore both the SM and potential new physics phenomena at unprecedented energies. The two largest general-purpose detectors — ATLAS [81] and CMS [82] — are optimized to measure a wide variety of final states with high precision, covering nearly the full solid angle around the IPs. They are complemented by specialized experiments: LHCb [83], dedicated to the study of heavy-flavor physics and CP violation; ALICE [84], focused on the properties of the quark-gluon plasma in heavy-ion collisions; TOTEM [85] and LHCf [86], which measure diffractive processes and forward particle production; and MoEDAL-MAPP [87], searching for magnetic monopoles. CERN, furthermore, hosts several other experimental facilities to conduct cutting-edge research in areas such as nuclear physics, medical isotopes, and neutron-induced reactions.

4.1.4 Future Hadron and Lepton Colliders

Preparations are underway for the High-Luminosity LHC (HL-LHC) upgrade [88], expected to begin operation (Run 4) in 2030, which will deliver about an order of magnitude more integrated luminosity. The HL-LHC operation plan is shown in Fig. 4.3.

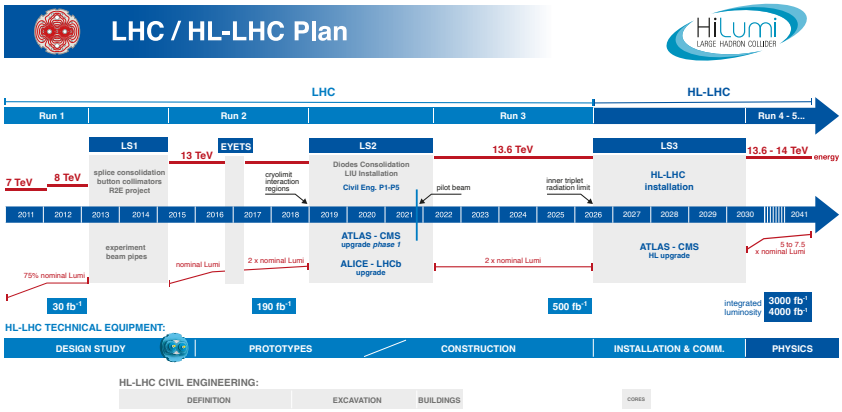


Figure 4.3: Schedule of the LHC and HL-LHC operation [88].

Beyond the HL-LHC, several next-generation facilities are being designed to push both the energy and precision frontiers of particle physics. At CERN, the Future Circular Collider (FCC) [89] programme envisions a 90 km tunnel that would first host an e^+e^- collider, FCC-ee, operating up to 400 GeV centre-of-mass energy, followed by a hadron collider, FCC-hh, reaching 90–100 TeV. A comparable initiative, the Circular Electron Positron Collider (CEPC) [90], is under development in China with similar staged goals. To achieve such energies in e^+e^- collisions, the possibility of bringing the beams from two 15 km long linear accelerators into collision is also being intensively studied.

Linear collider concepts aim to overcome synchrotron radiation limits inherent to circular lepton machines. The International Linear Collider (ILC) [91] proposes two opposing 15 km superconducting linacs to achieve up to 1 TeV in e^+e^- collisions. Alternatively, Muon Collider designs [92] exploit the muon's higher mass, reducing synchrotron radiation losses by a factor of $(m_\mu/m_e)^4 \approx 1.8 \times 10^9$. Although muon production and cooling remain technically challenging, such a facility could combine the clean environment of lepton collisions with hadron-collider energy scales.

4.2 The ATLAS Experiment

The ATLAS detector (A Toroidal LHC ApparatuS) [81, 93–95], depicted in Figure 4.4, is one of two general-purpose detectors at the LHC. It is designed to detect and measure a wide variety of final states produced in proton–proton collisions. ATLAS is located at Interaction Point 1 (IP1) and has a total length of 46 m, a diameter of 25 m, and weighs ∼7,000 tons. The detector comprises concentric layers of subdetectors providing tracking, calorimetry, and muon detection, all within

powerful magnetic fields.

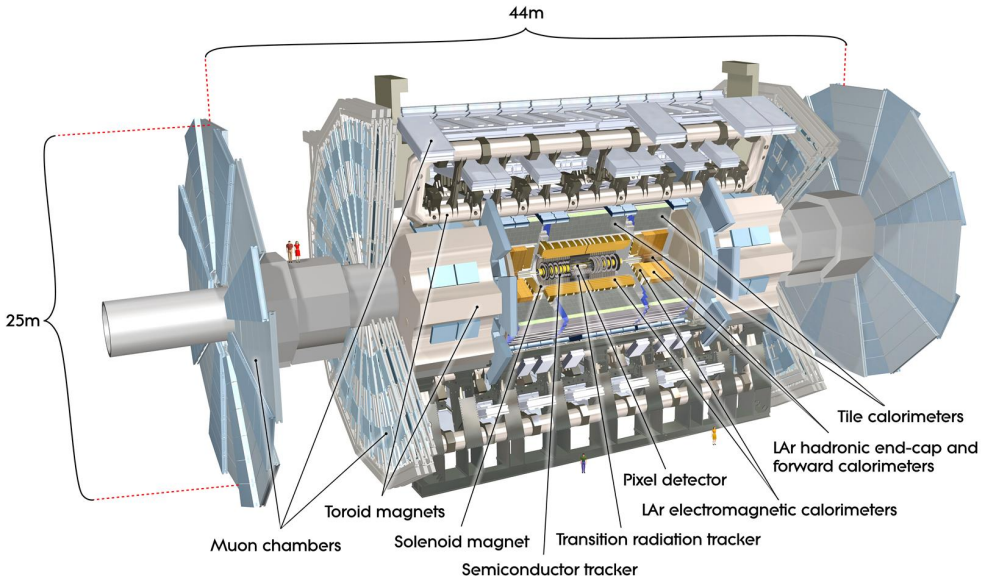


Figure 4.4: Schematic view of the ATLAS detector at the LHC [96].

4.2.1 Coordinate System

The ATLAS detector employs a right-handed coordinate system, as illustrated in Figure 4.5, with its origin at the nominal IP in the centre of the detector. The z-axis is aligned along the beam pipe, the x-axis points from the IP towards the centre of the LHC ring, and the y-axis points vertically upwards. The azimuthal angle ϕ is measured around the beam axis, and the polar angle θ is measured from the z-axis.

To describe particle directions, the pseudorapidity η is defined as

$$\eta = -\ln\left[\tan\left(\frac{\theta}{2}\right)\right], \tag{4.3}$$

which provides an approximately linear measure of detector coverage and is invariant under Lorentz boosts along the beam direction for ultrarelativistic particles. A related quantity, the rapidity y, is defined by

$$y = \frac{1}{2}\ln\left(\frac{E+p_z}{E-p_z}\right), \tag{4.4}$$

where E and p_z denote the energy and longitudinal momentum of the particle, respectively. For highly relativistic particles, $y \approx \eta$, allowing pseudorapidity to be used as a practical alternative in most analyses, including this one.

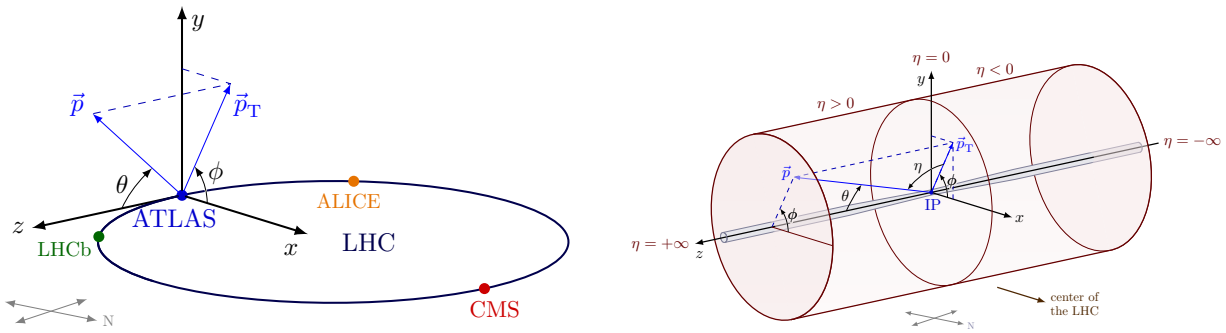


Figure 4.5: The ATLAS coordinate system [27].

The transverse momentum and energy are defined as

$$p_{\mathrm{T}} = \sqrt{p_x^2 + p_y^2}, \qquad E_{\mathrm{T}} = E \sin\theta, \tag{4.5}$$

where p_x, p_y are the momentum components. These quantities are conserved in the plane perpendicular to the beam axis and are therefore essential for event reconstruction in proton–proton collisions. The angular distance between two reconstructed objects in the detector is given by

$$\Delta R = \sqrt{(\Delta\eta)^2 + (\Delta\phi)^2}, \tag{4.6}$$

a measure commonly used in clustering and isolation algorithms. This dissertation makes use of these quantities (and more) to train machine learning algorithms for signal separation, as described in Chapter 11.

4.2.2 Inner Detector

The Inner Detector (ID) [97,98] reconstructs charged-particle tracks and determines their momenta through curvature in the 2 T solenoidal magnetic field. It consists of three subsystems: the Pixel Detector (PD), the Semiconductor Tracker (SCT), and the Transition Radiation Tracker (TRT).

Pixel Detector

The PD [101] is the innermost component of the ID, providing the highest-granularity measurements closest to the IP. It originally consisted of three concentric barrel layers and three disks on each end-cap, offering continuous tracking coverage up to $|\eta| < 2.5$. In 2014, the Insertable B-Layer (IBL) [102] was added at a radius of 33 mm to enhance vertexing and tracking performance under high-luminosity conditions. The PD comprises silicon pixel modules with integrated read-

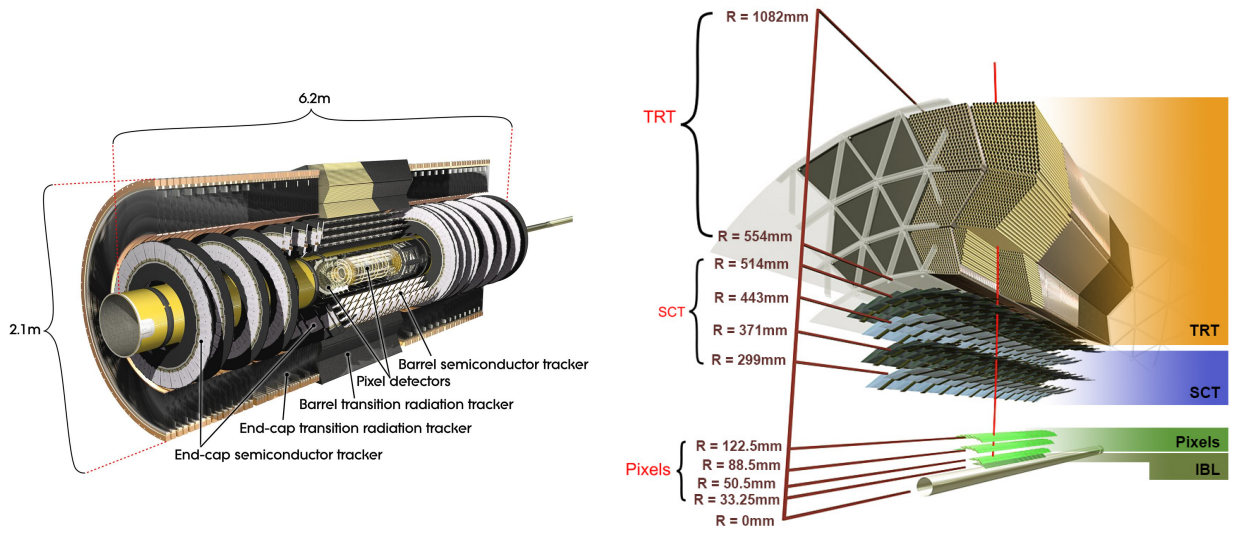


Figure 4.6: The ATLAS Inner Detector [99] showing its three sub-detectors: the pixel detector with IBL upgrade [100], the semiconductor tracker (SCT) and the transition radiation tracker (TRT). The distances to the interaction point are also shown.

out electronics, totaling about 80 million pixels. The outer layers employ pixels of 50×400 μm^2, while the IBL uses smaller pixels of 50×250 μm^2 for improved spatial resolution. Owing to its fine segmentation and proximity to the IP, the PD enables precise measurements of track impact parameters, essential for accurate vertex reconstruction and for identifying b-jets and τ leptons in dense collision environments.

Semiconductor Tracker

The SCT [103, 104] forms the middle layer of the ID and provides high-precision tracking in the radial region between the PD and the TRT. It is composed of 4088 silicon microstrip modules arranged in four barrel layers and nine endcap disks on each side. Each module consists of two pairs of back-to-back silicon sensors with strips oriented at a stereo angle of 40 mrad, enabling accurate measurement of both r–ϕ and z coordinates. The strip pitch is 80 μm in the barrel layer and ranges from $57 - 90$ μm in the endcap disks. The SCT provides the majority of precision hits used for track reconstruction, complementing the fine spatial information of the PD. Its robust performance and stability under high-radiation conditions are essential for maintaining high tracking efficiency and momentum resolution throughout LHC operations.

This dissertation includes work on the improvement of the SCT online calibration analysis software, involving the refinement of backend algorithms and the resolution of identified issues. Further details of this work are provided in Chapter 5.

Transition Radiation Tracker

The outermost component of the ID, the TRT [105,106], extends tracking coverage up to $|\eta| < 2.0$ and provides both tracking and electron identification capabilities. It consists of thousands of thin, gas-filled drift tubes ("straws") arranged in the barrel and endcap regions. Charged particles ionize the gas as they traverse the straws, and the drift time of the ionization electrons is used to measure the track position with a resolution of about 130 μm in r–ϕ per straw. The TRT also detects transition radiation photons produced when highly relativistic charged particles cross boundaries between materials with different dielectric constants, enabling discrimination between electrons and hadrons (pions).

By combining high-precision measurements from the PD and SCT with the electron-identification capability of the TRT, the ATLAS ID achieves excellent overall performance in vertexing, tracking, and particle identification across a wide range of physics analyses.

For the HL-LHC, the entire ID is going to be replaced with the Inner Tracker (ITk) [107–109], an all-silicon system composed of pixel and strip detectors. The ITk will provide improved radiation tolerance, higher granularity, and extended pseudorapidity coverage up to $|\eta| < 4.0$. Combined with the High-Granularity Timing Detector (HGTD) placed in the forward region, the ITk will maintain excellent track reconstruction efficiency under conditions with up to 200 simultaneous interactions per bunch crossing.

4.2.3 Calorimeter System

The calorimeter system [110–112], as illustrated in Fig. 4.7, is designed to measure the energy and direction of electrons, photons, and hadronic particles with high precision, while also contributing to jet reconstruction and missing transverse momentum measurements. It provides nearly full solid-angle coverage around the IP, spanning up to $|\eta| < 4.9$. The calorimeter system is divided into electromagnetic (EM) and hadronic sections, employing different technologies optimized for distinct particle types and radiation environments.

Electromagnetic Calorimeter

The EM calorimeter (ECal) is a lead–liquid argon (LAr) sampling calorimeter that measures the energy of electrons and photons through EM shower development. It consists of a barrel section covering $|\eta| < 1.475$ and two end-cap sections extending to $|\eta| < 3.2$. The absorber plates are made of lead, while the active medium is liquid argon, chosen for its excellent linearity, stabil-

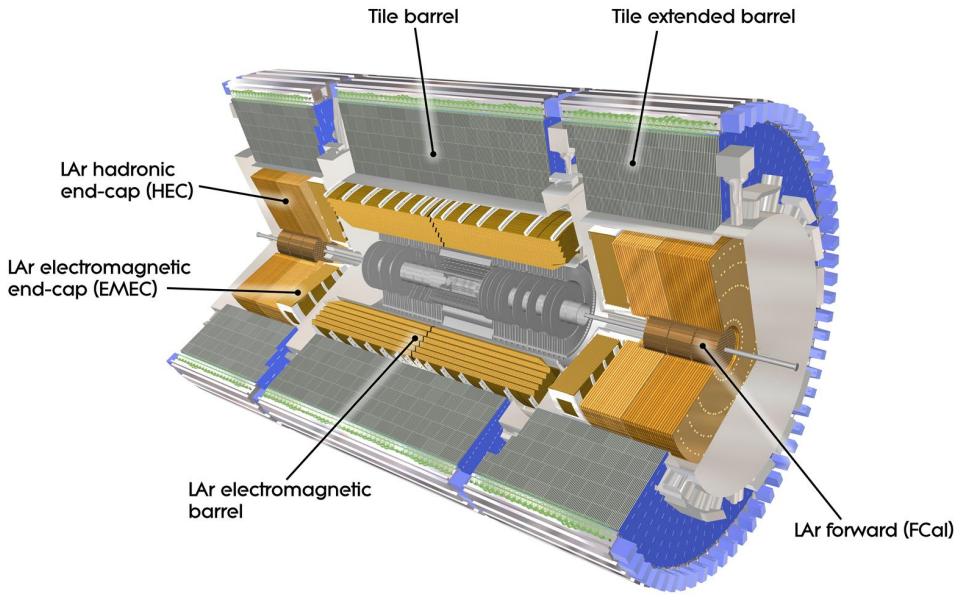


Figure 4.7: A schematic of the ATLAS calorimeter [113].

ity, and radiation hardness. The accordion-shaped geometry ensures complete azimuthal coverage without projective cracks. The ECal is longitudinally segmented into three layers of varying granularity, allowing precise position and shower-shape measurements for particle identification. A thin presampler detector covering $|\eta| < 1.8$ is installed in front of the ECal to correct for energy losses in upstream material.

Hadronic Calorimeter

Outside the ECal lies the hadronic calorimeter (HCal) system, which measures the energy of hadrons and jets. In the central region ($|\eta| < 1.7$), the Tile Calorimeter (TileCal) uses steel absorbers and plastic scintillating tiles as active material. Light produced in the scintillators is transmitted to photomultiplier tubes via wavelength-shifting fibers. The TileCal provides excellent response uniformity and contributes significantly to jet and missing transverse energy measurements. In the end-cap regions ($1.5 < |\eta| < 3.2$), the hadronic end-cap calorimeter (HEC) employs copper absorber plates and liquid argon as the active medium. It is optimized for higher particle fluxes and radiation levels.

Beyond the HEC, the forward calorimeter (FCal) extends the coverage up to $|\eta| < 4.9$. It consists of three modules per end-cap, using copper and tungsten absorbers with liquid argon as the active medium. The FCal is designed to withstand the intense radiation and particle fluxes in the forward region, providing robust measurements crucial for forward jet tagging and missing

transverse energy reconstruction.

The calorimeter energy resolution is parametrized as

$$\frac{\sigma_E}{E} = \frac{a}{\sqrt{E}} \oplus \frac{b}{E} \oplus c, \tag{4.7}$$

where a, b, and c represent the stochastic, noise, and constant terms, corresponding respectively to sampling fluctuations, electronic noise, and instrumental effects. The symbol $\oplus$ stands for quadratic sum. Ignoring noise, the calorimeter energy resolutions are approximately $10\%/\sqrt{E} \oplus 0.7\%$ for the ECal, $50\%/\sqrt{E} \oplus 3\%$ for the Tile and HEC hadronic calorimeters, and $100\%/\sqrt{E} \oplus 10\%$ for the FCal.

4.2.4 Muon Spectrometer

The Muon Spectrometer (MS) [114], as shown in Fig. 4.8, provides standalone momentum measurements for muons over $|\eta| < 2.7$ using large air-core toroidal magnetic fields. It combines precision tracking detectors – Monitored Drift Tubes (MDT) and Cathode Strip Chambers (CSC) – with fast trigger detectors – Resistive Plate Chambers (RPC) and Thin Gap Chambers (TGC).

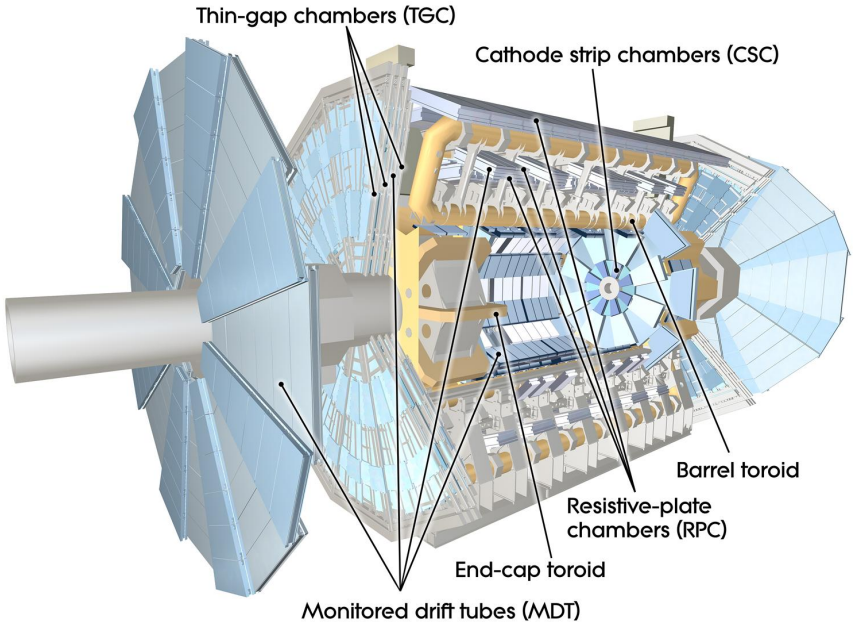


Figure 4.8: A schematic of the Muon Spectrometer [115].

During the second long shutdown (LS2), the innermost end-cap stations ("wheels") were replaced by the New Small Wheels (NSW) [116], incorporating MicroMegas and small-strip TGC (sTGC) technologies. These detectors deliver high spatial resolution ($\sim 100\ \mu$m) and fast timing,

enhancing both tracking and triggering capabilities in the forward region. Further upgrades for HL-LHC include new small-diameter MDT chambers, additional RPC layers, improved electronics, and integrated muon trigger logic for efficient operation under high pile-up.

4.2.5 Magnet System

ATLAS employs two primary magnetic systems [117–120]: a 2 T solenoid surrounding the ID and a large toroidal magnet system for the MS, as shown in Fig. 4.9. The toroid system, consisting of one barrel and two end-cap toroids, delivers an inhomogeneous magnetic field of roughly 0.5 T and 1 T in the central and end-cap regions, respectively. The entire system is maintained at cryogenic temperatures. The combination allows precise curvature measurement of charged particles over a wide pseudorapidity range while minimizing multiple scattering. Continuous alignment and field calibration ensure stability and accuracy over extended data-taking periods.

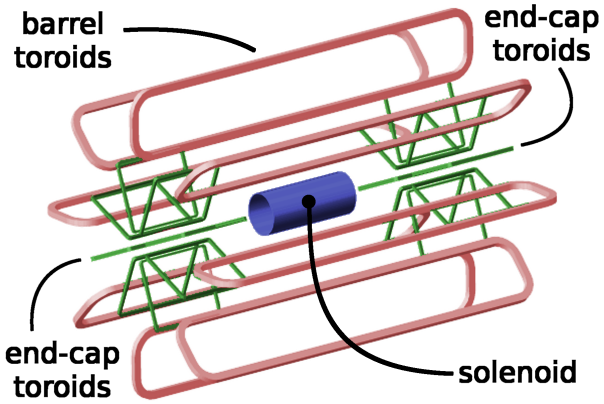


Figure 4.9: The ATLAS magnet system [121].

4.2.6 Luminosity Detectors

Precise luminosity determination is essential for converting the number of observed events into absolute cross sections. The ATLAS experiment employs multiple, largely independent detector systems to measure the instantaneous and integrated luminosity, each optimized for specific operational conditions and luminosity ranges. These measurements are combined to achieve a total systematic uncertainty of 1.7% [122] in Run 2.

During Run 2, the primary online luminosity measurement was provided by the LUCID (LUminosity Cherenkov Integrating Detector) system [123]. It consists of arrays of aluminum tubes filled with C_4F_{10} gas, positioned symmetrically at ± 17 m from the IP around the beam pipe.

Charged particles passing through the gas produce Cherenkov light, which is detected by photomultiplier tubes. The number of detected pulses is proportional to the interaction rate, providing a fast and radiation-hard luminosity monitor.

Complementary luminosity information is obtained from the Beam Conditions Monitor (BCM) and the FCal. The BCM, located at ± 1.9 m from the IP, consists of diamond sensors providing high time resolution and radiation tolerance, suitable for early luminosity measurements after beam setup and for monitoring beam backgrounds. The FCal, although primarily designed for energy measurements, contributes to luminosity determination via particle flux correlations in its forward region.

Absolute calibration of the luminosity scale is performed using dedicated van der Meer (vdM) scans [124], in which the transverse beam overlap integral is measured directly. This procedure allows the conversion of the detector response into an absolute luminosity measurement. Cross-checks using multiple detectors and calibration transfer methods ensure long-term stability across data-taking periods.

4.2.7 Trigger System and Data Acquisition

The LHC produces millions of collisions every second, yet only a small fraction are of interest. About 100 leptonically decaying W bosons are created each second, while electroweak same-sign $W^{\pm}W^{\pm}$ events appear only once every ten hours. The even rarer longitudinally polarized ($W_L^{\pm}W_L^{\pm}$) component occurs roughly once every few weeks[2].

The LHC delivers collisions at 40 MHz, producing data volumes far beyond storage capacity. The ATLAS Trigger and Data Acquisition (TDAQ) [125] system therefore selects the most interesting events in real time. It operates in two stages: a hardware-based Level-1 (L1) trigger [126] and a software-based High-Level Trigger (HLT) [125], as shown in Fig 4.10. The L1 trigger, using calorimeter and muon data, reduces the event rate from 40 MHz to about 100 kHz within 2.5 μs. The HLT further reconstructs events using full detector granularity and reduces the output rate to $\sim$1 kHz for permanent storage.

For the HL-LHC, the TDAQ will be significantly upgraded: the L1 acceptance rate will rise to 1 MHz, and the event building and filtering capacity will expand accordingly. The HLT output will reach up to 10 kHz. Track information from the ITk and timing data from the HGTD will be integrated at the trigger level, allowing more sophisticated selection criteria under high pile-up.

[2] Assuming $L = 2 \times 10^{34} \text{cm}^{-2}\text{s}^{-1}$.

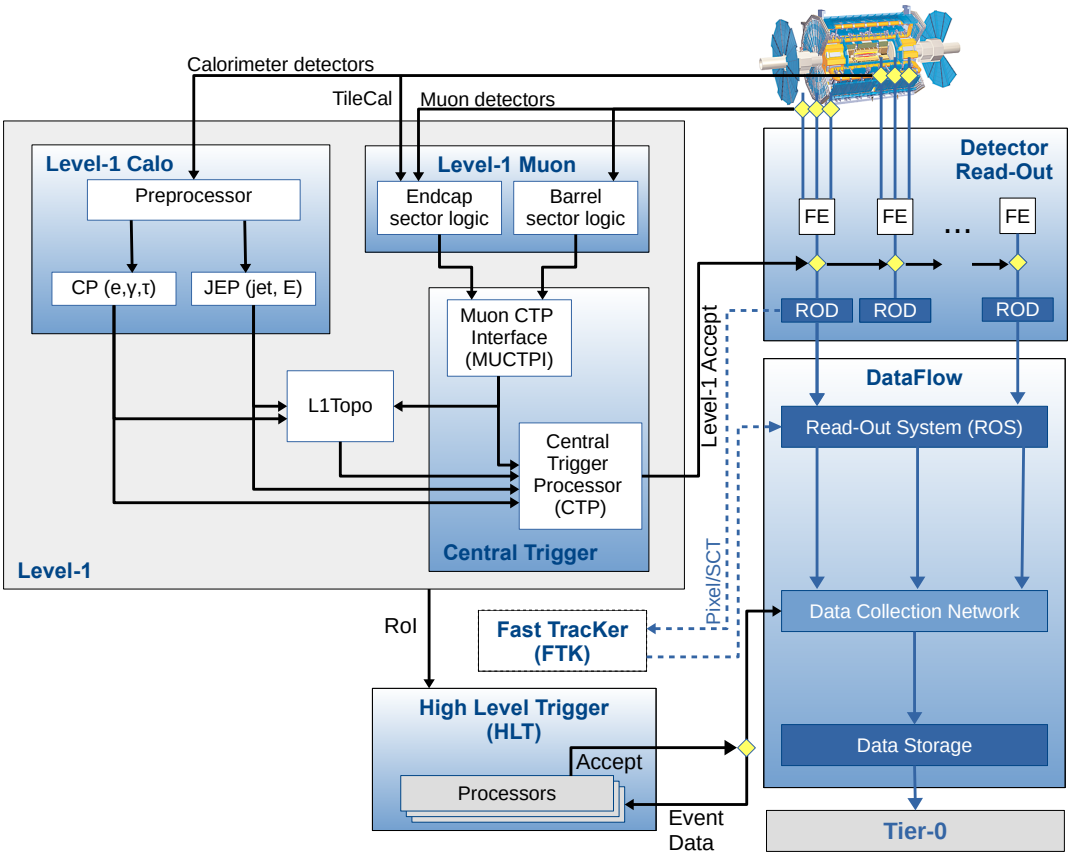


Figure 4.10: Schematic of the ATLAS trigger and data acquisition system in Run 2 [127].

Chapter 5

Semiconductor Tracker: Calibration and Trim Settings

This chapter delves into a study concerning the trimming of certain voltages linked with semiconductor tracker (SCT) calibration. The primary objective is to refine and rectify bugs within the SCT Data Acquisition (DAQ) online calibration analysis software, essential for calibrating SCT module configuration parameters. The main issue examined is the heightened strip masking rate and its association with trimming and its configurations. To address this, modifications are implemented in the trimming algorithm, incorporating sanity checks involving the half-occupancy threshold voltage. These adjustments are aimed at minimizing the unnecessary masking of numerous functional strips.

The role of trimming and trim tests is discussed in Section 5.1, while Section 5.2 elaborates on pertinent associated defects and required masking of channels. The issue leading to excessive masking is highlighted and addressed in Section 5.3. Information for this section is drawn from Refs. [128, 129], as well as my own work.

5.1 Trimming and Calibration tests

When a charged particle travels through a silicon strip, it deposits a residual charge that generates an induced voltage. This induced voltage is then processed by a pre-amplifier and compared to a threshold voltage via a comparator (as illustrated in Fig. 5.1). If the induced voltage exceeds the threshold, a hit is registered; otherwise, the output is 0 V. Hence, it is crucial to set the threshold voltage optimally while eliminating noise, and this is achieved through trim settings.

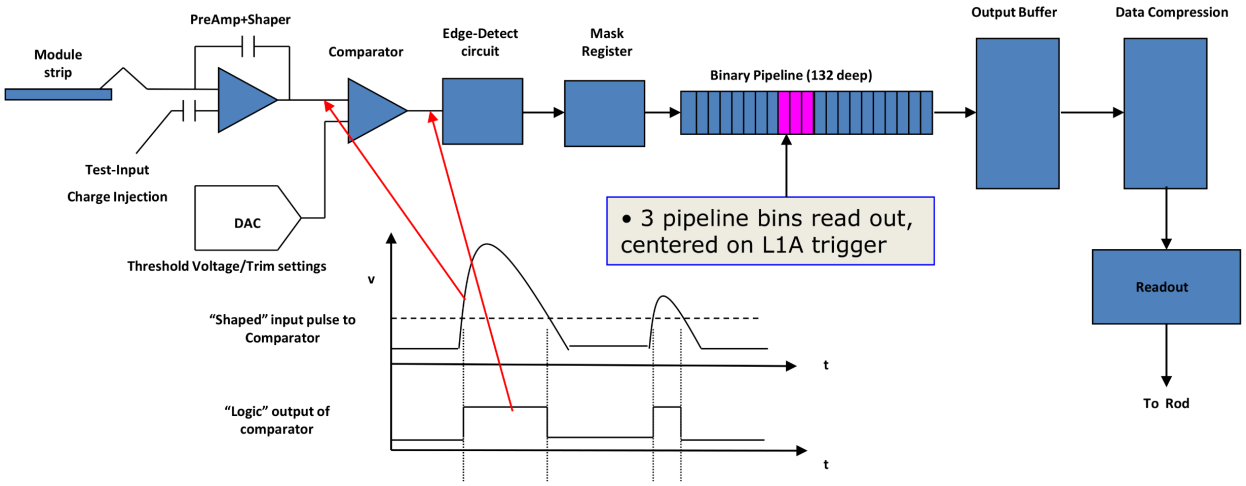


Figure 5.1: Response schematic of ABCD3TA[1] ASIC (Application Specific Integrated Circuit).

Trimming of a voltage refers to fine-tuning threshold voltage levels in a circuit to achieve precise values, ensuring they meet specific requirements and compensating for variations due to component tolerances, temperature changes, or aging. It is often performed using adjustable components such as trim potentiometers, digital-to-analog converters (DACs), or specific trim settings in software to achieve the desired voltage accuracy and stability across different channels or devices.

5.1.1 Trim Settings

SCT online calibrations are done fairly regularly to optimize detector efficiency and keep a low noise occupancy. Trimming tests are one of the important electrical analogue calibration tests that help in the optimization of trim settings, particularly the TrimDAC and TrimRange, and discriminator threshold (different from the threshold voltage) settings. These TrimDAC and TrimRange module configuration parameters are used to set the threshold voltage.

The TrimDAC setting ensures the uniformity of the threshold. It is set for every channel as a 4-bit digital signal (DAC) to compensate for channel-to-channel variations. It has 16 different settings (scan points) that determine the number of voltage steps. These voltage step sizes are set by the TrimRange setting but with the limitation that it is set for the entire chip. TrimRange has 4 different settings of 4, 8, 12, and 16 mV, which are added to the discriminator threshold. Therefore, the uniformity of thresholds can be maintained even as uncorrected channel-to-channel variations increase during irradiation.

The smallest TrimRange value, R0 corresponds to a step size of 4 mV. Thus, a TrimDAC value

[1] ABCD3TA: ATLAS Binary Chip in DMILL, version 3 with TrimDACs, revision A

of 1 equals a threshold voltage of 4 mV, 2 corresponds to 8 mV, and so on, up to a maximum of 15, which equals 60 mV. Increasing the TrimRange to R1 increases the step size to 8 mV, so TrimDAC values of 1, 2, and 15 correspond to thresholds of 8 mV, 16 mV, and 120 mV, respectively.

To optimize these settings, a series of threshold scans are performed during trim calibrations. The TrimRange scan identifies the best DAC configuration to achieve a threshold equivalent to 1 fC for each chip. In a threshold scan, occupancy is measured by varying a chip parameter (usually the discriminator threshold) with or without charge injection. The resulting occupancy vs. threshold plot is termed as the *S*-curve owing to its shape. The *S*-curve is fitted to a complementary error function. It provides the value of *vt50*, the threshold at 50% occupancy. The *vt50* corresponds to the median of the injected charge, and the spread around it serves as an measure of output noise. The narrower the spread of the *S*-curve, the lower the noise.

The trim configuration parameters and their settings are presented in Table 5.1.

Name	**Values**	**Normal Value**
TrimRange	0,1,2,3	Any, but lower is better

Name	**Level**	**Units**	**Minimum**	**Maximum**	**Step Size**
Discriminator Threshold	Chip	*mV*	0	640	2.5
TrimDAC	Channel	*mV*	0	60-240	4-16

Table 5.1: Configuration parameters for the modules relevant to trim settings, detailing both chip-level and channel-level settings.

5.1.2 Trimming Results

The trimming algorithm or *TrimRange Test*, selects the smallest range that trims the maximum number of strips or channels. A channel is considered trimmable when, for a given TrimRange setting, there exists a TrimDAC value for which all other channels align with the original channel across all discriminator threshold settings. Figure 5.2 illustrates how the application of trim settings aligns the channels for all thresholds.

The SCT calibration runs performed over the years can be accessed online. The raw or pre-fit data, post-fit results and the final calibration test result files are all saved in storage. The pre-fit data can be analysed to perform various tests with or without modifications. The TrimRange Test produces three major results used to determine the trim settings: (1) trim–*vt50* graph, (2) trim–channel graph, and (3) trim step histograms for each chip. These are depicted in Fig. 5.3, Fig. 5.4(a), and Fig. 5.4(b) respectively.

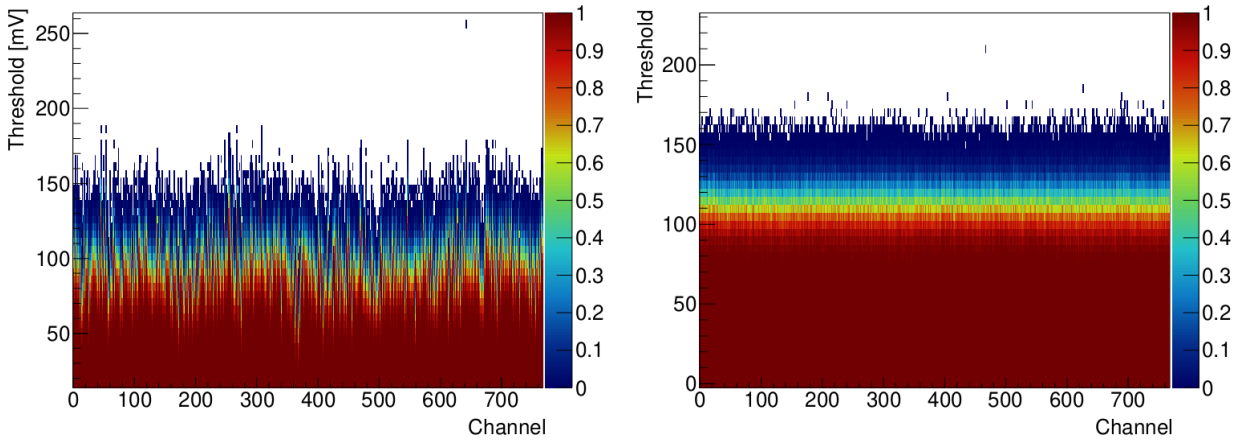


Figure 5.2: Raw/Pre-fit threshold scan data obtained from the same link (side of a module) during the same calibration run is displayed. On the left is the TrimRange scan data before trim settings are applied, and on the right is the ResponseCurve scan data after trim settings are applied.

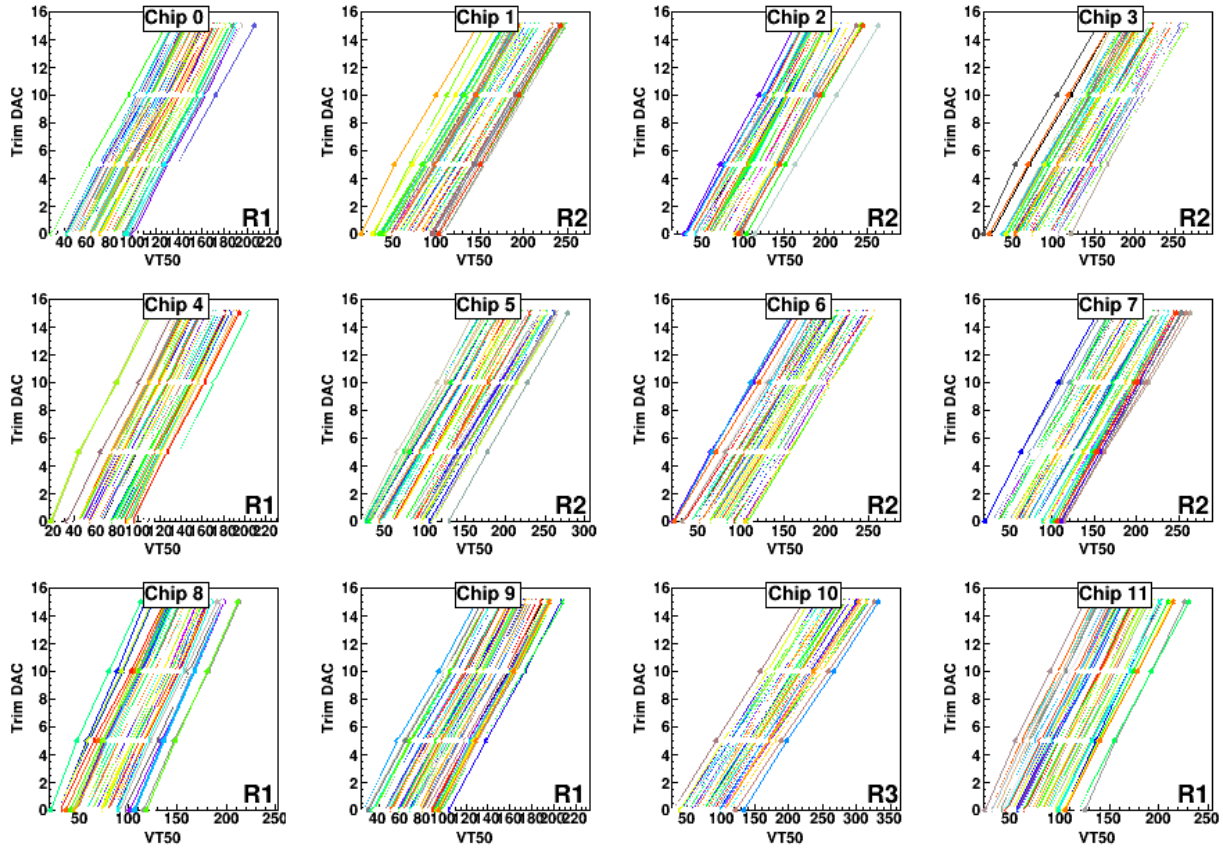
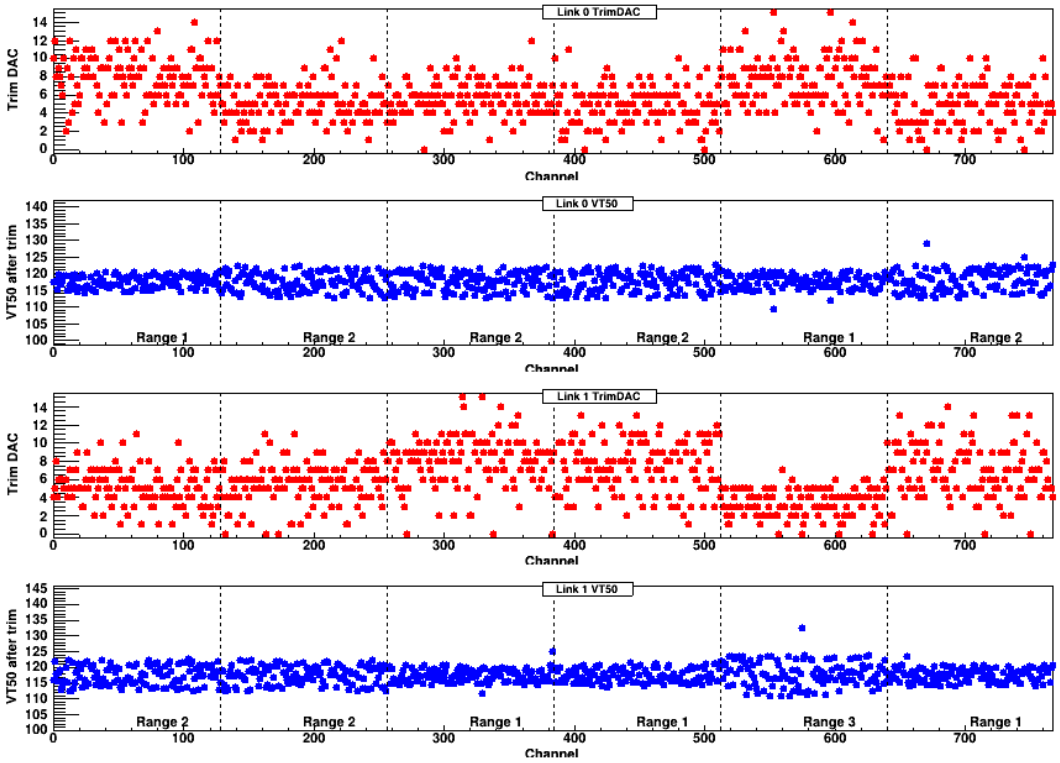
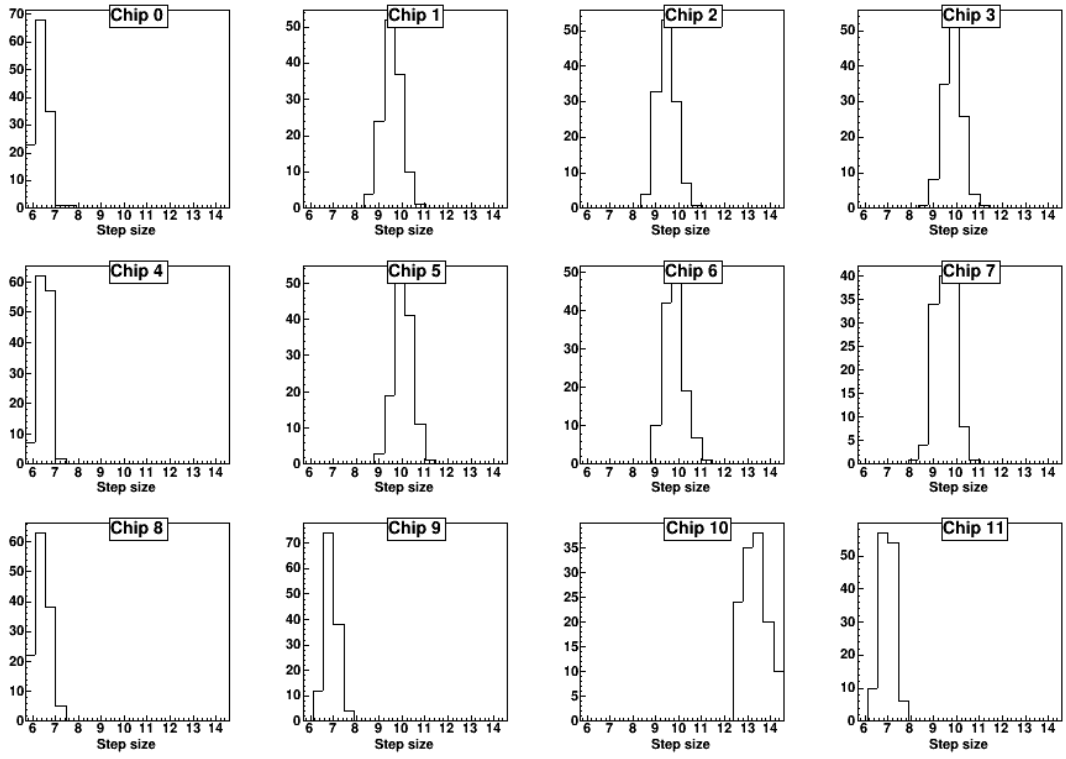


Figure 5.3: Graphs of trim against *vt50* for each chip, each channel and best range. Linear fit gives parameters `p0` = intercept (offset) and `p1` = gradient (1/step size).



(a) Trim vs. channel



(b) Trim step histograms for each chip

Figure 5.4: Trim–channel graph (top) shows the TrimDAC and *vt50* values corresponding to each channel in the module. Vertical dashed lines represent the divisions between the different chips. Step size (bottom) comes from the gradient of the fit and is given by `1/p1`.

The TrimDAC value is set using a `target` vector. It contains a value between 0 and 300 in steps of 2.5 and thus goes through all possible values of TrimDAC threshold voltage. One of the aims of TrimRange Test is to set the TrimDAC threshold voltage using this `target` vector.

The TrimRange Test performs threshold scans for every channel and for each of the 4 ranges (R0–R3). *vt50* points are extracted from the *S*-curve fits and are plotted against DAC values. These results are fairly linear and are fit with straight lines as: `trim` = `p0` + `target` × `p1`, where `p0` represents the offset, and `1/p1` represents the *mV* step from changing trim by a singular unit. The DAC setting for a certain discriminator threshold is found using this trim–*vt50* graph, as shown in Fig. 5.3.

5.2 Defects and Masking

The results produced by the analysis can sometimes exhibit unexpected outputs originating from various tests. If these outliers fall outside specific permissible ranges or fail to meet acceptable criteria, they are flagged as defects. These defects may affect an entire chip or individual strips, with the latter being more common. This section discusses the defects associated with trimming and required masking for obtaining the best results. Masking is performed entirely via the SCT software, allowing implementation and deployment during an ongoing run[2].

The TrimRange Test conducts a threshold scan for each trim option, optimizing the settings. The trim settings encompass defects at: (i) chip-level like the Range defect, and (ii) channel-level such as Step, Offset, and Untrimmable defects.

The limitation of setting TrimRange for the entire chip (and not for each channel) can potentially lead to the program choosing larger TrimRange than necessary, even if only one or two channels are problematic. A smaller TrimRange value allows the TrimDAC to take more spread-out values across different channels. Therefore, masks are applied to such troublesome channels to reduce the TrimRange required to trim all channels within a given chip. The chip-level Range defect identifies unusual chip trim step sizes and helps in necessary masking.

Channel-level defects include Step and Offset defects, which determine whether a channel's trim step size or offset, respectively, differs from that of the chip. These defects are flagged but not masked. Lastly, the Untrimmable defect identifies channels that are not trimmable (as described in Sec. 5.1). Permissible trim values range from 0 to 15, while also allowing -1 and 16 by rounding to the nearest permissible value. Outside this range, the channel is deemed untrimmable and is consequently masked.

[2]While taking data, usually particle collisions are halted for some hours in the day to fix any accelerator and detector issues.

Other than the trim defects, a couple of relevant fit-level defects emerge while fitting the occupancy *S*-curves: (i) Dead, and (ii) Under defects for a channel, as depicted in Fig. 5.5. A channel is labelled Dead if the occupancy is always $< 1\%$ and is masked, while if the occupancy is always $< 95\%$, it is only flagged as Under.

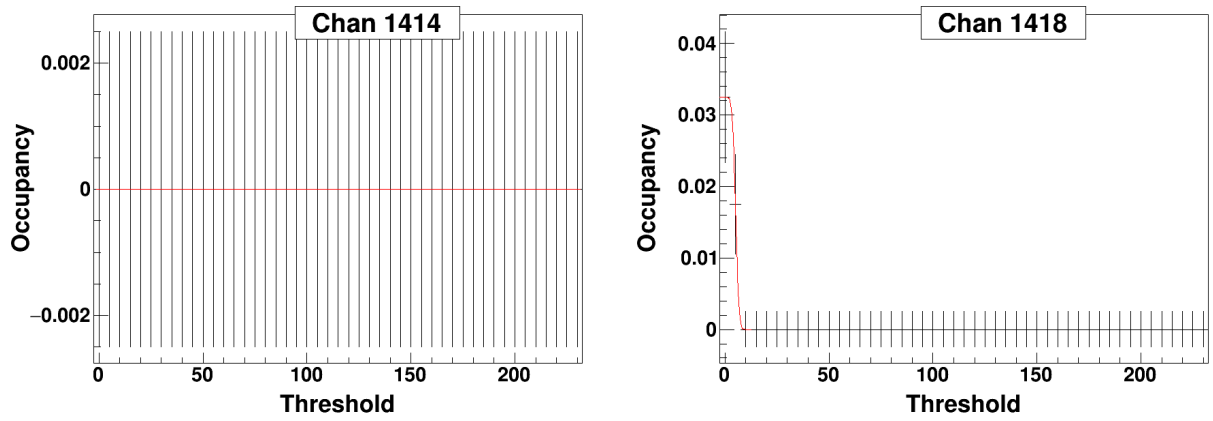


Figure 5.5: Fit defects: a channel with Dead defect (left), and another with Under defect (right).

5.3 High Masking Rates and Troubleshooting

Around late 2018, the masking algorithm masked unusually large number of strips/channels in some modules upon performing the Trim scan. The number of masked strips were in hundreds or sometimes thousands. Manual configuration changes were done to check this anomaly. To highlight the issue, one such case was observed where 14767 strips were masked originally but with all strips enabled (corresponding to TrimRange test) only 28 failed and 24 were with problem.This issue motivated the study presented here about investigating the possible reason(s) behind it.

The study involved examining a large number of trim analyses and their corresponding results. Checks were conducted to observe the performance of a module over time, before and after configuration changes, etc. A key finding emerged from a particular run, involving a specific module, which exhibited an abnormally high number of defects, leading to a high masking rate. Detailed examination of the output plots allowed identifying the problematic strip. This strip had consistently shown a Dead defect in previous runs as well as later runs. However, unexpectedly this strip showed some occupancy in this run with an abnormally large *vt50* value as shown in Fig. 5.7(a) and Fig. 5.8(a). A pre-fit or raw scan of this channel is shown in Fig. 5.6.

A solution was proposed and implemented to address this issue. A sanity check was introduced in the analysis to ensure that the final *vt50* value for each strip falls within a certain range for the selected TrimRange. This prevents the unnecessary masking of the entire chip, instead masking

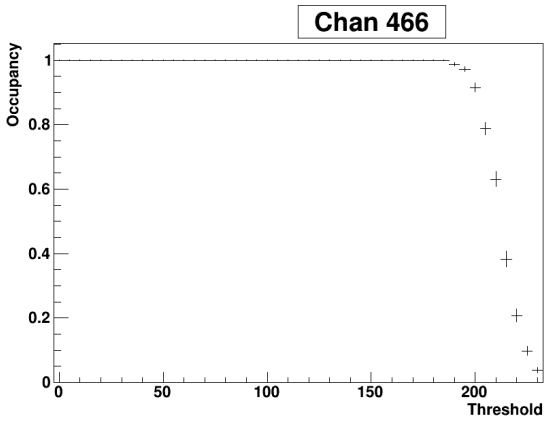
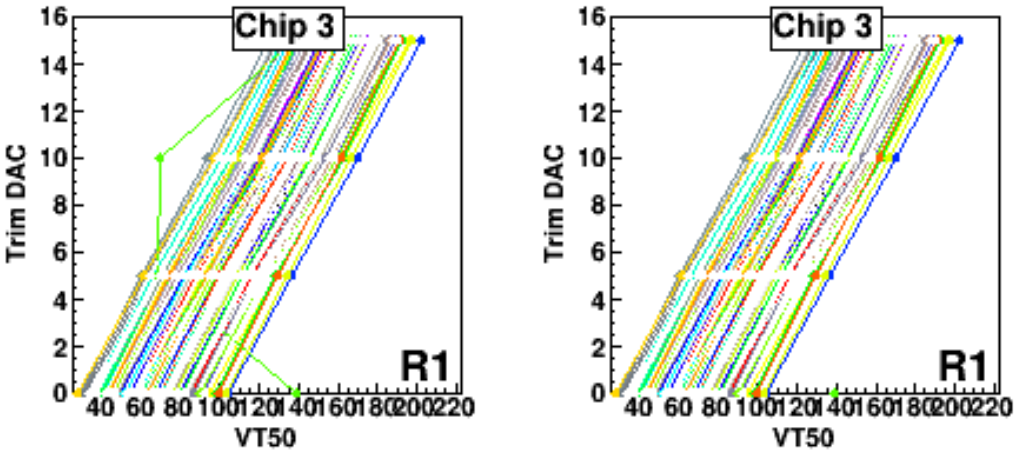


Figure 5.6: Pre-fit scan of the problematic channel showing the occupancy *S*-curve.

only the defective strip, thereby preserving data for the remaining 127 strips in a module which contains a total of 1536 strips.

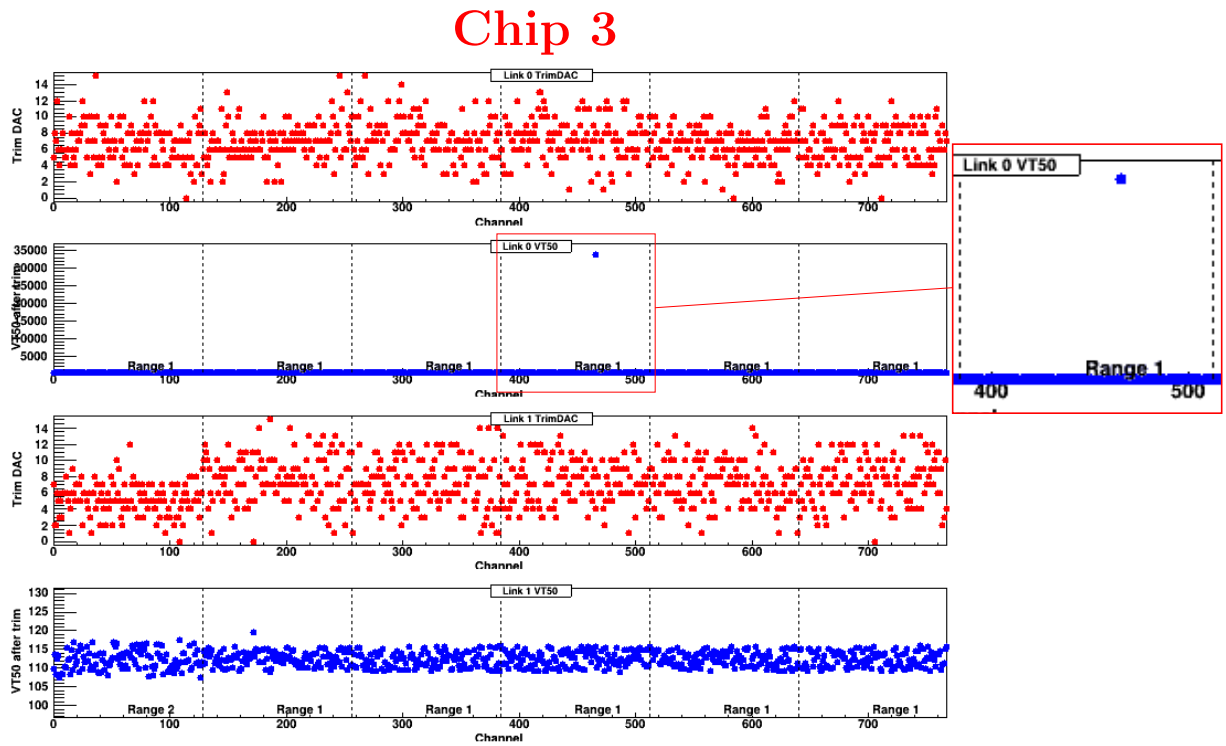
The solution has two parts. The first part checks for abnormal behavior in the trim–*vt50* graph. The second part labels any channel with an unnatural *vt50* value as having the Untrimmable defect. By excluding the problematic channel at the fit-level, the entire chip is saved from being masked off due to the Range defect. Additionally, the problematic channel is not considered for Step and Offset defects. Strips with *vt50* values outside the allowed range are labeled as Untrimmable and masked accordingly. The result plots after applying the fix are shown in Fig. 5.7(b) and Fig. 5.8(b) alongside the original plots displaying a clear comparison.



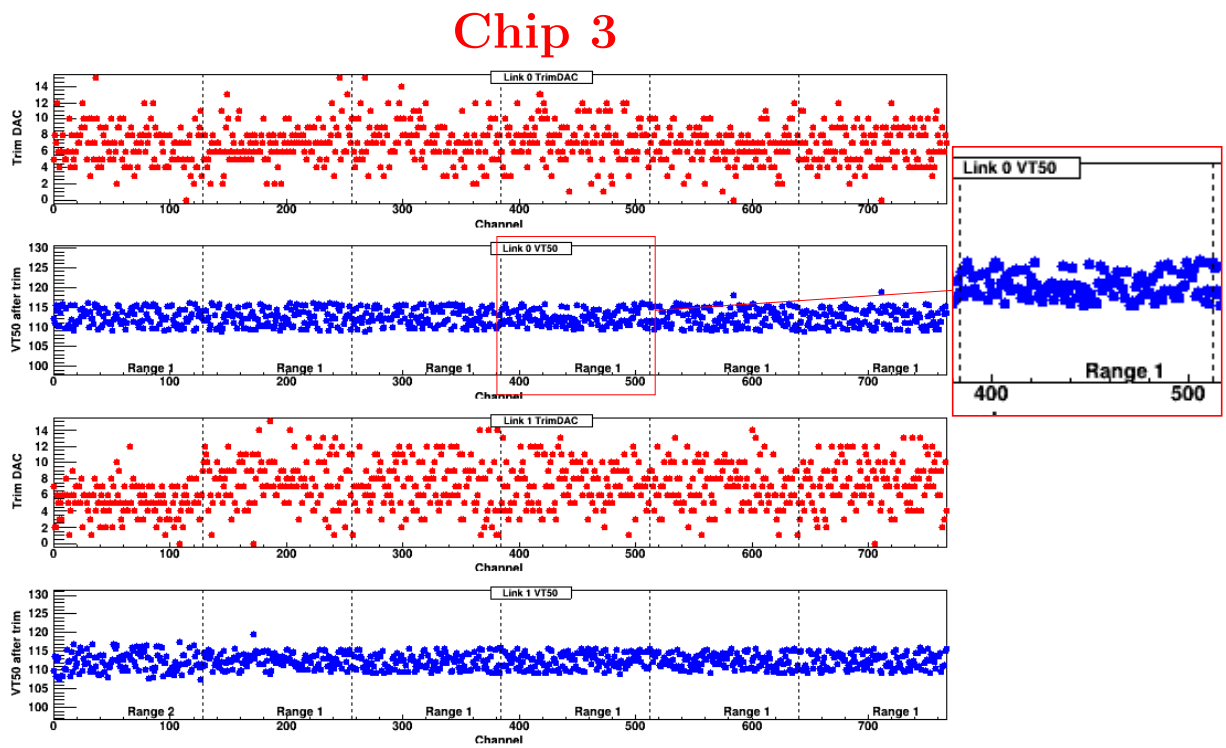
(a) Original Chip3 trim–*vt50* graph

(b) Fixed Chip3 trim–*vt50* graph

Figure 5.7: One of the threshold scans shows an irregular non-linear curve. A *vt50* value check for all channels at the fit-level ensures that channels with *vt50* values outside allowed range are skipped.



(a) Original trim–channel graph



(b) Fixed trim–channel graph

Figure 5.8: The channel with problematic *vt50* value in chip 3 (fourth square, link 0) can be clearly spotted in the original graph (Fig. 5.8(a)). After masking off the troublesome channel, the chip and the module become trimmable (Fig. 5.8(b)).

Conclusion

The study presents an improvement to the SCT DAQ online calibration analysis software involving TrimRange Test. In some instances, an abnormal value of the module parameter for the half-occupancy voltage threshold (*vt50*) in a single strip can result in the masking of an entire chip. This study shows the implementation of a check for the allowed *vt50* range for each strip and the targeted masking of only the problematic strip instead of the entire chip. This saves the rest of the 127 trimmable strips within the chip from being masked off when it is not actually required.

Chapter 6

Reconstruction and Particle Identification in ATLAS

The reconstruction of physics objects from the raw signals recorded by the ATLAS detector is a fundamental step in any analysis. The process translates low-level detector measurements — such as energy deposits in calorimeters or hits in tracking detectors — into high-level quantities like electrons, muons, jets, and missing transverse momentum. Accurate and efficient reconstruction is essential for identifying the underlying physics processes in proton–proton collisions and for distinguishing the rare signal events from the dominant Standard Model backgrounds.

In this chapter, the main principles and algorithms used in ATLAS object reconstruction are outlined, with particular focus on those relevant for the identification of the $W^{\pm}W^{\pm}jj$ final state. Several abbreviations follow definitions given in Chapter 4.

6.1 Reconstruction Techniques

Reconstruction in ATLAS relies on two complementary methods: *tracking* and *calorimetry*. Tracking determines the trajectories of charged particles in the magnetic field of ID, allowing precise measurement of their momentum and charge. Calorimetry measures the energy of both charged and neutral particles through the absorption of particle-induced showers in the calorimeters, with the shower pattern providing information on the particle's type and direction.

At low and moderate energies, tracking offers superior momentum resolution, while calorimetry dominates at high energies, where energy resolution improves with increasing energy. Their combined use enables accurate particle identification and overall event reconstruction across the

full kinematic range of ATLAS.

6.2 Tracking and Vertex Reconstruction

The reconstruction of charged particle trajectories and collision vertices forms the foundation of event reconstruction in ATLAS. Charged particles traversing the ID leave a series of hits in the PD, SCT, and TRT subsystems. Details about tracking and vertexing can be found in Refs. [130–133].

Tracks are built by connecting hits in the ID along the full ϕ range and $|\eta| < 2.5$ to form continuous trajectories. The MS also comes into play for the case of muons. Track reconstruction begins with the formation of hit clusters, which are combined into seeds representing possible particle trajectories. Candidate tracks are then built and refined using a global fit based on the Kalman filter technique. Ambiguities arising from shared hits are resolved by assigning quality scores to competing track candidates, ensuring an optimal set of reconstructed tracks. The curvature of each track in the solenoidal magnetic field determines the particle's transverse momentum (p_{T}) and charge.

In the magnetic field of 2 T, charged particles follow helical paths that appear circular in the transverse (x–y) plane. Each reconstructed track is described by five parameters defined at the point of closest approach to a reference position (typically the beam spot): the transverse and longitudinal impact parameters (d_0 and z_0), the azimuthal and polar angles (ϕ, θ), and the charge-over-momentum ratio (q/p). These quantities allow precise determination of a particle's momentum, direction, and origin. Figure 6.1 illustrates the definitions of the parameters graphically.

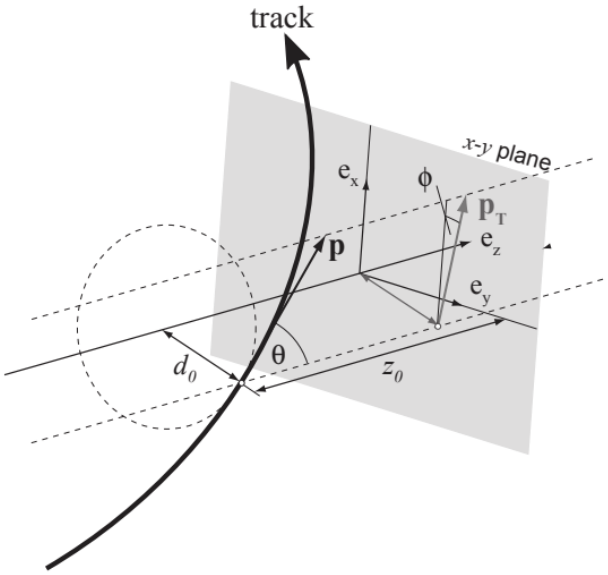


Figure 6.1: Visualization of a track defined with five parameters d_0, z_0, ϕ, θ and q/p [134].

Vertices are reconstructed by fitting groups of tracks that are consistent with originating from a common point in space. The *primary vertex (PV)* is identified as the one with the largest $\sum p_{\mathrm{T}}^2$ of its associated tracks, corresponding to the hard-scatter pp interaction. Additional vertices can arise from pile-up collisions, while *secondary vertices* may be reconstructed from the decays of long-lived particles such as b-hadrons.

Accurate tracking and vertex reconstruction are essential for associating physics objects to the correct interaction, suppressing pile-up, and enabling precise measurements of momentum, impact parameters, and isolation.

6.3 Physics Objects

In this measurement, $W^{\pm}W^{\pm}jj$ events are reconstructed using electrons, muons, jets, and neutrinos in the final state, as discussed in Chapter 3. The four-momenta of all final-state objects are reconstructed directly, except for neutrinos, which are inferred from the event's missing transverse momentum ($E_{\mathrm{T}}^{\mathrm{miss}}$). Figure 6.2 illustrates the interaction of different particles with the ATLAS detector. This section outlines the reconstruction of the physics objects relevant to this analysis.

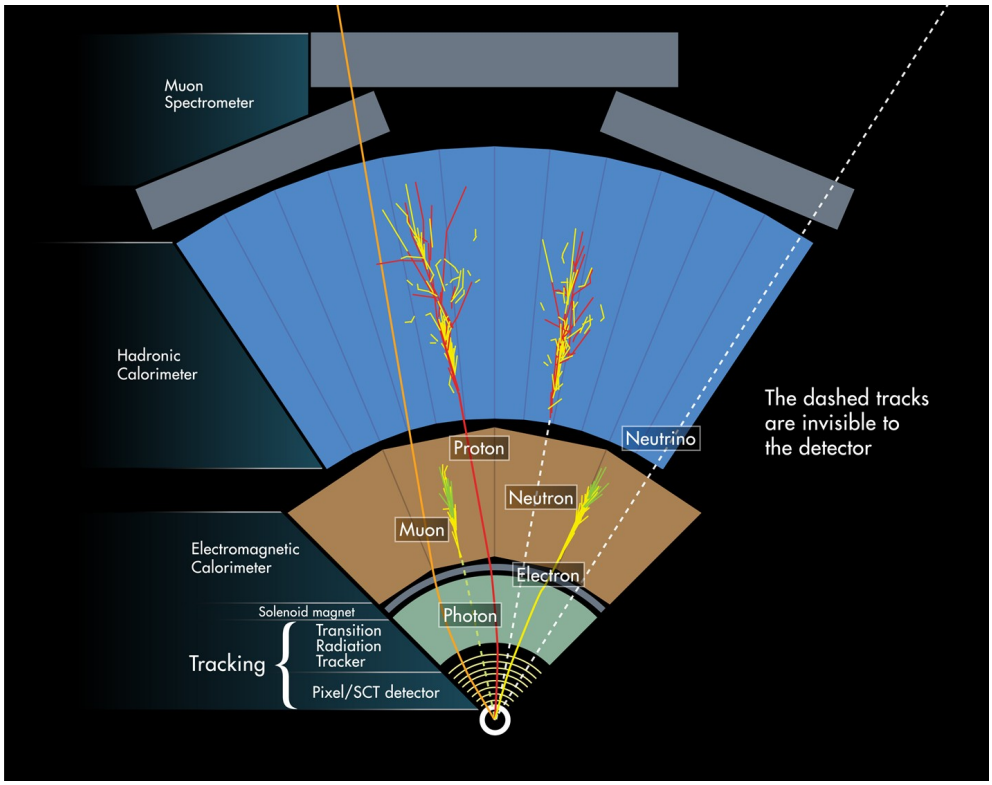


Figure 6.2: Illustration of particle detection in ATLAS [135].

6.3.1 Electrons

Electrons are reconstructed by combining information from ID and ECal [2, 136]. A schematic of an electron's trajectory while passing through the various detector layers is shown in Figure 6.3. A charged particle track in the ID is matched to an energy cluster in the ECal to form an electron candidate. This approach exploits the excellent spatial and energy resolution of the calorimeter together with the precise momentum and vertex information from the ID.

Electron *reconstruction* begins with the formation of *topological clusters* in the ECal, corresponding to localized energy deposits produced by electromagnetic showers. Tracks reconstructed in the ID are then extrapolated to the calorimeter surface and matched to these clusters based on position and energy–momentum compatibility (E/p). The matched track–cluster pair defines an electron candidate.

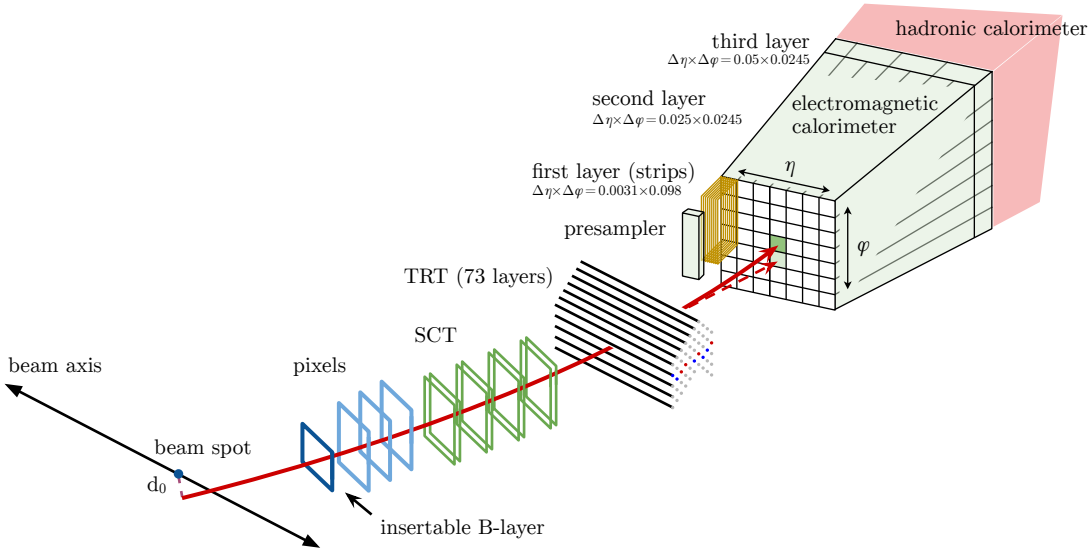


Figure 6.3: A schematic view of the passage of an electron through the various detector layers depicting the technique of electron reconstruction [2].

Electron *identification* is performed using a multivariate likelihood-based algorithm that combines several discriminating variables. These include shower-shape variables describing the lateral and longitudinal development of the energy deposit in the calorimeter, track–cluster matching quality, and transition radiation information from the TRT, which helps distinguish electrons from charged hadrons. The selection is provided in multiple *working points* (Loose, Medium, Tight) offering different balances between efficiency and background rejection.

To ensure high-quality or *prompt* candidates, electrons are required to originate from PV and satisfy isolation requirements, thereby suppressing *non-prompt* and *fake* electrons arising from hadron decays and jet misidentification, respectively. Some electron canditates also come from

photon conversions ($\gamma \to e^+e^-$). Isolation is evaluated using both calorimeter- and track-based quantities within a cone around the electron direction, corrected for pile-up effects.

The electron energy is calibrated in several steps [137, 138], starting from the EM scale and refined using data-driven corrections derived from well-known resonances such as $Z \to e^+e^-$ and $J/\psi \to e^+e^-$. The final energy scale and resolution are tuned to match data and simulation.

In this analysis, to select prompt electrons in the signal region[1], reconstructed electrons are required to satisfy the Tight identification and Gradient isolation working points. The Tight identification provides strong rejection of background-like and non-prompt electrons, while the Gradient isolation combines track- and calorimeter-based isolation using cones of $\Delta R = 0.2$ in both the ECal and the ID. This requirement selects "well-isolated" electrons, with an efficiency that rises from about 90% at $E_{\mathrm{T}} = 25$ GeV to over 99% for $E_{\mathrm{T}} > 60$ GeV.

6.3.2 Muons

Muon reconstruction [139] is performed by combining information from ID and MS, which together provide precise momentum measurement over a wide range of pseudorapidity. Their long lifetime and minimal energy loss in the calorimeters allow them to penetrate the detector and leave distinct tracks in the MS. ID measures the track of the charged particle in the solenoidal magnetic field close to the interaction point, while MS measures the trajectory of the penetrating particle after passing through the calorimeters, which absorb most other charged particles.

Muon candidates are classified according to the detector information used in the reconstruction, as illustrated in Fig. 6.4. *Combined (CB)* muons use both ID and MS measurements and represent the highest quality category. *Segment-tagged (ST)* muons are reconstructed from an ID track associated with at least one MS segment, improving acceptance in regions with incomplete MS coverage. *Standalone or Extrapolated (ME)* muons are reconstructed using only MS tracks, extending the acceptance to the forward region, $2.5 < |\eta| < 2.7$, which lies outside ID coverage. *Calorimeter-tagged (CT)* muons are identified from isolated energy deposits consistent with a minimum-ionising particle in the calorimeter, extending acceptance to very forward or geometrically limited regions. Muons used in this measurement are CB muons reconstructed in $|\eta| < 2.5$.

The momentum *calibration* of muons is performed by applying small corrections to the reconstructed track parameters to account for residual misalignments and energy losses in the detector material. The scale and resolution are derived from data using resonant decays such as $J/\psi \to \mu^+\mu^-$ and $Z \to \mu^+\mu^-$, ensuring consistency between data and simulation.

[1] The signal region description can be found in Section 7.2.1.

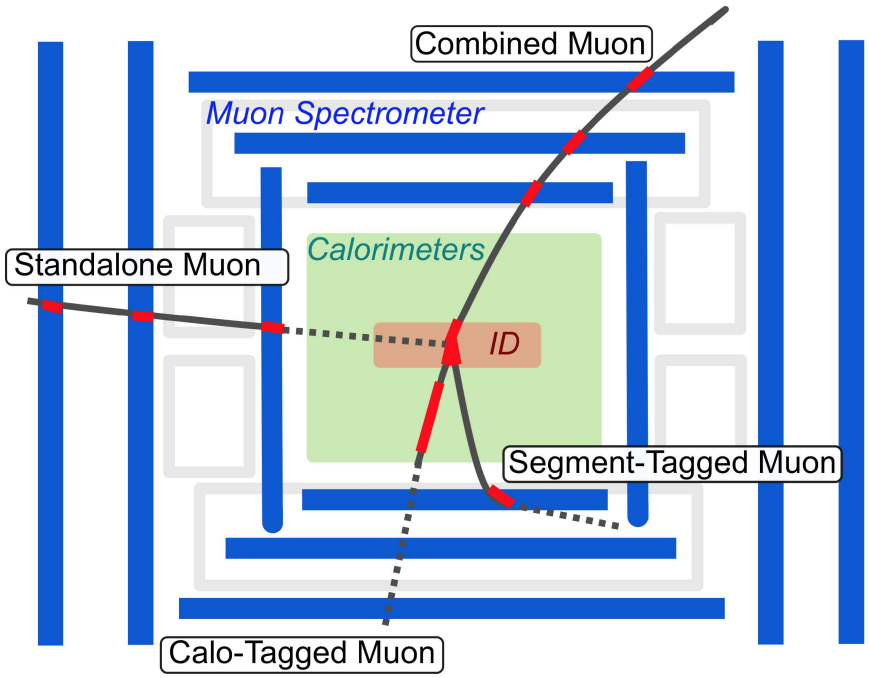


Figure 6.4: Different kinds of muons reconstructed in the ATLAS detector [3].

Reconstructed muons include prompt, non-prompt, and fake candidates, similar to electrons. Photon conversion contributions are negligible, and muons are selected from prompt candidates using identification and isolation criteria.

Muon *identification* relies on track quality variables such as the number of hits in the precision chambers, fit χ^2, and consistency between the ID and MS momentum measurements. As for electrons, multiple working points (Loose, Medium, Tight) are defined in increasing order of background rejection, with the Medium working point typically used for ATLAS analyses as it provides high efficiency with good background suppression [139]. In addition, *isolation* is an effective tool to select prompt muons. Isolation working points are defined using track-based isolation, with or without calorimeter information, such as Loose, Tight, HighPtTrackOnly, PFlowLoose, PFlowTight, etc. The PFlow working points, introduced in Run 2, use a particle-flow algorithm where calorimeter information is applied only to neutral particles, reducing overlap between track and calorimeter isolation.

In this analysis, prompt muons in the signal region are required to be CB muons that satisfy the Medium identification and PFlowTight isolation working points. The Medium identification provides about 97% efficiency for muons with $p_{\mathrm{T}} > 5$ GeV and around 70% for 3 GeV $< p_{\mathrm{T}} < 5$ GeV, while suppressing fake muons and those from light-hadron decays. The PFlowTight isolation, using both track and calorimeter information, maintains high efficiency for prompt muons and reduces contamination from heavy-flavour decays.

6.3.3 Jets

Jets are reconstructed from clusters of energy deposits in the calorimeters originating from the hadronization of quarks and gluons. The reconstruction is performed using the anti-k_t algorithm [140] with a radius parameter $R = 0.4$, using the particle flow implemention [141]. The inputs to the algorithm are topo-clusters built from neighboring calorimeter cells with significant energy deposits above noise thresholds. Each cluster is treated as a massless four-vector and calibrated to the EM energy scale before jet finding [142]. The algorithm improves pile-up stability by removing energy contributions from pile-up interactions through track-to-vertex association, with additional corrections applied to further reduce residual effects. Jet clustering by anti-k_t algorithm is shown in Fig. 6.5.

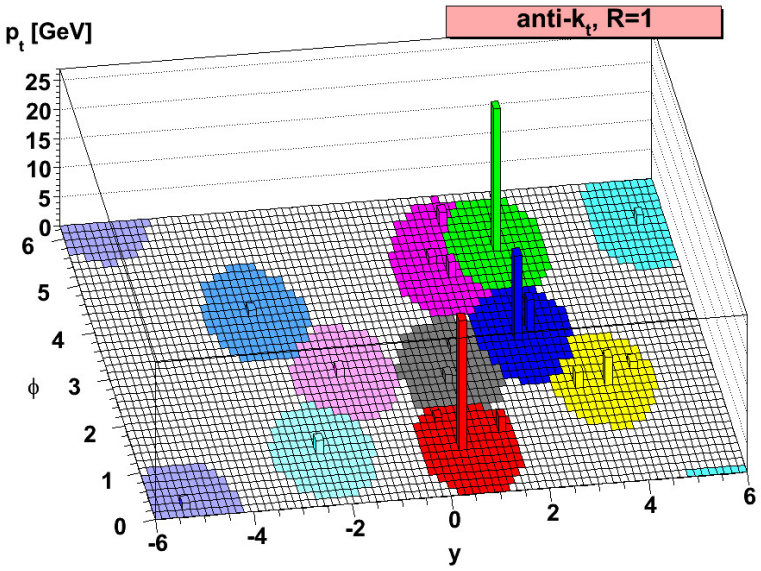


Figure 6.5: Illustration of the anti-k_t clustering algorithm forming a conical structure around the highest-momentum track [140].

After pile-up correction, jet energies are calibrated [143] to account for the calorimeter's non-compensating response[2], where the EM-scale energy underestimates the true jet energy. Simulation-based calibrations use the jet energy response, $R = E_{\text{reco}}/E_{\text{true}}$, to derive energy- and η-dependent correction factors. Residual mismodeling is corrected through *in-situ* calibrations using photon, Z boson, and dijet events. An additional η inter-calibration aligns the forward ($0.8 < |\eta| < 4.5$) and central ($|\eta| < 0.8$) jet responses, essential for analyses involving forward jets such as this VBS analysis. Further corrections account for jet flavour dependence, as quark and gluon jets exhibit different calorimeter responses.

[2]The calorimeter response is better for electromagnetic showers compared to hadronic showers.

b-jet Identification

Jets originating from *b*-quarks are identified using dedicated algorithms that exploit the long lifetime and characteristic decay properties of *b*-hadrons. These hadrons typically travel a few millimeters before decaying, leaving displaced tracks and secondary vertices within the jet cone. The identification is performed using the DL1r algorithm, a deep neural network that combines information from track impact parameters, reconstructed secondary vertices, and the presence of soft leptons inside jets. It is optimized for PFlow jets and is currently the default tagger in ATLAS [144].

The algorithm provides a continuous discriminant output, and different working points are defined to achieve target efficiencies for identifying b-jets in simulated $t\bar{t}$ events, as shown in Fig. 6.6. The 85% efficiency working point is commonly used, corresponding to about 85% efficiency for *b*-jets, with rejection factors of roughly 3 for *c*-jets and 30 for light-flavour jets. Calibration factors derived from data control samples are applied to correct residual differences between data and simulation.

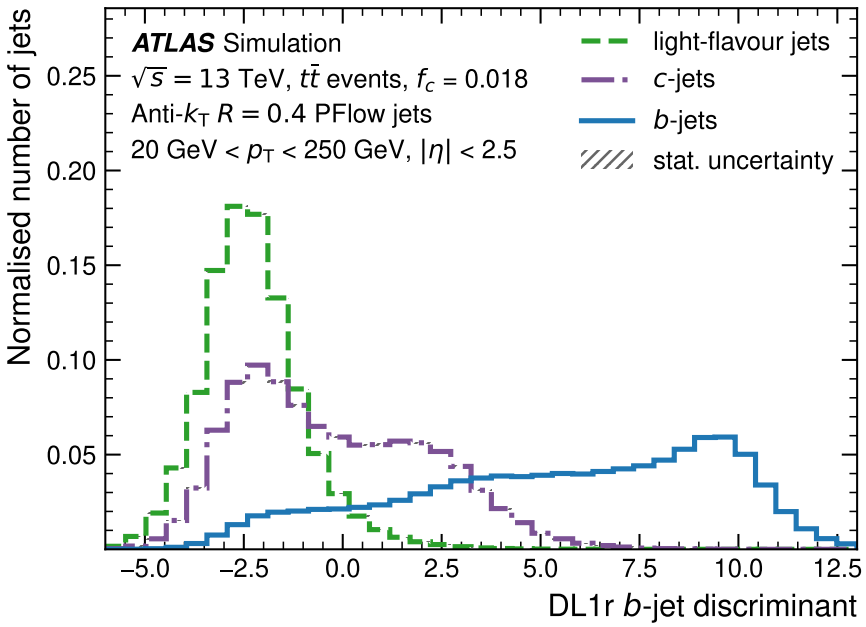


Figure 6.6: Distributions of the outputs of the `DL1r` *b*-tagging algorithm for *b*-jets, *c*-jets and light-flavour jets in $t\bar{t}$ simulated events [145].

In this analysis, non-prompt leptons from *b*-quark initiated jets form a major background. To suppress their contribution, events containing *b*-tagged jets are rejected. The DL1r algorithm, trained to distinguish *b*-jets from *c*- and light-flavour jets, is used with an 85% efficiency working point, providing strong *c*-jet rejection while maintaining high *b*-jet identification efficiency.

6.3.4 Missing Transverse Momentum

Neutrinos are weakly interacting particles that traverse the ATLAS detector without leaving a measurable signal. Their presence is inferred from an imbalance in the total transverse momentum of visible particles. The observable used to quantify this imbalance is the missing transverse momentum, $\vec{E}_{\mathrm{T}}^{\mathrm{miss}}$ [146].

Since the colliding protons travel along the z-axis, the net transverse momentum of the interacting partons before collision is approximately zero. By momentum conservation, the vector sum of the transverse momenta of all particles produced in an event should also be zero. Any imbalance therefore corresponds to the transverse momentum carried by undetected particles such as SM neutrinos:

$$\vec{p}_{\mathrm{T}}^{\mathrm{miss}} = -\sum_{\substack{\text{detected}\\ \text{particles}}} \vec{p}_{\mathrm{T}} = \sum_{\substack{\text{undetected}\\ \text{particles}}} \vec{p}_{\mathrm{T}}\,. \tag{6.1}$$

The magnitude of this vector defines the missing transverse energy:

$$E_{\mathrm{T}}^{\mathrm{miss}} = |\vec{E}_{\mathrm{T}}^{\mathrm{miss}}| = \sqrt{(E_x^{\mathrm{miss}})^2 + (E_y^{\mathrm{miss}})^2}, \tag{6.2}$$

where the x- and y-components are given by the sum of the contributions from all reconstructed and calibrated physics objects in the event:

$$E_{x(y)}^{\mathrm{miss}} = -\sum_{e} p_{x(y)} - \sum_{\mu} p_{x(y)} - \sum_{\gamma} p_{x(y)} - \sum_{\tau} p_{x(y)} - \sum_{\text{jets}} p_{x(y)} - \sum_{\substack{\text{unused}\\ \text{tracks}}} p_{x(y)}\,. \tag{6.3}$$

The reconstruction of $E_{\mathrm{T}}^{\mathrm{miss}}$ uses all ATLAS sub-detectors and depends on the calibration of individual physics objects. The track-based soft term, built from tracks associated with the primary vertex but not linked to any reconstructed object, provides pile-up stability and improves the resolution. Accurate reconstruction of $E_{\mathrm{T}}^{\mathrm{miss}}$ is crucial for identifying neutrinos in events such as $W^{\pm}W^{\pm}jj$, where they are produced in W boson decays.

Chapter 7

Object and Event Selection

The ATLAS detector produces a massive amount of collision data, far exceeding what can be fully analyzed. Since only a small fraction of these collisions contains events of physical interest, a detailed set of selection criteria is used to identify relevant events. These selections are applied at two levels: object-level, to select physics objects originating from the hard-scatter vertex, and event-level, to isolate events with the $W^{\pm}W^{\pm}jj$ signature. The criteria adopted for this polarization measurement are identical to those in the published unpolarized EW–$W^{\pm}W^{\pm}jj$ ATLAS analysis [4], which has already demonstrated their effectiveness for this process.

This chapter outlines the selection criteria used for the measurement of the polarized EW $W^{\pm}W^{\pm}jj$ process. The object-level selections and trigger requirements are described in Section 7.1. The overall event selection procedure, including the definitions of the signal and control regions, is given in Section 7.2.

7.1 Object Selection

Collisions in the ATLAS detector produce many particles that are reconstructed as object candidates. In the analysis, the objects used are electrons, muon, jets (and b-jets), and $E_{\mathrm{T}}^{\mathrm{miss}}$. The general procedure for object reconstruction is described in Chapter 6. These reconstructed objects, are subject to a selection process to categorize them as baseline (loose) or signal (tight), depending on the selection criteria applied. Alongside these reconstructed objects, the missing transverse momentum ($p_{\mathrm{T}}^{\mathrm{miss}}$) is calculated to account for undetected particles, primarily neutrinos. Finally, an overlap removal procedure ensures that no single physical particle is counted multiple times through different object reconstructions.

7.1.1 Reconstructed Vertices and Triggers

Each recorded collision originates from the overlap of two proton bunches at the LHC. In a single bunch crossing, several proton–proton interactions may occur simultaneously, producing multiple reconstructed vertices. To identify the *primary vertex* — the one most likely associated with the hard-scattering process of interest — the vertex with the largest sum of squared transverse momenta of its associated tracks is chosen. Other vertices, arising from additional interactions, are termed as pileup. Only events where the primary vertex has at least three associated tracks are considered for further analysis.

The $W^{\pm}W^{\pm}jj$ signal consists of two leptons, and the analysis uses unprescaled single-electron and single-muon triggers to select events. Distinct trigger conditions are applied for electrons and muons, with stricter object quality requirements imposed for lower transverse momenta. The triggers used during the various Run 2 data-taking years are summarized in Table 7.1 and discussed in detail in Refs. [147, 148]. Within each data-taking period, a logical `OR` of all electron triggers is applied to select electron events, and an analogous combination is used for muons. An event is retained for analysis if at least one electron or muon originating from the primary vertex satisfies one of these trigger requirements.

Lepton	**Trigger**	**Year(s)**	E_T/p_T **threshold**	**Identification**	**Isolation**
Electron	`HLT_e24_lhmedium_L1EM20VH`	2015	24 GeV	`Medium`	–
	`HLT_e60_lhmedium`		60 GeV	`Medium`	–
	`HLT_e120_lhloose`		120 GeV	`Loose`	–
	`HLT_e26_lhtight_nod0_ivarloose`	2016–2018	26 GeV	`Tight`	`ivarloose`
	`HLT_e60_lhmedium_nod0`		60 GeV	`Medium`	–
	`HLT_e140_lhloose_nod0`		140 GeV	`Loose`	–
Muon	`HLT_mu20_iloose_L1MU15`	2015	20 GeV	–	`iloose`
	`HLT_mu50`		50 GeV	–	–
	`HLT_mu26_ivarmedium`	2016–2018	26 GeV	–	`ivarmedium`
	`HLT_mu50`		50 GeV	–	–

Table 7.1: Summary of single-lepton triggers used in the analysis. Separate trigger selections are applied for electrons and muons in each data-taking period. The listed parameters correspond to the transverse energy (E_{T}) or momentum (p_{T}) thresholds, as well as identification and isolation requirements applied in the HLT definitions.

7.1.2 Electrons

The origin of reconstructed electrons is ensured to be the primary collision vertex by evaluating the impact parameters of the associated track. Requirements on both the transverse and longitudinal impact parameters suppress contributions from secondary or misidentified tracks.

Electron identification (introduced in Section 6.3.1) is performed using a likelihood(LH)-based discriminant that combines information from the tracking and calorimeter systems. Variables such as shower-shape properties, track quality, and track–cluster matching are used to define several working points (`VeryLooseLH`, `LooseLH`, `MediumLH`, `TightLH`). Baseline electrons satisfy the `LooseLH` requirement, while signal electrons meet the tighter `TightLH` criteria to ensure high purity.

Electrons are accepted within the fiducial region of the detector ($|\eta| < 2.47$), excluding the calorimeter transition region. A transverse momentum threshold (27 GeV) ensures consistency with electrons originating from $W^{\pm}$ decays, while looser kinematic requirements are applied for baseline objects.

Additional selection requirements improve the object quality and suppress background contributions. Isolation criteria, based on the activity around the electron track, reduce contamination from nearby particles. The `Author` variable distinguishes true electrons from photons by considering tracking and calorimeter information, requiring unambiguous electron reconstruction. Finally, the Electron Charge ID Selector (ECIDS), a boosted decision tree trained to identify charge misreconstruction, is applied to signal electrons to suppress the charge-flip background (refer to Sec. 8.2.1).

A summary of the baseline and signal electron selection criteria is provided in Table 7.2.

7.1.3 Muons

Muons, in contrast to electrons, penetrate all layers of the ATLAS detector, leaving tracks in the inner detector, energy deposits in the calorimeters, and hits in the muon spectrometer. These measurements are combined to reconstruct muon candidates and distinguish them from background sources such as hadron decays or detector noise.

Signal muons are identified using the `Medium` working point to ensure high purity and stability, while baseline muons employ the `Loose` selection for higher efficiency. Tracks are required to be consistent with the primary vertex based on impact-parameter constraints, ensuring that selected muons originate from the hard-scatter interaction rather than from pile-up or secondary decays.

Criterion	Baseline		Signal	
	Electron	**Muon**	**Electron**	**Muon**
Identification	`LooseLH`	`Loose`	`TightLH`	`Medium`
Kinematic Acceptance	$p_{\mathrm{T}} > 4.5$ GeV	$p_{\mathrm{T}} > 3$ GeV	$p_{\mathrm{T}} > 27$ GeV	
Geometrical Acceptance	$\lvert\eta\rvert < 2.47$	$\lvert\eta\rvert < 2.7$	$\lvert\eta\rvert < 2.47$, excluding $1.37 \leq \lvert\eta\rvert \leq 1.52$	$\lvert\eta\rvert < 2.5$
Longitudinal IP	$\lvert z_0 \times \sin\theta\rvert < 0.5$ mm	$\lvert z_0 \times \sin\theta\rvert < 1.5$ mm	as for baseline	$\lvert z_0 \times \sin\theta\rvert < 0.5$ mm
Transverse IP	$\lvert\frac{d_0}{\sigma_{d_0}}\rvert < 5$	$\lvert\frac{d_0}{\sigma_{d_0}}\rvert < 15$	as for baseline	$\frac{d_0}{\sigma_{d_0}} < 3$
Isolation	`none`	`none`	`Gradient`	`FixedCutPflowTight`
`Author`	-	-	1	-
Charge-flip rejection	-	-	Pass `ECIDS`	-

Table 7.2: Baseline (or preselected) and signal lepton selections. IP denotes Impact Parameter.

Kinematic and geometrical requirements restrict the muon candidates to the detector's fiducial acceptance and suppress low-p_{T} or pile-up contributions. Additional isolation based on calorimeter and tracking activity is imposed on signal muons to further reduce contamination from non-prompt sources.

A summary of all selection criteria for baseline and signal muons is provided in Table 7.2.

7.1.4 Jets

Jets are reconstructed using the anti-k_t [140] and `PFlow` [141] algorithms, combining information from the calorimeters and the inner detector. To enhance signal purity, additional quality and kinematic requirements are applied. A transverse momentum of $p_{\mathrm{T}} > 20$ GeV is required for baseline jets, while signal jets are selected with $p_{\mathrm{T}} > 25$ GeV. In $W^{\pm}W^{\pm}jj$ events, the two jets are typically produced in the forward detector regions. Accordingly, jets are reconstructed within $\lvert\eta\rvert < 4.5$, significantly larger acceptance than leptons. As with leptons, jets must be consistent with the primary collision vertex. For jets with $p_{\mathrm{T}} < 60$ GeV and $\lvert\eta\rvert < 2.4$, the jet vertex tagging (JVT) [149] algorithm is used to suppress pile-up contributions.

7.1.5 Reconstruction of the Missing Transverse Momentum

The leptonic decays of $W^{\pm}$ bosons ($W^{\pm} \to \ell^{\pm}\nu$) produce neutrinos that escape detection, making sensitivity to occurence of neutrinos essential in this analysis. Since the colliding protons have

zero net transverse momentum, momentum conservation requires that the sum of the transverse momenta of all reconstructed particles in the event should also vanish. Any imbalance therefore indicates the presence of undetected particles, primarily neutrinos.

The missing transverse momentum, $p_{\mathrm{T}}^{\mathrm{miss}}$ [146], is reconstructed from the transverse momenta of baseline leptons and jets, together with contributions from soft hadronic activity not associated with these objects. An internal overlap removal procedure is applied to prevent double counting of energy deposits.

7.1.6 Overlap Removal

The reconstruction of electrons, muons, and jets in the ATLAS detector can lead to multiple objects being associated with the same physical particle. To prevent such double counting, an overlap removal procedure is applied. Objects are sequentially removed based on their spatial proximity and detector signatures. This step ensures that each reconstructed object in the event uniquely represents a single physical particle.

Lepton-Lepton Overlap. If two electrons share the same inner detector track or overlapping calorimeter clusters, only the electron with the higher p_{T} is retained. When an electron and a muon share a track, the muon is kept if it is confirmed in the muon spectrometer; otherwise, the electron is retained. Duplicate muons are removed at the time of reconstruction.

Lepton-Jet Overlap. The overlap removal scheme gives precedence to b-jets, which are preserved in all cases of overlap. Since events containing b-jets are vetoed in this analysis, this approach helps reject sources of non-prompt leptons effectively. The two cases of overlap between leptons and light-flavor jets are handled as follows:

- **Electron–jet:** An electron is considered to overlap with a jet when their separation satisfies $\Delta R < 0.4$. If the electron lies close to the jet center ($\Delta R < 0.2$), the jet is removed unless it is b-tagged; in that case, the electron is discarded and the jet retained. For $0.2 < \Delta R < \min(0.4, 0.04 + \frac{10\ \mathrm{GeV}}{p_{\mathrm{T}}^{e}})$, the electron is discarded instead.
- **Muon–jet:** The muon–jet overlap is treated analogously to the electron–jet case. In addition, jets in this category are required to have more than two associated tracks to be retained.

7.2 Event Selections

Once the reconstructed objects satisfy the selection criteria described in the previous section, events are selected for the $W^{\pm}W^{\pm}jj$ polarization analysis. The event selection is defined through specific kinematic regions or phase spaces relevant to the measurement. The primary measurement is performed in the *signal region* (SR), while dedicated *control regions* (CRs) are used to constrain background contributions in the statistical fit. Two control regions are defined in this analysis: the *Low-*m_{jj} CR and the $W^{\pm}Z$ CR.

7.2.1 Signal Region

All selected events are required to pass at least one of the single-lepton triggers listed in Table 7.1. Events must contain exactly two leptons with the same electric charge that satisfy the identification and isolation requirements described previously, with p_{T} thresholds above those used in the trigger definition.

Since two neutrinos are expected in the final state, a missing transverse momentum requirement of $E_{\mathrm{T}}^{\mathrm{miss}} \geq 30$ GeV is imposed. At least two jets are required within $|\eta| < 4.5$, ordered by decreasing transverse momenta. The leading jet must satisfy $p_{\mathrm{T}} > 65$ GeV and the sub-leading jet $p_{\mathrm{T}} > 35$ GeV. To enhance the EW signal over QCD-induced production, VBS topology selections are applied: a large di-jet invariant mass of $m_{jj} \geq 500$ GeV and a rapidity separation of $|\Delta y_{jj}| > 2$ between the two leading jets.

Backgrounds from processes with additional leptons, such as WZ and ZZ, are reduced by vetoing events with a third baseline lepton surviving the overlap removal. Events are also rejected if a third lepton, even when removed by the overlap algorithm, forms an opposite-sign, same-flavour pair with either signal lepton consistent with a Z boson decay ($|m_{\ell\ell} - m_Z| < 15$ GeV). To suppress top-quark and non-prompt lepton backgrounds, events containing any b-tagged jets are vetoed, while Drell–Yan contributions from low-mass resonances are removed by requiring $m_{\ell\ell} \geq 20$ GeV.

Because charge misidentification is more significant in the dielectron channel, two additional selections are applied for ee events: both electrons must be within the barrel region ($|\eta| < 1.37$), and events near the Z boson mass peak are removed by requiring $|m_{ee} - m_Z| > 15$ GeV. These selections collectively enhance the purity of EW–$W^{\pm}W^{\pm}jj$ events while maintaining high signal efficiency. A complete summary of the SR selection is provided in Table 7.3.

Signal Region Selection
$n_\ell = 2$ with same electric charge ($\ell^\pm\ell^\pm$)
Veto event if n_ℓ (baseline) ≥ 3
$p_{\mathrm{T}}^{\ell} > 27$ GeV
$\lvert\eta^{\mu}\rvert < 2.5$
$\lvert\eta^{e}\rvert < 2.47$ excluding $1.37 \leq \lvert\eta^{e}\rvert \leq 1.52$
$\lvert\eta^{e}\rvert < 1.37$ in the ee channel
$m_{\ell\ell} \geq 20$ GeV
$\lvert m_{ee} - m_{\mathrm{Z}}\rvert > 15$ GeV in the ee-channel
$E_{\mathrm{T}}^{\mathrm{miss}} \geq 30$ GeV
$n_{\mathrm{jets}} \geq 2$ with $\lvert\eta^{j}\rvert < 4.5$
Leading (Subleading) jet $p_{\mathrm{T}} > 65(35)$ GeV
Veto b-jets
$m_{jj} \geq 500$ GeV
$\lvert\Delta y_{jj}\rvert > 2$

Table 7.3: Event selection criteria for the Signal Region. Note that $\ell = e/\mu$.

7.2.2 Low-m_{jj} Control Region

Several SM background processes (discussed in Chapter 8) contribute significantly to the overall event yield. To constrain these backgrounds in the statistical fit, a dedicated Low-m_{jj} CR is defined. This region follows the same selection criteria as the SR (refer to Table 7.3), except for the di-jet invariant mass requirement, which is relaxed to

$$200 \text{ GeV} < m_{jj} < 500 \text{ GeV}.$$

The di-jet invariant mass is among the most powerful discriminants between EW–$W^{\pm}W^{\pm}jj$ production and its backgrounds. Consequently, the Low-m_{jj} CR is kinematically similar to the SR but contains a much smaller signal fraction, making it ideal for constraining background normalizations in the fit.

7.2.3 $W^{\pm}Z$ Control Region

The fully leptonic decay of the $W^{\pm}Z$ system constitutes the dominant background in the SR. Monte Carlo simulations of this process are known to exhibit limited modeling accuracy [4]. Therefore, a

dedicated $W^{\pm}Z$ CR is constructed to correct the shape and normalization of this background using data.

The $W^{\pm}Z$ CR is designed to be kinematically close to the SR but requires the presence of a third signal lepton with $p_{\mathrm{T}} > 15$ GeV. To suppress contributions from Z+jets and $Z\gamma$ processes, a tri-lepton invariant mass requirement of $m_{\ell\ell\ell} > 106$ GeV is applied. All other selection criteria are consistent with the merged Low-m_{jj} and SR definitions. This region provides a reliable, data-driven constraint on the $W^{\pm}Z$ background normalization and shape, ensuring accurate background estimation in the polarization fit. Table 7.4 summarizes the selections in $W^{\pm}Z$ CR.

$W^{\pm}Z$ **Control Region Selection**
$n_{\ell} = 2$ with same electric charge $(\ell^{\pm}\ell^{\pm})$ and a additional veto lepton
Opposite sign di-lepton pair forming a Z boson candidate
$p_{\mathrm{T}}^{\ell} > 27$ GeV (leading pair), $p_{\mathrm{T}}^{\ell} > 15$ GeV (third)
$\lvert\eta^{\mu}\rvert < 2.5$
$\lvert\eta^{e}\rvert < 2.47$ excluding $1.37 \leq \lvert\eta^{e}\rvert \leq 1.52$
$\lvert\eta^{e}\rvert < 1.37$ in the ee channel
$m_{\ell\ell} \geq 20$ GeV satisfied by at least 2 leptons
$m_{\ell\ell\ell} \geq 106$ GeV
$\lvert m_{ee} - m_{Z}\rvert > 15$ GeV in the ee-channel
$E_{\mathrm{T}}^{\mathrm{miss}} \geq 30$ GeV
$n_{\mathrm{jets}} \geq 2$ with $\lvert\eta^{j}\rvert < 4.5$
Leading (Subleading) jet $p_{\mathrm{T}} > 65(35)$ GeV
Veto b-jets
$m_{jj} \geq 200$ GeV
$\lvert\Delta y_{jj}\rvert > 2$

Table 7.4: Event selection criteria for the $W^{\pm}Z$ control region. Note that $\ell = e/\mu$. The characteristic selections of the region are given in blue color.

7.2.4 Fiducial signal region

The selections described above are applied to reconstructed objects within the ATLAS detector and depend on detector performance and reconstruction efficiencies. To enable direct comparison with theoretical predictions, a particle-level *fiducial signal region* is defined. This region mirrors the kinematic selections of the reconstruction-level signal region (Table 7.3) while remaining

independent of detector effects.

At particle level, leptons are required to satisfy $p_{\mathrm{T}} > 27$ GeV and $|\eta| < 2.5$, and are dressed with prompt photons within $\Delta R < 0.1$. Jets are reconstructed using the anti-k_t algorithm with a radius parameter $R = 0.4$. Overlap removal between electrons and jets follows a simplified procedure: if $\Delta R(e, j) < 0.4$, the electron is removed when $p_{\mathrm{T},e}/p_{\mathrm{T},j} < 0.5$, while the jet is discarded if the electron carries more than 50% of the jet transverse momentum. A summary of the fiducial region requirements is provided in Table 7.5.

Fiducial Signal Region Selection
$n_\ell = 2$ with same electric charge $(\ell^\pm\ell^\pm)$
Veto events with τs from $W^\pm$ in ME calculation
$p_{\mathrm{T}}^{\ell} > 27$ GeV
$\lvert\eta^{\ell}\rvert < 2.5$
$m_{\ell\ell} \geq 20$ GeV
$\lvert m_{ee} - m_Z\rvert > 15$ GeV in the ee-channel
$E_{\mathrm{T}}^{\mathrm{miss}} \geq 30$ GeV
$n_{\mathrm{jets}} \geq 2$ with $\lvert\eta^{j}\rvert < 4.5$
Leading (Subleading) jet $p_{\mathrm{T}} > 65(35)$ GeV
Veto b-jets
$m_{jj} \geq 500$ GeV
$\lvert\Delta y_{jj}\rvert > 2$

Table 7.5: Event selection criteria for the fiducial signal region. Note that $\ell = e/\mu$. The characteristic selections of the region are given in blue color.

The fiducial signal region provides a well-defined reference phase space that simplifies theoretical interpretations and comparisons. It is used in Chapter 12 to define the fiducial cross sections extracted in the final statistical fit. This definition thus bridges the experimental measurement and theoretical calculations, enabling a consistent interpretation of the polarization results.

Chapter 8

Background Processes

The event selections defined at both reconstruction and particle levels establish the foundation for the polarization measurement of the $W^{\pm}W^{\pm}jj$ electroweak process. With these regions defined, the next step is to accurately estimate and constrain the background contributions that enter the signal region (SR) and control regions (CRs). These background processes populate the SR either due to genuine same-sign leptons in the final state or through detector effects such as charge misidentification or misreconstruction of objects.

The backgrounds contributing to the SR can be broadly classified into three categories: *prompt lepton* backgrounds, e/γ *conversion* backgrounds, and *non-prompt* or *fake lepton* backgrounds. Dominant backgrounds for this analysis, together with other relevant backgrounds associated with each category, are described in this chapter. The background estimations used in this chapter follow those reported in Ref. [1].

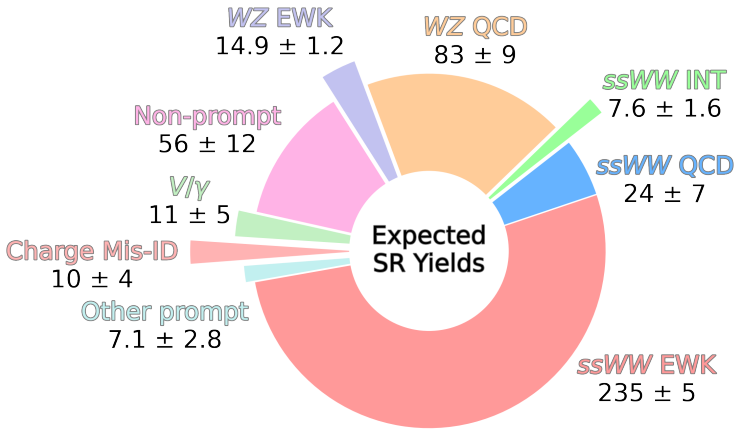


Figure 8.1: Expected yields in the Signal Region according to Ref. [4]

8.1 Prompt Lepton Backgrounds

The prompt lepton background arises from SM processes that genuinely produce two same-sign prompt leptons in the final state, similar to the EW VBS signal. Prompt leptons are the largest sources of background in the analysis. These processes primarily include diboson, triboson, and top-associated productions, and are estimated using MC simulations. The main contributions are as follows:

8.1.1 $W^{\pm}Zjj$

The dominant background contribution in the SR originates from the $W^{\pm}Zjj \to \ell^{\pm}\nu\,\ell^{\pm}\ell^{\mp}jj$ process. Although the SR requires exactly two same-sign leptons, this background is not fully suppressed because one of the leptons from the Z boson decay ($\ell^{\mp}$) may fall outside the detector acceptance, fail reconstruction, or not satisfy the baseline lepton selection. In such cases, the remaining two leptons appear as a same-sign pair and, together with two jets and missing transverse momentum, fulfil the signal requirements.

The $W^{\pm}Z$ background is composed of electroweak scattering ($W^{\pm}Z$-EW) and QCD-induced scattering ($W^{\pm}Z$-QCD). The $W^{\pm}Z$-EW contribution is well predicted by the MadGraph sample, whereas the $W^{\pm}Z$-QCD contribution is known to be poorly modelled by simulation [4]. Moving to a newer Sherpa 2.2.12 sample (as described in Ref. [150]) reduces, but does not eliminate, the mismodelling and therefore still requires a data-driven correction as in Ref. [4].

To improve the $W^{\pm}Z$-QCD prediction, the $W^{\pm}Z$ control region (CR) introduced in Section 7.2.3 is used. The m_{jj} variable, which is highly sensitive to the mismodelling and plays a key role in separating $W^{\pm}W^{\pm}jj$-EW from background, is corrected using data. After subtracting non-$W^{\pm}Z$-QCD contributions from the measured m_{jj} distribution, the remaining distribution is normalized to unity and divided by the normalized $W^{\pm}Z$-QCD simulation. The resulting ratio is fitted with an exponential function:

$$f(x) = ae^{-bx}, \tag{8.1}$$

in the range 200 GeV $< m_{jj} <$ 2500 GeV. This analytic fit is then applied as a reweighting function to the $W^{\pm}Z$-QCD prediction in both the SR and the Low-m_{jj} CR.

Three sources of uncertainty are assigned to this shape correction:

- *PDF and α_S variations:* the uncertainty envelope obtained from fits using different PDF and α_S choices,
- *Higher-order effects:* based on the envelope of fits using different scale variations,

- *Statistical uncertainty:* arising from limited statistics in both measured data and MC samples.

In addition to the shape correction, the overall normalization of the $W^{\pm}Z$-QCD background is determined in the final likelihood fit discussed in Section 12.1. A free parameter θ_{WZQCD} is introduced to scale the normalization using the total number of events observed in the $W^{\pm}Z$ CR. Since the exponential reweighting already captures shape differences, only the event yield is used for this normalization.

8.1.2 $W^{\pm}W^{\pm}jj$–QCD

This process corresponds to the strong production of $W^{\pm}W^{\pm}$ in association with two jets via QCD interactions. Despite having the same final state as the EW signal, it differs in production mechanism and kinematic properties, particularly in jet separation and invariant mass. It therefore constitutes an irreducible background to the signal.

8.1.3 $W^{\pm}W^{\pm}jj$–INT

This contribution arises from the interference between the EW- and QCD-induced production amplitudes of the $W^{\pm}W^{\pm}jj$ process. The interference term is generally small but is accounted for separately in the simulation to avoid bias in the signal extraction.

8.1.4 Other Prompt Lepton Backgrounds

Top-associated processes ($t\bar{t}W$,$t\bar{t}Z$,tZ): Events containing top quarks can also enter the SR if one or more of the objects, especially b-jets, are not reconstructed or are misidentified. For example, $t\bar{t}W$ events produce multiple leptons, and misreconstruction can yield an apparent same-sign dilepton topology. These backgrounds are typically suppressed by b-jet vetoes but remain non-negligible.

$ZZjj$: When both Z bosons decay leptonically, the final state contains four charged leptons. If two oppositely charged leptons escape detection, the remaining pair of same-sign leptons can mimic the signal. Although this background is small, it is included for completeness.

Triboson production (WWZ, WZZ, ZZZ): Triboson processes can also produce same-sign dilepton events if one of the leptons is not reconstructed. For instance, in $WWZ \to \ell^+\nu jj\ell^+\ell^-$, the event appears signal-like if the negatively charged lepton is missed. However, due to their relatively small cross sections and the stringent VBS-like event selection (particularly large m_{jj} and rapidity separation requirements), triboson contributions are typically minor.

8.2 e/γ Conversion Backgrounds

Events containing *electron candidates* can be affected by bremsstrahlung and photon conversion effects, leading to apparent same-sign dilepton signatures. These backgrounds are significant in the electron channels and are divided into two main types: (1) Charge misidentification, and (2) $V\gamma$ conversions.

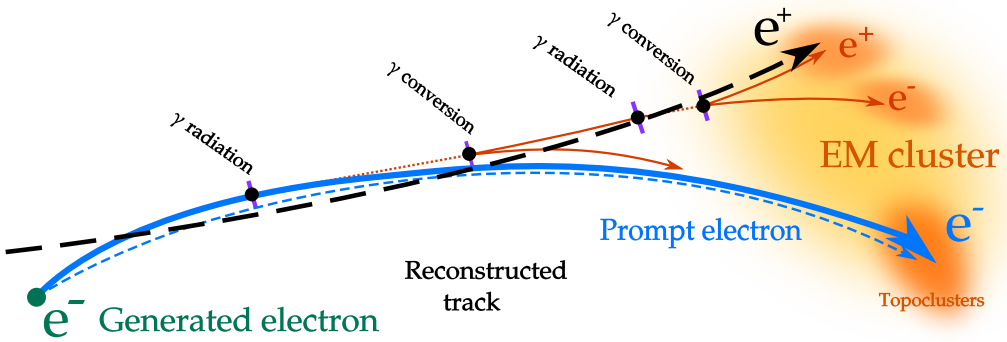
8.2.1 Charge misidentification

The charge misidentification background consists of SM processes producing two opposite-sign prompt leptons, such as $Z \to e^+e^- +$ jets and $t\bar{t}$, in which the charge of one electron is incorrectly reconstructed. Such events mimic the same-sign $W^\pm W^\pm jj$ signal. The background is also referred to as the *charge-flip* background since the electron is reconstructed with its charge flipped.

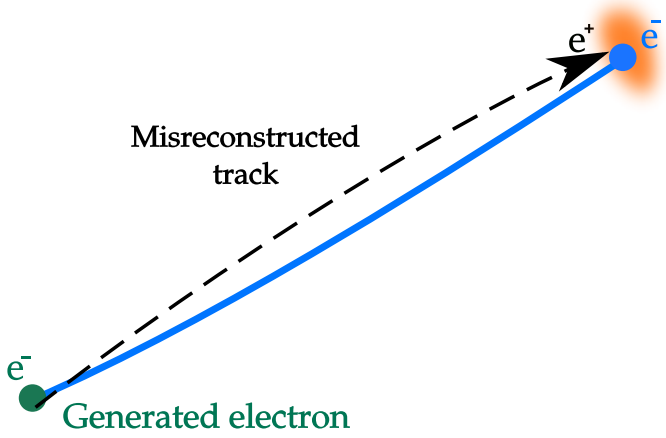
The charge of an electron is determined from the curvature of the reconstructed track in the Inner Detector. Charge misidentification arises primarily from two mechanisms:

- *Incorrect track-to-electron association*: At large $|\eta|$, electrons traverse substantial detector material, increasing the probability of bremsstrahlung and subsequent photon conversion into an e^+e^- pair. The reconstructed track may originate from a secondary electron rather than the original particle, resulting in an incorrect charge assignment, as illustrated in Fig. 8.2(a).
- *Incorrect measurement of track curvature*: The charge sign is inferred from the bending direction of the trajectory in the magnetic field. For very high-p_{T} electrons, the trajectory is nearly straight and small uncertainties in curvature measurement can lead to a wrong charge sign, as shown in Fig. 8.2(b).

The charge-flip background is estimated using a data-driven method developed in Ref. [5]. The Electron Charge ID Selector (ECIDS), a boosted decision tree trained to reject electrons passing identification and isolation requirements but reconstructed with the wrong charge, is applied to signal electrons to suppress the charge-flip background. The ECIDS selection reduces the back-



(a) Incorrect track-to-electron association



(b) Incorrect track curvature measurement

Figure 8.2: A schematic illustrating the two main sources of electron charge misidentification: Fig. 8.2(a) illustrates incorrect track-to-electron association, and Fig. 8.2(b) shows mismeasurement of track curvature. Figs. taken from [5].

ground by approximately a factor of four relative to the previous analysis iteration without it [151]. Events satisfying SR requirements but containing opposite-sign leptons are then weighted by the probability that one electron flips charge, providing an effective prediction of the same-sign background.

Measurement of charge misidentification probabilities. The charge-flip probabilities are measured using simulated $Z \to e^+e^- +$ jets events with truth-level information. Events must pass the single-electron triggers in Table 7.1 and contain two reconstructed ID electrons passing ECIDS with $p_{\mathrm{T}} > 20$ GeV and $m_{ee} > 20$ GeV. Dedicated scale factors are applied to emulate the misidentification rates observed in data. The misidentification probability $\varepsilon_{i,j}^{\mathrm{misid}}$ is computed in bins of p_{T}

and η as

$$\varepsilon_{i,j}^{\text{misid}} = \frac{N_{i,j}^{\text{misid}}}{N_{i,j}^{\text{all}}}, \tag{8.2}$$

where $N_{i,j}^{\text{misid}}$ and $N_{i,j}^{\text{all}}$ denote the numbers of electrons with incorrect and total reconstructed charge assignments in the bin.

Background estimation. The number of same-sign events originating from opposite-sign lepton pairs is obtained by reweighting opposite-sign events using the probability that one lepton flips its charge. For the *ee* channel, the weight applied to opposite-sign events is

$$w = \frac{\varepsilon_1(1-\varepsilon_2)+\varepsilon_2(1-\varepsilon_1)}{(1-\varepsilon_1)(1-\varepsilon_2)+\varepsilon_1\varepsilon_2}. \tag{8.3}$$

where ε_1 and ε_2 are the charge-flip probabilities for the leading and subleading electrons respectively. In the $e\mu$ or μe channels, the muon charge-flip probability is assumed to be zero and the expression simplifies to

$$w = \frac{\varepsilon}{1-\varepsilon}. \tag{8.4}$$

Systematic uncertainties. The systematic uncertainty on the charge-flip background arises from the uncertainties in the scale factors applied to simulated $Z+$jets events for electrons reconstructed with the wrong charge after ECIDS selection. To propagate the uncertainty, the scale factors are varied, the charge-flip probabilities recomputed, and the differences in background yields assigned as systematic uncertainties. Validation is performed in the $Z(ee)$ peak region. The uncertainties of the scale factors are explained in Refs. [152, 153].

8.2.2 $V\gamma jj$ Processes

These processes involve the production of a heavy vector boson ($V \in \{W,Z\}$) in association with a photon and two jets. When the boson decays leptonically and the photon converts into an e^+e^- pair, the event may contain two same-sign leptons if one of the leptons from the conversion is not reconstructed. For example, $W^+\gamma jj \to \ell^+\nu e^+e^- jj$ appears as a same-sign dilepton final state if the e^- is not identified. While generally subdominant, these events contribute non-negligibly to the electron channels and are estimated from MC simulations.

8.3 Non-Prompt and Fake Lepton Backgrounds

A significant background contribution arises from non-prompt leptons, which do not originate from the primary hard scatter but instead result from heavy-flavour hadron decays or from jets misidentified as leptons. A simplified visual comparison of real, non-prompt, and fake leptons is provided in Fig. 8.3. As MC simulations provide a poor description of these processes, a data-driven Fake Factor method — an approximation of the matrix method [154] — is used to estimate this background. The implementation followed in this analysis is based on Ref. [6].

For simplicity, the terms fakes and non-prompt are used interchangeably for the sum of fake leptons and non-prompt leptons.

An alternative lepton selection, referred to as Anti-ID, is introduced with looser requirements than the signal lepton selection described in Section 7.1.2. Anti-ID electrons satisfy the `MediumLH` identification and have no isolation requirement. Anti-ID muons fulfil the `FixedCutPflowLoose` isolation and the transverse impact parameter requirement $|d_0|/\sigma(d_0) < 10$. To avoid overlap with the signal lepton selection, Anti-ID leptons must additionally fail at least one of the tighter criteria. Leptons passing this Anti-ID selection are therefore significantly more likely to be non-prompt.

The fake factor is defined as

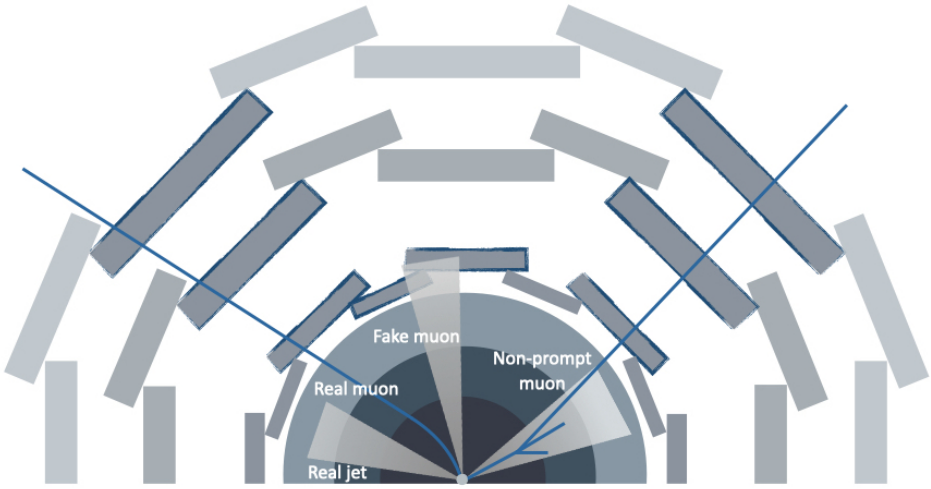
$$F = \frac{N_f^{\text{signal}}}{N_f^{\text{Anti-ID}}}\,, \tag{8.5}$$

where N_f^{signal} and $N_f^{\text{Anti-ID}}$ denote the number of fake leptons passing the signal and Anti-ID selections respectively. The value of F is measured in a single-lepton CR enriched in non-prompt leptons. Exactly one signal or Anti-ID lepton with $p_{\text{T}} > 27$ GeV is required, and at least one signal jet with $p_{\text{T}} > 25\,(30)$ GeV for $|\eta| < 2.5\,(2.5 < |\eta| < 4.5)$. The tagging jet must be back-to-back with the lepton, with $|\Delta\phi_{\ell j}| > 2.8$. To suppress prompt W+jets events, the quantity $p_{\text{T}}^{\text{miss}} + m_{\text{T}}$ must be below 50 GeV. The fake factor is evaluated in regions with and without a b-jet veto. The average of the two is taken as the nominal result, while uncertainties are derived from the b-jet veto region to better match the SR topology.

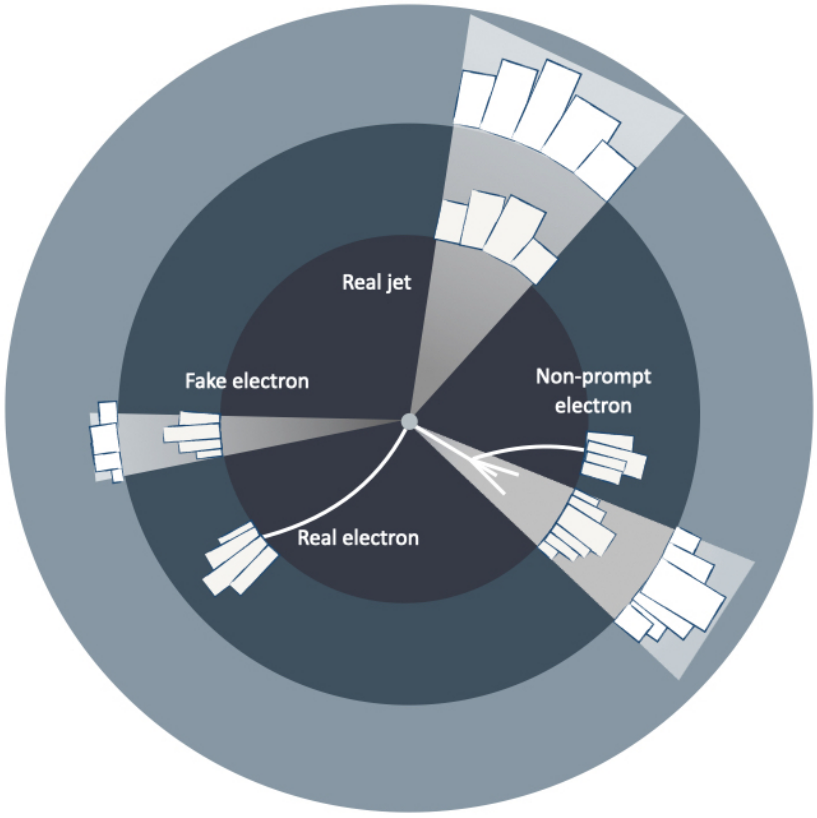
In this non-prompt CR, the number of signal-selected leptons N^{signal} and Anti-ID leptons $N^{\text{Anti-ID}}$ is extracted from data. After subtracting the expected prompt contributions from simulation, the fake factor is computed as

$$F(p_{\text{T}}) = \frac{N^{\text{signal}} - N_{\text{prompt}}^{\text{signal}}}{N^{\text{Anti-ID}} - N_{\text{prompt}}^{\text{Anti-ID}}}\,, \tag{8.6}$$

as a function of the lepton transverse momentum p_{T}. Separate fake factors F_e and F_μ are deter-



(a) Muon Fakes



(b) Electron Fakes

Figure 8.3: Schematic illustration of (a) muon and (b) electron fake leptons. In Fig. 8.3(a), a partial ATLAS cross section shows fake and non-prompt muons leaving signals comparable to real muons. In Fig. 8.3(b), the detector cross section excluding the MS shows fake and non-prompt electrons producing lepton-like calorimeter deposits in the ECal and HCal, leading to misidentification. Figs. taken from [6].

mined for electrons and muons.

A transfer region is defined with the same selection as the SR, except that one of the two leptons must satisfy the Anti-ID selection. After prompt subtraction, the remaining events correspond to the expected non-prompt contribution with one signal and one Anti-ID lepton. Applying the fake factor projects this to the non-prompt estimate for the SR with two signal-selected leptons:

$$N_f^{\text{signal } \ell + \text{signal } \ell} = \sum_{i \in \{e,\mu\}} F_i(p_T) \cdot \sum_{j \in \{e,\mu\}} \left(N^{\text{signal } j + \text{Anti-ID } i} - N_{\text{prompt}}^{\text{signal } j + \text{Anti-ID } i} \right). \tag{8.7}$$

For the application, the p_{T} of the Anti-ID lepton is used.

Several systematic uncertainties are considered for the fake factor method:

- $E_{\mathrm{T}}^{\mathrm{miss}}$+ m_{T} *variation:* Fake factors are recalculated after varying the $E_{\mathrm{T}}^{\mathrm{miss}}$+ m_{T} selection by 5 GeV, and the resulting differences are taken as systematic uncertainties.
- *Prompt background subtraction:* The total prompt contribution is varied by $\pm 5\%$ in the fake-factor extraction, and the resulting changes are assigned as systematic uncertainties.
- *Sample composition difference:* Fake factors derived separately from $n_{b\text{-jet}} = 0$ and $n_{b\text{-jet}} \geq 1$ samples are used to quantify systematic uncertainty from sample composition differences.
- *Statistical uncertainty:* Variations of the fake factors within their statistical uncertainties are propagated as systematic uncertainties.

Chapter 9

Polarized Signal Sample Generation

This chapter describes the setup used to generate and validate polarized signal Monte Carlo samples with MadGraph5_aMC@LO [43]. The generation requires explicit control of the helicity states of the intermediate W bosons and a clear definition of subprocesses, particularly for channels involving τ leptons. The chapter also examines how the matrix-element code handles helicity assignments internally and how event weights behave when the samples are interfaced to parton-shower generators. These details are important to ensure that the polarized samples are generated consistently across different lepton flavours and that the event weights remain correct after showering.

The generation and validation of the polarized signal samples described in this chapter constitute original work by the author. These samples are employed in the recent ATLAS publication [1] to benchmark the Sherpa signal prediction at LO-QCD+PS accuracy against the MadGraph setup described here, ensuring consistency across generator frameworks. Sherpa samples have higher-order QCD and EW corrections, and form the primary signal simulation for the ATLAS publication.

9.1 Sample Generation Configuration

For the analysis presented in this thesis, the signal MC samples are generated using the MadGraph5_aMC@NLO (MG5) event generator. The aim is to produce samples of same-sign VBS processes with individually polarized W bosons, enabling the study of longitudinal (L or 0) versus transverse (T) contributions.

Since the primary physics interest lies in the VBS topology, the polarized samples are produced

for the $\mathcal{O}(\alpha_W^6)$ electroweak process with exclusive polarization configurations (LL, TL, TT) applied to the intermediate W bosons. For this purpose, the W bosons are required to be on-shell. The polarized signal samples are generated using MadGraph at leading-order accuracy, interfaced with the `NNPDF3.0nlo` parton distribution functions.

The model in use is `sm-no_b_mass`, and the MG5 syntax explicitly requests the desired W boson polarisation states. A representative process configuration is

```
import model sm-no_b_mass
define l+ = e+ mu+ ta+
define vl = ve vm vt
define l- = e- mu- ta-
define vl~ = ve~ vm~ vt~
define p = g u c d s u~ c~ d~ s~ b b~
define j = g u c d s u~ c~ d~ s~ b b~

generate p p > w+{X} w+{Y} j j QED=4 QCD=0, w+ > l+ vl @1
add process p p > w-{X} w-{Y} j j QED=4 QCD=0, w- > l- vl~ @1
```

where the placeholders X,Y correspond to polarization states 0 (longitudinal) or T (transverse). In *unordered mode*, the 0T and T0 polarization combinations should be physically equivalent and therefore produce identical final-state distributions [155].

9.2 Observed Behaviour and Validation Strategy

Validation is performed independently in each lepton-flavour channel (e, μ, τ) to ensure that the behaviour of polarized samples is consistent across decay modes. In particular, angular observables such as the cosine of the lepton decay angle ($\cos\theta$) reconstructed in the W-boson helicity frame are examined, as they provide direct sensitivity to the underlying polarization state. Eq. 3.4 introduced in Sec. 3.3.1 can be written in the following form to emphasise the contribution from different polarization modes:

$$\begin{aligned} \frac{1}{\sigma}\frac{d\sigma(W_T^{\pm}\to\ell^{\pm}\nu)}{d\cos\theta} &= \frac{3}{8}(1\mp\cos\theta)^2 f_{T,L} + \frac{3}{8}(1\pm\cos\theta)^2 f_{T,R}\,, \\ \frac{1}{\sigma}\frac{d\sigma(W_L^{\pm}\to\ell^{\pm}\nu)}{d\cos\theta} &= \frac{3}{4}\sin^2 f_L\,. \end{aligned} \tag{9.1}$$

The distribution of TT process is expected to be propotional to $\cos\theta^2$ while the distribution of LL process is propotional to $\sin\theta^2$ ($-\cos\theta^2$).

The following behaviour is observed:

- In the channels with electrons and muons ($\ell = e, \mu$) the expected equivalence between 0T and T0 samples is preserved, as shown in Fig. 9.1(a).
- In channels containing τ leptons, the symmetry broke down: in the 0T sample, the transverse W consistently decayed via the τ ($W_T \to \tau\nu$), while in the T0 sample the longitudinal W did ($W_L \to \tau\nu$), as shown in Figs. 9.1(b) and 9.1(c).
- The polarization sum (00 + 0T + TT) did not reproduce the unpolarized distribution, showing a significant bias associated with τ final states.

This indicates that the τ flavour triggered an incorrect polarization assignment inside the matrix-element code.

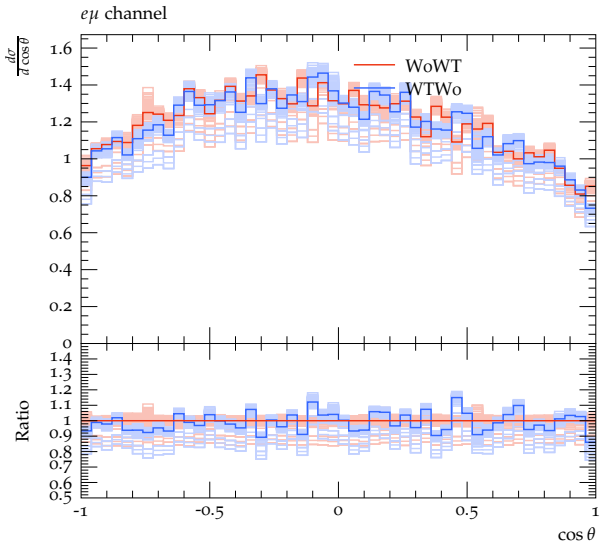
9.3 Diagnosis of the Issue

Inspection of the backend Fortran code in the MG5 `SubProcesses` directory shows that the τ lepton helicity is treated in a fixed manner that implicitly ties it to the longitudinal W polarization for the T0 syntax and transverse W polarization for the 0T syntax. A representative snippet appears in the file '`matrix.f`':

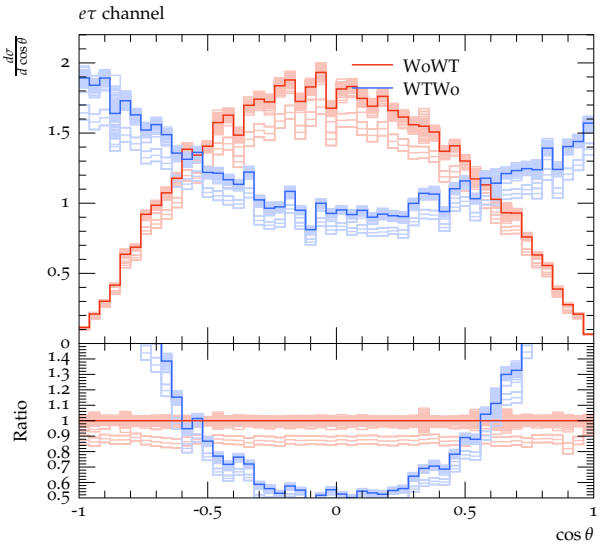
```
CALL IXXXXX(P(0,5),MDL_MTA,NHEL(5),-1*IC(5),W(1,4))
CALL FFV2P1L_3(W(1,4),W(1,3),GC_100,MDL_MW,FK_MDL_WW,W(1,6))
```

This structure forces consistency between helicity sign choices and breaks the expected symmetry when τ leptons are present.

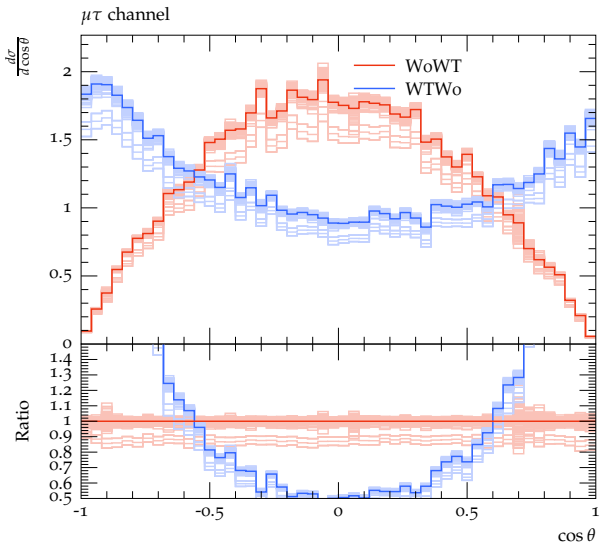
Another aspect of the diagnosis concerns the cross section observed after the parton showering stage. The decision to assign the same subprocess label (@1) to all subprocesses in the configuration is motivated by technical behaviour observed when interfacing MadGraph with Herwig for parton showering. In configurations involving multiple subprocesses, Herwig applies an internal rescaling of event weights, whereby the weight of each subprocess i is multiplied by $(\sigma_1 + \sigma_2)/\sigma_i$. Consequently, the total event weight after showering, and therefore the effective cross section, becomes significantly larger than the value produced by MadGraph (for example, by a factor of two in the case of two subprocesses). Using a single common label for all subprocesses prevents this rescaling and preserves the correct cross section. This effect is not present when using Pythia, suggesting that the issue originates within Herwig.



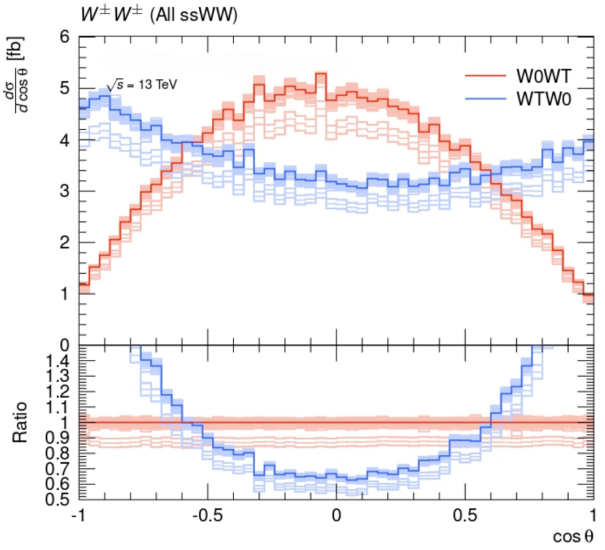
(a) Before Fix: $e\mu$ channel



(b) Before Fix: $e\tau$ channel



(c) Before Fix: $\mu\tau$ channel



(d) Before Fix: All channels

Figure 9.1: Observed $\cos\theta$ distributions for mixed polarization modes (LT and TL) showing incorrect polarization assignment for final states with τ leptons. Note that 0 denotes L in plot legend.

9.4 Resolution and Generator Fix

The complete solution can be implemented in one of two methods: (1) Syntax workaround, or (2) Generator patch.

9.4.1 Syntax workaround

An explicit enumeration of subprocesses is implemented to ensure that channels involving tau decays are handled independently. In this configuration, ℓ denotes only the light leptons (e, μ), and dedicated subprocess labels are assigned to the τ decay modes, separating them from those associated with the light-lepton channels.

```
...
define l+ = e+ mu+
define l- = e- mu-
...
generate p p > w+{0} w+{T} j j QED=4 QCD=0, w+ > l+ vl @1
add process p p > w+{0} w+{T} j j QED=4 QCD=0, w+ > l+ vl, w+ > ta+ vl @1
add process p p > w+{0} w+{T} j j QED=4 QCD=0, w+ > ta+ vl, w+ > l+ vl @2
add process p p > w+{0} w+{T} j j QED=4 QCD=0, w+ > ta+ vl @1
add process p p > w-{0} w-{T} j j QED=4 QCD=0, w- > l- vl~ @1
add process p p > w-{0} w-{T} j j QED=4 QCD=0, w- > l- vl~, w- > ta- vl~ @1
add process p p > w-{0} w-{T} j j QED=4 QCD=0, w- > ta- vl~, w- > l- vl~ @2
add process p p > w-{0} w-{T} j j QED=4 QCD=0, w- > ta- vl~ @1
```

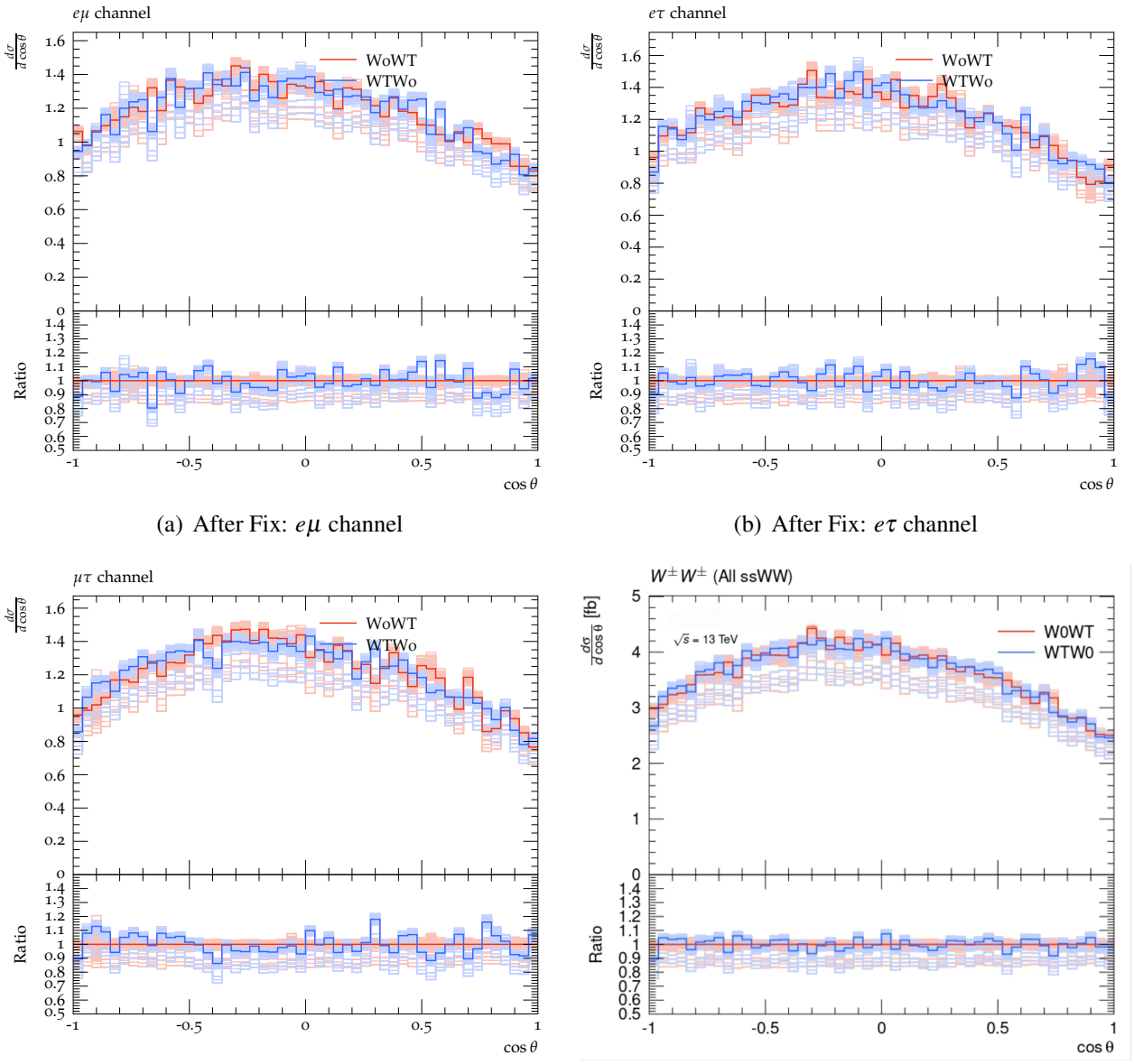
9.4.2 Generator patch

Following the public report of the issue [156], an official fix is committed to a branch of MG5 by the authors, correcting the helicity handling logic so that τ leptons no longer impose a fixed polarization association. With this version, the simpler command syntax again produces correct behaviour.

9.5 Outcome

After regeneration of samples using the explicit workaround, the closure between unpolarized samples and the sum of polarized components is fully restored. The 0T and T0 samples became

statistically consistent across all lepton final states, including those involving τ leptons. It is well demostrated by Fig. 9.2 showing agreements in individual channels as well as all channels combined.



(a) After Fix: $e\mu$ channel

(b) After Fix: $e\tau$ channel

(c) After Fix: $\mu\tau$ channel

(d) After Fix

Figure 9.2: $\cos\theta$ distributions for mixed polarization modes (LT and TL) after applying the fix. Clear agreement can be seen between the syntaxes. Note that 0 denotes L in the plot legend.

Chapter 10

Data and Simulated Samples

This chapter describes the datasets and simulated samples employed in the analysis. An overview of the ATLAS data and Monte Carlo (MC) processing chains is provided, followed by details of the data and MC samples used.

10.1 From Detector Signals to Analysis Samples

The ATLAS data processing workflow governs the conversion of detector readout signals into formats suitable for physics analyses. During data taking, the trigger and data acquisition system records selected events in RAW format, containing the full detector information required for event reconstruction. Reconstruction algorithms, discussed in Chapter 6, transform the RAW detector signals into high-level reconstructed objects stored in the Analysis Object Data (AOD) format.

Because AODs are large datasets of order $\mathcal{O}$(PB), they are further processed through derivation algorithms that reduce the size to $\mathcal{O}$(TB), producing Derived AODs (DAODs). Various derivation formats exist, such as STDM3 and HIGG3D3, each optimized for specific physics applications. For detailed analyses, DAODs are often reduced into flat n-tuples or Physics AOD (PAOD) files containing only the required event-level quantities, typically $\mathcal{O}$(GB). The measurement presented in this thesis uses PAODs as the final input format.

A parallel workflow is applied to MC simulations. The production chain begins with event generation of the hard-scattering process, followed by parton showering and hadronization to produce stable final-state particles. The generated events are stored in EVNT format and passed to a GEANT4-based detector simulation [157], which models the particle interactions with the ATLAS detector material, including the detailed energy deposition within the subdetector systems. A dig-

itization stage converts the simulated energy deposits into raw detector-like signals. Subsequent reconstruction and derivation steps then follow the same procedure applied to data, leading to the final PAOD format.

Corrections applied to simulated samples in order to match detector performance observed in data, such as pile-up reweighting and object-level scale factors, are implemented event-by-event via dedicated weight factors. A schematic overview of the complete data and simulation processing chain is shown in Fig. 10.1.

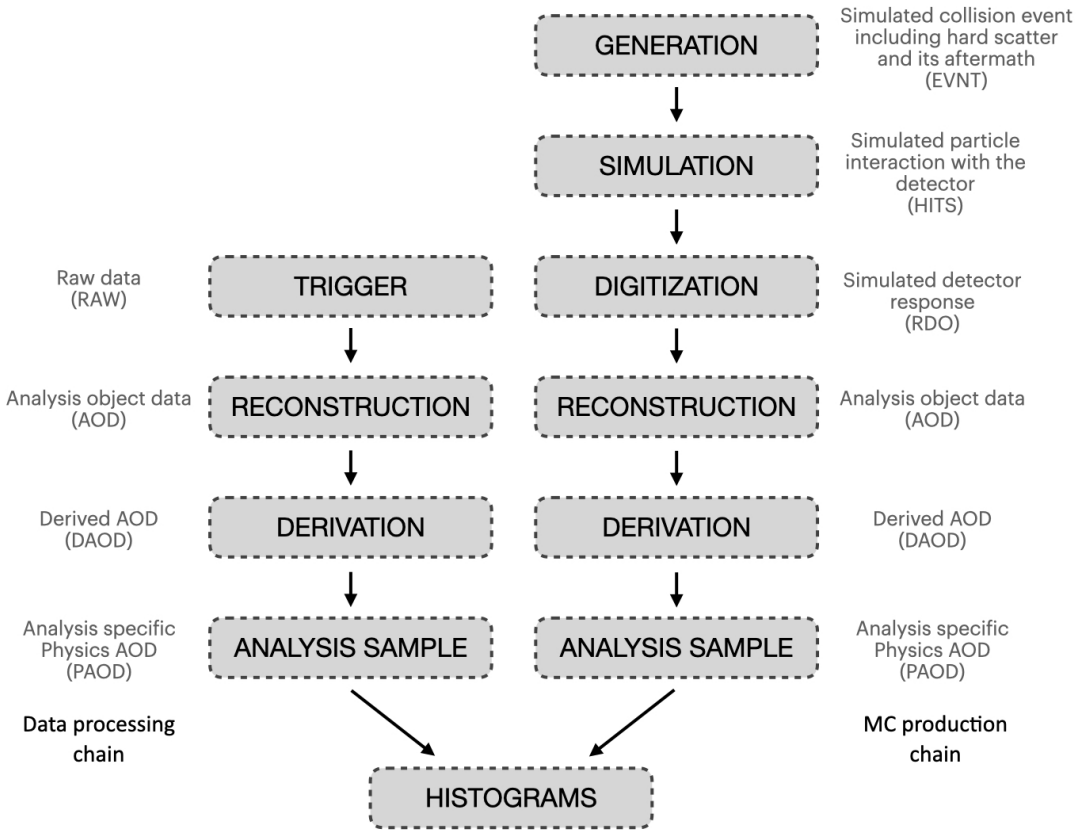


Figure 10.1: A schematic overview of the ATLAS data and Monte Carlo processing chains. The data path is shown on the left and the MC production path on the right. The final PAOD samples from both data and simulation are used as inputs to the analysis. Fig. taken from [6].

10.2 Datasets

The dataset used in this analysis consists of proton–proton collision data recorded at a centre-of-mass energy of $\sqrt{s} = 13$ TeV by the ATLAS detector during the 2015–2018 LHC Run 2 period, corresponding to an integrated luminosity of 139 fb^{-1}. The LHC operated with 25ns bunch spacing, while the instantaneous luminosity and average pile-up varied throughout the running period.

In total, the LHC delivered 156 fb^{-1} of stable beams, of which ATLAS recorded 147 fb^{-1} [158, 159]. Only events satisfying standard detector and data quality requirements, defined by the Good Runs List (GRL), are retained for physics analyses. After the application of GRL selection, the integrated luminosity used for this analysis is 139 fb^{-1} with an associated uncertainty of 1.7% [122]. The delivered, recorded, and usable luminosities are summarized in Table 10.2.

Data Period	Pile-up	Delivered [fb^{-1}]	Recorded [fb^{-1}]	Good for Physics [fb^{-1}]
2015	13.4	4.2	3.9	3.2
2016	25.1	38.5	35.6	33.0
2017	37.8	50.2	46.9	44.3
2018	36.1	63.3	60.6	58.5
Run 2 total	33.7	156.2	147.0	139.0

Table 10.1: Summary of the LHC Run 2 ATLAS data-taking periods, including average pile-up and integrated luminosities. "Delivered" refers to the luminosity provided by the LHC, "Recorded" to luminosity successfully recorded by ATLAS, and "Good for Physics" to data passing ATLAS data quality requirements.

10.3 Monte Carlo Samples

The generation and validation of MadGraph signal samples is covered in Chapter 9. The following sections cover the remainder of the details about their MC simulation.

10.3.1 Signal Samples

The MadGraph event generator is used to simulate polarized $W^{\pm}W^{\pm}jj$ processes at leading-order (LO) accuracy. The NNPDF3.0nlo parton distribution function set is employed for the generation of the individual polarization templates. In addition to an unpolarized sample, events corresponding to the LL, TL and TT polarization states are produced both in the WW centre-of-mass frame and in the partonic centre-of-mass frame.

The impact of the interference between different polarization states is expected to be small. The estimation of this interference depends on the event generator used for the polarization simulation. For MadGraph, the interference contribution is computed as the difference between the unpolarized sample and the sum of the polarized components:

$$N_{\text{int}} = N_{\text{unpol}} - \sum_{\text{pol}} N_{\text{pol}}. \tag{10.1}$$

The resulting polarization samples are validated against the expected $W^{\pm}$ decay angular distribution given in Eq. 3.4 as detailed in Chapter 9, and the sum of the polarized components is found to be consistent with the unpolarized $W^{\pm}W^{\pm}jj$–EW cross section. As the generation is performed at LO, higher-order corrections are incorporated through event-by-event reweighting.

A summary of the signal samples is provided in Table 10.2.

Process	**Polarization**	**Frame**	**Generator**	**PDF**
$W^{\pm}W^{\pm}jj$	Unpol.	–	MADGRAPH5_AMC@LO+PYTHIA 8	NNPDF3.0nlo
$W_T^{\pm}W_T^{\pm}jj$	*TT*	*ppcmf*	MADGRAPH5_AMC@LO+PYTHIA 8	NNPDF3.0nlo
$W_T^{\pm}W_T^{\pm}jj$	*TT*	*WWcmf*	MADGRAPH5_AMC@LO+PYTHIA 8	NNPDF3.0nlo
$W_T^{\pm}W_L^{\pm}jj$	*TL*	*ppcmf*	MADGRAPH5_AMC@LO+PYTHIA 8	NNPDF3.0nlo
$W_T^{\pm}W_L^{\pm}jj$	*TL*	*WWcmf*	MADGRAPH5_AMC@LO+PYTHIA 8	NNPDF3.0nlo
$W_L^{\pm}W_L^{\pm}jj$	*LL*	*ppcmf*	MADGRAPH5_AMC@LO+PYTHIA 8	NNPDF3.0nlo
$W_L^{\pm}W_L^{\pm}jj$	*LL*	*WWcmf*	MADGRAPH5_AMC@LO+PYTHIA 8	NNPDF3.0nlo

Table 10.2: A summary of the Standard Model Monte Carlo samples used as signal in the analysis.

The particle-level selection corresponding to SR and Low-m_{jj} CR are the same as SR event selections described in Table 7.3 with one change to accommodate Low-m_{jj} CR: $m_{jj} > 200$ GeV. The number of events predicted by MadGraph and Sherpa [1] at LO-QCD+PS are listed in Table 10.3.

	MC events	σ_{total} [fb]	*WWcmf*			*ppcmf*		
			LL	*LT+TL*	*TT*	*LL*	*LT+TL*	*TT*
MG unpol	73 261	2.880		–			–	
MG *ppcmf*	149 321	2.925		–		0.177	1.030	1.718
				–		6.07%	35.20%	58.73%
MG *WWcmf*	1 426 669	2.896	0.277	0.874	1.744		–	
			9.58%	30.18%	60.24%		–	
Sh $W^{\pm}W^{\pm}jj$	1 269 306	2.933	0.285	0.909	1.778	0.182	1.072	1.732
			9.60%	30.59%	59.81%	6.09%	35.91%	58.00%

Table 10.3: Comparison of cross sections, polarization fractions, and generated MC events for MadGraph and Sherpa samples. Event counts correspond to selections in the particle-level phase space. The numbers for Sherpa are from Ref. [1].

10.3.2 Background Samples

The dominant simulated backgrounds include QCD- and interference-induced $W^{\pm}W^{\pm}jj$ production, modelled with MadGraph5_aMC@NLO interfaced to Herwig 7 with the coupling orders adjusted to α^4 and α^5, respectively. The primary background is $WZjj$, whose electroweak and interference components are simulated with MadGraph5_aMC@NLO and Pythia 8, while the QCD-induced mode is produced with Sherpa 2.2.2. The subdominant prompt process $V\gamma jj$ is generated using Sherpa 2.2.2, and for small ΔR between the lepton and photon, the background is modelled using $V+$jets samples produced with MadGraph5_aMC@NLO and Pythia 8. Table 10.4 summarizes all the background samples used in this analysis, including the marginally contributing prompt backgrounds such as top and other multi-boson processes.

Process	**Generator**	**PDF**
$W^{\pm}W^{\pm}jj$-QCD	MADGRAPH5_AMC@NLO+HERWIG 7	NNPDF3.0nlo
$W^{\pm}W^{\pm}jj$-INT	MADGRAPH5_AMC@NLO+HERWIG 7	NNPDF3.0nlo
$WZjj$-EWK	MADGRAPH5_AMC@NLO+PYTHIA 8	NNPDF3.0nlo
$WZjj$-QCD	SHERPA 2.2.2	NNPDF3.0nnlo
$WZjj$-INT	MADGRAPH5_AMC@NLO+PYTHIA 8	NNPDF3.0nlo
$W\gamma jj$	SHERPA 2.2.2	NNPDF3.0nlo
$Z\gamma jj$	SHERPA 2.2.2	NNPDF3.0nlo
$W+$jets	MADGRAPH5_AMC@NLO+PYTHIA 8	N30NLO
$Z+$jets	MADGRAPH5_AMC@NLO+PYTHIA 8	N30NLO A14NNPDF23LO
$t\bar{t}Z$	AMC@NLO+PYTHIA 8	MEN30NLO
$t\bar{t}W$	AMC@NLO+PYTHIA 8	MEN30NLO
tZ	MADGRAPH5_AMC@NLO+PYTHIA 8	NNPDF3.0
ZZ	SHERPA 2.2.2	NNPDF3.0nnlo

Table 10.4: A summary of the Standard Model Monte Carlo samples used as background in the analysis.

Charge misidentification and non-prompt lepton backgrounds are derived from data. For the estimation of the latter, single-lepton MC samples are employed and listed separately in Table 10.5.

Process	**Generator**	**PDF**
$W+$jets	SHERPA 2.2.1	NNPDF3.0nnlo
$Z+$jets	POWHEG-BOX+PYTHIA 8	AZNLOCTEQ6L1
$t\bar{t}$	POWHEG-BOX+PYTHIA 8	NNPDF3.0nlo
Single top	POWHEG-BOX+PYTHIA 8	NNPDF3.0nlo
Single photon	SHERPA 2.2.2	NNPDF3.0nnlo

Table 10.5: A summary of the Standard Model Monte Carlo samples used as prompt lepton sources in the data-driven estimation of the non-prompt and fake background.

Chapter 11

Machine Learning for Classification

This chapter focuses on the application of machine learning, particularly deep neural networks, to distinguish longitudinal polarization modes in electroweak $W^{\pm}W^{\pm}jj$ production against the background processes. Given the subtle kinematic differences between signal and background and the complexity of high-dimensional feature spaces, machine learning provides a powerful framework for extracting weak signals. The selection of input variables used for model training are outlined in Section 11.1, while Section 11.2 describes the structured optimization strategy employed to train and refine the models. The final optimized neural networks are presented in Section 11.3.

11.1 Variables separating longitudinal modes

The polarization of gauge bosons influences the kinematic distributions for the final state particles observed in the laboratory frame (refer to Sec. 3.3.1). Variables such as transverse momenta, invariant masses, angular differences, spatial separations, etc. can carry discriminative information useful for distinguishing purely longitudinal polarization modes ($W_L^{\pm}W_L^{\pm}$) from the backgrounds. Accordingly, an initial set of variables is prepared as input features for training the deep neural networks.

11.1.1 Validation of Kinematic Variable Modelling

To ensure that the DNN trained on the polarization-sensitive input variables can be reliably interpreted, it is crucial to validate that these observables are well modeled in data and Monte Carlo

(MC) simulation within the Signal Region (SR). Since the DNN output depends on the correlations among the input features, any mismodelling could bias the shape of the discriminant and hence the extraction of longitudinal polarization fractions.

The DNN inputs include approximately 50 kinematic and topological observables related to the $W^{\pm}W^{\pm}jj$ electroweak production topology, many of which are designed to separate longitudinally polarized modes from transverse ones. Among these, the dijet invariant mass m_{jj} and rapidity separation Δy_{jj} of the two leading jets are particularly sensitive to the VBS topology and contribute to the separation between longitudinally polarized signal and background processes, such as QCD-induced $W^{\pm}W^{\pm}jj$ or events with non-prompt leptons. Table 11.1 provides a comprehensive overview of all variables considered, highlighting a balanced selection that includes leptonic, jet, dilepton, and dijet observables, as well as $\Delta\eta$, $\Delta\phi$, ΔR, Zeppenfeld variables [161], and invariant masses.

Fig. 11.1 shows the SR distributions of m_{jj} and Δy_{jj} compared between data and MC. Full set of SR variable distributions can be found in Appendix D. The observed agreement across the full range of these distributions, including the high-end tails critical for VBS sensitivity, demonstrates that the MC simulation accurately reproduces the key features of the data.

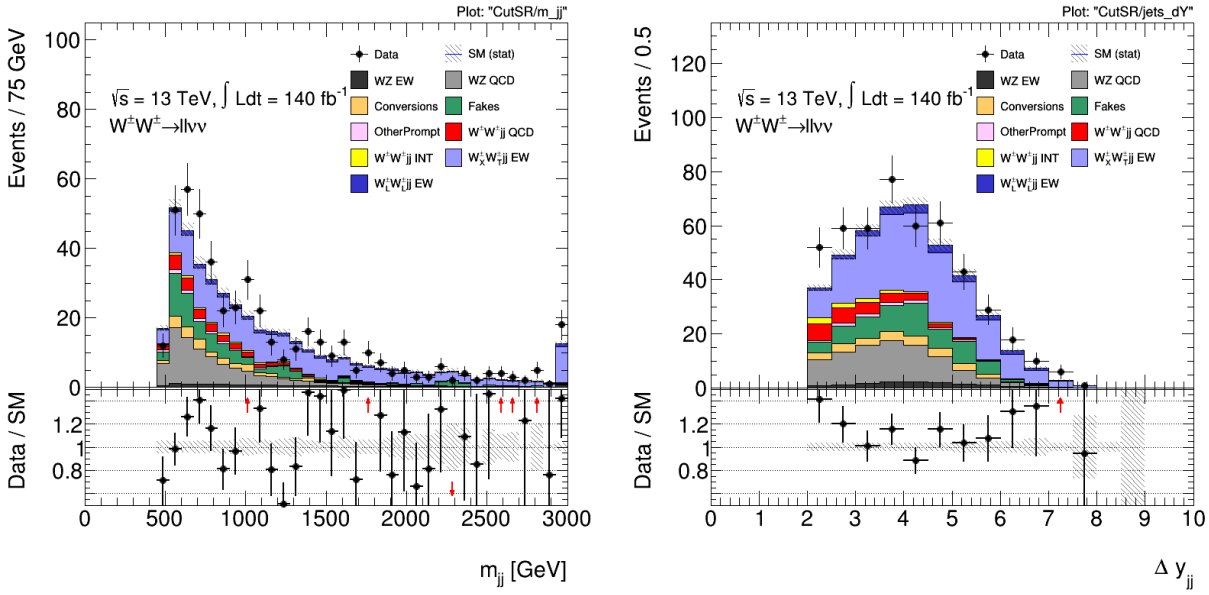


Figure 11.1: Distributions of variables m_{jj} and Δy_{jj} in the Signal Region.

This validation confirms that the shape of the DNN output in the SR is robust and can be reliably used in the final likelihood fit to extract the polarized $W^{\pm}W^{\pm}$ signal and measure the longitudinal polarization fraction.

Variable	Description	Definition
	Jets, Dijet system	
$p_{\mathrm{T}}^{j_1}$	Transverse momentum of leading jet	
$p_{\mathrm{T}}^{j_2}$	Transverse momentum of subleading jet	
n_{jets}	Number of jets	
η_{j_1}	Pseudorapidity of leading jet	
η_{j_2}	Pseudorapidity of subleading jet	
$\Delta\phi_{jj}$	Azimuthal angle difference b/w leading and subleading jets	
$\Delta\eta_{jj}$	Pseudorapidity difference b/w leading and subleading jets	
ΔR_{jj}	Spatial separation b/w leading and subleading jets	$\sqrt{(\Delta\phi_{jj})^2+(\Delta y_{jj})^2}$
m_{jj}	Invariant mass of dijet system	
	Leptons, Dilepton system	
$p_{\mathrm{T}}^{\ell_1}$	Transverse momentum of leading lepton	
$p_{\mathrm{T}}^{\ell_2}$	Transverse momentum of subleading lepton	
E^{ℓ_1}	Energy of leading lepton	
E^{ℓ_2}	Energy of subleading lepton	
ID_{ℓ_1}	Flavor of leading lepton	
ID_{ℓ_2}	Flavor of subleading lepton	
$m_T^{\ell_1}$	Transverse mass of leading lepton [160]	$\sqrt{(\sum_i E_i)^2-(\sum_i p_{z,i})^2}$
$m_T^{\ell_2}$	Transverse mass of subleading lepton [160]	
η_{ℓ_1}	Pseudorapidity of leading lepton	
η_{ℓ_2}	Pseudorapidity of subleading lepton	
$m_{\ell\ell}$	Invariant mass of dilepton system	
$p_{\mathrm{T}}^{\ell\ell}$	Transverse momentum of dilepton system	
$\Delta\phi_{\ell\ell}$	Azimuthal angle difference b/w leading and subleading leptons	
$\Delta\eta_{\ell\ell}$	Pseudorapidity difference b/w leading and subleading leptons	
$\Delta R_{\ell\ell}$	Spatial separation b/w leading and subleading leptons	
	Dijet and Dilepton vectors	
$\Delta\phi_{\ell\ell-jj}$	Azimuthal angle difference b/w dilepton and dijet systems	$\cos^{-1}(\cos(\lvert\Delta\phi_{\ell\ell}-\Delta\phi_{jj}\rvert))$
$\Delta\phi_{jj-\ell\ell}$	Azimuthal angle difference b/w dijet and dilepton systems	$\Delta\phi_{jj}-\Delta\phi_{\ell\ell}$
$\Delta\eta_{jj-\ell\ell}$	Pseudorapidity difference b/w dijet and dilepton systems	
$\Delta p_{\mathrm{T}}^{jj-\ell\ell}$	Transverse momentum difference b/w dijet and dilepton systems	
$\Delta R_{\ell\ell-j_1}$	Spatial separation b/w leading jet and dilepton systems	
$\Delta R_{\ell\ell-j_2}$	Spatial separation b/w subleading jet and dilepton systems	
	Missing transverse energy	
$E_{\mathrm{T}}^{\mathrm{miss}}$	Missing transverse energy (MET)	
$\Delta\phi_{\ell\ell-E_{\mathrm{T}}^{\mathrm{miss}}}$	Azimuthal angle difference b/w dilepton system and MET	
$\Delta\phi_{j_1-E_{\mathrm{T}}^{\mathrm{miss}}}$	Azimuthal angle difference b/w leading jet and MET	
$\Delta\phi_{\ell_1-E_{\mathrm{T}}^{\mathrm{miss}}}$	Azimuthal angle difference b/w leading lepton and MET	
$\Delta\phi_{\ell_2-E_{\mathrm{T}}^{\mathrm{miss}}}$	Azimuthal angle difference b/w subleading lepton and MET	
	Zeppenfeld variables (Centrality) [161]	
$z_2^{\ell_1}$	Single-object Zeppenfeld variable of leading lepton	$\lvert(\eta_{\ell_1}-0.5\cdot(\eta_{j_1}+\eta_{j_2}))/\Delta\eta_{jj}$
$z_2^{\ell_2}$	Single-object Zeppenfeld variable of subleading lepton	
$max(z_2)$	Higher of the single-object Zeppenfeld variables of two leading leptons	$max(z_2^{\ell_1}, z_2^{\ell_2})$
$z_1^{\ell\ell}$	Multi-object Zeppenfeld variable of dilepton system	$\eta_{\ell\ell}-0.5\cdot(\eta_{j_1}+\eta_{j_2})$
$\lvert z_1^{\ell\ell}\rvert$	Modulus of multi-object Zeppenfeld variable of dilepton system	
	η,ϕ	
$\Delta\phi_{\ell_1-j_1}$	Azimuthal angle difference b/w leading lepton and leading jet	
$\Delta\phi_{\ell_1-j_2}$	Azimuthal angle difference b/w leading lepton and subleading jet	
$\Delta\phi_{\ell_2-j_1}$	Azimuthal angle difference b/w subleading lepton and leading jet	
$\Delta\phi_{\ell_2-j_2}$	Azimuthal angle difference b/w subleading lepton and subleading jet	
$\Delta\eta_{\ell_1-j_1}$	Pseudorapidity difference b/w leading lepton and leading jet	
$\Delta\eta_{\ell_1-j_2}$	Pseudorapidity difference b/w leading lepton and subleading jet	
$\Delta\eta_{\ell_2-j_1}$	Pseudorapidity difference b/w subleading lepton and leading jet	
$\Delta\eta_{\ell_2-j_2}$	Pseudorapidity difference b/w subleading lepton and subleading jet	
	Misc	
$p_{\mathrm{T}}(\ell_1\ell_2)/p_{\mathrm{T}}(j_1j_2)$	Ratio of transverse momenta of two leading leptons & jets [162]	$(p_{\mathrm{T}}^{\ell_1}\cdot p_{\mathrm{T}}^{\ell_2})/(p_{\mathrm{T}}^{j_1}\cdot p_{\mathrm{T}}^{j_2})$
m_T^{WW}	Invariant mass of diboson system in the transverse plane [160]	

Table 11.1: Complete list of variables considered in this study. Definitions given for one instance apply analogously to all similar variables.

11.1.2 Variable Correlations

The initial set of variables includes a wide range of features describing the final state particles, comprising 50 distinct variables, as listed in Table 11.1. However, some of these variables may be highly correlated, leading to redundancy. To address this, a correlation matrix is constructed, displaying the correlation coefficients that quantify the strength and direction of linear relationships between pairs of variables:

$$\rho_{X,Y} = \frac{\mathrm{cov}(X,Y)}{\sigma_X \sigma_Y} = \frac{\sum_{i=1}^{n}(X_i - \bar{X})(Y_i - \bar{Y})}{\sqrt{\sum_{i=1}^{n}(X_i - \bar{X})^2}\sqrt{\sum_{i=1}^{n}(Y_i - \bar{Y})^2}}, \tag{11.1}$$

where $\rho_{X,Y}$ represents the sample Pearson correlation coefficient between variables X and Y, defined using the sample means, standard deviations, and covariance of X and Y. $\rho_{X,Y}$ ranges from -1 to +1, where -1 indicates a perfect negative correlation, +1 indicates a perfect positive correlation, and 0 signifies no linear correlation.

The correlation matrix, as shown in Fig. 11.2, reveals four pairs of variables exhibiting strong (anti-)correlations exceeding 80%. Applying a conservative threshold of 95%, only one pair – ΔR_{jj} and $\Delta\eta_{jj}$ – shows a correlation as high as 96%. Since η is a fundamental variable while R is a derived quantity, ΔR_{jj} is dropped from the initial set. The resulting set of 49 variables serves as the input for training neutral networks to distinguish $W_L^{\pm}W_L^{\pm}$ events.

11.2 Classification using Deep Neural Networks

A deep neural network (DNN) is a type of artificial neural network with multiple hidden layers between the input and output layers (Fig. 11.3). DNNs are designed to automatically learn and represent complex patterns and features from data, making them well-suited for various machine learning tasks. The input layer receives raw data, with each neuron/unit corresponding to a specific feature. These features are progressively transformed through one or more hidden layers. These layers consist of neurons which perform linear operations on their respective input data. In this analysis, DNNs are used primarily for binary classification through supervised learning, where the dataset is typically split into a training set for fitting model parameters, a validation set for tuning hyperparameters and mitigating overfitting, and a test set for unbiased evaluation of the final model.

Hidden layers are activated using functions that introduce non-linearity into the network, enabling it to model complex relationships in data. Some activation functions are shown in Fig. 11.4. Rectified Linear Unit or ReLU returns element-wise $max(x,0)$ simply like a half-wave rectifier. It

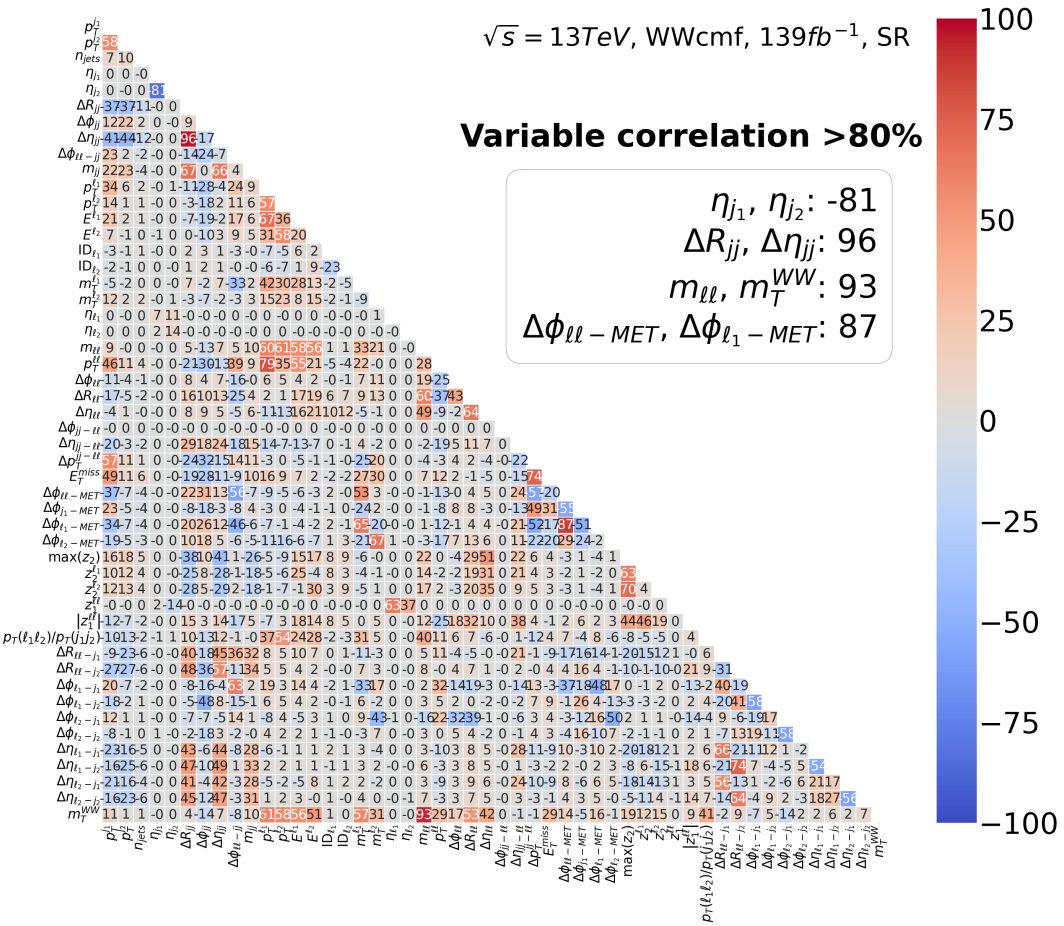


Figure 11.2: Correlation matrix displaying the correlation coefficients (in %) between the variables.

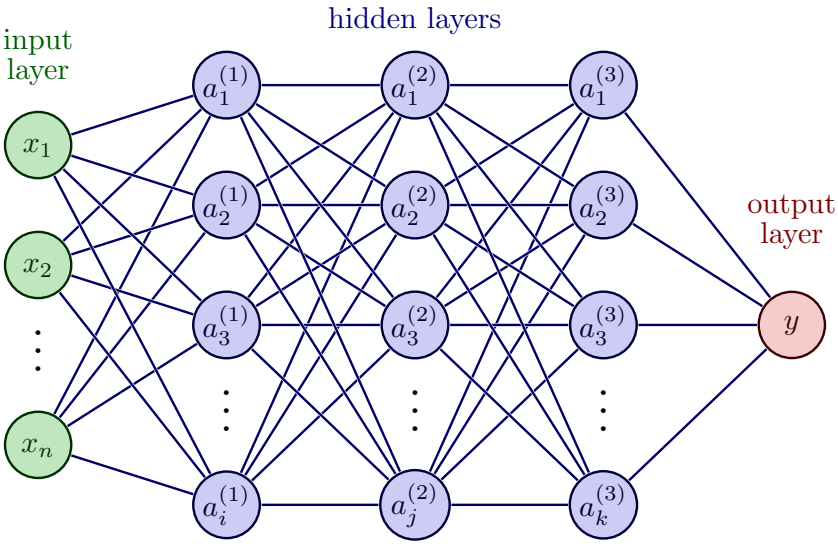


Figure 11.3: Representative DNN for classification where x_n are the n input features, $a_p^{(q)}$ represents the q^{th} hidden layer with $p = i, j, k$ neurons in the three respective layers shown and the output layer has node y which classifies the data into one of the two classes. Figure adapted from [27].

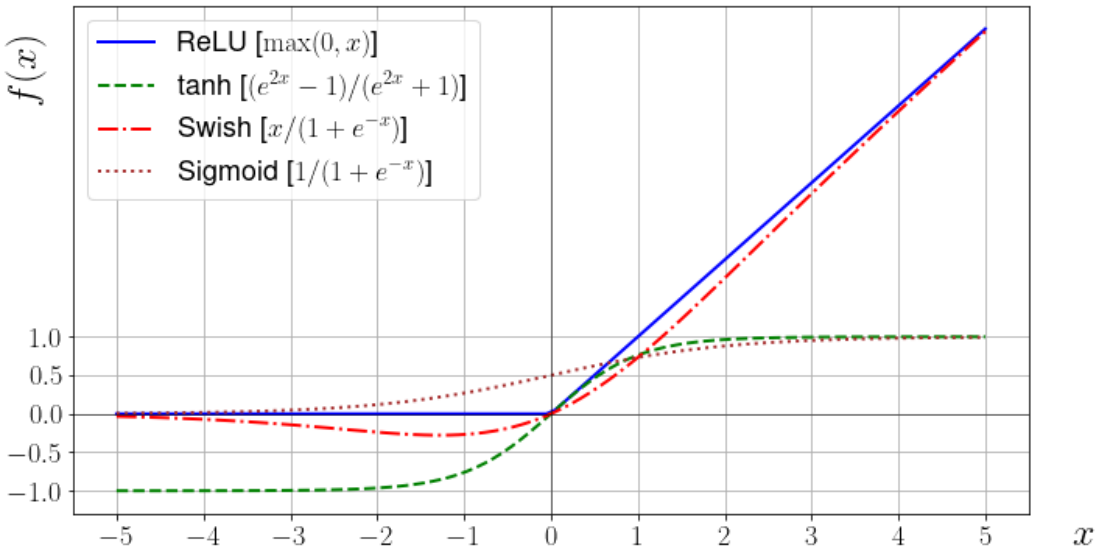


Figure 11.4: Illustration of commonly used activation functions that introduce non-linearity into neural networks, enabling them to model complex patterns.

has sparsity property while suffering less from diminishing gradient flow [163]. The output layer uses sigmoid activation function,

$$\sigma(x) = \frac{1}{1+e^{-x}}, \tag{11.2}$$

ensuring the output between 0 and 1 while maintaining non-linearity of the model. Neurons in adjacent hidden layers are connected and a weight is accociated with each connection corresponding to their respective strength. These are learned during training in addition to biases. Each neuron has a bias term which allows for shifts and translations in the activation functions.

Overfitting to data is prevented by introducing dropout regularization technique [164] and callbacks like early stopping and model checkpoint. Dropout deactivates a fraction of neurons while training. Early stopping halts the training when the model's performance on a validation set stops improving and a model checkpoint is created where the weights of the best model are saved.

One of the metrics to evaluate the performance of a network is a loss or cost function. It quantifies how close the model's predictions are to the actual values. Lower the loss function, closer are the predictions to the original values. Binary cross-entropy or log loss function is commonly used for binary classifications. It is given by,

$$\log\text{loss} = -\frac{1}{N}\sum_{i=1}^{N}\left[y_i \cdot \log(P(y_i)) + (1-y_i)\cdot\log(1-P(y_i))\right], \tag{11.3}$$

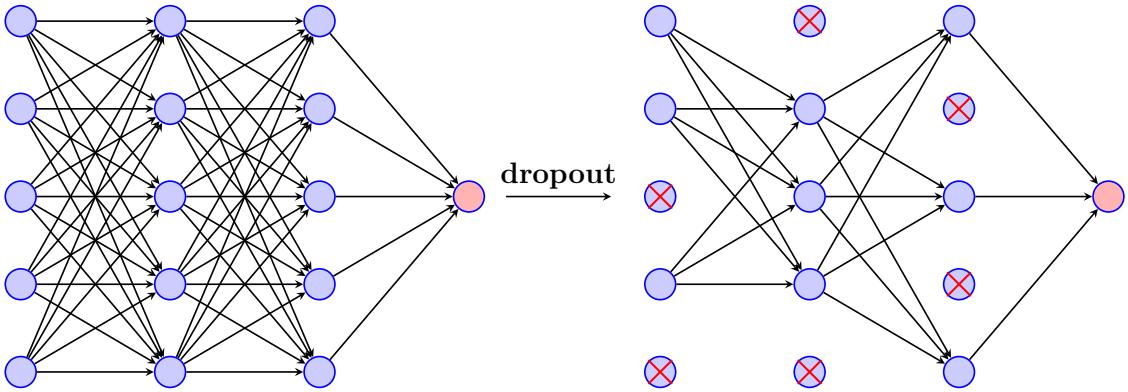


Figure 11.5: The effect of dropout regularization technique is shown where 40% units from the hidden layers are dropped at random during training *(dropout rate = 0.4)*. Fig. adapted from [27].

where probability of the two classes are given by $P(y_i)$ and $(1-P(y_i))$.

Adam optimizer algorithm [165] is used to minimize the loss function by adjusting weights and biases of the model. It can be used as an alternative/extension to stochastic gradient descent for computational efficiency and other advantages. The training is done over the entire dataset in iterations called epochs. In each epoch, the training or testing is done in batches and batch size gives the number of samples per gradient update.

In this analysis, DNNs are trained for binary classification considering the diboson frame or *WWcmf*, where the signal is defined as events containing longitudinally polarized modes $W_L^{\pm}W_L^{\pm}$, and the background comprises other polarization modes as well as the SM background processes. The Signal Region (as defined in Section 7.2.1) consists of approximately 22,000 signal events and 250,000 background events. Background processes (as detailed in Chapter 8) include $W_T^{\pm}W_L^{\pm}$ and $W_T^{\pm}W_T^{\pm}$ polarization modes, $W^{\pm}W^{\pm}$ QCD and interference, WZ (QCD and EW6), ZZ, V/γ, charge flip, triboson processes, ttX, and fakes from W+jets and semi-leptonic $t\bar{t}$ decays. The input features comprise variables of final state particles in the laboratory frame. Prior to training, each variable is standardized to have zero mean and unit variance in the pre-processing step. Monte Carlo event weights are applied during both pre-processing and training to account for the correct cross sections. To mitigate class imbalance – given the relative rarity of the signal – the signal dataset is scaled such that its sum of weights matches that of the background dataset at the time of training. This scaling helps reduce bias during model training. The full dataset is then split into training, validation, and testing subsets in a 3:1:1 ratio.

11.2.1 Hyperparameter Optimization

Hyperparameters are configurations and settings that determine the DNN architecture and training behaviour. Hyperparameter optimization plays a key role in achieving the best performance of a DNN by improving the precision and accuracy of a model. One has to tune a large number of hyperparameters which makes manual tuning time-consuming and suboptimal. Libraries like `Optuna` [166] automate this process and can efficiently search through a range of hyperparameters, automatically select the best values, and iteratively improve the model's performance.

The hyperparameters are optimized with respect to two key metrics. During training, the validation loss is minimized on a per-epoch basis to ensure good generalization. After training, the model's performance is further evaluated by maximizing the statistical significance (Z)[1] of the signal, guiding the final selection of hyperparameter values:

$$\begin{aligned} q_0 = -2\ln\lambda(0) = -2\ln\frac{L(\mu=0)}{L(\mu=1)} = -2(\ln_0 - \ln_1)\,. \\ Z = \sqrt{q_0}\,. \end{aligned} \tag{11.4}$$

Here, $L(\mu)$ denotes the likelihood function for signal strength μ, $\ln_0 \equiv \ln L(\mu=0)$ and $\ln_1 \equiv \ln L(\mu=1)$ are the log-likelihood values under the background-only and signal-plus-background hypotheses, respectively, q_0 is the profile likelihood ratio test statistic for $\mu=0$, and Z is the corresponding local significance in units of Gaussian standard deviations (σ). The statistical formalism regarding likelihood estimates is further detailed in Section 12.1.

Some parameters are manually tuned, while the remaining hyperparameters are optimized through 1000 iterations of automated grid search. The hidden layers are configured with a *random normal* kernel initializer, *ReLU* activation functions, and the *Adam* optimizer. The output layer consists of a single neuron with a *random uniform* kernel initializer and a *sigmoid* activation function. The hyperparameters optimized using `Optuna` grid search include the number of hidden layers, number of neurons per layer, presence of optional dropout layers, dropout rate, learning rate, and batch size (refer to Table 11.2).

Hyperparameter optimization is performed twice during the analysis. The first round is conducted using the initial set of 49 input variables. A second round is then carried out using a reduced subset of high-ranking variables (refer to Sec. 11.2.2), leading to the final optimized DNN model.

[1] The expected significance is calculated for the luminosity of 139fb^{-1} for the Run 2 LHC dataset.

Hyperparameter	Optimization Range	Sampling
No. of Hidden layers	$[3, 8]$	In steps of 1
Dropout layers	True/False	Optionally inserted after every hidden layer
Dropout Rate	$[0.05, 0.40]$	In steps of 0.05
No. of Units per layer	$[16, 32, 64, 128, 256, 512]$	In exponents of 2
Learning Rate (Adam)	$[10^{-5}, 10^{-2}]$	Logarithmic
Batch Size	$[16, 32, 64, 128, 256, 512]$	In exponents of 2

Table 11.2: DNN hyperparameters optimized using `Optuna`.

11.2.2 Input Feature Ranking

The *permutation feature importance* algorithm [167] ranks input features of a neural network by evaluating the impact of permuting these features. It involves creating modified input datasets where values for a specific feature (denoted as j) are systematically swapped with each other across the entire dataset. This process does not introduce new values but effectively disrupts the association of the j value with a particular input observable. By breaking this association, the algorithm also disrupts the correlations between the j value and other input observables. This methodology helps in identifying the significance of input features without requiring the retraining of the neural network, making it computationally less extensive and a valuable tool in feature selection and model interpretability.

The algorithm takes as inputs a trained model f, an input dataset X, and a figure-of-merit measure L. It evaluates the model's performance using the original performance measure

$$e^{\text{orig}} = L(f(X)),$$

where f is applied to the input dataset X. To assess the model's reliance on individual input features, it computes the permuted performance measure

$$e_j^{\text{perm}} = L(f(X_j^{\text{perm}})),$$

where the j-th feature values in X (denoted as X_j^{perm}) are randomly shuffled. The Model Reliance or Feature Importance (FI) is then quantified as

$$FI_j = \frac{e_j^{\text{perm}}}{e_j^{\text{orig}}}, \tag{11.5}$$

where FI values indicate the model's reliance on specific features. An FI value of 1 implies no reliance on the feature, while a value much greater than 1 indicates heavy reliance. FI values less than 1 suggest less reliance than random chance, making interpretation challenging. To estimate

the error in FI, the shuffling process is repeated multiple times, and statistics such as the mean(FI_j) and standard deviation (ΔFI_j) are computed. This error estimation provides insights into the stability and robustness of the feature importance assessments.

The trained input model f is obtained from the first round of hyperparameter optimization. It is trained using the set of 49 input variables, denoted by X. The figure-of-merit measure L is chosen to be the validation loss. The resulting feature importance ranking is presented in Fig. 11.6. The shuffling process is performed 500 times to ensure sufficient statistics. To assess how the model responds to progressively stricter feature selection, a few FI thresholds are chosen. By applying thresholds on FI values of 1.04, 1.06, and 1.07, the top 20, 10, and 5 most important variables are selected, respectively. The reduced feature sets are subject to a second round of hyperparameter optimization using `Optuna`.

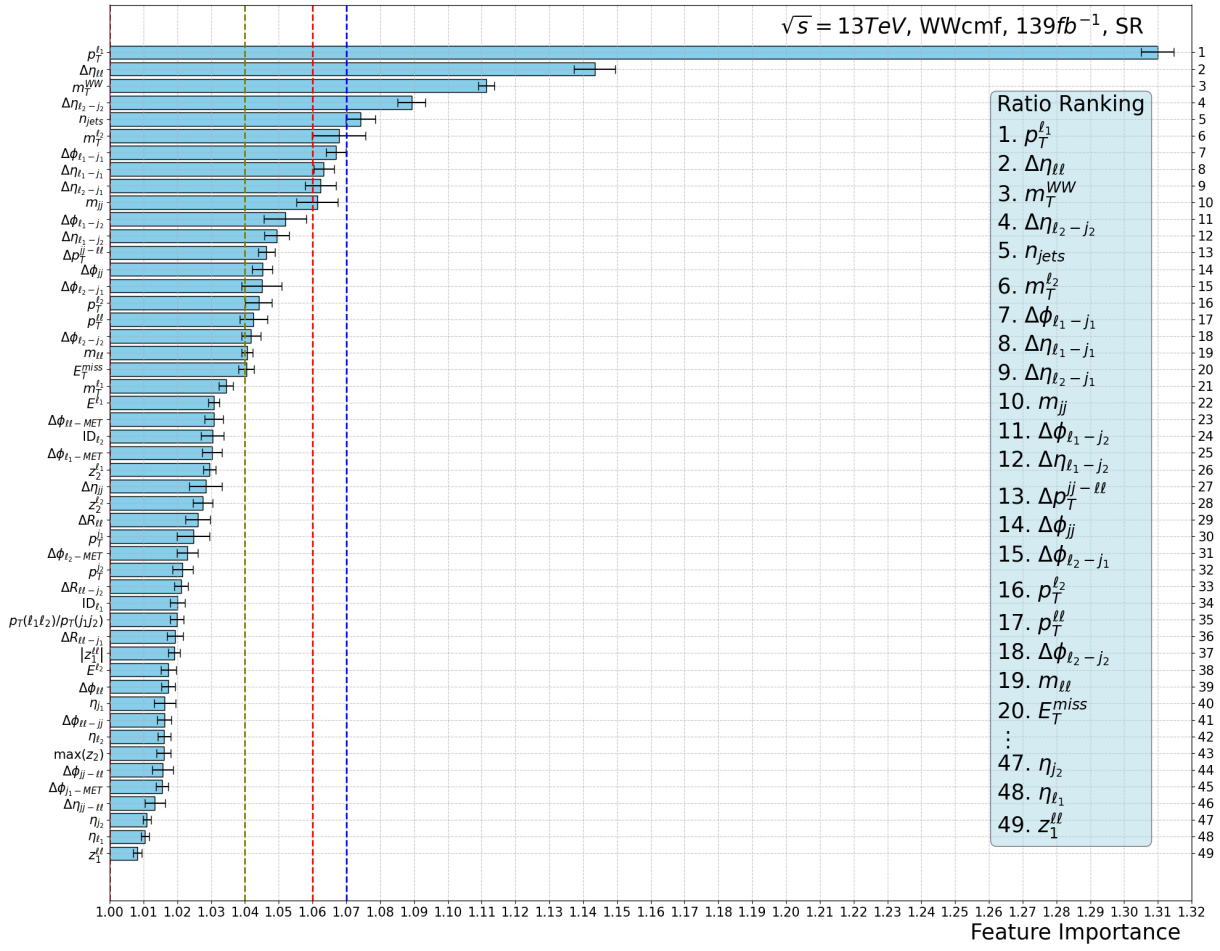


Figure 11.6: Permutation feature importance algorithm showing ranks of input features following the first round of hyperparameter optimization. Each variable is permuted 500 times. To explore varying levels of strictness in feature selection, FI thresholds of 1.04, 1.06, and 1.07 are applied.

11.3 DNN Optimization Results

The first round of hyperparameter optimization yields a best-performing model with a significance of $Z = 2.24$, and its performance is shown in Fig. 11.7. This DNN is subsequently used to rank the input features, enabling a reduction in the input variable set. Based on the feature importance ranking shown in Fig. 11.6, three different thresholds are considered – reflecting varying degrees of strictness in feature selection. A second round of hyperparameter optimization is then performed for each of these three reduced input sets. The resulting significance values for models trained on the top 5, 10, and 20 variables are $Z = 1.25$, 1.69, and 2.12, respectively. Their performances are shown in Fig. 11.8. Details about the various model architectures and best hyperparameters are shown in Table 11.3, while additional details can be found in Appendix C.

Hyperparameter	**49-var DNN**	**20-var DNN**	**10-var DNN**	**5-var DNN**
No. of Hidden layers	8	8	3	5
Dropout layers	$[F,F,F,T,T,F,T,F]$	$[F,F,F,T,F,F,F,F]$	$[F,F,T]$	$[T,F,F,F,F]$
Dropout Rate	$[0.35,0.35,0.1,0.05,$ $0.25,0.35,0.2,0.25]$	$[0.35,0.35,0.1,0.35,$ $0.3,0.4,0.15,0.3]$	$[0.3,0.15,0.25]$	$[0.15,0.35,0.1,0.1,0.2]$
No. of Units per layer	$[512,32,512,16,$ $16,256,512,512]$	$[64,256,512,128,$ $512,16,16,256]$	$[512,512,256]$	$[256,128,128,512,256]$
Learning Rate (Adam)	9.68×10^{-5}	1.16×10^{-5}	1.29×10^{-5}	3.32×10^{-5}
Batch Size	128	128	128	128
Significance (Z)	2.24	2.12	1.69	1.25

Table 11.3: Best hyperparameter configurations for each DNN architecture, obtained from 1000 `Optuna` trials per model, selected to maximize the significance Z as defined in Eq. 11.4.

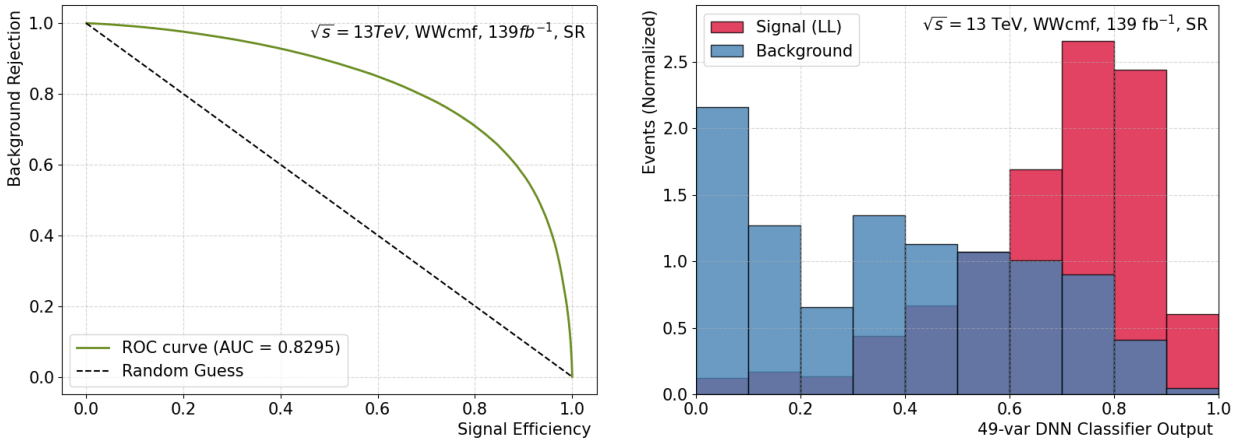


Figure 11.7: ROC curve (left) and DNN output distribution (right) for signal and background, highlighting the 49-variable model's classification performance and discriminative power.

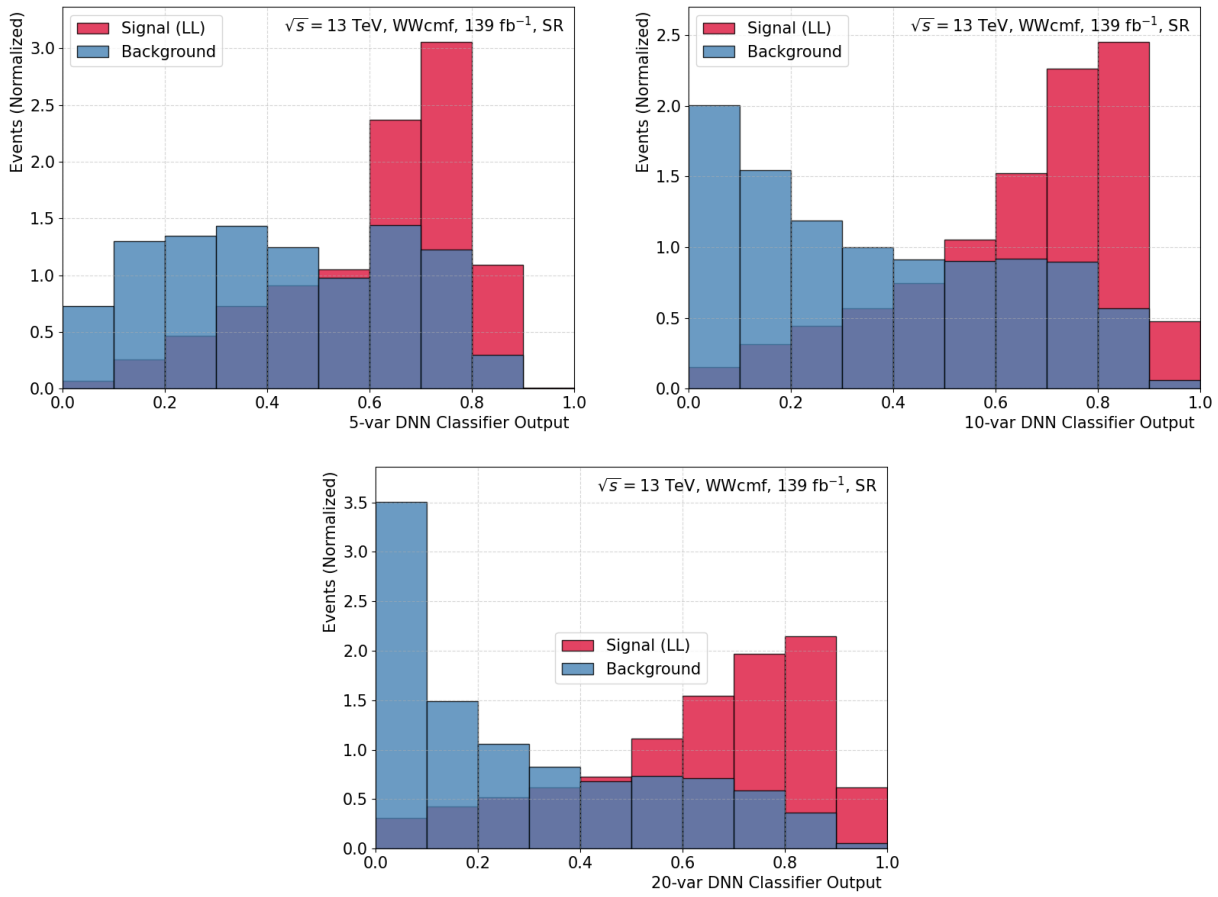


Figure 11.8: Comparison of DNN classifier outputs after second round of hyperparameter optimization for models trained on the top 5, 10, and 20 input variables.

These results strongly support the choice of the 20-variable DNN architecture. Although 29 input variables are removed relative to the original 49-variable model, the achieved expected significance remains comparable, demonstrating that the additional variables carry limited discriminating power. The reduced input space also provides clear advantages in the evaluation and propagation of systematic uncertainties while performing fits to extract the signal. In addition, the 20-variable model delivers superior signal–background separation compared to the networks trained with only 5 or 10 variables, validating it as the optimal choice for the analysis. Fig. 11.9 shows the separating power of the 20-variable DNN in the SR.

To summarize, the DNN-based classification framework is executed through a structured four-step workflow designed to optimize performance and reduce redundancy. The process begins with a variable correlation study, where the initial set of 50 input variables is pruned by removing those exhibiting pairwise linear correlations exceeding 95%, thereby enhancing model robustness. Next, a deep neural network is trained using the full variable set, with its hyperparameters optimized through an initial round of 1000 `Optuna` trials. The model yielding the highest significance is retained. In the third stage, this model is used to assess the relative importance of input fea-

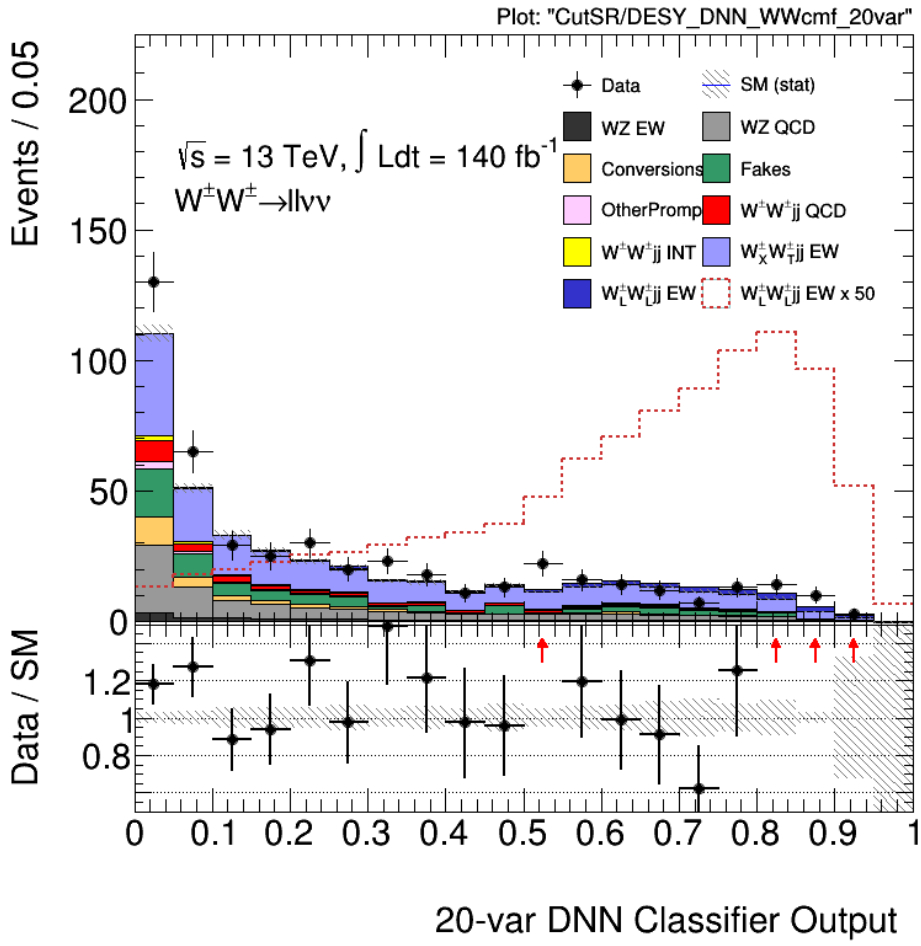


Figure 11.9: DNN classifier output in the signal region for the 20-variable model. The signal is additionally shown as a red dashed line scaled by a factor 50 to enhance visibility relative to the background.

tures via the Permutation Feature Importance method. Based on the resulting rankings, reduced feature sets are constructed. A second round of hyperparameter optimization — again using 1000 `Optuna` trials — is then performed for each reduced set. The best-performing model from each case is selected, ensuring that the final classifier balances complexity with predictive power. This workflow establishes a robust and interpretable approach to feature selection and DNN optimization. As a result, the 20-variable DNN is chosen as the discriminator DNN for further analysis.

Chapter 12

Extraction of $W_L^{\pm}W_L^{\pm}$ polarization fraction

The extraction of the quantity of interest — $W_L^{\pm}W_L^{\pm}$polarization fraction — is performed via a maximum-likelihood fit to the distribution of the DNN output, which serves as a powerful discriminant between signal and background processes. The 20-variable DNN, as decribed in Chapter 11, is the one chosen for this analysis. When multivariate discriminants, such as DNNs, are employed to enhance separation power, the final statistical inference step must rigorously combine this information into a likelihood model that can yield quantitative statements about signal strength, significance, and confidence limits.

The chapter covers the statistical formalism, fit strategy, expected and observed sensitivities, culminating in the extraction of the fraction of doubly longitudinally-polarized W bosons in EW $W^{\pm}W^{\pm}jj$ (f_{LL}) and estimation of the corresponding fiducial cross sections. `TRExFitter`[1] — a framework for binned template profile likelihood fits — is employed for fitting and limit-setting, using `HistFactory` [168], `RooFit` [169] and `RooStats` [170].

12.1 Statistical Analysis

Making sense of observations in particle physics requires a rigorous statistical framework, most often realized through *statistical hypothesis testing*. In hypothesis testing, we compare two competing assumptions about the data: the *background-only hypothesis* (the null hypothesis) and an *alternative hypothesis* that includes both background and signal contributions. The degree to which the observed data agree with the null hypothesis is quantified by the *p-value*, which represents the probability of observing data at least as incompatible with the null hypothesis as the actual

[1] stands for Top Related Experiment Fitter

observation. In other words, smaller p-values indicate a lower likelihood that the observed excess arises from background fluctuations alone.

When the p-value falls below a chosen threshold, the background-only hypothesis is rejected. In high-energy physics, this probability is typically expressed using a *significance*, Z, which converts the p-value into the equivalent number of standard deviations of a Gaussian distribution:

$$Z = \phi^{-1}(1-p), \tag{12.1}$$

where ϕ^{-1} denotes the inverse of the cumulative distribution function of the standard normal distribution. Conventionally, in LHC analyses, a 3σ significance is required to claim *evidence* for a process, while a 5σ result constitutes an *observation*.

The significance and normalization of the longitudinally polarized component are obtained from a profile likelihood fit. The methodology used here follows the standard statistical framework of LHC analyses, as detailed in Ref. [171]. A brief overview of the utilized concepts is presented in this section.

12.1.1 Profile Likelihood Fit

Statistical inference in this work is performed using a *profile likelihood fit*, which is a maximum-likelihood method that incorporates systematic uncertainties and correlations across analysis regions.

If s denotes the expected MC signal yield and b represents the estimated background, then the total predicted event yield v in a bin is written as

$$v = \mu s + b, \tag{12.2}$$

where μ is the *signal strength* parameter. A value of $\mu = 1$ corresponds to the SM prediction, while $\mu = 0$ represents the background-only hypothesis.

The signal strength μ is treated as the *parameter of interest (POI)*, and all other quantities that affect the yield are treated as *nuisance parameters*. These nuisance parameters, collectively denoted by θ, encode the effects of systematic and statistical uncertainties and can be divided into the following groups:

- θ_α: experimental and theoretical systematic uncertainties,
- θ_γ: statistical uncertainties on background estimates,
- θ_τ: free normalization parameters for background processes.

Thus, the total expected yield in each bin can be written as $v(\mu,\theta) = \mu s(\theta) + b(\theta)$.

Given n observed events, the likelihood function for a binned distribution is defined as the product of Poisson probabilities across all bins:

$$L(\mu,\theta|n) = \prod_{\text{bins}} P(n|v(\mu,\theta)). \tag{12.3}$$

The profile likelihood is obtained by maximizing this function with respect to all nuisance parameters for each value of μ, producing a likelihood curve as a function of the signal strength.

To prevent the fit from taking unphysical or extreme values for nuisance parameters, additional constraint terms are introduced based on prior knowledge from auxiliary measurements. Systematic uncertainties (θ_α) are modeled using Gaussian constraint terms $G(\theta_\alpha|0,1)$, where $\pm1\sigma$ corresponds to the up and down variations of each uncertainty. This ensures that nuisance parameters remain close to their prior expectations unless the observed data strongly favor a deviation.

Statistical uncertainties in the background predictions (θ_γ) are modeled with Poisson distributions $P(\theta_\gamma|b)$. Background normalization factors (θ_τ) are treated as free-floating parameters without constraints, allowing the fit to adjust their values based on the observed data.

The complete likelihood function can therefore be written as:

$$L(\mu,\theta|n) = \prod_{\text{bins}} P(n|v(\mu,\theta)) \prod_{\text{bins}} P(\theta_\gamma|b) \prod_{\text{syst.}} G(\theta_\alpha|0,1). \tag{12.4}$$

The best-fit signal strength $\hat{\mu}$ is obtained by maximizing this likelihood. The fitted signal and background yields, known as *post-fit yields*, represent the configuration that best describes the observed data.

Pulls and Impacts of Nuisance Parameters

To assess how the fit modifies the nuisance parameters compared to their pre-fit values, the *pull* of each parameter is defined as:

$$\text{pull}(\theta) = \frac{\hat{\theta} - \theta_0}{\Delta\theta}, \tag{12.5}$$

where $\hat{\theta}$ is the post-fit value, and $\theta_0 \pm \Delta\theta$ denote the pre-fit estimate and its uncertainty. A pull significantly different from zero indicates that the data prefer a different value than the *prior*. When the post-fit uncertainty becomes much smaller than the pre-fit uncertainty ($\pm1\sigma$), the corresponding parameter is said to be *overconstrained*, implying that the data provide tighter constraints than

the auxiliary measurements.

The *impact* of each nuisance parameter on the fitted signal strength is quantified by varying it within its uncertainty and recording the resulting shift in $\hat{\mu}$:

$$\text{impact}(\theta) = \Delta\mu = \hat{\hat{\mu}}_{\hat{\theta}\pm\Delta\theta,\Delta\hat{\theta}} - \hat{\mu}\,, \tag{12.6}$$

where $\hat{\hat{\mu}}$ is the POI's value at the post-fit value of θ. The pre- and post-fit uncertainties are used while calculating their respective impacts. This measure helps identify the uncertainties that most strongly influence the final result.

12.1.2 Hypothesis Testing

To determine whether the data are compatible with the background-only scenario ($\mu = 0$), the analysis employs the *profile likelihood ratio* as the test statistic:

$$q_\mu = -2\ln\frac{L(\mu|\hat{\theta}_\mu)}{L(\hat{\mu}|\hat{\theta})} = -2\ln\lambda(\mu)\,, \tag{12.7}$$

where $\hat{\theta}_\mu$ are the nuisance parameters that maximize the likelihood for a fixed μ, while $\hat{\mu}$ and $\hat{\theta}$ correspond to the global maximum of the likelihood function.

According to *Wilks' theorem* [172], the distribution of q_μ approaches a chi-squared distribution with one degree of freedom in the asymptotic limit. Large values of q_μ imply greater disagreement between the observed data and the tested hypothesis. The level of incompatibility is expressed in terms of the *significance*, which, under the asymptotic approximation, can be written as:

$$Z = \sqrt{q_\mu}. \tag{12.8}$$

The discovery significance, Z_0, can be written as

$$Z_0 = \sqrt{q_0}, \quad \text{where} \quad q_0 = \begin{cases} -2\ln\lambda(0) & \hat{\mu} \geq 0\,, \\ 0 & \hat{\mu} < 0\,. \end{cases} \tag{12.9}$$

This statistic was used in DNN training to evaluate model performance during hyperparameter optimization, as detailed in Section 11.2.1.

12.1.3 Setting Upper Limits

In the absence of a statistically significant signal, it is important to determine how large the signal contribution could be, given the observed data. This is achieved by setting an *upper limit* on the signal strength parameter, μ, or equivalently on the cross section of the process under study. The limit defines the maximum signal rate compatible with the data at a chosen confidence level (CL), typically 95%.

Upper limits are evaluated using the *modified frequentist approach*, commonly referred to as the CL_s method [173]. This approach employs a test statistic based on the profile likelihood ratio to compare the data's compatibility with the signal-plus-background and background-only hypotheses. To ensure correct coverage and avoid unphysical signal estimates, a modified test statistic $\tilde{q}_\mu$ is defined as:

$$\tilde{q}_\mu = \begin{cases} -2\ln \dfrac{L(\mu \mid \hat{\theta}_\mu)}{L(0 \mid \hat{\theta}_0)}, & \hat{\mu} < 0, \\ -2\ln \dfrac{L(\mu \mid \hat{\theta}_\mu)}{L(\hat{\mu} \mid \hat{\theta})}, & 0 \leq \hat{\mu} \leq \mu, \\ 0, & \hat{\mu} > \mu. \end{cases} \tag{12.10}$$

Here, $L(\mu \mid \hat{\theta}_\mu)$ is the likelihood maximized for a fixed signal strength μ, while $L(0 \mid \hat{\theta}_0)$ and $L(\hat{\mu} \mid \hat{\theta})$ are the maxima for the background-only and global (unconstrained) fits, respectively. This piecewise definition ensures that negative signal strength estimates are treated consistently and prevents unphysical signal contributions in the calculation of upper limits.

The probability distributions of $\tilde{q}_\mu$ are evaluated under both hypotheses: p_{s+b}, the probability of obtaining a value of $\tilde{q}_\mu$ at least as large as that observed, assuming the signal-plus-background hypothesis, and p_b, the probability of obtaining a similar or larger $\tilde{q}_\mu$ under the background-only hypothesis. The corresponding CLs are defined as:

$$\mathrm{CL}_{s+b} = 1 - p_{s+b}, \qquad \mathrm{CL}_b = 1 - p_b, \tag{12.11}$$

and the modified confidence level $\mathrm{CL_s}$ is given by:

$$\mathrm{CL_s} = \frac{\mathrm{CL}_{s+b}}{\mathrm{CL}_b}. \tag{12.12}$$

This definition ensures a conservative limit, avoiding the exclusion of signal hypotheses in cases where the background model fluctuates downward.

The *95% confidence level upper limit* on the signal strength, μ_{95}, is defined as the largest value

of μ for which $\mathrm{CL_s} \geq 0.05$. In practice, the distributions of $\tilde{q}_\mu$ are obtained either through asymptotic approximations or by performing pseudo-experiments to build the expected and observed limits. In this analysis, an asymptotic approach is used in which the upper limit (UL) is computed as $\mu_{95} = \mu + 1.64\Delta\mu$.

Expected limits are derived under the assumption of the background-only hypothesis, and the corresponding $\pm 1\sigma$ and $\pm 2\sigma$ variations represent the ranges of possible outcomes due to statistical fluctuations. The observed limit, derived from real data, is then compared to this expectation. If no significant excess is found, the resulting upper limit constrains the possible contribution of new physics or deviations from the SM prediction. The following sections in this chapter detail the evaluation of these limits for our analysis.

This method provides a unified and statistically robust approach to reporting null results, ensuring consistency across analyses and enabling direct comparison between measurements from different experiments.

12.1.4 Estimation of Polarization Fraction

The fraction of the longitudinal mode, f_{LL}, is a key observable in this analysis. A multi-parameter profile likelihood fit is performed to simultaneously extract the signal strengths μ_{LL} and μ_{TX}, corresponding to the LL and TX polarization components, respectively. The signal strengths are defined as

$$\mu_X = \frac{\sigma_X^{\mathrm{meas}}}{\sigma_X^{\mathrm{SM}}}, \tag{12.13}$$

where σ_X^{meas} and σ_X^{SM} are the measured and SM predicted fiducial cross sections for each polarization state $X \in \{LL, TX\}$.

The SM fiducial cross sections obtained from `MadGraph` are:

$$\begin{aligned} \sigma_{\mathrm{SM}}^{LL} &= 0.277 \text{ fb}, & \sigma_{\mathrm{SM}}^{LT} &= 0.874 \text{ fb}, \\ \sigma_{\mathrm{SM}}^{TT} &= 1.744 \text{ fb}, & \sigma_{\mathrm{SM}}^{\mathrm{tot}} &= 2.896 \text{ fb}. \end{aligned} \tag{12.14}$$

The transverse (TX) contribution is therefore $\sigma_{\mathrm{SM}}^{TX} = \sigma_{\mathrm{SM}}^{LT} + \sigma_{\mathrm{SM}}^{TT} = 2.618$ fb.

The polarization fraction of the LL component is expressed as:

$$f_{LL} = \frac{\mu_{LL}\,\sigma_{\mathrm{SM}}^{LL}}{\mu_{LL}\,\sigma_{\mathrm{SM}}^{LL} + \mu_{TX}\,\sigma_{\mathrm{SM}}^{TX}}. \tag{12.15}$$

Further discussion of the mathematical formalism employed in deriving the results reported in this

Chapter can be found in Appendix E.

12.2 Expected Sensitivity

Before applying the fit to the actual data, its performance is tested and validated using an *Asimov* dataset. This dataset is a pseudo-sample constructed by replacing observed data with the sum of the predicted signal and background expectations. All results in this section are derived from a *partially unblinded fit* using a carefully defined fit strategy designed to avoid bias while preserving realistic normalization for key background processes. When fitting this dataset, the resulting signal strength normalization factors should return $\mu_{LL} = \mu_{TX} = 1$, and all nuisance parameters should have zero pull by construction.

The measured data are used only in the $W^{\pm}Z$ control region (CR), which does not affect the signal normalization but provides the correct normalization for the $W^{\pm}Z$-QCD background component. In contrast, the signal region (SR) and the Low-m_{jj} CR are both "blinded" by replacing the measured data with Asimov data. This treatment is necessary because these regions contain non-negligible signal contributions. Since the $W^{\pm}Z$ CR is "unblinded" using real data, while the SR and Low-m_{jj} CR are "blinded" using Asimov pseudo-data, this configuration is referred to as a *partially unblinded fit*.

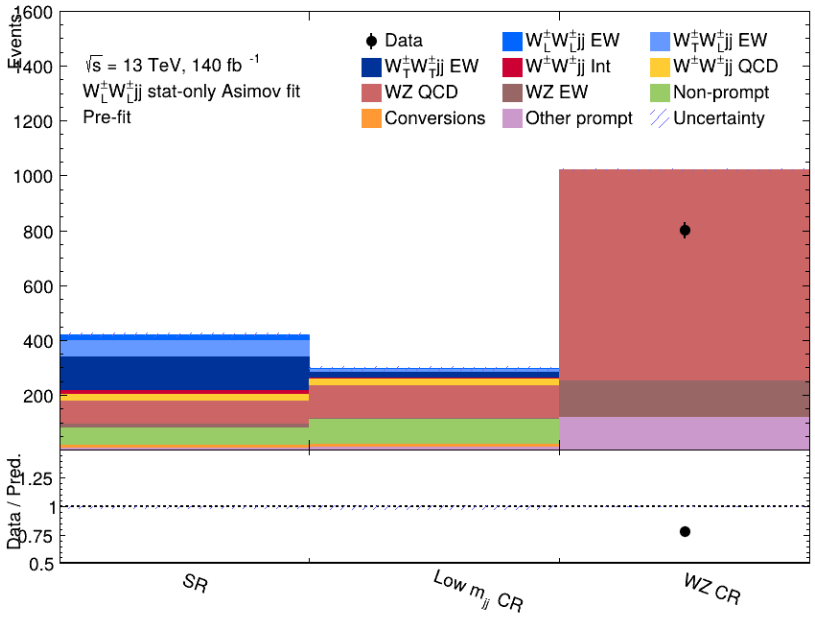


Figure 12.1: A summary of the pre-fit yields in the signal and control regions under the partially blinded fit strategy.

Both CRs are implemented as single-bin distributions, using only the total number of events to

constrain the overall normalization of the dominant backgrounds. The pre-fit summary of events in SR and CRs is shown in Fig. 12.1. It hints that the $W^{\pm}Z$-QCD background needs to be scaled down. The normalization factor θ_{WZQCD} extracted from the fit, as shown in Fig. 12.2, is:

$$\theta_{\mathrm{WZQCD}} = 0.71 \pm 0.04\,. \tag{12.16}$$

It is found to be consistent with the measurements in Ref. [1, 4, 151, 174]. In the SR, the DNN output fit is carried out with 10 uniform bins, following manual optimization through iterative trial and error. The corresponding SR pre- and post-fit distributions are presented in Fig. 12.3. Unlike CRs where uncertainties typically shrink after the fit, in this SR they expand due to statistical limitations. Only statistical uncertainties are considered in the fits shown, systematic contributions are not included since they have minimal impact in this analysis as discussed in Section 12.4.

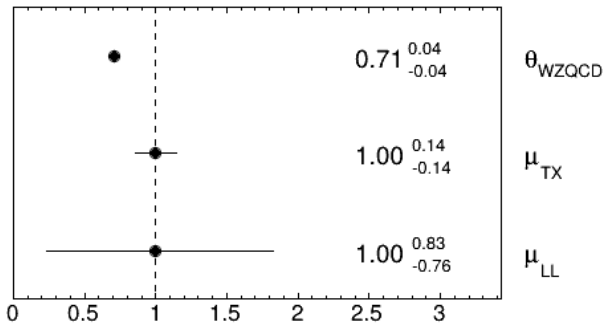


Figure 12.2: Signal strengths and the normalization factor of $W^{\pm}Z$-QCD obtained from the maximized likelihood fit on partially unblinded data.

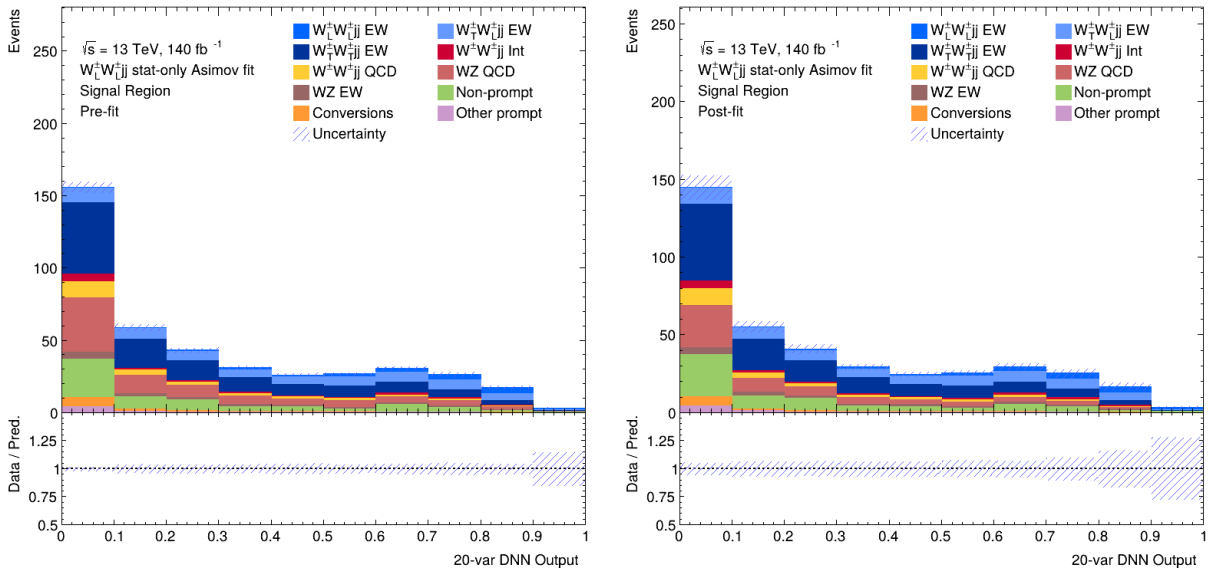


Figure 12.3: Asimov pre-fit (left) and post-fit (right) distributions of the DNN output in the signal region. The hashed band represents the statistical uncertainties on the Standard Model predictions.

12.2.1 Expected Limits and Significance

From this partially unblinded Asimov fit, the expected 95% CL upper limit on the signal strength parameter is determined to be:

$$\mu_{95}^{\text{exp}} = 1.55^{+1.55}_{-0.75}\,, \tag{12.17}$$

where the uncertainties correspond to the $\pm 2\sigma$ variations from the median expected limit. This result implies that, assuming no true signal, the analysis is expected to exclude signal strengths above approximately 1.6 times the nominal SM prediction.

The expected discovery significance, computed from the same Asimov dataset, is:

$$Z_{\text{exp}} = 1.30\sigma \quad (p_{\text{exp}} = 0.096)\,, \tag{12.18}$$

corresponding to a 9.6% probability that the background-only model fluctuates to a signal-like outcome at least as large as the one expected.

12.2.2 Polarization Fraction and Fiducial Cross Section

Expected fiducial cross sections can now be calculated using the Asimov fit. The normalization factors — μ_{LL}, μ_{TX}— have a correlation coefficient of $\rho(\mu_{\text{LL}}, \mu_{\text{TX}}) = -0.619$ which is used in error estimation (details in Appendix E). From Eq. 12.15, these values correspond to:

$$\sigma_{LL}^{\text{exp}} = 0.28^{+0.23}_{-0.21}\ \text{fb}, \tag{12.19}$$

$$\sigma_{TX}^{\text{exp}} = 2.6 \pm 0.4\ \text{fb}, \tag{12.20}$$

$$\sigma_{\text{tot}}^{\text{exp}} = 2.9 \pm 0.3\ \text{fb}. \tag{12.21}$$

The corresponding expected longitudinal fraction is

$$f_{LL}^{\text{exp}} = 0.10^{+0.08}_{-0.07}\,, \tag{12.22}$$

and the corresponding 95% CL upper limit (UL) on the *LL* fiducial cross section is

$$\sigma_{LL}^{\text{UL,exp}} \approx 0.77\ \text{fb}\,, \tag{12.23}$$

resulting in the *LL* fraction

$$f_{LL}^{\text{UL,exp}} \approx 0.27\,. \tag{12.24}$$

A comprehensive set of fit results, including limits, significances, pre- and post-fit distributions in the CRs, as well as fitted event yields, is documented in Appendix F.

12.3 Observed Sensitivity

The analysis is finally unblinded in all regions, including the SR and Low-m_{jj} CR, and is performed on ATLAS data. The same statistical procedure is applied to the observed data to obtain the final results. The WZ and Low-m_{jj} CRs constrain background contributions in the fit. The post-fit summary of events in all regions is depicted in Fig. 12.4. The fit results in an excellent agreement with data in the CRs, with μ_{LL}= 0.22 and θ_{WZQCD}= 0.72, as depicted in Fig. 12.5 and discussed in the following subsections. The SR DNN output fit, now with fully unblinded regions, is presented in Fig. 12.6.

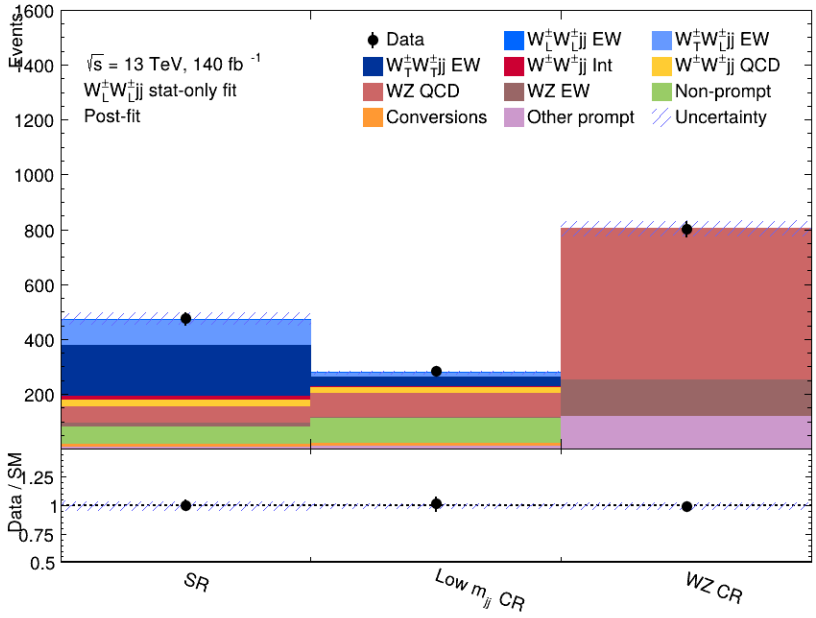


Figure 12.4: A summary of the post-fit yields in the signal and control regions after unblinding. The total expectations agree with the observed data in the three regions.

12.3.1 Observed Limits and Significance

The observed 95% CL upper limit on the signal strength parameter is determined to be:

$$\mu_{95}^{\mathrm{obs}} = 1.82\,, \tag{12.25}$$

which agrees well with the expected limit of $\mu_{95}^{\text{exp}} = 1.72^{+1.70}_{-0.83}$. The expected limits in the unblinded results are computed using the post-fit nuisance parameters from the data, providing a realistic background-only benchmark for comparison with the observed limits, particularly when notable background normalizations modify the background relative to pre-fit predictions. The close agreement between the observed and expected limits indicates that the data are consistent with the SM background prediction, showing no evidence for an excess compatible with the targeted signal.

The normalization factor θ_{WZQCD} extracted from the unblinded fit, changes very slightly as shown in Fig. 12.5:

$$\theta_{\text{WZQCD}} = 0.72 \pm 0.04\,. \tag{12.26}$$

It is found to be consistent with the Asimov value and measurements in Ref. [1, 4, 151, 174]. While the observed normalization of the transverse polarization (μ_{TX}) is higher than expected, the longitudinal polarization states (μ_{LL}) are scaled down by the fit. As in the previous section, only statistical uncertainties are considered here.

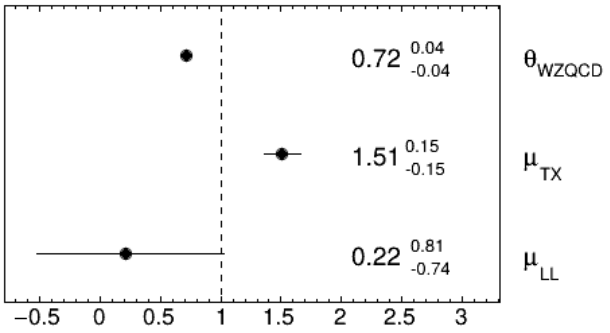


Figure 12.5: Signal strengths and the normalization factor of $W^{\pm}Z$-QCD obtained from the maximized likelihood fit on measured data.

The observed significance of the *LL* signal is found to be

$$Z_{\text{obs}} = 0.28\sigma \quad (p_{\text{obs}} = 0.39)\,, \tag{12.27}$$

corresponding to a background-only compatibility of 39%. This low significance is compatible with a statistical fluctuation and does not indicate any significant deviation from the background expectation.

Interpretation of Observed Post-fit Results

The post-fit SR event distribution shown in Fig. 12.6 demonstrates good overall agreement between the fitted model and the observed data. In the lower and intermediate DNN regions (< 0.7),

where the TX backgrounds dominate, the data lie slightly above the pre-fit expectation, leading to an enhanced normalization of $\mu_{\mathrm{XT}} = 1.51$. In contrast, the absence of a visible excess in the high DNN-score region (> 0.7), which is most sensitive to the LL signal, results in a downward pull on μ_{LL}, reducing it to 0.22. This behaviour is consistent with the expected anti-correlation between the two components ($\rho = -0.6$), arising from their overlapping kinematic characteristics in the selected phase space. The overall fit quality is good, and the observed pattern aligns with the limited sensitivity of the measurement, corresponding to an observed significance of 0.28σ compared to an expected 1.2σ. The shifts in the fitted parameters are therefore consistent with statistical fluctuations and the correlation between the polarization components, rather than a genuine deviation from SM prediction.

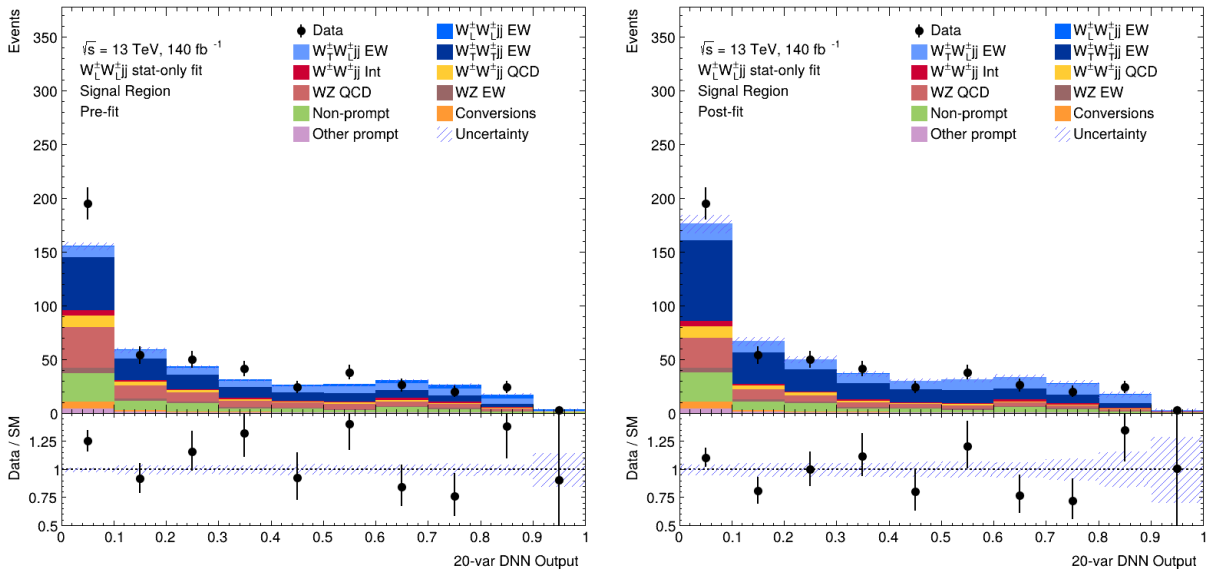


Figure 12.6: Unblinded pre-fit (left) and post-fit (right) distributions of the DNN output in the signal region. The hashed band represents the statistical uncertainties on the Standard Model predictions.

12.3.2 Polarization Fraction and Fiducial Cross Section

In the unblinded fit to data, both μ_{LL} and μ_{TX} were allowed to float simultaneously. The best-fit signal strengths are:

$$\mu_{LL} = 0.22^{+0.81}_{-0.74}\,, \tag{12.28}$$

$$\mu_{TX} = 1.51 \pm 0.15\,, \tag{12.29}$$

with a correlation coefficient of $\rho(\mu_{LL}, \mu_{TX}) = -0.60$.

Observed fiducial cross sections are similarly calculated as for the Asimov fit. Using Eq. 12.15,

the following observed fiducial cross sections are measured:

$$\sigma_{LL}^{\text{obs}} = 0.06^{+0.22}_{-0.21}\ \text{fb}, \tag{12.30}$$

$$\sigma_{TX}^{\text{obs}} = 4.0 \pm 0.4\ \text{fb}, \tag{12.31}$$

$$\sigma_{\text{tot}}^{\text{obs}} = 4.0 \pm 0.3\ \text{fb}. \tag{12.32}$$

The corresponding observed longitudinal fraction is

$$f_{LL}^{\text{obs}} = 0.02^{+0.06}_{-0.05}\,. \tag{12.33}$$

The measured total fiducial cross section ($\sigma_{\text{tot}}^{\text{obs}}$) is slightly above the SM prediction, but consistent within the combined uncertainty. The *LL* component remains compatible with zero within its statistical uncertainty, showing no significant evidence. An approximate one-sided 95% CL upper limit (upper; denoted by σ^{+}) is obtained using

$$\mu_{LL}^{\text{UL,obs}} = \mu_{LL} + 1.645 \times \sigma^{+}_{\mu_{LL}}\,, \tag{12.34}$$

yielding

$$\sigma_{LL}^{\text{UL,obs}} = 0.43\ \text{fb}\,, \tag{12.35}$$

corresponding to an *LL* fraction of

$$f_{LL}^{\text{UL,obs}} \approx 0.15\,. \tag{12.36}$$

12.4 Impact of a Flat Systematic Uncertainty

To evaluate the potential influence of missing or unmodelled systematic uncertainties on the fitted fiducial cross sections, a robustness test was performed by introducing a flat 10% systematic uncertainty that affects both signal and background. This choice is motivated by the uncertainty breakdown in the most recent ATLAS publication [1]. In that result, the category *Experimental and modelling* contributes 11.1 percent, but this includes a 7.2 percent *Background modelling statistical* component already accounted for in our fit. Removing this in quadrature leaves approximately 8.4 percent as the true size of the missing systematics. Using a rounded 10 percent provides a simple and slightly conservative approximation.

This test enables a direct comparison between statistical-only and statistical-plus-systematic scenarios to assess the relative importance of unmodelled systematics in the final result.

The results in Table 12.1 show that the 10 percent flat uncertainty produces only a modest increase in the total uncertainty, well within the statistical precision of the measurement. The fitted

Component	Scenario	σ_{LL} [fb]	σ_{tot} [fb]
Expected	Stat-only	$0.28^{+0.23}_{-0.21}$	2.9 ± 0.3
	Stat + Syst	$0.28^{+0.24}_{-0.22}$	2.9 ± 0.4
Observed	Stat-only	$0.06^{+0.22}_{-0.21}$	4.0 ± 0.3
	Stat + Syst	$0.06^{+0.23}_{-0.22}$	4.0 ± 0.5

Table 12.1: Comparison of statistical-only and statistical plus flat systematic (10%) uncertainties for the expected and observed fiducial cross sections.

cross sections remain stable, indicating that the analysis is statistically dominated. The results are therefore reported as statistical-only without loss of robustness or interpretability for the *LL* signal.

12.5 Summary of the Longitudinal Polarization Results

The longitudinally polarized component of same-sign $W^{\pm}W^{\pm}jj$ scattering is extracted from a multi-parameter profile likelihood fit with μ_{LL} and μ_{XT} as independent signal strength parameters. The fitted value of μ_{LL} determines the fiducial cross section and the longitudinal polarization fraction f_{LL}, as summarised in Table 12.2.

The expected result demonstrates the statistical sensitivity of the analysis, while the unblinded fit to data shows no statistically significant evidence for a longitudinally polarized contribution. The observed fraction is consistent with zero and remains compatible with SM expectation within the large statistical uncertainty. The corresponding 95% CL upper limit on f_{LL} is also in agreement with SM prediction and previous measurements [1]. Ref. [1] reports an observed (expected) 95% CL upper limit of 0.45 (0.70) fb on the EW production of two longitudinally polarized same-sign W bosons.

The smaller observed value of f_{LL} compared to the expected estimate arises from a downward statistical fluctuation in the SR event yield, which suppresses the fitted μ_{LL} and, through its strong anti-correlation with μ_{XT}, further reduces the inferred longitudinal contribution. This fluctuation also leads to a stronger observed upper limit than expected, as the likelihood curve intersects the CL threshold earlier. The tighter observed limit therefore reflects limited statistical precision rather than increased sensitivity.

Given the limited event yield and small impact of systematic effects relative to statistical uncertainties for the *LL* signal, the result is reported as *statistical-only*. Future analyses with larger datasets will significantly improve the sensitivity to VBS $W_L^{\pm}W_L^{\pm}$ production.

Parameter	**Expected**	**Observed**	**Unit**
μ_{LL}	$1.0^{+0.8}_{-0.8}$	$0.22^{+0.81}_{-0.74}$	–
μ_{TX}	1.0 ± 0.1	1.51 ± 0.15	–
σ_{LL}	$0.28^{+0.23}_{-0.21}$	$0.06^{+0.22}_{-0.21}$	fb
σ_{TX}	2.6 ± 0.4	4.0 ± 0.4	fb
σ_{tot}	2.9 ± 0.3	4.0 ± 0.3	fb
f_{LL}	$0.10^{+0.08}_{-0.07}$	$0.02^{+0.06}_{-0.05}$	–
σ_{LL}^{UL} (95% CL)	0.77	0.43	fb
f_{LL}^{UL} (95% CL)	0.27	0.15	–
Z_{LL} (significance)	1.3 σ	0.28 σ	–
p-value	0.10	0.39	–

Table 12.2: Summary of the expected and observed fit results for the longitudinal (LL) and transverse (TX=TL+TT) polarization components in the $W^{\pm}W^{\pm}jj$ electroweak process. All uncertainties are statistical only. The 95% CL upper limits (UL) are derived assuming a one-sided Gaussian approximation.

Chapter 13

Conclusion and Outlook

This dissertation has presented a measurement of vector boson scattering (VBS) in the same-sign $W^{\pm}W^{\pm}jj$ final state using proton–proton collision data recorded at $\sqrt{s}$ = 13 TeV, corresponding to an integrated luminosity of 140 fb^{-1}, by the ATLAS detector at the LHC. The scattering of two W bosons with the same electric charge in their lepton decay modes, $pp \to W^{\pm}W^{\pm}jj \to \ell^{\pm}\nu\ell^{\pm}\nu jj$, is considered a golden channel characterizing VBS. The analysis focused on the extraction of the longitudinally polarized component of the process, which provides a direct probe of the unitarization mechanism of electroweak symmetry breaking in the Standard Model.

The Monte Carlo simulation of the polarized signal process was performed using MadGraph, and validated using the decay angle determined by W polarization. Machine learning methods were employed to differentiate the doubly longitudinal (LL) signal from the combined transverse (TX) polarization and a plethora of other background processes. A multi-parameter profile likelihood fit was performed to extract the signal strengths associated with the LL and TX polarization contributions. A partially unblinded fit strategy was employed to avoid bias while retaining sensitivity to background normalization.

The expected sensitivity demonstrates that the current dataset provides statistical power approaching the level required to probe the longitudinal component at the scale predicted by the Standard Model. In the unblinded fit using data, no significant evidence for a longitudinal contribution was observed. The extracted longitudinal polarization fraction was found to be consistent with zero and compatible with the Standard Model expectation within the large statistical uncertainty. A one-sided 95% CL upper limit on the longitudinal component was derived, and is in agreement with theoretical predictions and previous measurements.

These results represent an important step toward an observation of the longitudinally polarized mode of same-sign $W^{\pm}W^{\pm}jj$ production, demonstrating a robust methodology, stable background

modelling, and a statistically driven result in which systematic uncertainties play a subdominant role. The measurement confirms that the current ATLAS dataset is approaching the sensitivity required to access this rare and theoretically critical component of VBS, with the most recent ATLAS publication [1] reporting the first evidence with 3.3σ significance using singly longitudinally-polarized *LX* modes.

Outlook

Significant progress is anticipated with the forthcoming Run 3 dataset and, ultimately, with the full HL-LHC program, where the integrated luminosity will increase by more than an order of magnitude. The expected improvement in statistical precision will enable a definitive measurement of the *LL* contribution and potentially achieve observation-level significance. Enhancements in analysis techniques, including improved machine-learning–based discriminants, refined treatment of polarization separation, and more precise theoretical predictions, will further strengthen the measurement.

Moreover, the ability to measure the longitudinal mode with increasing precision opens a unique window onto possible Beyond the Standard Model or BSM extensions affecting electroweak symmetry breaking, such as anomalous quartic gauge couplings and effects from strongly coupled electroweak dynamics. The methodology established in this dissertation sets the foundation for such future explorations.

In summary, while no significant excess has yet been observed, the analysis confirms compatibility with the Standard Model and establishes a strong basis for the next generation of measurements. Continued study of polarized vector boson scattering will remain one of the most powerful probes of the electroweak sector in the coming decade.

Appendix A

Theory and VBS

A.1 Mandelstam Variables

Mandelstam variables $-s,t,u-$ are used to convey important information in a $2 \to 2$ scattering about the momenta, energy and scattering angles of incoming and outgoing particles involved in the process. They are defined to be:

$$\begin{aligned} s &= (p_1 + p_2)^2 = (p_3 + p_4)^2 , \\ t &= (p_1 - p_3)^2 = (p_2 - p_4)^2 , \\ u &= (p_1 - p_2)^2 = (p_2 - p_3)^2 , \end{aligned} \tag{A.1}$$

where p_1, p_2 are four-momenta of incoming particles and p_3, p_4 are that of outgoing particles.

A.2 VBS Event Signature Theoretical Justification

For the diboson scattering of the W boson ($WW \to WW$) shown in Fig. A.1, squared matrix element [53] is given by

$$|\mathscr{M}|^2 \propto \frac{p_1 \cdot p_2 \cdot p_3 \cdot p_4}{(k_1^2 - M_W^2)^2 \cdot (k_2^2 - M_W^2)^2} , \tag{A.2}$$

where $k_1 = p_1 - p_3$ and $k_2 = p_2 - p_4$ denote the four momenta of the two W bosons. The partonic center-of-mass energy is given by $\sqrt{s} = \sqrt{2p_1 \cdot p_2}$. For fixed center-of-mass energy, the scattering amplitude can be maximized by either increasing the numerator or decreasing the denominator. The two salient features of VBS signature: (i) large di-jet invariant mass (m_{jj}), and (ii) large rapidity separation between the tagging jets (Δy_{jj}) can be derived mathematically through maximizing

the amplitude.

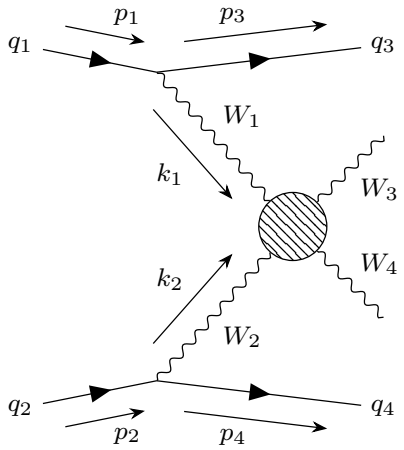


Figure A.1: VBS diboson scattering involving W bosons.

Assuming massless quarks, *i.e.* $p^2 = m^2 \approx 0$ and $E = |\vec{p}|$,

(i) the di-jet invariant mass is calculated as $m_{jj} = \sqrt{(p_3 + p_4)^2} = \sqrt{2p_3 \cdot p_4}$. As the momenta of the outgoing tagging jets p_3 and p_4 increase, so does their product $p_3 \cdot p_4$, thereby leading to an increase in the numerator of Eq. A.2.

(ii) the scattering angles (θ) dictate W boson momenta (k):

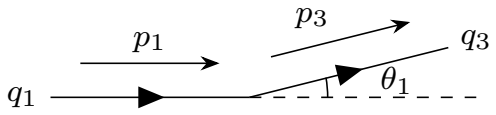


Figure A.2: Scattering angle θ_1 between quarks q_1 and q_3.

$$
\begin{aligned}
k_1^2 &= (p_1 - p_3)^2 , \\
&= -2p_1 \cdot p_3 , \\
&= -2(E_1E_3 - E_1E_3 \cos\theta_1) , \\
&= -2E_1E_3(1 - \cos\theta_1) \cdot \frac{(1+\cos\theta_1)}{(1+\cos\theta_1)} \cdot \frac{E_3}{E_3} , \\
&= -\frac{2}{1+\cos\theta_1} \cdot \frac{E_1}{E_3} \cdot (E_3 \sin\theta_1)^2 , \\
&= -\frac{2}{1+\cos\theta_1} \cdot \frac{E_1}{E_3} \cdot p_{T,3}^2 .
\end{aligned}
\tag{A.3}
$$

Here, θ_1 describes the scattering angle between $\vec{p}_1$ and $\vec{p}_3$, and $|\vec{p}_{T,3}| = E_3 \sin\theta_1$. As k_1^2 approaches its upper bound of zero, the inverse W boson propagator can be written as $(k_1^2 -$

$M_W^2) \simeq -(\frac{E_1}{E_3} p_{T,3}^2 + M_W^2)$. It becomes smaller when the scattering angle becomes smaller. Thus, smaller scattering angles correspond to larger amplitude in Eq. A.2. Note that smaller θ values indicate larger rapidity separation between the tagging jets Δy_{jj}.

Appendix B

Standard Model Lagrangian

The SM Lagrangian ($\mathscr{L}_{\rm SM}$) obeys $SU(3)_C \times SU(2)_L \times U(1)_Y$ gauge symmetries. It is given by

$$\begin{aligned}\mathscr{L}_{\rm SM} = &-\frac{1}{4}G^A_{\mu\nu}G^{A\mu\nu} - \frac{1}{4}W^I_{\mu\nu}W^{I\mu\nu} - \frac{1}{4}B_{\mu\nu}B^{\mu\nu} + (D_\mu H)^\dagger (D^\mu H) + \mu^2 H^\dagger H - \lambda (H^\dagger H)^2 \\ &+ i\left(\overline{L} D_\mu \gamma^\mu L + \overline{e}_R D_\mu \gamma^\mu e_R + \overline{Q} D_\mu \gamma^\mu Q + \overline{u}_R D_\mu \gamma^\mu u_R + \overline{d}_R D_\mu \gamma^\mu d_R\right) \\ &- \left(\overline{L} Y_e e_R H + \overline{Q} Y_u u_R \widetilde{H} + \overline{Q} Y_d d_R H + \text{h.c.}\right), \end{aligned} \tag{B.1}$$

where $\widetilde{H} = i\sigma_2 H^*$, and the gauge-field strengths are defined as

$$G^A_{\mu\nu} = \partial_\mu G^A_\nu - \partial_\nu G^A_\mu + g_s f^{ABC} G^B_\mu G^C_\nu , \tag{B.2}$$

$$W^I_{\mu\nu} = \partial_\mu W^I_\nu - \partial_\nu W^I_\mu + g\varepsilon^{IJK} W^J_\mu W^K_\nu , \tag{B.3}$$

$$B_{\mu\nu} = \partial_\mu B_\nu - \partial_\nu B_\mu , \tag{B.4}$$

where f^{ABC} and ε^{IJK} are the structure constants of $SU(3)$ and $SU(2)$: $[T^A, T^B] = if^{ABC}T^C$ with $f^{ABC} = i(T^A)^{BC}$ for $SU(3)$, and $[\sigma^I/2, \sigma^J/2] = i\varepsilon^{JIK}\sigma^K/2$ with ε^{JIK} being the totally antisymmetric tensor. We define the covariant derivative as

$$D_\mu q_L = (\partial_\mu - ig_s T^A G^A_\mu - igS^I W^I_\mu - ig' Y_q B_\mu) q_L \tag{B.5}$$

for the left-handed quark, where $T^A = \lambda^A/2$, $S^I = \sigma^I/2$, and the hyper charge is normalized as $Y_q = 1/6$. The gauge quantum numbers of each field are summarized in Table 2.1.

The electroweak (EW) symmetry is spontaneously broken as the Higgs field acquires the non-zero vacuum expectation value (VEV), $v = \mu/\sqrt{\lambda}$. In unitary gauge, the Higgs field H is written

in terms of v and the physical Higgs field h:

$$H = \frac{v}{\sqrt{2}} \begin{pmatrix} 0 \\ 1+\frac{h}{v} \end{pmatrix}. \tag{B.6}$$

For a general 2x2 matrix between $H^\dagger$ and H,

$$\begin{aligned} H^\dagger \begin{pmatrix} a_{11} & a_{12} \\ a_{21} & a_{22} \end{pmatrix} H &= \frac{1}{\sqrt{2}} \begin{pmatrix} 0 & (v+h)^\dagger \end{pmatrix} \begin{pmatrix} a_{11} & a_{12} \\ a_{21} & a_{22} \end{pmatrix} \frac{1}{\sqrt{2}} \begin{pmatrix} 0 \\ v+h \end{pmatrix}, \\ &= \frac{1}{2}|v+h|^2 a_{22}. \end{aligned} \tag{B.7}$$

The Higgs kinetic term then yield the mass terms of the gauge bosons as well as hVV and $hhVV$

interactions:

$$
\begin{aligned}
(D_\mu H)^\dagger (D^\mu H) &= \left(\partial_\mu H - ig\frac{\sigma^I}{2}W_\mu^I H - ig'\frac{1}{2}B_\mu H\right)^\dagger \left(\partial^\mu H - ig\frac{\sigma^J}{2}W^{J\mu} H - ig'\frac{1}{2}B^\mu H\right), \\
&= (\partial_\mu H)^\dagger(\partial^\mu H) + \frac{g^2}{4}H^\dagger W_\mu^{I\dagger}\sigma^I\sigma^J W^{J\mu}H + \frac{g'^2}{4}H^\dagger B_\mu^\dagger B^\mu H \\
&\quad + \left[i\frac{g}{2}H^\dagger W_\mu^{I\dagger}\sigma^I(\partial^\mu H) + i\frac{g'}{2}H^\dagger B_\mu^\dagger(\partial^\mu H) + \frac{gg'}{4}H^\dagger W_\mu^{I\dagger}\sigma^I B^\mu H + \text{h.c.}\right], \\
&= \frac{1}{2}(\partial_\mu h)^\dagger(\partial^\mu h) + \frac{g^2}{8}|v+h|^2 W_\mu^{I\dagger}(\sigma^I\sigma^J)_{22}W^{J\mu} + \frac{g'^2}{8}|v+h|^2 B_\mu^\dagger B^\mu \\
&\quad + \left[i\frac{g}{4}(v+h)^\dagger W_\mu^{I\dagger}(\sigma^I)_{22}(\partial^\mu h) + i\frac{g'}{4}(v+h)^\dagger B_\mu^\dagger(\partial^\mu h)\right. \\
&\quad \left. + \frac{gg'}{8}|v+h|^2 W_\mu^{I\dagger}(\sigma^I)_{22}B^\mu + \text{h.c.}\right], \\
&= \frac{1}{2}(\partial_\mu h)^\dagger(\partial^\mu h) + \frac{g^2}{8}|v+h|^2\left(W_\mu^{1\dagger}W^{1\mu} + W_\mu^{2\dagger}W^{2\mu} + W_\mu^{3\dagger}W^{3\mu} - iW_\mu^{1\dagger}W^{2\mu}\right. \\
&\quad \left. + iW_\mu^{2\dagger}W^{1\mu}\right) + \frac{1}{8}|v+h|^2\left(g'^2 B_\mu^\dagger B^\mu - gg' B_\mu^\dagger W^{3\mu} - gg' W_\mu^{3\dagger}B^\mu\right) \\
&\quad - \left[\frac{i}{4}(v+h)^\dagger\left(gW_\mu^{3\dagger} - g'B_\mu^\dagger\right)(\partial^\mu h) + \text{h.c.}\right], \\
&= \frac{1}{2}(\partial_\mu h)^\dagger(\partial^\mu h) + \frac{g^2}{8}|v+h|^2\left(W_\mu^1 - iW_\mu^2\right)^\dagger\left(W_\mu^1 - iW^{2\mu}\right) \\
&\quad + \frac{1}{8}|v+h|^2\left(gW_\mu^3 - g'B_\mu\right)^\dagger\left(gW^{3\mu} - g'B^\mu\right) \\
&\quad - \left[\frac{i}{4}(v+h)^\dagger\left(gW_\mu^3 - g'B_\mu\right)^\dagger(\partial^\mu h) + \text{h.c.}\right], \\
&= \frac{1}{2}(\partial_\mu h)^\dagger(\partial^\mu h) + \frac{g^2v^2}{4}\left(1 + \frac{2h}{v} + \frac{h^2}{v^2}\right)W_\mu^{+\dagger}W^{+\mu} \\
&\quad + \frac{1}{2}\frac{(g^2+g'^2)v^2}{4}\left(1 + \frac{2h}{v} + \frac{h^2}{v^2}\right)Z_\mu^\dagger Z^\mu \\
&\quad \underbrace{- \left[\frac{i(g^2+g'^2)^{1/2}v}{4}\left(1 + \frac{h^\dagger}{v}\right)Z_\mu^\dagger(\partial^\mu h) + \text{h.c.}\right]}_{\text{vanishes because } Z_\mu^\dagger = Z_\mu}, \\
&= \frac{1}{2}(\partial_\mu h)^\dagger(\partial^\mu h) + M_W^2 W_\mu^- W^{+\mu} + \frac{1}{2}M_Z^2 Z_\mu Z^\mu \\
&\quad + \frac{g^2v^2}{4}\left(\frac{2h}{v} + \frac{h^2}{v^2}\right)W_\mu^- W^{+\mu} + \frac{1}{2}\frac{(g^2+g'^2)v^2}{4}\left(\frac{2h}{v} + \frac{h^2}{v^2}\right)Z_\mu Z^\mu, \qquad \text{(B.8)}
\end{aligned}
$$

where the physical gauge-boson fields are defined as

$$W_\mu^\pm = \frac{1}{\sqrt{2}}(W_\mu^1 \mp i W_\mu^2)\,, \tag{B.9}$$

$$\begin{pmatrix} Z_\mu \\ A_\mu \end{pmatrix} = \begin{pmatrix} \cos\theta_W & -\sin\theta_W \\ \sin\theta_W & \cos\theta_W \end{pmatrix} \begin{pmatrix} W_\mu^3 \\ B_\mu \end{pmatrix}, \tag{B.10}$$

with the weak mixing angle θ_W defining through the relations,

$$c_W \equiv \cos\theta_W = \frac{g}{\sqrt{g^2+g'^2}}\,, \tag{B.11}$$

$$s_W \equiv \sin\theta_W = \frac{g'}{\sqrt{g^2+g'^2}}\,, \tag{B.12}$$

$$e^2 = g^2\sin^2\theta_W = g^2 s_W^2\,. \tag{B.13}$$

For the electric charge, we adopt the sign convention $e = g s_W$. In the lagrangian density, mass term for real vector field Z is $\frac{1}{2}m^2 Z_\mu Z^\mu$ and that for complex vector field W is $m^2 W_\mu^* W^\mu$. The masses of the W and Z bosons are then given by

$$M_W^2 = \frac{g^2 v^2}{4}\,, \qquad M_Z^2 = \frac{(g^2+g'^2)v^2}{4}\,, \tag{B.14}$$

which imply $c_W^2 = M_W^2/M_Z^2$. The Higgs VEV v can be estimated as

$$v = \frac{1}{(\sqrt{2}\,G_F)^{1/2}} \approx 246\ \text{GeV}, \tag{B.15}$$

where $G_F = \sqrt{2}g^2/(8M_W^2)$.

The kinetic terms of the W gauge bosons involve the triple and quartic gauge-boson couplings:[1]

$$
\begin{aligned}
-\frac{1}{4}W^I_{\mu\nu}W^{I\mu\nu} &= -\frac{1}{4}(\partial_\mu W^I_\nu - \partial_\nu W^I_\mu + g\varepsilon^{IJK}W^J_\mu W^K_\nu)(\partial^\mu W^{I\nu} - \partial^\nu W^{I\mu} + g\varepsilon^{ILM}W^{L\mu}W^{M\nu}),\\
&= -\frac{1}{4}(\partial_\mu W^I_\nu - \partial_\nu W^I_\mu)(\partial^\mu W^{I\nu} - \partial^\nu W^{I\mu})\\
&\quad - \frac{g}{2}\varepsilon^{IJK}(\partial_\mu W^I_\nu - \partial_\nu W^I_\mu)W^{J\mu}W^{K\nu} - \frac{g^2}{4}\varepsilon^{IJK}\varepsilon^{ILM}W^J_\mu W^K_\nu W^{L\mu}W^{M\nu},\\
&= -\frac{1}{4}(\partial_\mu W^I_\nu - \partial_\nu W^I_\mu)(\partial^\mu W^{I\nu} - \partial^\nu W^{I\mu})\\
&\quad - g(\partial_\mu W^1_\nu - \partial_\nu W^1_\mu)W^{2\mu}W^{3\nu} - g(\partial_\mu W^2_\nu - \partial_\nu W^2_\mu)W^{3\mu}W^{1\nu}\\
&\quad - g(\partial_\mu W^3_\nu - \partial_\nu W^3_\mu)W^{1\mu}W^{2\nu} - \frac{g^2}{4}(\delta^{JL}\delta^{KM} - \delta^{JM}\delta^{KL})W^J_\mu W^K_\nu W^{L\mu}W^{M\nu},\\
&= -\frac{1}{2}(\partial_\mu W^+_\nu - \partial_\nu W^+_\mu)(\partial^\mu W^{-\nu} - \partial^\nu W^{-\mu}) - \frac{c_W^2}{4}(\partial_\mu Z_\nu - \partial_\nu Z_\mu)(\partial^\mu Z^\nu - \partial^\nu Z^\mu)\\
&\quad - \frac{s_W c_W}{2}(\partial_\mu Z_\nu - \partial_\nu Z_\mu)(\partial^\mu A^\nu - \partial^\nu A^\mu) - \frac{s_W^2}{4}(\partial_\mu A_\nu - \partial_\nu A_\mu)(\partial^\mu A^\nu - \partial^\nu A^\mu)\\
&\quad + ig(\partial_\mu W^+_\nu - \partial_\nu W^+_\mu)W^{-\mu}W^{3\nu} - ig(\partial_\mu W^-_\nu - \partial_\nu W^-_\mu)W^{+\mu}W^{3\nu}\\
&\quad + ig(\partial_\mu W^3_\nu - \partial_\nu W^3_\mu)W^{+\mu}W^{-\nu} - \frac{g^2}{4}W^J_\mu W^{J\mu}W^K_\nu W^{K\nu} + \frac{g^2}{4}W^J_\mu W^J_\nu W^{K\mu}W^{K\nu},\\
&= -\frac{1}{2}(\partial_\mu W^+_\nu - \partial_\nu W^+_\mu)(\partial^\mu W^{-\nu} - \partial^\nu W^{-\mu}) - \frac{c_W^2}{4}(\partial_\mu Z_\nu - \partial_\nu Z_\mu)(\partial^\mu Z^\nu - \partial^\nu Z^\mu)\\
&\quad - \frac{s_W c_W}{2}(\partial_\mu Z_\nu - \partial_\nu Z_\mu)(\partial^\mu A^\nu - \partial^\nu A^\mu) - \frac{s_W^2}{4}(\partial_\mu A_\nu - \partial_\nu A_\mu)(\partial^\mu A^\nu - \partial^\nu A^\mu)\\
&\quad + i\sum_{V=Z,\gamma} g_{WWV}\Big[(\partial_\mu W^+_\nu - \partial_\nu W^+_\mu)W^{-\mu}V^\nu - (\partial_\mu W^-_\nu - \partial_\nu W^-_\mu)W^{+\mu}V^\nu\\
&\qquad\qquad + (\partial_\mu V_\nu - \partial_\nu V_\mu)W^{+\mu}W^{-\nu}\Big]\\
&\quad + \frac{g^2}{2}\left(W^+_\mu W^{+\mu}W^-_\nu W^{-\nu} - W^+_\mu W^{-\mu}W^+_\nu W^{-\nu}\right)\\
&\quad + g^2c_W^2\left(W^+_\mu Z^\mu W^-_\nu Z^\nu - W^+_\mu W^{-\mu}Z_\nu Z^\nu\right) + g^2s_W^2\left(W^+_\mu A^\mu W^-_\nu A^\nu - W^+_\mu W^{-\mu}A_\nu A^\nu\right)\\
&\quad + g^2s_W c_W\left(W^+_\mu Z^\mu W^-_\nu A^\nu + W^+_\mu A^\mu W^-_\nu Z^\nu - 2W^+_\mu W^{-\mu}Z_\nu A^\nu\right)
\end{aligned}
\tag{B.16}
$$

where the triple gauge boson couplings are written as $g_{WWZ} = gc_W = ec_W/s_W$ and $g_{WW\gamma} = gs_W = e$.

Moreover, the Yukawa terms read

$$
\begin{aligned}
\mathscr{L}_{\text{Yukawa}} &= -\left(\overline{L}Y_e e_R H + \overline{Q}Y_u u_R \widetilde{H} + \overline{Q}Y_d d_R H\right) + \text{h.c.},\\
&= -\frac{v+h}{\sqrt{2}}\left(\overline{e}_L Y_e e_R + \overline{u}_L Y_u u_R + \overline{d}_L Y_d d_R\right) + \text{h.c.}
\end{aligned}
\tag{B.17}
$$

[1] Here we employ $W^1_\mu = (W^+_\mu + W^-_\mu)/\sqrt{2}$, $W^2_\mu = i(W^+_\mu - W^-_\mu)/\sqrt{2}$, $W^3_\mu = c_W Z_\mu + s_W A_\mu$, and $W^J_\mu W^J_\nu = W^+_\mu W^-_\nu + W^-_\mu W^+_\nu + c_W^2 Z_\mu Z_\nu + s_W c_W(Z_\mu A_\nu + A_\mu Z_\nu) + s_W^2 A_\mu A_\nu$.

The interactions between the gauge bosons and the left-handed fermions are then given by

$$\begin{aligned}\bar{f}_L i\not{D} f_L &\supset \bar{f}_L \gamma^\mu \left(g_s T^A G^A_\mu + g I^I_f W^I_\mu + g' Y_{f_L} B_\mu \right) f_L \,, \\ &= \bar{f}_L \gamma^\mu \Bigg\{ g_s T^A G^A_\mu + \frac{e}{\sqrt{2} s_W} \left[(I^1_f + i I^2_f) W^+_\mu + (I^1_f - i I^2_f) W^-_\mu \right] \\ &\qquad + \frac{e}{s_W c_W} (I^3_f - Q_f s^2_W) Z_\mu + e Q_f A_\mu \Bigg\} f_L \,, \end{aligned} \tag{B.18}$$

where $I^I_f = \sigma^I/2$ and $Q_f = I^3_f + Y_{f_L}$. Similarly, the right-handed fermions have the following interactions:

$$\begin{aligned}\bar{f}_R i\not{D} f_R &\supset \bar{f}_R \gamma^\mu \left(g_s T^A G^A_\mu + g' Y_{f_R} B_\mu \right) f_R \,, \\ &= \bar{f}_R \gamma^\mu \left[g_s T^A G^A_\mu + \frac{e}{s_W c_W} (-Q_f s^2_W) Z_\mu + e Q_f A_\mu \right] f_R \,. \end{aligned} \tag{B.19}$$

We define the effective couplings g^f_V and g^f_A for the interaction of the Z boson with the neutral current as

$$\mathscr{L}^{Zf\bar{f}}_{\text{eff}} = \frac{e}{2 s_W c_W} Z_\mu \sum_f \bar{f} \gamma^\mu \left(g^f_V - g^f_A \gamma_5 \right) f = \frac{e}{s_W c_W} Z_\mu \sum_f \bar{f} \gamma_\mu \left(g^f_L P_L + g^f_R P_R \right) f \,, \tag{B.20}$$

where $P_L = (1-\gamma_5)/2$ and $P_R = (1+\gamma_5)/2$, and the tree-level couplings are given by $g^f_V = I^3_f - 2 Q_f s^2_W$, $g^f_A = I^3_f$, $g^f_L = I^3_f - Q_f s^2_W$ and $g^f_R = -Q_f s^2_W$ with $g^f_L = (g^f_V + g^f_A)/2$ and $g^f_R = (g^f_V - g^f_A)/2$.

Appendix C

Neural Network Details

C.1 DNN Training Details

Deep Neural Network trained to separate *LL*-polarization modes against all backgrounds:

- **Statistics (Signal Region):**
  - WWcmf – Signal (LL) events $\sim$ 22k, Background events $\sim$ 250k
  - ppcmf – Signal (LL) events $\sim$ 20k, Background events $\sim$ 250k
- **Signal:** LL pol. ($W_L^{\pm}W_L^{\pm}$)
- **Background:** TL, TT pol., ssWW QCD, ssWW INT, WZ QCD, WZ EW6, ZZ, V/γ, charge Flip, triboson, ttX, Fakes (W+jets, $t\bar{t}$ semi-leptonic)
- **Preprocessing:** Scaled to MC event weights & standardized normally distributed data
  - Distribution with zero mean and unit variance
- **Scaling:** Datasets are balanced to avoid bias – scale factor $(Sig) = \sigma(Bkg)/\sigma(Sig)$
- **Dataset Split:** Training = 60%, Testing = 20%, Validation = 20%
- **Avoiding Overtraining:** Dropout layers, Early stopping, Model checkpoint

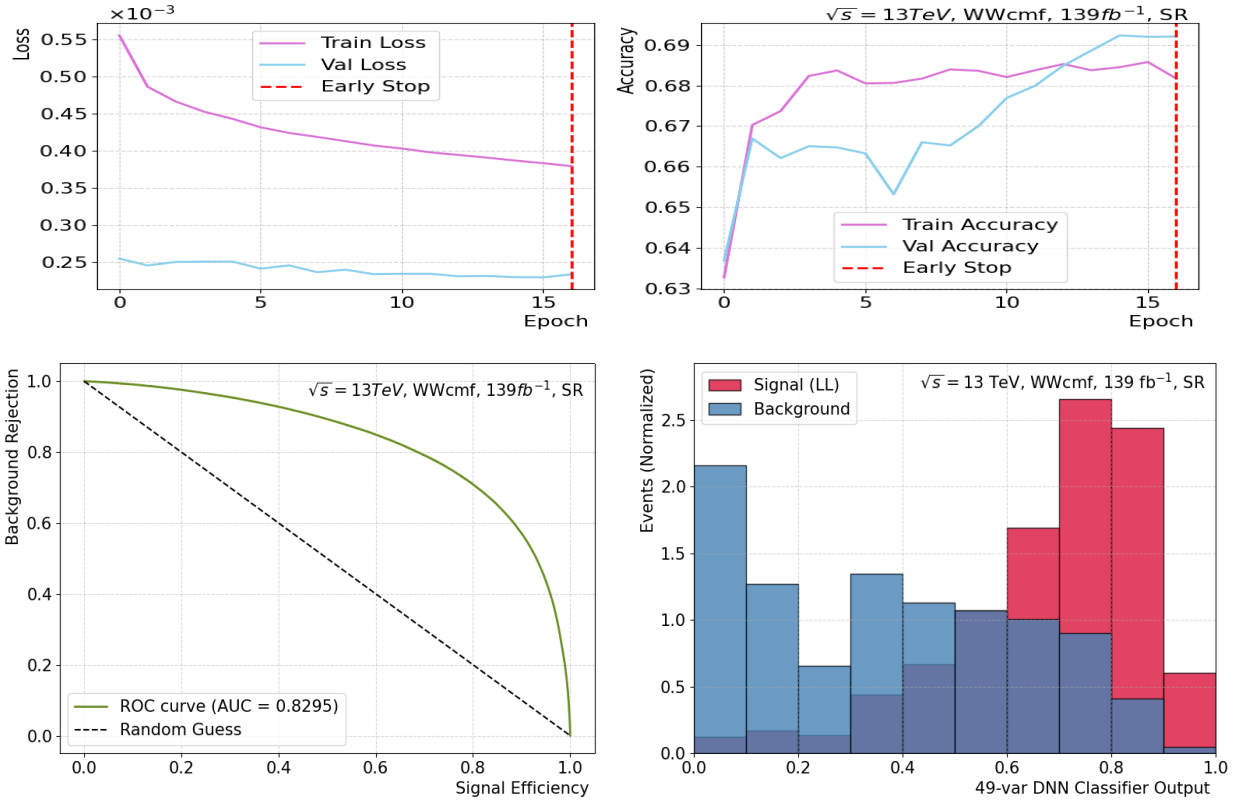


Figure C.1: 49-variable DNN performance plots. $Z = 2.2407$.

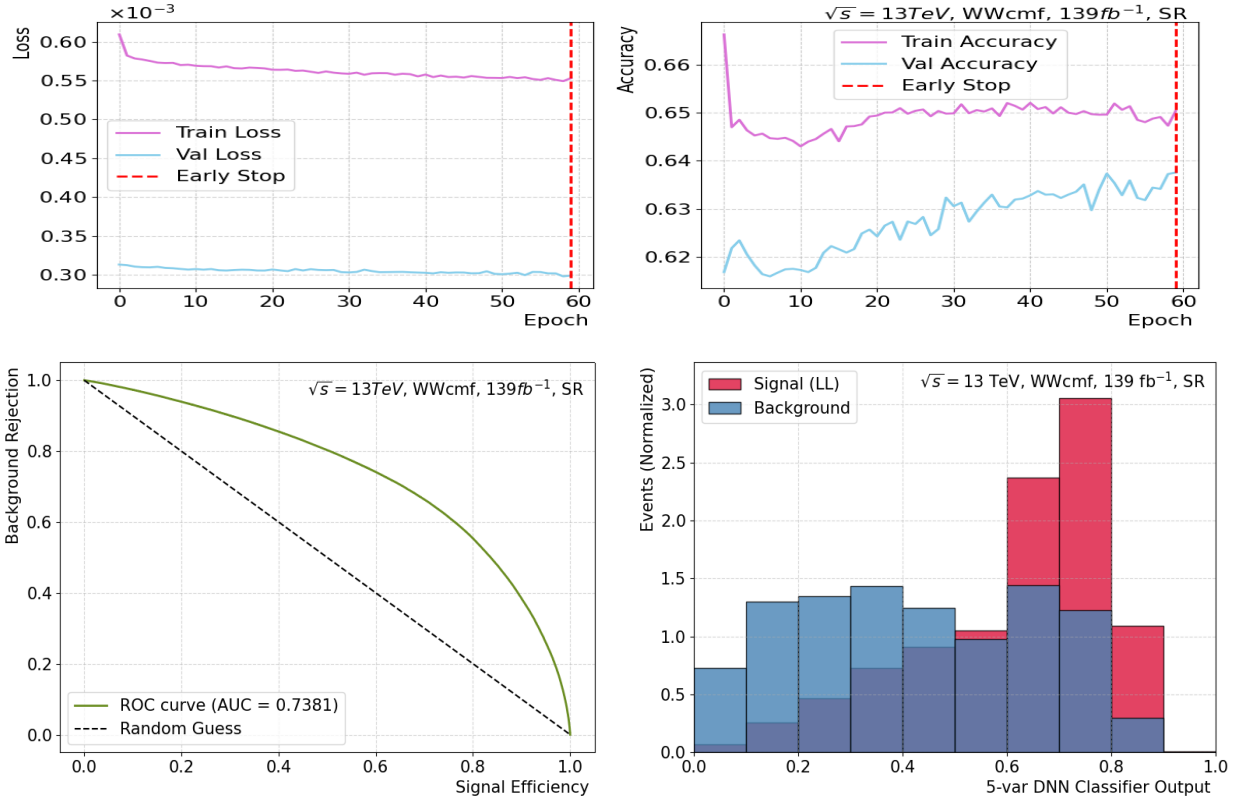


Figure C.2: 5-variable DNN performance plots. $Z = 1.2513$.

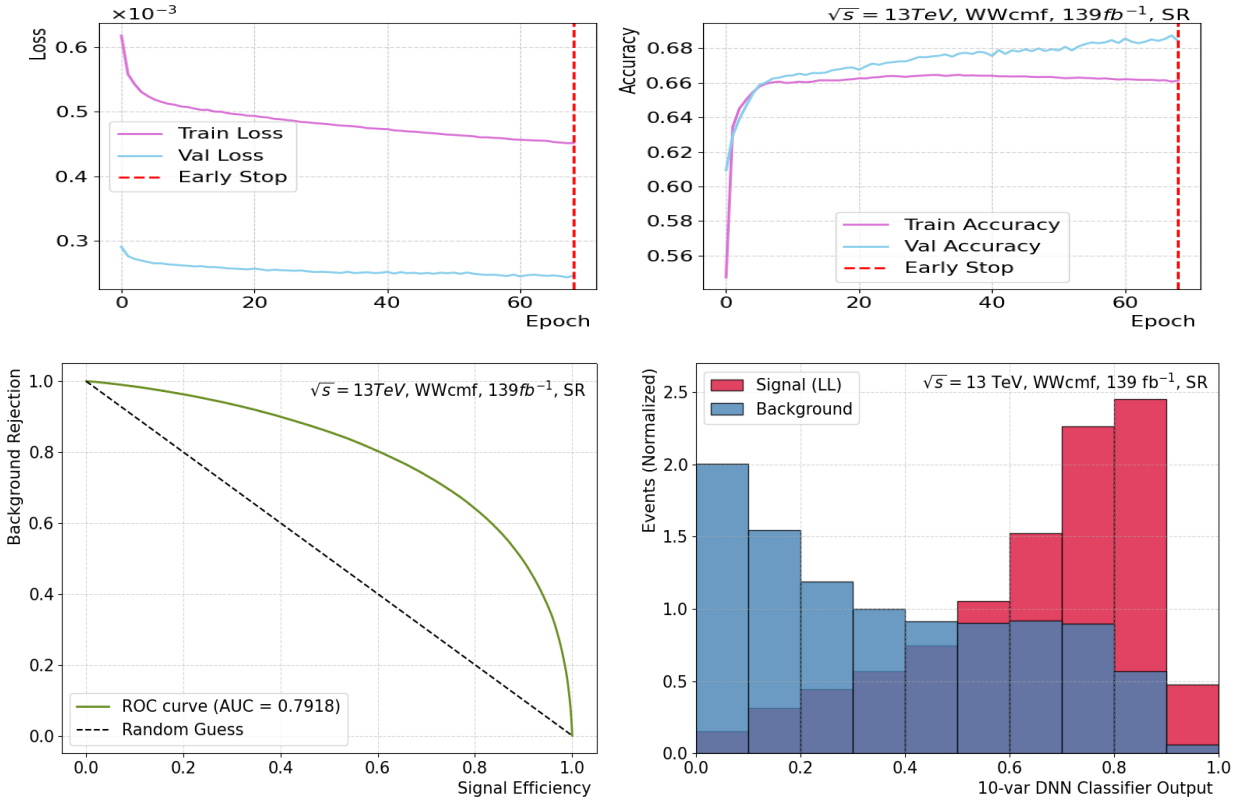


Figure C.3: 10-variable DNN performance plots. $Z = 1.6922$.

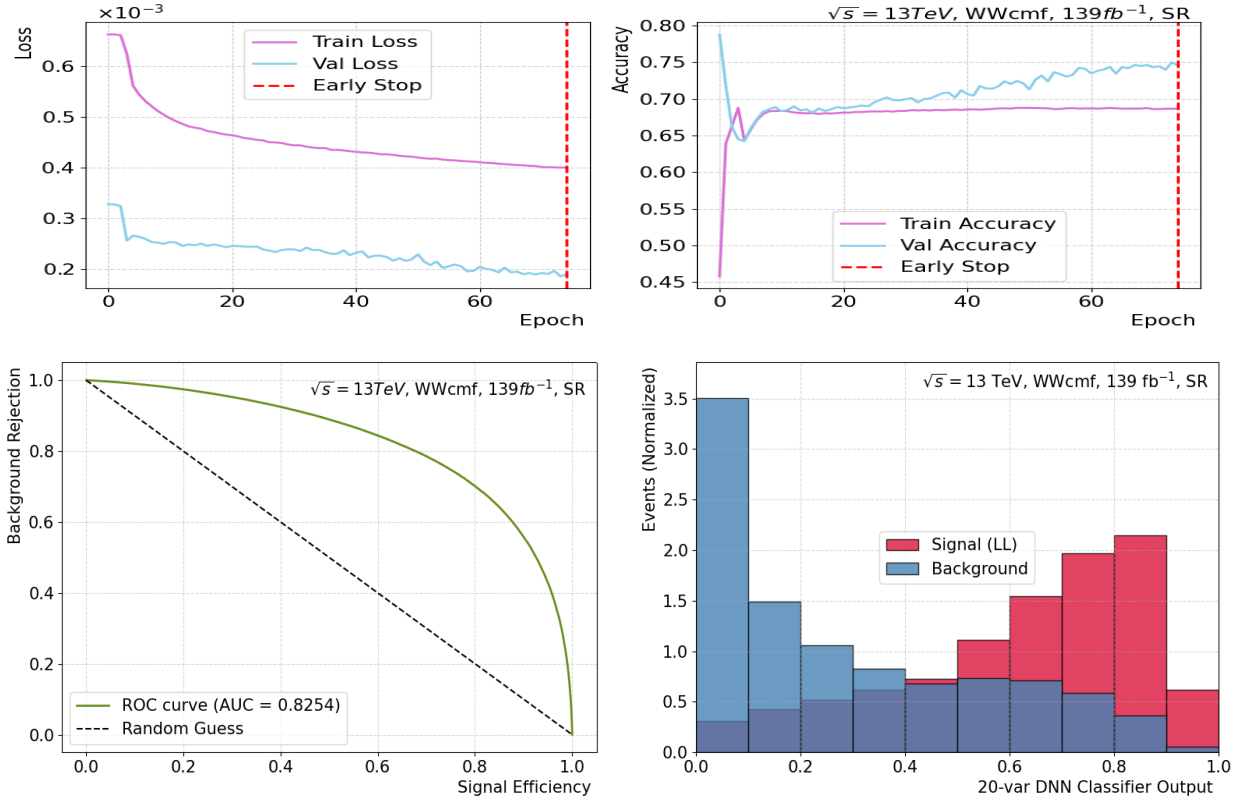


Figure C.4: 20-variable DNN performance plots. $Z = 2.1249$.

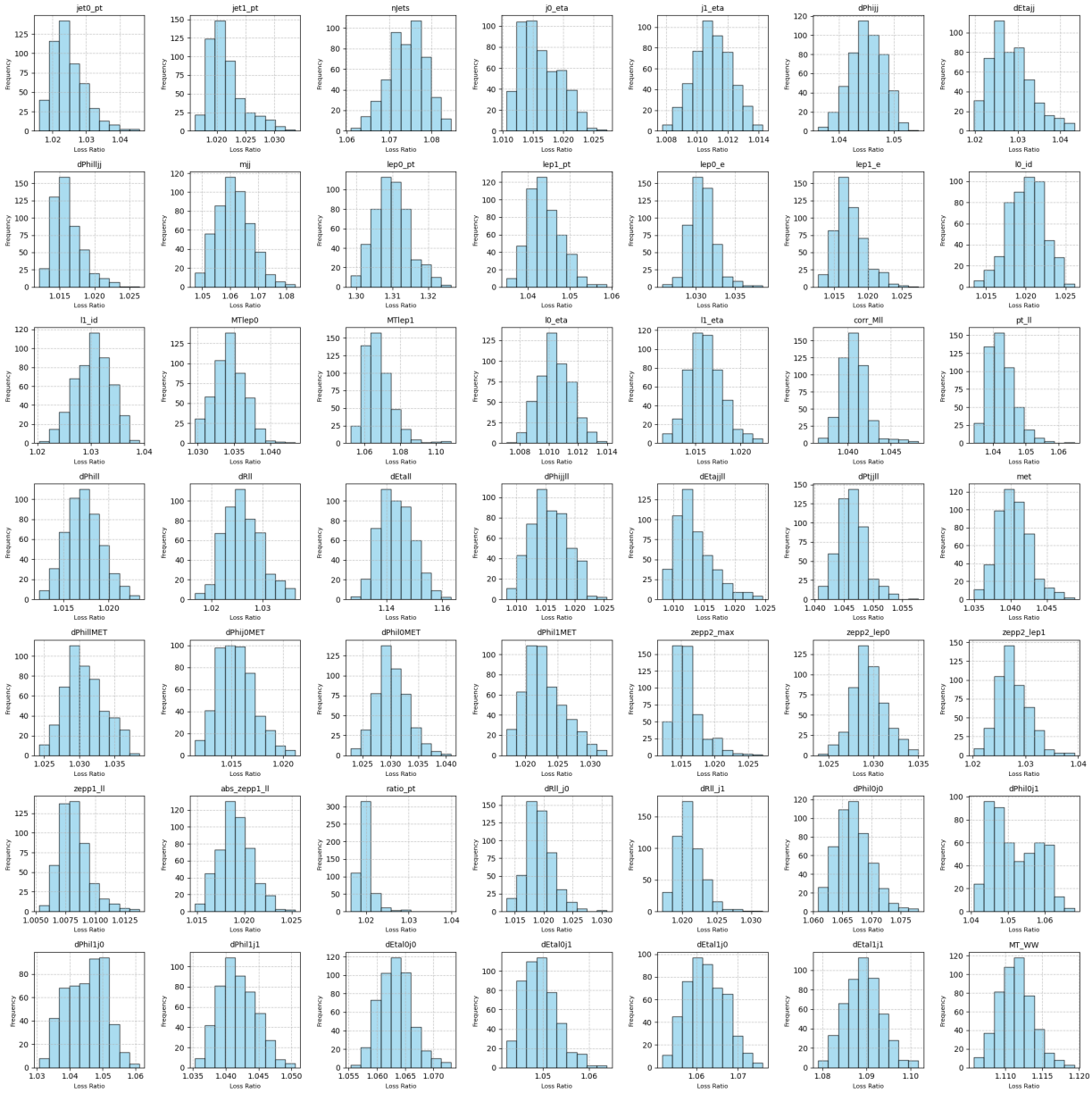


Figure C.5: Validation loss (FI) ratio distributions are shown for all 49 variables after 500 permutations. They are all roughly Guassians and indicate sufficient statistics being used.

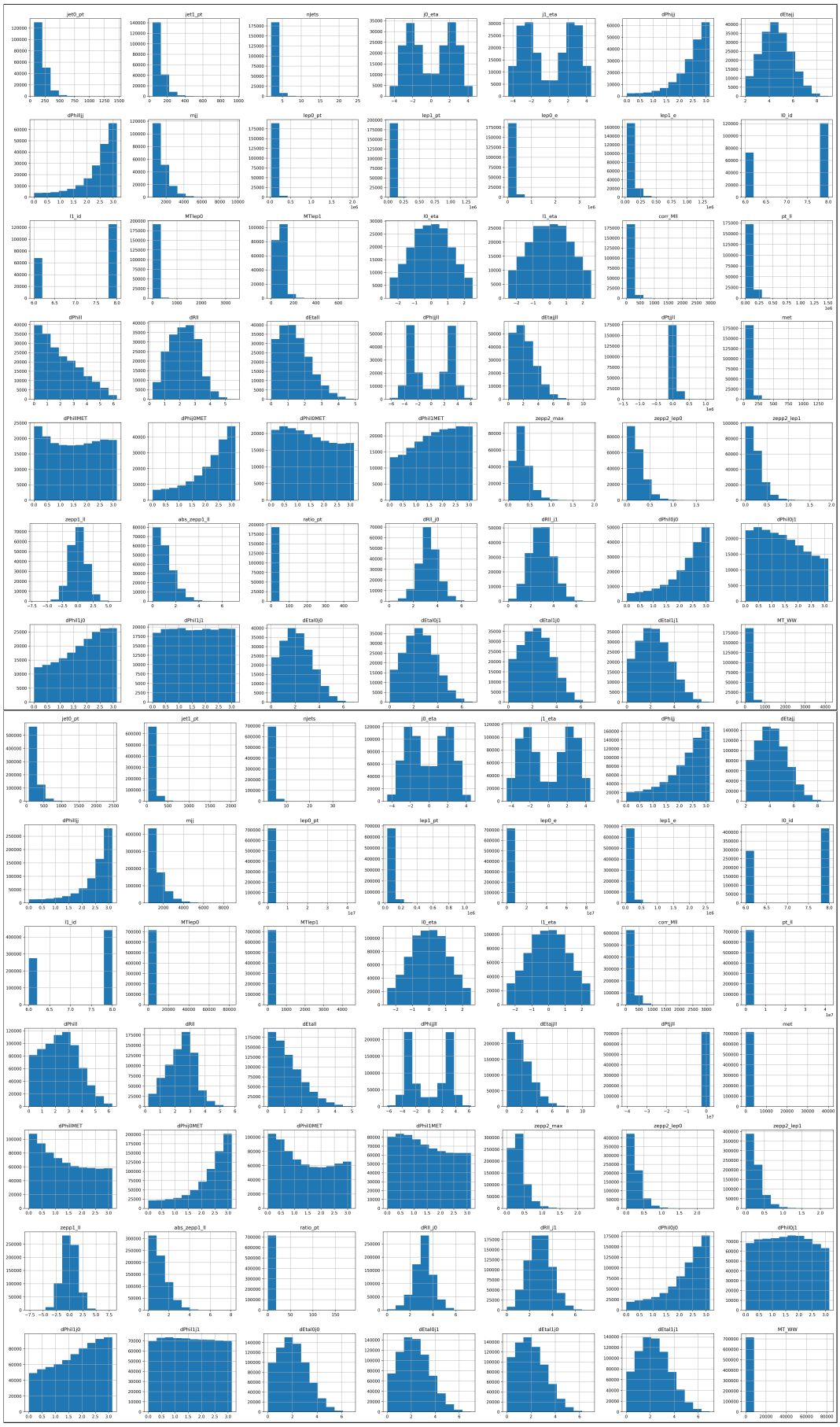


Figure C.6: Variables distributions of all 49 variables for signal (top) and backrounds (bottom).

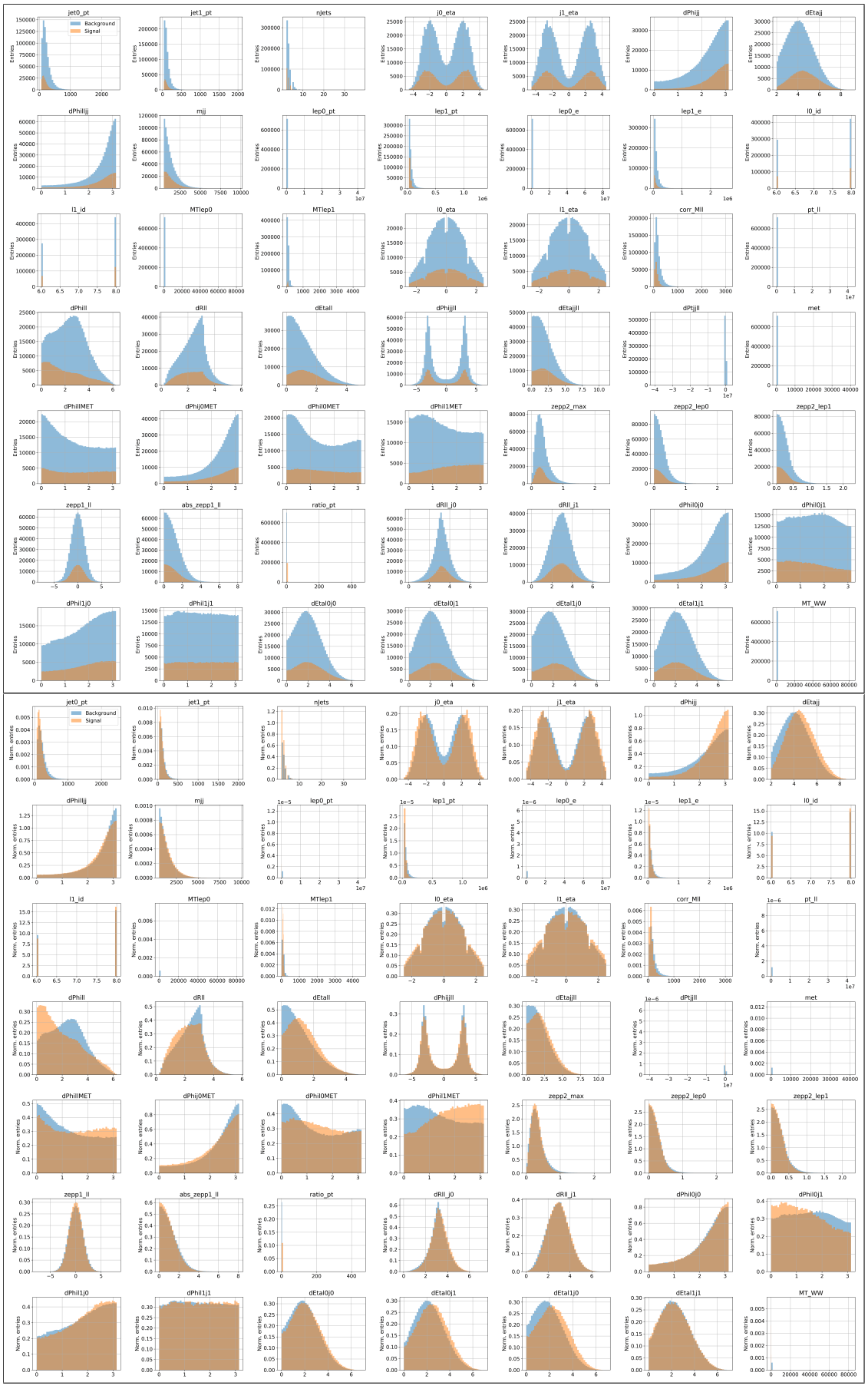


Figure C.7: Comparison of overlaid distributions for all 49 variables: raw distributions (top) and normalized distributions (bottom).

Appendix D

Signal Region Variable Distributions

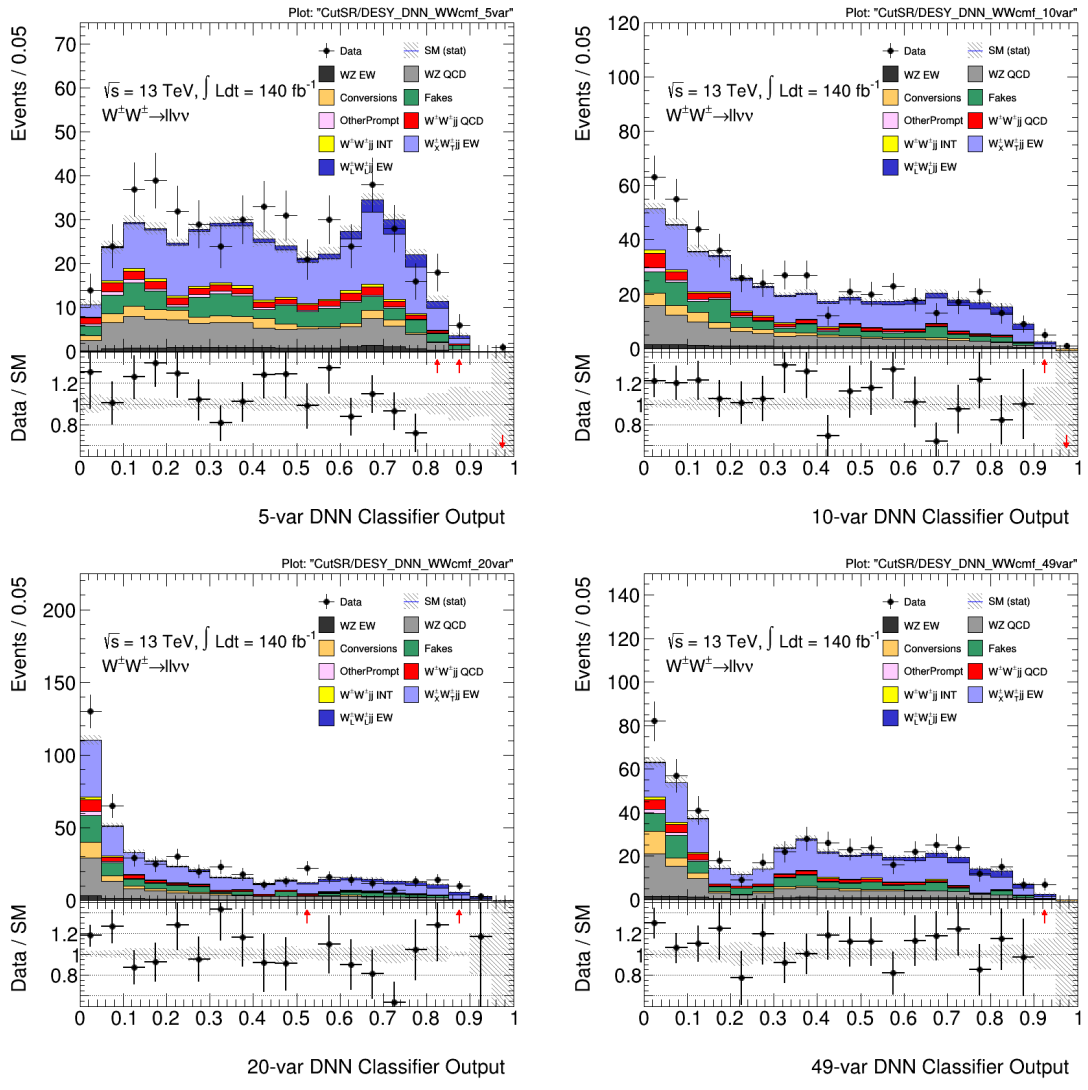


Figure D.1: Variable plots in Signal Region: Part 1.

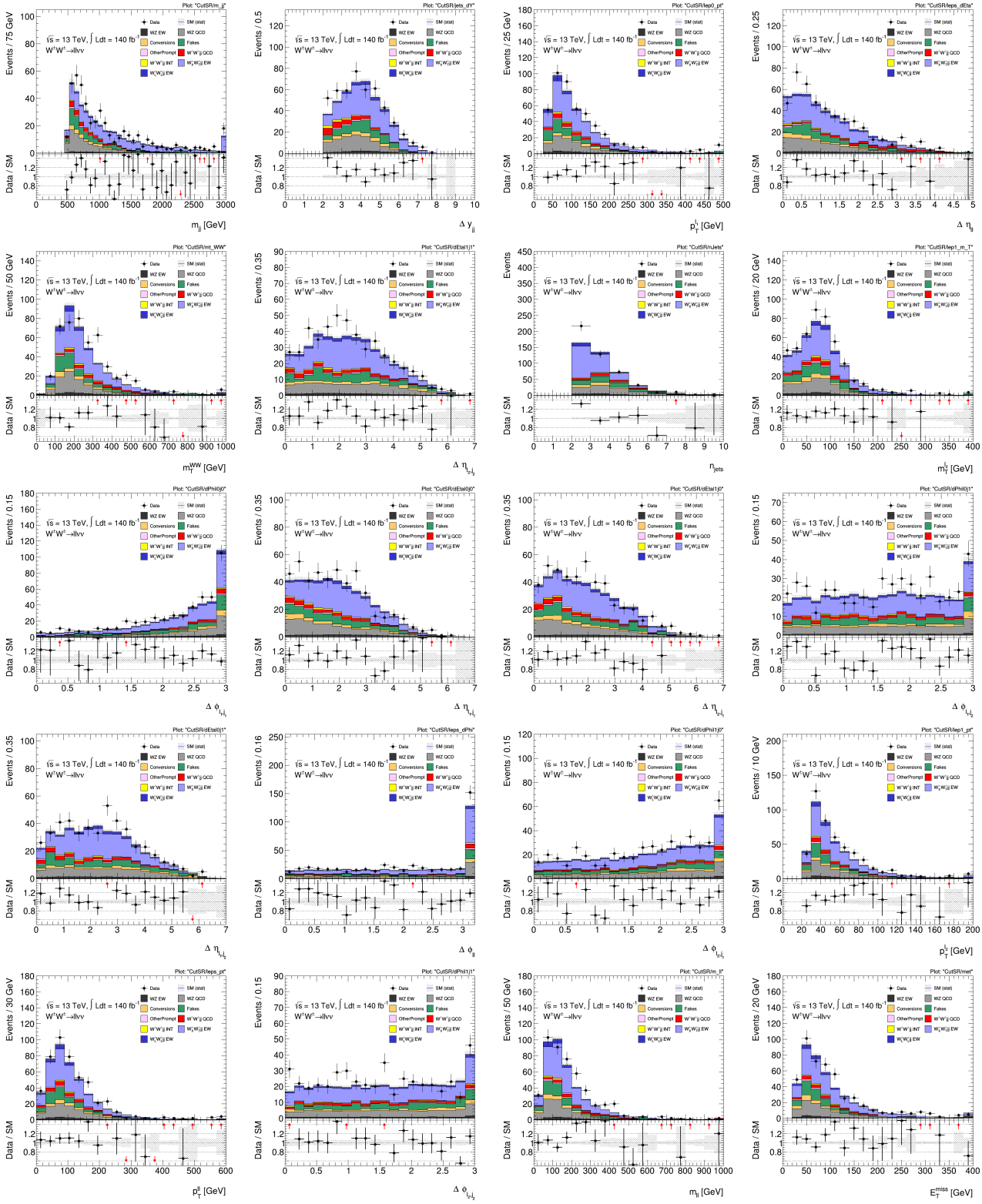


Figure D.2: Variable plots in Signal Region: Part 2.

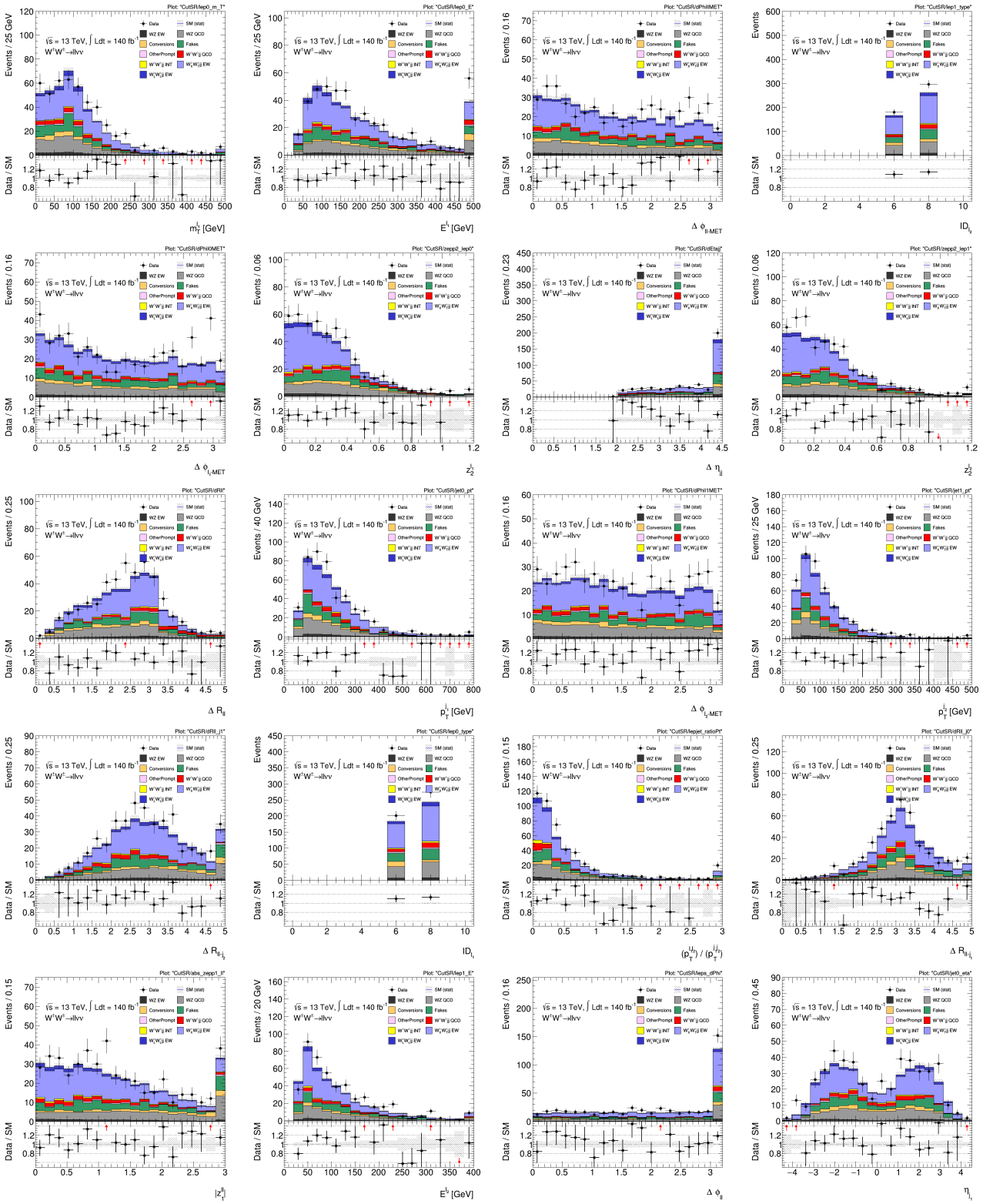


Figure D.3: Variable plots in Signal Region: Part 3.

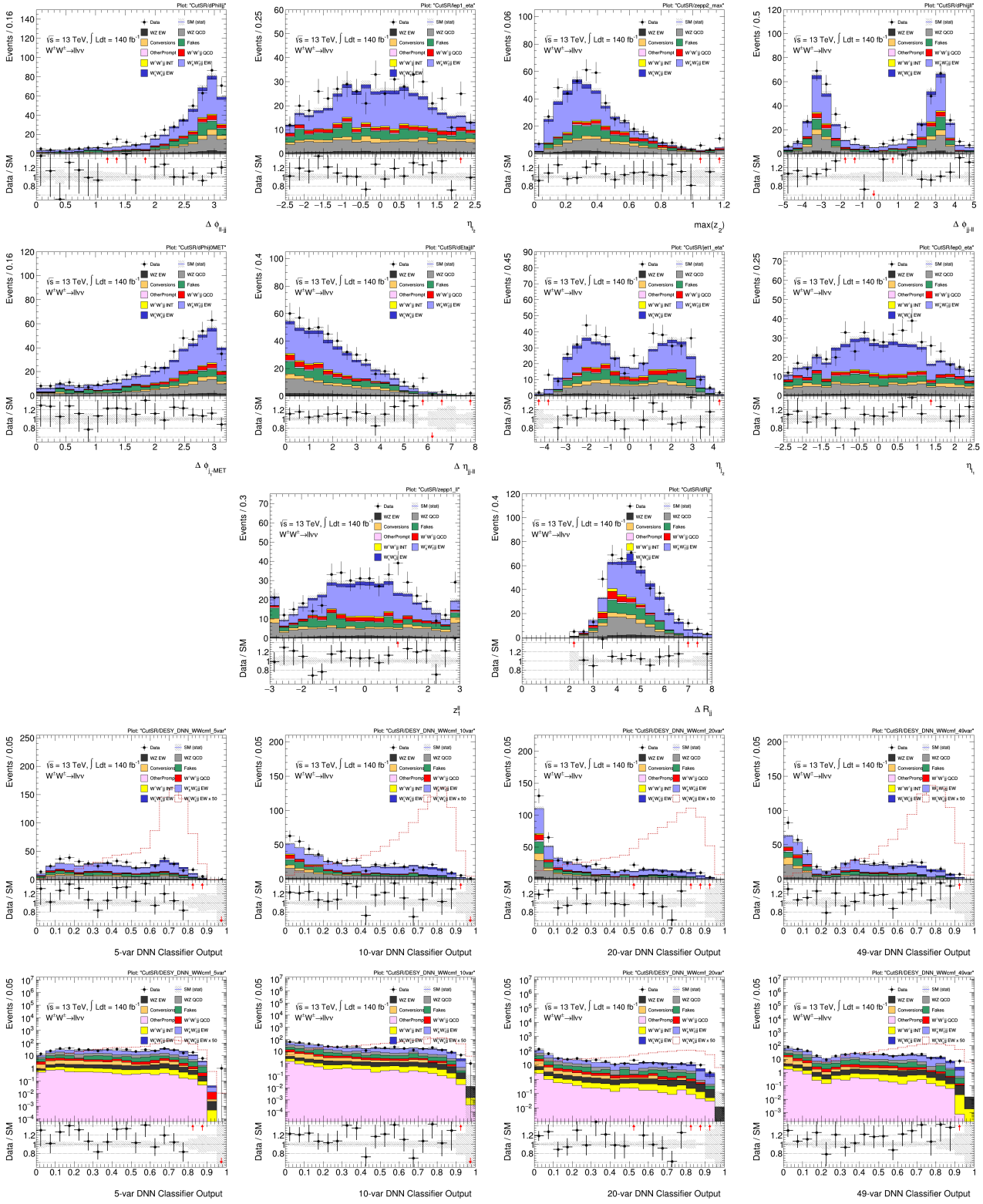


Figure D.4: Variable plots in Signal Region: Part 4.

Appendix E

Mathematical Formalism for Polarization Results

This appendix outlines the mathematical formalism used to extract the fiducial cross sections and polarization fractions for the signal process, based on the results of the profile-likelihood fit described in the main text.

E.1 Profile-Likelihood Fit and Signal Strength Parameters

The signal extraction is performed using a simultaneous binned likelihood fit across the signal and control regions, where two signal strength parameters (POIs) are introduced:

$$\mu_{LL} = \frac{\sigma_{LL}^{\text{meas}}}{\sigma_{LL}^{\text{SM}}}, \qquad \mu_{XT} = \frac{\sigma_{XT}^{\text{meas}}}{\sigma_{XT}^{\text{SM}}}, \tag{E.1}$$

with σ_{LL}^{SM} and σ_{XT}^{SM} denoting the SM predictions for the longitudinally polarized and transversely polarized (XT $\equiv$ LT + TT) components, respectively.

The likelihood function L is defined as

$$L(\mu_{LL}, \mu_{XT}, \theta) = \prod_i \text{Pois}(n_i | \nu_i(\mu_{LL}, \mu_{XT}, \theta)) \prod_{\text{bins}} P(\theta_\gamma | b) \prod_k G(\theta_k | 0, 1), \tag{E.2}$$

where n_i is the observed event count in bin i, ν_i is the expected yield parameterized in terms of $\mu_{LL}$and μ_{TX}, and θ represents nuisance parameters constrained by Gaussian terms G. The test

statistic is the profile likelihood ratio:

$$q(\mu_{LL},\mu_{XT}) = -2\ln\frac{\mathscr{L}(\mu_{LL},\mu_{XT},\hat{\hat{\theta}})}{\mathscr{L}(\hat{\mu}_{LL},\hat{\mu}_{XT},\hat{\theta})}, \tag{E.3}$$

where $\hat{\hat{\theta}}$ and $\hat{\theta}$ denote the conditional and global MLEs, respectively.

E.2 Fiducial Cross Section Determination

From Eq. E.1, the fiducial cross sections corresponding to each polarization mode are directly obtained as:

$$\sigma_{LL}^{\text{meas}} = \mu_{LL}\,\sigma_{LL}^{\text{SM}}, \tag{E.4}$$
$$\sigma_{XT}^{\text{meas}} = \mu_{XT}\,\sigma_{XT}^{\text{SM}}. \tag{E.5}$$

The total fiducial cross section is defined as the sum of both polarization contributions:

$$\sigma_{\text{tot}}^{\text{meas}} = \sigma_{LL}^{\text{meas}} + \sigma_{XT}^{\text{meas}}. \tag{E.6}$$

The uncertainties on $\sigma_{LL}^{\text{meas}}$ and $\sigma_{XT}^{\text{meas}}$ are propagated from the fitted signal strengths, taking into account their correlation $\rho(\mu_{LL},\mu_{XT})$:

$$\text{Var}(\sigma_{\text{tot}}) = (\sigma_{LL}^{\text{SM}})^2\text{Var}(\mu_{LL}) + (\sigma_{XT}^{\text{SM}})^2\text{Var}(\mu_{XT}) + 2\rho(\mu_{LL},\mu_{XT})\sigma_{LL}^{\text{SM}}\sigma_{XT}^{\text{SM}}\text{Cov}(\mu_{LL},\mu_{XT}). \tag{E.7}$$

E.3 Polarization Fraction and Upper Limit

The longitudinal polarization fraction within the fiducial phase space is defined as:

$$f_{LL} = \frac{\sigma_{LL}^{\text{meas}}}{\sigma_{\text{tot}}^{\text{meas}}}. \tag{E.8}$$

The uncertainty on f_{LL} is obtained via standard error propagation:

$$\text{Var}(f_{LL}) = \left(\frac{\partial f_{LL}}{\partial \sigma_{LL}}\right)^2\text{Var}(\sigma_{LL}) + \left(\frac{\partial f_{LL}}{\partial \sigma_{XT}}\right)^2\text{Var}(\sigma_{XT}) + 2\frac{\partial f_{LL}}{\partial \sigma_{LL}}\frac{\partial f_{LL}}{\partial \sigma_{XT}}\text{Cov}(\sigma_{LL},\sigma_{XT}). \tag{E.9}$$

A 95% CL upper limit on the longitudinal component is derived using the asymptotic approximation [171]:

$$\mu_{LL}^{\mathrm{UL}} = \hat{\mu}_{LL} + 1.64\,\sigma_{\mu_{LL}}, \tag{E.10}$$

which is then translated into a fiducial upper limit as

$$\sigma_{LL}^{\mathrm{UL}} = \mu_{LL}^{\mathrm{UL}} \times \sigma_{LL}^{\mathrm{SM}}, \qquad f_{LL}^{\mathrm{UL}} = \frac{\sigma_{LL}^{\mathrm{UL}}}{\sigma_{\mathrm{tot}}^{\mathrm{SM}}}. \tag{E.11}$$

Appendix F

Fit Results

F.1 Limits and Significances

Asimov:

Listing F.1: Asimov limits

```
obs upperlimit  = -1
exp upperlimit  = 1.55072
exp upperlimit plus1 = 2.23097
exp upperlimit plus2 = 3.10544
exp upperlimit minus1 = 1.08989
exp upperlimit minus2 = 0.798075
inj upperlimit  = 2.46843
parameter       = 0
```

Listing F.2: Asimov significance

```
obs pvalue      = -1
exp pvalue      = 0.0960724
inj pvalue      = 0.0960724
obs significance = -1
exp significance = 1.30426
inj significance = 1.30426
```

Unblinded:

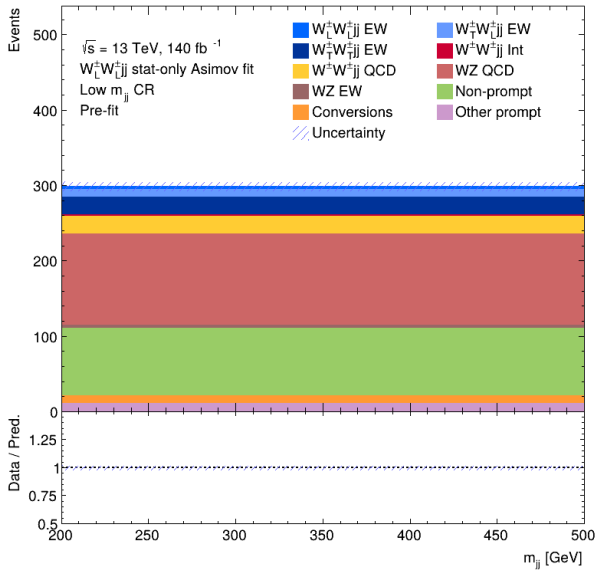
Listing F.3: Unblinded limits

```
obs upperlimit  = 1.82481
exp upperlimit  = 1.71628
exp upperlimit plus1 = 2.46224
exp upperlimit plus2 = 3.41733
exp upperlimit minus1 = 1.20888
exp upperlimit minus2 = 0.886734
inj upperlimit  = 2.46843
parameter       = 0
```

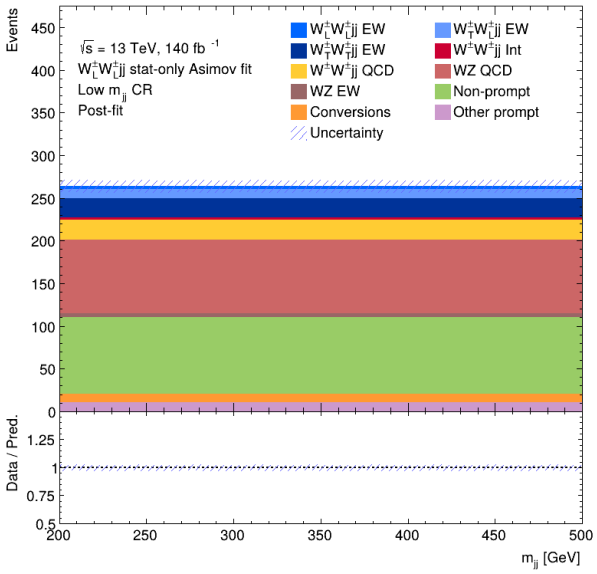
Listing F.4: Unblinded significance

```
obs pvalue      = 0.388995
exp pvalue      = 0.11415
inj pvalue      = 0.0960724
obs significance = 0.281939
exp significance = 1.20475
inj significance = 1.30426
```

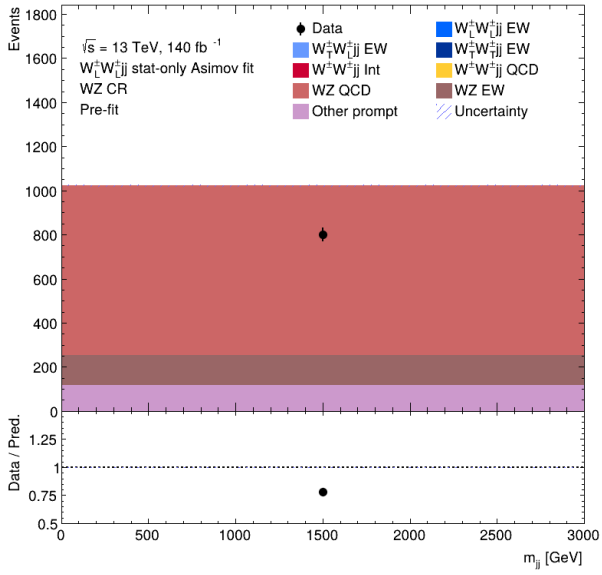
F.2 Fit Plots and Tables



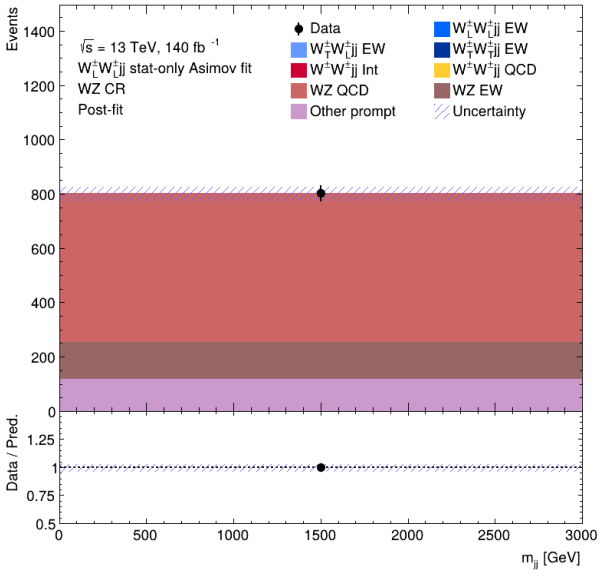
(a) Asimov LowMjjCR pre-fit: m_{jj}



(b) Asimov LowMjjCR post-fit: m_{jj}

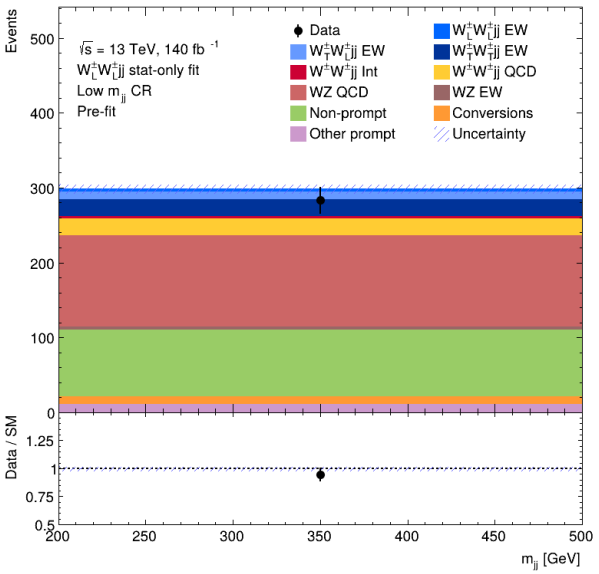


(c) Asimov WZ pre-fit: m_{jj}

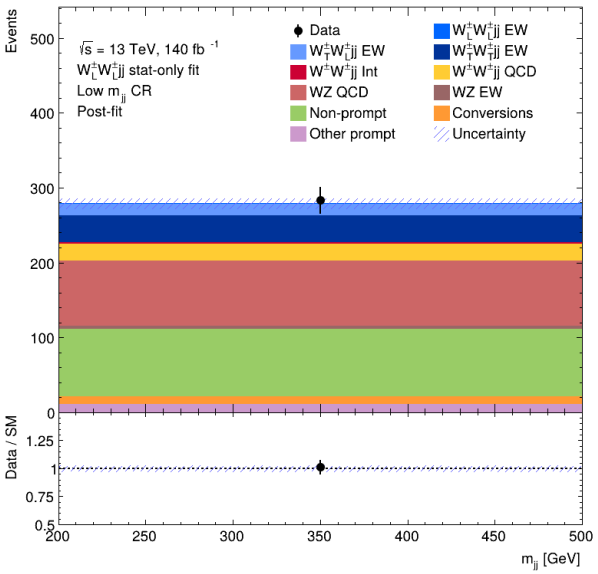


(d) Asimov WZ post-fit: m_{jj}

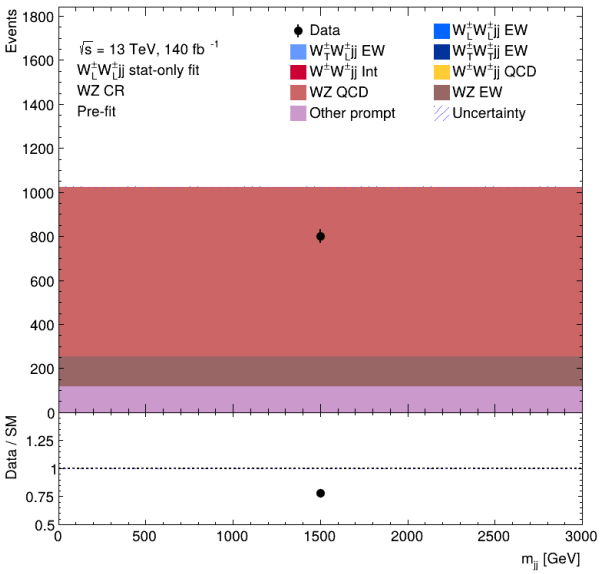
Figure F.1: Asimov fit: CRs (stat-only).



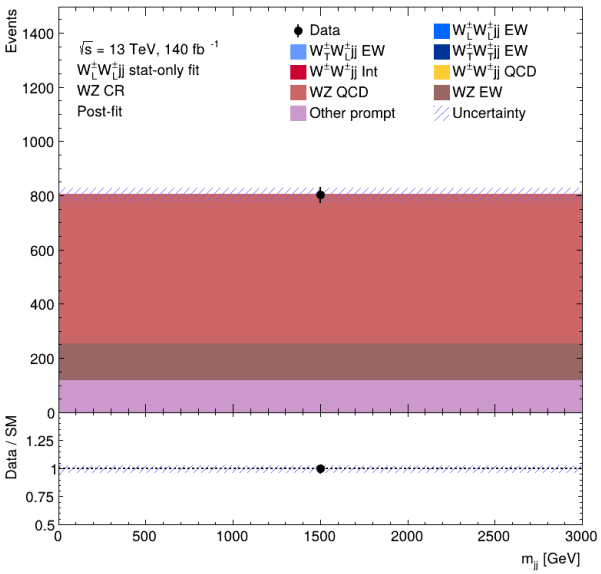
(a) Unblinded LowMjjCR pre-fit: m_{jj}



(b) Unblinded LowMjjCR post-fit: m_{jj}

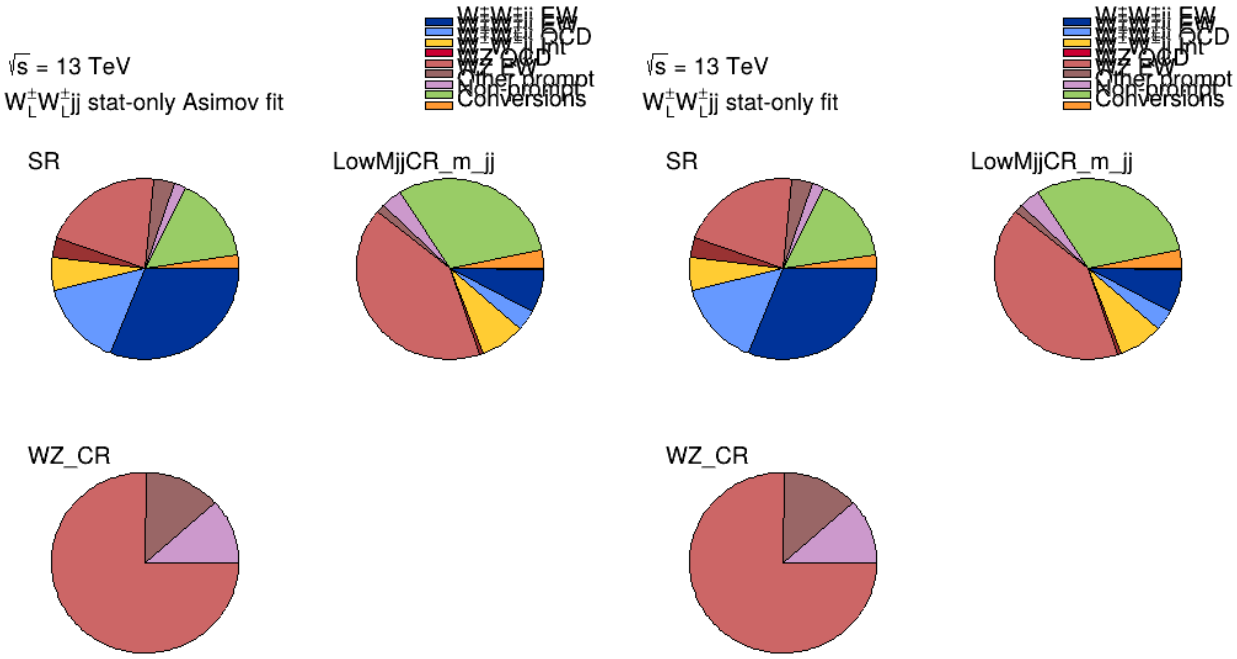


(c) Unblinded WZ pre-fit: m_{jj}



(d) Unblinded WZ post-fit: m_{jj}

Figure F.2: Unblinded fit: CRs (stat-only).



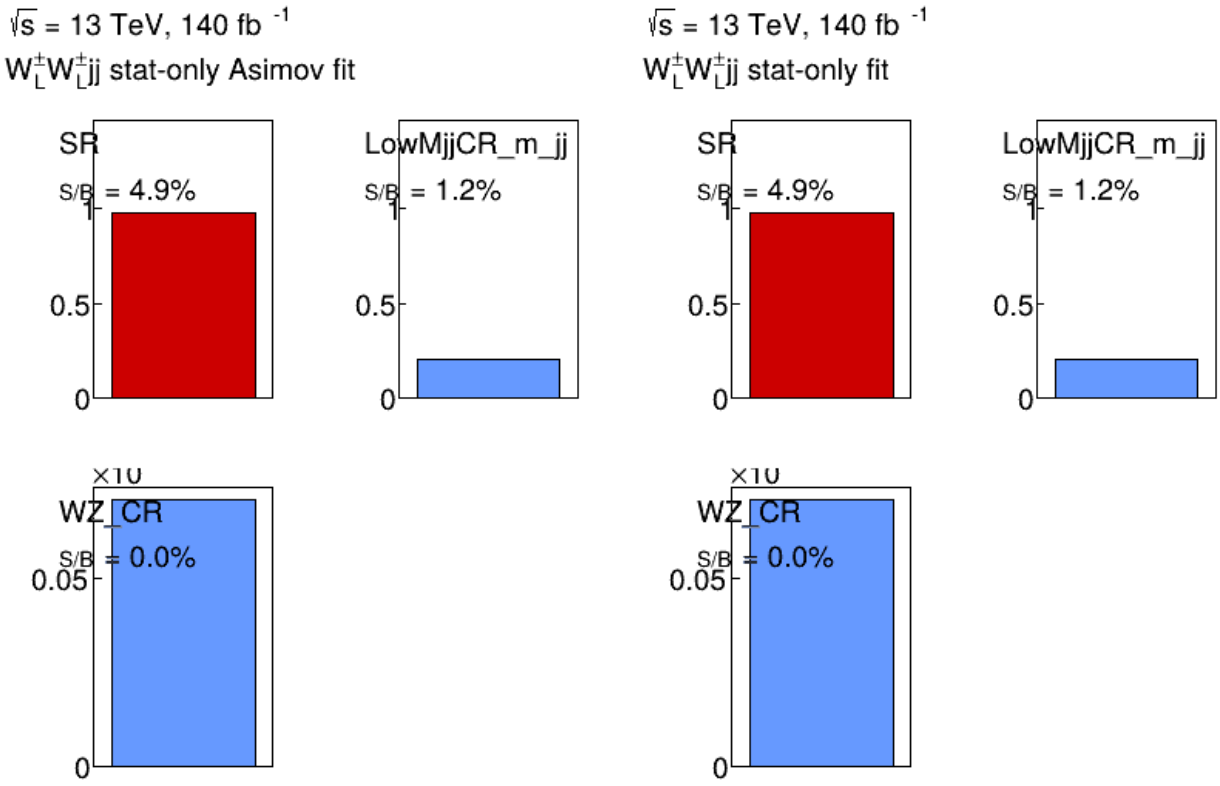
(a) Asimov pre-fit: Yields

(b) Unblinded post-fit: Yields

Figure F.3: Asimov and Unblinded fit: Yields (stat-only).

	Signal Region	Low-m_{jj} CR	WZ CR
$W_L^\pm W_L^\pm jj$ EW	19.56 ± 0.39	3.53 ± 0.07	0.00 ± 0.00
$W_T^\pm W_L^\pm jj$ EW	60.15 ± 0.84	10.51 ± 0.22	0.01 ± 0.00
$W_T^\pm W_T^\pm jj$ EW	124.52 ± 1.72	23.17 ± 0.49	0.02 ± 0.00
$W^\pm W^\pm jj$ Int	13.63 ± 0.19	2.40 ± 0.05	0.02 ± 0.00
$W^\pm W^\pm jj$ QCD	24.26 ± 0.34	22.97 ± 0.48	0.01 ± 0.00
WZ QCD	83.48 ± 1.18	121.21 ± 2.56	769.80 ± 2.20
WZ EW	15.08 ± 0.20	4.18 ± 0.09	135.44 ± 0.39
Non-prompt	61.28 ± 0.87	89.87 ± 1.90	0.00 ± 0.00
Conversions	10.10 ± 0.16	10.29 ± 0.22	0.00 ± 0.00
Other prompt	8.16 ± 0.12	10.64 ± 0.22	117.93 ± 0.34
Total	420.21 ±5.64	298.77 ±6.30	1023.23 ±2.92
Data	475	283	802

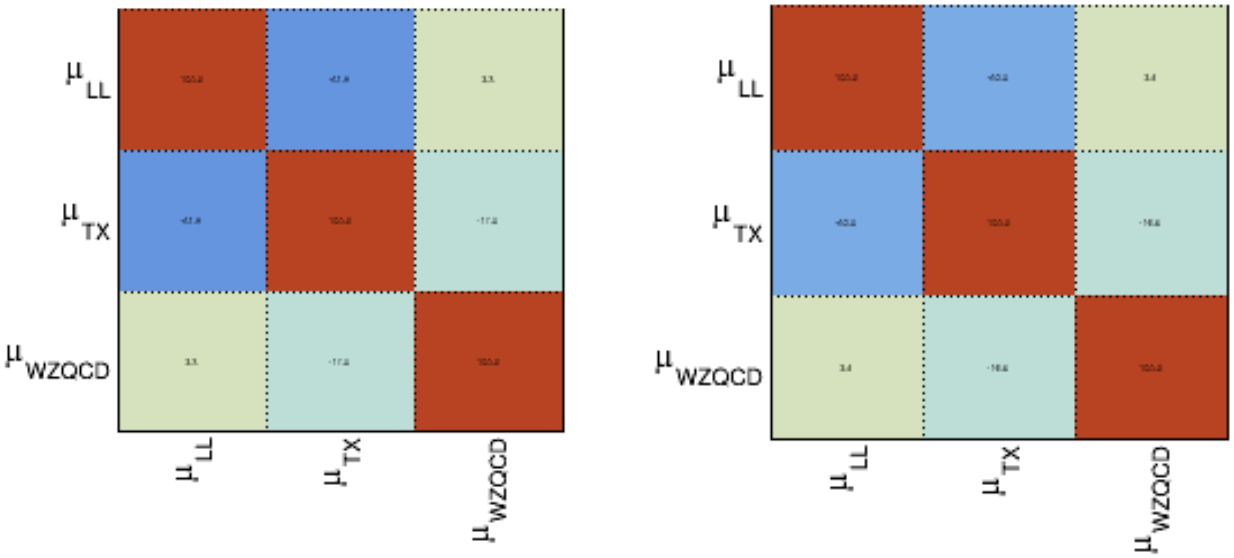
Table F.1: Yields of the analysis (Asimov pre-fit).



(a) Asimov: Signal Contribution

(b) Unblinded: Signal Contribution

Figure F.4: Asimov and Unblinded fit: Signal Contribution (stat-only).



(a) Asimov fit: Correlation Matrix ($\mu_{LL}-\mu_{TX}$=-0.619)

(b) Unblinded fit: Correlation Matrix ($\mu_{LL}-\mu_{TX}$=-0.6)

Figure F.5: Asimov and Unblinded fit: Correlation Matrix.

Bibliography

[1] G. Aad *et al.*, [ATLAS], "Evidence for Longitudinally Polarized W Bosons in the Electroweak Production of Same-Sign W Boson Pairs in Association with Two Jets in pp Collisions at s=13 TeV with the ATLAS Detector," *Phys. Rev. Lett.* **135** no. 11, (2025) 111802, arXiv:2503.11317 [hep-ex].

[2] M. Aaboud *et al.*, [ATLAS], "Electron reconstruction and identification in the ATLAS experiment using the 2015 and 2016 LHC proton-proton collision data at $\sqrt{s}$ = 13 TeV," *Eur. Phys. J. C* **79** no. 8, (2019) 639, arXiv:1902.04655 [physics.ins-det].

[3] S. Rettie, [ATLAS], "Muon identification and performance in the ATLAS experiment," *PoS* **DIS2018** (2018) 097.

[4] G. Aad *et al.*, [ATLAS], "Measurement and interpretation of same-sign W boson pair production in association with two jets in pp collisions at $\sqrt{s}$ = 13 TeV with the ATLAS detector," *JHEP* **04** (2024) 026, arXiv:2312.00420 [hep-ex].

[5] J. A. Fernandez Pretel, "Estimation of the electron charge misidentification background for the same-sign *ww* measurement with the atlas detector at $\sqrt{s} = 13$ tev," 2020.

[6] S. Solomon, *The first measurement of the differential cross-section of electroweak $W^{\pm}W^{\pm}jj$ production at 13 TeV with the ATLAS detector*. PhD thesis, Freiburg U., University of Freiburg, 2023.

[7] M. E. Peskin and D. V. Schroeder, *An Introduction to quantum field theory*. Addison-Wesley, Reading, USA, 1995.

[8] C. P. Burgess and G. D. Moore, *The standard model: A primer*. Cambridge University Press, 12, 2006.

[9] W. Hollik, "Quantum field theory and the standard model," 2010. https://arxiv.org/abs/1012.3883.

[10] C. Berger and G. Herten, *Particle Physics: From the Basics to Modern Experiments*. Springer Berlin, Heidelberg, 1 ed., 2025.

[11] A. Purcell, "Go on a particle quest at the first CERN webfest. Le premier webfest du CERN se lance à la conquête des particules,". https://cds.cern.ch/record/1473657.

[12] S. L. Glashow, "Partial Symmetries of Weak Interactions," *Nucl. Phys.* **22** (1961) 579–588.

[13] S. Weinberg, "A Model of Leptons," *Phys. Rev. Lett.* **19** (1967) 1264–1266.

[14] A. Salam, "Weak and Electromagnetic Interactions," *Conf. Proc. C* **680519** (1968) 367–377.

[15] ATLAS Collaboration, "Observation of a new particle in the search for the Standard Model Higgs boson with the ATLAS detector at the LHC," *Phys. Lett. B* **716** (2012) 1, arXiv:1207.7214 [hep-ex].

[16] CMS Collaboration, "Observation of a new boson at a mass of 125 GeV with the CMS experiment at the LHC," *Phys. Lett. B* **716** (2012) 30, arXiv:1207.7235 [hep-ex].

[17] Y. Nambu, "The Confinement of Quarks," *Sci. Am.* **235N5** (1976) 48–70.

[18] A. R. *et al.*, [LHCb Collaboration], "Observation of $j/\psi p$ resonances consistent with pentaquark states in $\Lambda_b^0 \to j/\psi K^- p$ decays," *Phys. Rev. Lett.* **115** (Aug, 2015) 072001. https://link.aps.org/doi/10.1103/PhysRevLett.115.072001.

[19] D. J. Gross and F. Wilczek, "Ultraviolet behavior of non-abelian gauge theories," *Phys. Rev. Lett.* **30** (Jun, 1973) 1343–1346. https://link.aps.org/doi/10.1103/PhysRevLett.30.1343.

[20] H. D. Politzer, "Reliable perturbative results for strong interactions?," *Phys. Rev. Lett.* **30** (Jun, 1973) 1346–1349. https://link.aps.org/doi/10.1103/PhysRevLett.30.1346.

[21] P. W. Higgs, "Broken symmetries, massless particles and gauge fields," *Phys. Lett.* **12** (1964) 132–133.

[22] P. W. Higgs, "Broken Symmetries and the Masses of Gauge Bosons," *Phys. Rev. Lett.* **13** (1964) 508–509.

[23] F. Englert and R. Brout, "Broken Symmetry and the Mass of Gauge Vector Mesons," *Phys. Rev. Lett.* **13** (1964) 321–323.

[24] G. Guralnik, C. Hagen, and T. Kibble, "Global Conservation Laws and Massless Particles," *Phys. Rev. Lett.* **13** (1964) 585–587.

[25] P. W. Higgs, "Spontaneous symmetry breakdown without massless bosons," *Phys. Rev.* **145** (1966) 1156–1163.

[26] T. Kibble, "Symmetry breaking in non-Abelian gauge theories," *Phys. Rev.* **155** (1967) 1554–1561.

[27] S. Kottwitz, I. Neutelings, and A. Tsagkaropolulos, "TikZ.net – Graphics with TikZ in LaTeX." https://tikz.net/, 2021. A gallery of TikZ examples and figures. Accessed: 2025-10-05.

[28] N. Arkani–Hamed, S. Dimopoulos, and G. Dvali, "The hierarchy problem and new dimensions at a millimeter," *Physics Letters B* **429** no. 3, (1998) 263–272. https://www.sciencedirect.com/science/article/pii/S0370269398004663.

[29] D. Clowe, M. Bradač, A. H. Gonzalez, M. Markevitch, S. W. Randall, C. Jones, and D. Zaritsky, "A direct empirical proof of the existence of dark matter*," *The Astrophysical Journal* **648** no. 2, (Aug, 2006) L109. https://doi.org/10.1086/508162.

[30] A. G. Riess, A. V. Filippenko, P. Challis, A. Clocchiatti, A. Diercks, P. M. Garnavich, R. L. Gilliland, C. J. Hogan, S. Jha, R. P. Kirshner, B. Leibundgut, M. M. Phillips, D. Reiss, B. P. Schmidt, R. A. Schommer, R. C. Smith, J. Spyromilio, C. Stubbs, N. B. Suntzeff, and J. Tonry, "Observational evidence from supernovae for an accelerating universe and a cosmological constant," *The Astronomical Journal* **116** no. 3, (Sep, 1998) 1009. https://doi.org/10.1086/300499.

[31] A. D. Sakharov, "Violation of cp invariance, c asymmetry, and baryon asymmetry of the universe," *Soviet Physics Uspekhi* **34** no. 5, (May, 1991) 392. https://doi.org/10.1070/PU1991v034n05ABEH002497.

[32] Y. Fukuda *et al.*, [Super-Kamiokande Collaboration], "Evidence for oscillation of atmospheric neutrinos," *Phys. Rev. Lett.* **81** (Aug, 1998) 1562–1567. https://link.aps.org/doi/10.1103/PhysRevLett.81.1562.

[33] Q. R. Ahmad *et al.*, [SNO Collaboration], "Measurement of the rate of $\nu_e + d \to p + p + e^-$ interactions produced by ^8b solar neutrinos at the sudbury neutrino observatory," *Phys. Rev. Lett.* **87** (Jul, 2001) 071301. https://link.aps.org/doi/10.1103/PhysRevLett.87.071301.

[34] R. P. Feynman, "Very high-energy collisions of hadrons," *Phys. Rev. Lett.* **23** (1969) 1415–1417.

[35] V. N. Gribov and L. N. Lipatov, "Deep inelastic e p scattering in perturbation theory," *Sov. J. Nucl. Phys.* **15** (1972) 438–450.

[36] G. Altarelli and G. Parisi, "Asymptotic Freedom in Parton Language," *Nucl. Phys. B* **126** (1977) 298–318.

[37] Y. L. Dokshitzer, "Calculation of the Structure Functions for Deep Inelastic Scattering and e+ e- Annihilation by Perturbation Theory in Quantum Chromodynamics.," *Sov. Phys. JETP* **46** (1977) 641–653.

[38] R. D. Ball *et al.*, [NNPDF], "Parton distributions from high-precision collider data," *Eur. Phys. J. C* **77** no. 10, (2017) 663, arXiv:1706.00428 [hep-ph].

[39] J. C. Collins and D. E. Soper, "The Theorems of Perturbative QCD," *Ann. Rev. Nucl. Part. Sci.* **37** (1987) 383–409.

[40] S. Höche, "Introduction to parton-shower event generators," 2015. https://arxiv.org/abs/1411.4085.

[41] B. Andersson, G. Gustafson, G. Ingelman, and T. Sjostrand, "Parton Fragmentation and String Dynamics," *Phys. Rept.* **97** (1983) 31–145.

[42] J.-C. Winter, F. Krauss, and G. Soff, "A Modified cluster hadronization model," *Eur. Phys. J. C* **36** (2004) 381–395, arXiv:hep-ph/0311085.

[43] S. Frixione and B. R. Webber, "Matching NLO QCD computations and parton shower simulations," *JHEP* **06** (2002) 029, arXiv:hep-ph/0204244.

[44] J. Alwall, R. Frederix, S. Frixione, V. Hirschi, F. Maltoni, O. Mattelaer, H. S. Shao, T. Stelzer, P. Torrielli, and M. Zaro, "The automated computation of tree-level and next-to-leading order differential cross sections, and their matching to parton shower simulations," *JHEP* **07** (2014) 079, arXiv:1405.0301 [hep-ph].

[45] T. Sjöstrand, S. Ask, J. R. Christiansen, R. Corke, N. Desai, P. Ilten, S. Mrenna, S. Prestel, C. O. Rasmussen, and P. Z. Skands, "An introduction to PYTHIA 8.2," *Comput. Phys. Commun.* **191** (2015) 159, arXiv:1410.3012 [hep-ph].

[46] E. Bothmann *et al.*, [Sherpa], "Event Generation with Sherpa 2.2," *SciPost Phys.* **7** no. 3, (2019) 034, arXiv:1905.09127 [hep-ph].

[47] J. Bellm *et al.*, "Herwig 7.2 release note," *Eur. Phys. J. C* **80** no. 5, (2020) 452, arXiv:1912.06509 [hep-ph].

[48] W. Kilian, M. Sekulla, T. Ohl, and J. Reuter, "High-energy vector boson scattering after the higgs boson discovery," *Phys. Rev. D* **91** (May, 2015) 096007. https://link.aps.org/doi/10.1103/PhysRevD.91.096007.

[49] A. Denner and T. Hahn, "Radiative corrections to W+ W- —> W+ W- in the electroweak standard model," *Nucl. Phys. B* **525** (1998) 27–50, arXiv:hep-ph/9711302.

[50] C. Bittrich, "Study of Polarization Fractions in the Scattering of Massive Gauge Bosons $W^{\pm}Z \to W^{\pm}Z$ with the ATLAS Detector at the Large Hadron Collider," 2015. https://cds.cern.ch/record/2014124. Presented 2015.

[51] [ATLAS], "Standard Model Summary Plots October 2023," tech. rep., CERN, Geneva, 2023. https://cds.cern.ch/record/2882448. All figures including auxiliary figures are available at https://atlas.web.cern.ch/Atlas/GROUPS/PHYSICS/PUBNOTES/ATL-PHYS-PUB-2023-039.

[52] [ATLAS], "Standard Model Summary Plots June 2024," tech. rep., CERN, Geneva, 2024. https://cds.cern.ch/record/2903866. All figures including auxiliary figures are available at https://atlas.web.cern.ch/Atlas/GROUPS/PHYSICS/PUBNOTES/ATL-PHYS-PUB-2024-011.

[53] M. Rauch, "Vector-Boson Fusion and Vector-Boson Scattering," arXiv:1610.08420 [hep-ph].

[54] R. L. Workman and Others, [Particle Data Group], "Review of Particle Physics," *PTEP* **2022** (2022) 083C01.

[55] C. Gumpert, "Measurement of Electroweak Gauge Boson Scattering in the Channel $pp \to W^{\pm}W^{\pm}jj$ with the ATLAS Detector at the Large Hadron Collider," 2014. https://cds.cern.ch/record/2003240. Presented 27 Feb 2015.

[56] B. Biedermann, A. Denner, and M. Pellen, "Large electroweak corrections to vector-boson scattering at the Large Hadron Collider," *Phys. Rev. Lett.* **118** no. 26, (2017) 261801, arXiv:1611.02951 [hep-ph].

[57] A. Ballestrero *et al.*, "Precise predictions for same-sign W-boson scattering at the LHC," *Eur. Phys. J. C* **78** no. 8, (2018) 671, arXiv:1803.07943 [hep-ph].

[58] R. Covarelli, M. Pellen, and M. Zaro, "Vector-Boson scattering at the LHC: Unraveling the electroweak sector," *Int. J. Mod. Phys. A* **36** no. 16, (2021) 2130009, arXiv:2102.10991 [hep-ph].

[59] B. Biedermann, A. Denner, and M. Pellen, "Complete NLO corrections to W^+W^+ scattering and its irreducible background at the LHC," *JHEP* **10** (2017) 124, arXiv:1708.00268 [hep-ph].

[60] ATLAS Collaboration, "Evidence for Electroweak Production of $W^{\pm}W^{\pm}jj$ in pp Collisions at $\sqrt{s} = 8$ TeV with the ATLAS Detector," *Phys. Rev. Lett.* **113** (2014) 141803, arXiv:1405.6241 [hep-ex].

[61] CMS Collaboration, "Study of vector boson scattering and search for new physics in events with two same-sign leptons and two jets," *Phys. Rev. Lett.* **114** (2015) 051801, arXiv:1410.6315 [hep-ex].

[62] CMS Collaboration, "Observation of Electroweak Production of Same-Sign W Boson Pairs in the Two Jet and Two Same-Sign Lepton Final State in Proton–Proton Collisions at 13 TeV," *Phys. Rev. Lett.* **120** (2018) 081801, arXiv:1709.05822 [hep-ex].

[63] ATLAS Collaboration, "Observation of Electroweak Production of a Same-Sign W Boson Pair in Association with Two Jets in pp Collisions at $\sqrt{s} = 13$ TeV with the ATLAS Detector," *Phys. Rev. Lett.* **123** (2019) 161801, arXiv:1906.03203 [hep-ex].

[64] A. Collaboration, "Support note for measurement of fiducial and differential $W^{\pm}W^{\pm}$jj production cross-sections at $\sqrt{s} = 13$ TeV using the full Run-2 dataset," tech. rep., CERN, Geneva, 2021. https://cds.cern.ch/record/2790652.

[65] CMS Collaboration, "Measurements of production cross sections of WZ and same-sign WW boson pairs in association with two jets in proton–proton collisions at $\sqrt{s} = 13$ TeV," *Phys. Lett. B* **809** (2020) 135710, arXiv:2005.01173 [hep-ex].

[66] W. Stirling and E. Vryonidou, "Electroweak gauge boson polarisation at the LHC," *JHEP* **07** (2012) 124, arXiv:1204.6427 [hep-ph].

[67] O. S. Brüning, P. Collier, P. Lebrun, S. Myers, R. Ostojic, J. Poole, and P. Proudlock, *LHC Design Report*. CERN Yellow Reports: Monographs. CERN, Geneva, 2004. https://cds.cern.ch/record/782076.

[68] O. S. Brüning, P. Collier, P. Lebrun, S. Myers, R. Ostojic, J. Poole, and P. Proudlock, *LHC Design Report*. CERN Yellow Reports: Monographs. CERN, Geneva, 2004. https://cds.cern.ch/record/815187.

[69] M. Benedikt, P. Collier, V. Mertens, J. Poole, and K. Schindl, *LHC Design Report*. CERN Yellow Reports: Monographs. CERN, Geneva, 2004. https://cds.cern.ch/record/823808.

[70] "LHC Machine," *JINST* **3** (2008) S08001.

[71] F. Hasert *et al.*, [Gargamelle Neutrino], "Observation of Neutrino-Like Interactions Without Muon or Electron in the Gargamelle Neutrino Experiment," *Phys. Lett. B* **46** (1973) 138–140.

[72] G. Arnison *et al.*, [UA1], "Experimental Observation of Isolated Large Transverse Energy Electrons with Associated Missing Energy at $\sqrt{s} = 540$ GeV," *Phys. Lett. B* **122** (1983) 103–116.

[73] M. Banner *et al.*, [UA2], "Observation of Single Isolated Electrons of High Transverse Momentum in Events with Missing Transverse Energy at the CERN anti-p p Collider," *Phys. Lett. B* **122** (1983) 476–485.

[74] G. Arnison *et al.*, [UA1], "Experimental Observation of Lepton Pairs of Invariant Mass Around 95-GeV/c^2*attheCERNSPSCollider*," *Phys.Lett.B*126(1983)398 – –410.

[75] P. Bagnaia *et al.*, [UA2], "Evidence for $Z^0 \to e^+e^-$ at the CERN $\bar{p}p$ Collider," *Phys. Lett. B* **129** (1983) 130–140.

[76] *LEP design report*. Report. CERN, Geneva, 1984. https://cds.cern.ch/record/102083.

[77] F. Landua, "The CERN accelerator complex layout in 2022. Complexe des accélérateurs du CERN en janvier 2022,". https://cds.cern.ch/record/2813716. General Photo.

[78] M. Vretenar, J. Vollaire, R. Scrivens, C. Rossi, F. Roncarolo, S. Ramberger, U. Raich, B. Puccio, D. Nisbet, R. Mompo, S. Mathot, C. Martin, L. A. Lopez-Hernandez, A. Lombardi, J. Lettry, J. B. Lallement, I. Kozsar, J. Hansen, F. Gerigk, A. Funken, J. F. Fuchs, N. Dos Santos, M. Calviani, M. Buzio, O. Brunner, Y. Body, P. Baudrenghien, J. Bauche, and T. Zickler, *Linac4 design report*, vol. 6 of *CERN Yellow Reports: Monographs*. CERN, Geneva, 2020. https://cds.cern.ch/record/2736208.

[79] "Design Report Tevatron 1 project,".

[80] ATLAS Collaboration, "ATLAS Luminosity Public Results: Run 3." HTTPS://TWIKI.CERN.CH/TWIKI/BIN/VIEW/ATLASPUBLIC/LUMINOSITYPUBLICRESULTSRUN3, 2025. Accessed: 2025-11-06.

[81] ATLAS Collaboration, "The ATLAS Experiment at the CERN Large Hadron Collider," *JINST* **3** (2008) S08003.

[82] CMS Collaboration, "The CMS Experiment at the CERN LHC," *JINST* **3** (2008) S08004.

[83] A. A. Alves, Jr. *et al.*, [LHCb], "The LHCb Detector at the LHC," *JINST* **3** (2008) S08005.

[84] K. Aamodt *et al.*, [ALICE], "The ALICE experiment at the CERN LHC," *JINST* **3** (2008) S08002.

[85] G. Anelli *et al.*, [TOTEM], "The TOTEM experiment at the CERN Large Hadron Collider," *JINST* **3** (2008) S08007.

[86] O. Adriani *et al.*, [LHCf], "The LHCf detector at the CERN Large Hadron Collider," *JINST* **3** (2008) S08006.

[87] [MoEDAL], J. Pinfold, R. Soluk, Y. Yao, S. Cecchini, G. Giacomelli, M. Giorgini, L. Patrizii, G. Sirri, D. H. Lacarrère, K. Kinoshita, J. Jakubek, M. Platkevic, S. Pospísil, Z. Vykydal, T. Hott, A. Houdayer, C. Leroy, J. Swain, D. Felea, D. Hasegan, G. E. Pavalas, and V. Popa, "Technical Design Report of the MoEDAL Experiment," tech. rep., 2009. https://cds.cern.ch/record/1181486.

[88] CERN, "The HL-LHC project." HTTPS://HILUMILHC.WEB.CERN.CH/CONTENT/HL-LHC-PROJECT, 2025. Accessed: 2025-10-06.

[89] A. Abada *et al.*, [FCC], "FCC-ee: The Lepton Collider: Future Circular Collider Conceptual Design Report Volume 2," *Eur. Phys. J. ST* **228** no. 2, (2019) 261–623.

[90] W. Abdallah *et al.*, [CEPC Study Group], "CEPC Technical Design Report: Accelerator," *Radiat. Detect. Technol. Methods* **8** no. 1, (2024) 1–1105, arXiv:2312.14363 [physics.acc-ph]. [Erratum: Radiat.Detect.Technol.Methods 9, 184–192 (2025)].

[91] P. Bambade *et al.*, "The International Linear Collider: A Global Project," arXiv:1903.01629 [hep-ex].

[92] D. Neuffer and V. Shiltsev, "On the feasibility of a pulsed 14 TeV c.m.e. muon collider in the LHC tunnel," *JINST* **13** no. 10, (2018) T10003, arXiv:1811.10694 [physics.acc-ph].

[93] ATLAS Collaboration, "ATLAS Detector and Physics Performance: Technical Design Report, Volume 1," 1999. https://cds.cern.ch/record/391176.

[94] ATLAS Collaboration, "ATLAS Detector and Physics Performance: Technical Design Report, Volume 2," 1999. https://cds.cern.ch/record/391177.

[95] ATLAS Collaboration, "ATLAS: Letter of Intent for a General-Purpose pp Experiment at the Large Hadron Collider at CERN," 1992. https://cds.cern.ch/record/291061.

[96] J. Pequenao, "Computer generated image of the whole ATLAS detector." 2008.

[97] ATLAS Collaboration, "ATLAS Inner Detector: Technical Design Report, Volume 1," 1997. https://cds.cern.ch/record/331063.

[98] ATLAS Collaboration, "ATLAS Inner Detector: Technical Design Report, Volume 2," 1997. https://cds.cern.ch/record/331064.

[99] J. Pequenao, "Computer generated image of the ATLAS inner detector." 2008.

[100] [ATLAS], K. Potamianos, "The upgraded Pixel detector and the commissioning of the Inner Detector tracking of the ATLAS experiment for Run-2 at the Large Hadron Collider," tech. rep., CERN, Geneva, 2016. arXiv:1608.07850. https://cds.cern.ch/record/2209070. 15 pages, EPS-HEP 2015 Proceedings.

[101] ATLAS Collaboration, "ATLAS Pixel Detector: Technical Design Report," 1998. https://cds.cern.ch/record/381263.

[102] ATLAS Collaboration, "ATLAS Insertable B-Layer Technical Design Report," 2010. https://cds.cern.ch/record/1291633.

[103] A. Abdesselam *et al.*, "The barrel modules of the ATLAS semiconductor tracker," *Nucl. Instrum. Meth. A* **568** (2006) 642–671.

[104] A. Abdesselam *et al.*, [ATLAS], "The ATLAS semiconductor tracker end-cap module," *Nucl. Instrum. Meth. A* **575** (2007) 353–389.

[105] E. Abat *et al.*, [ATLAS TRT], "The ATLAS TRT barrel detector," *JINST* **3** (2008) P02014.

[106] E. Abat *et al.*, "The ATLAS TRT end-cap detectors," *JINST* **3** (2008) P10003.

[107] ATLAS Collaboration, "ATLAS Inner Tracker Strip Detector: Technical Design Report," 2017. https://cds.cern.ch/record/2257755.

[108] ATLAS Collaboration, "ATLAS Inner Tracker Pixel Detector: Technical Design Report," 2017. https://cds.cern.ch/record/2285585.

[109] ATLAS Collaboration, "A High-Granularity Timing Detector for the ATLAS Phase-II Upgrade: Technical Design Report," 2020. https://cds.cern.ch/record/2719855.

[110] ATLAS Collaboration, "ATLAS Calorimeter Performance: Technical Design Report," 1996. https://cds.cern.ch/record/331059.

[111] ATLAS Collaboration, "ATLAS Liquid Argon Calorimeter: Technical Design Report," 1996. https://cds.cern.ch/record/331061.

[112] ATLAS Collaboration, "ATLAS Tile Calorimeter: Technical Design Report," 1996. https://cds.cern.ch/record/331062.

[113] J. Pequenao, "Computer Generated image of the ATLAS calorimeter." 2008.

[114] ATLAS Collaboration, "ATLAS Muon Spectrometer: Technical Design Report," 1997. https://cds.cern.ch/record/331068.

[115] J. Pequenao, "Computer generated image of the ATLAS Muons subsystem." 2008.

[116] ATLAS Collaboration, "ATLAS New Small Wheel: Technical Design Report," 2013. https://cds.cern.ch/record/1552862.

[117] ATLAS Collaboration, "ATLAS Magnet System: Magnet Project Technical Design Report, Volume 1," 1997. https://cds.cern.ch/record/338080.

[118] ATLAS Collaboration, "ATLAS Barrel Toroid: Magnet Project Technical Design Report, Volume 2," 1997. https://cds.cern.ch/record/331065.

[119] ATLAS Collaboration, "ATLAS End-Cap Toroids: Magnet Project Technical Design Report, Volume 3," 1997. https://cds.cern.ch/record/331066.

[120] ATLAS Collaboration, "ATLAS Central Solenoid: Magnet Project Technical Design Report, Volume 4," 1997. https://cds.cern.ch/record/331067.

[121] J. Goodson, "Magnet systems." http://www.jetgoodson.com/images/thesisImages/magnetSystems.png, n.d. Accessed: 2025-10-06.

[122] [ATLAS Collaboration], "Luminosity determination in pp collisions at $\sqrt{s} = 13$ TeV using the ATLAS detector at the LHC," tech. rep., CERN, Geneva, Jun, 2019. https://cds.cern.ch/record/2677054. All figures including auxiliary figures are available at https://atlas.web.cern.ch/Atlas/GROUPS/PHYSICS/CONFNOTES/ATLAS-CONF-2019-021.

[123] P. Jenni and M. Nessi, "ATLAS Forward Detectors for Luminosity Measurement and Monitoring," tech. rep., CERN, Geneva, 2004. https://cds.cern.ch/record/721908. revised version number 1 submitted on 2004-03-22 14:56:11.

[124] P. Grafström and W. Kozanecki, "Luminosity determination at proton colliders," *Prog. Part. Nucl. Phys.* **81** (2015) 97–148.

[125] ATLAS Collaboration, "ATLAS High-Level Trigger, Data Acquisition and Controls: Technical Design Report," 2003. https://cds.cern.ch/record/616089.

[126] ATLAS Collaboration, "ATLAS Level-1 Trigger: Technical Design Report," 1998. https://cds.cern.ch/record/381429.

[127] G. Aad *et al.*, [ATLAS], "Operation of the ATLAS trigger system in Run 2," *JINST* **15** no. 10, (2020) P10004, arXiv:2007.12539 [physics.ins-det].

[128] B. J. Gallop, "ATLAS SCT Readout and Barrel Macro-assembly Testing and Design of MAPS Test Structures," 2005. https://cds.cern.ch/record/2137993.

[129] D. Duvnjak, "Search for Supersymmtery in Final States with 2 or 3 Leptons with Data collected by the ATLAS Experiment," 2020. https://cds.cern.ch/record/2767791. Presented 09 Mar 2021.

[130] M. Aaboud *et al.*, [ATLAS], "Performance of the ATLAS Track Reconstruction Algorithms in Dense Environments in LHC Run 2," *Eur. Phys. J. C* **77** no. 10, (2017) 673, arXiv:1704.07983 [hep-ex].

[131] T. Cornelissen, M. Elsing, I. Gavrilenko, W. Liebig, E. Moyse, and A. Salzburger, "The new ATLAS track reconstruction (NEWT)," *J. Phys. Conf. Ser.* **119** (2008) 032014.

[132] M. Aaboud *et al.*, [ATLAS], "Reconstruction of primary vertices at the ATLAS experiment in Run 1 proton–proton collisions at the LHC," *Eur. Phys. J. C* **77** no. 5, (2017) 332, arXiv:1611.10235 [physics.ins-det].

[133] [fortheATLAS], F. Meloni, "Primary vertex reconstruction with the ATLAS detector," Tech. Rep. 12, CERN, Geneva, 2016. https://cds.cern.ch/record/2222390.

[134] T. G. Cornelissen, N. Van Eldik, M. Elsing, W. Liebig, E. Moyse, N. Piacquadio, K. Prokofiev, A. Salzburger, and A. Wildauer, "Updates of the ATLAS Tracking Event Data Model (Release 13)," tech. rep., CERN, Geneva, 2007. https://cds.cern.ch/record/1038095. All figures including auxiliary figures are

available at https://atlas.web.cern.ch/Atlas/GROUPS/PHYSICS/PUBNOTES/ATL-SOFT-PUB-2007-003.

[135] J. Pequenao and P. Schaffner, "How ATLAS detects particles: diagram of particle paths in the detector." 2013.

[136] [ATLAS], "Electron efficiency measurements with the ATLAS detector using the 2015 LHC proton-proton collision data," tech. rep., CERN, Geneva, 2016. https://cds.cern.ch/record/2157687. All figures including auxiliary figures are available at https://atlas.web.cern.ch/Atlas/GROUPS/PHYSICS/CONFNOTES/ATLAS-CONF-2016-024.

[137] M. Aaboud *et al.*, [ATLAS], "Electron and photon energy calibration with the ATLAS detector using 2015–2016 LHC proton-proton collision data," *JINST* **14** no. 03, (2019) P03017, arXiv:1812.03848 [hep-ex].

[138] [ATLAS], "Electron and photon energy calibration with the ATLAS detector using data collected in 2015 at $\sqrt{s} = 13$ TeV," tech. rep., CERN, Geneva, 2016. https://cds.cern.ch/record/2203514. All figures including auxiliary figures are available at https://atlas.web.cern.ch/Atlas/GROUPS/PHYSICS/PUBNOTES/ATL-PHYS-PUB-2016-015.

[139] G. Aad *et al.*, [ATLAS], "Muon reconstruction and identification efficiency in ATLAS using the full Run 2 pp collision data set at $\sqrt{s} = 13$ TeV," *Eur. Phys. J. C* **81** no. 7, (2021) 578, arXiv:2012.00578 [hep-ex].

[140] M. Cacciari, G. P. Salam, and G. Soyez, "The anti-k_t jet clustering algorithm," *JHEP* **04** (2008) 063, arXiv:0802.1189 [hep-ph].

[141] M. Aaboud *et al.*, [ATLAS], "Jet reconstruction and performance using particle flow with the ATLAS Detector," *Eur. Phys. J. C* **77** no. 7, (2017) 466, arXiv:1703.10485 [hep-ex].

[142] G. P. Salam, "Towards Jetography," *Eur. Phys. J. C* **67** (2010) 637–686, arXiv:0906.1833 [hep-ph].

[143] G. Aad *et al.*, [ATLAS], "Jet energy scale and resolution measured in proton–proton collisions at $\sqrt{s} = 13$ TeV with the ATLAS detector," *Eur. Phys. J. C* **81** no. 8, (2021) 689, arXiv:2007.02645 [hep-ex].

[144] G. Aad *et al.*, [ATLAS], "ATLAS b-jet identification performance and efficiency measurement with $t\bar{t}$ events in pp collisions at $\sqrt{s} = 13$ TeV," *Eur. Phys. J. C* **79** no. 11, (2019) 970, arXiv:1907.05120 [hep-ex].

[145] G. Aad *et al.*, [ATLAS], "ATLAS flavour-tagging algorithms for the LHC Run 2 pp collision dataset," *Eur. Phys. J. C* **83** no. 7, (2023) 681, arXiv:2211.16345 [physics.data-an].

[146] M. Aaboud *et al.*, [ATLAS], "Performance of missing transverse momentum reconstruction with the ATLAS detector using proton-proton collisions at $\sqrt{s}$ = 13 TeV," *Eur. Phys. J. C* **78** no. 11, (2018) 903, arXiv:1802.08168 [hep-ex].

[147] G. Aad *et al.*, [ATLAS], "Performance of electron and photon triggers in ATLAS during LHC Run 2," *Eur. Phys. J. C* **80** no. 1, (2020) 47, arXiv:1909.00761 [hep-ex].

[148] G. Aad *et al.*, [ATLAS], "Performance of the ATLAS muon triggers in Run 2," *JINST* **15** no. 09, (2020) P09015, arXiv:2004.13447 [physics.ins-det].

[149] G. Aad *et al.*, [ATLAS], "Performance of pile-up mitigation techniques for jets in pp collisions at $\sqrt{s} = 8$ TeV using the ATLAS detector," *Eur. Phys. J. C* **76** no. 11, (2016) 581, arXiv:1510.03823 [hep-ex].

[150] L. Nedic, *Probing polarised production of two same-charge W± bosons produced in association with two jets with the ATLAS detector*. PhD thesis, University of Oxford, 2025.

[151] M. Aaboud *et al.*, [ATLAS], "Observation of electroweak production of a same-sign W boson pair in association with two jets in pp collisions at $\sqrt{s} = 13$ TeV with the ATLAS detector," *Phys. Rev. Lett.* **123** no. 16, (2019) 161801, arXiv:1906.03203 [hep-ex].

[152] G. Aad *et al.*, [ATLAS], "Electron and photon performance measurements with the ATLAS detector using the 2015–2017 LHC proton-proton collision data," *JINST* **14** no. 12, (2019) P12006, arXiv:1908.00005 [hep-ex].

[153] C. Anastopoulos, J.-F. Arguin, C. Becot, O. Dartsi, L. Di Ciaccio, A. Fell, L. M. Flores, D. Godin, S. Heim, J. Kroll, Y. Liu, K. Lohwasser, K. Mochizuki, E. Monnier, M. Muskinja, A. Petridis, P. Podberezko, T. D. Powell, P. Pralavorio, J. Reichert, E. M. Ruettinger, A. Sharma, P. Sommer, G. Tarna, S. J. Thais, E. Thomson, A. Trofymov, and H. Xu, "Electron identification and efficiency measurements in 2017 data," tech. rep., CERN, Geneva, 2019. https://cds.cern.ch/record/2652163.

[154] N. A. Asbah, "Search for the production of a standard model higgs boson in association with top-quarks and decaying into a pair of bottom-quarks with 13 tev atlas data," Nov., 2018.

[155] D. Buarque Franzosi, O. Mattelaer, R. Ruiz, and S. Shil, "Automated predictions from polarized matrix elements," *JHEP* **04** (2020) 082, arXiv:1912.01725 [hep-ph].

[156] P. Jain, "Polarized same-sign *ww*: wrong polarization assignment for final states with tau leptons," Sep, 2021. https://answers.launchpad.net/mg5amcnlo/+question/698671. Accessed: 2025-11-18.

[157] G. Aad *et al.*, [ATLAS], "The ATLAS Simulation Infrastructure," *Eur. Phys. J. C* **70** (2010) 823–874, arXiv:1005.4568 [physics.ins-det].

[158] G. Aad *et al.*, [ATLAS], "ATLAS data quality operations and performance for 2015–2018 data-taking," *JINST* **15** no. 04, (2020) P04003, arXiv:1911.04632 [physics.ins-det].

[159] ATLAS Collaboration, "Luminosity public results run2." https://twiki.cern.ch/twiki/bin/view/AtlasPublic/LuminosityPublicResultsRun2.

[160] G. Aad *et al.*, [ATLAS], "Observation and measurement of Higgs boson decays to WW* with the ATLAS detector," *Phys. Rev. D* **92** no. 1, (2015) 012006, arXiv:1412.2641 [hep-ex].

[161] D. Rainwater, R. Szalapski, and D. Zeppenfeld, "Probing color-singlet exchange in Z + 2-jet events at the CERN LHC," *Phys. Rev. D* **54** (1996) 6680–6689, arXiv:hep-ph/9605444.

[162] K. Doroba, J. Kalinowski, J. Kuczmarski, S. Pokorski, J. Rosiek, M. Szleper, and S. Tkaczyk, "The $W_L W_L$ Scattering at the LHC: Improving the Selection Criteria," *Phys. Rev. D* **86** (2012) 036011, arXiv:1201.2768 [hep-ph].

[163] X. Glorot, A. Bordes, and Y. Bengio, "Deep sparse rectifier neural networks," in *Proceedings of the Fourteenth International Conference on Artificial Intelligence and Statistics*, G. Gordon, D. Dunson, and M. Dudík, eds., vol. 15 of *Proceedings of Machine Learning Research*, pp. 315–323. PMLR, Fort Lauderdale, FL, USA, 11–13 apr, 2011. http://proceedings.mlr.press/v15/glorot11a.html.

[164] N. Srivastava, G. Hinton, A. Krizhevsky, I. Sutskever, and R. Salakhutdinov, "Dropout: A simple way to prevent neural networks from overfitting," *Journal of Machine Learning Research* **15** no. 56, (2014) 1929–1958. http://jmlr.org/papers/v15/srivastava14a.html.

[165] D. P. Kingma and J. Ba, "Adam: A method for stochastic optimization," 2014.

[166] T. Akiba, S. Sano, T. Yanase, T. Ohta, and M. Koyama, "Optuna: A next-generation hyperparameter optimization framework," in *Proceedings of the 25th ACM SIGKDD International Conference on Knowledge Discovery and Data Mining*. 2019.

[167] C. Molnar, *Interpretable Machine Learning*. 2 ed., 2022. https://christophm.github.io/interpretable-ml-book.

[168] [ROOT], K. Cranmer, G. Lewis, L. Moneta, A. Shibata, and W. Verkerke, "HistFactory: A tool for creating statistical models for use with RooFit and RooStats," tech. rep., New York U., New York, 2012. https://cds.cern.ch/record/1456844.

[169] W. Verkerke and D. Kirkby, "The roofit toolkit for data modeling," 2003. https://arxiv.org/abs/physics/0306116.

[170] L. Moneta, K. Belasco, K. Cranmer, S. Kreiss, A. Lazzaro, D. Piparo, G. Schott, W. Verkerke, and M. Wolf, "The roostats project," 2011. https://arxiv.org/abs/1009.1003.

[171] G. Cowan, K. Cranmer, E. Gross, and O. Vitells, "Asymptotic formulae for likelihood-based tests of new physics," *Eur. Phys. J. C* **71** (2011) 1554, arXiv:1007.1727 [physics.data-an].

[172] S. S. Wilks, "The large-sample distribution of the likelihood ratio for testing composite hypotheses," *Ann. Math.Stat.* **9** (1938) 60–62.

[173] A. L. Read, "Presentation of search results: the CL_S technique," *J. Phys. G* **28** (2002) 2693.

[174] M. Aaboud *et al.*, [ATLAS], "Observation of electroweak $W^{\pm}Z$ boson pair production in association with two jets in pp collisions at $\sqrt{s} = 13$ TeV with the ATLAS detector," *Phys. Lett. B* **793** (2019) 469–492, arXiv:1812.09740 [hep-ex].

Erklärung

Hiermit versichere ich, die eingereichte Dissertation selbstständig verfasst und keine anderen als die von mir angegebenen Quellen und Hilfsmittel benutzt zu haben. Wörtlich oder inhaltlich verwendete Quellen wurden entsprechend den anerkannten Regeln wissenschaftlichen Arbeitens (lege artis) zitiert. Ich erkläre weiterhin, dass die vorliegende Arbeit noch nicht anderweitig als Dissertation eingereicht wurde.

Freiburg, den 13. February 2026



Prasham Jain